Superconductivity. Lecture Notes of Basic Courses

Andersen, N.H.; Mortensen, K.

Publication date:
1988

Document Version
Publisher's PDF, also known as Version of record

Link back to DTU Orbit

Citation (APA):
Andersen, N. H., & Mortensen, K. (Eds.) (1988). *Superconductivity. Lecture Notes of Basic Courses*. Roskilde: Risø National Laboratory. Risø-M, No. 2756

Risø-M-2756

RISØ

Risø-M-2756

DK89C0171 - DK89C0178

Superconductivity

Lecture notes of basic courses presented at

1st Topsøe Summer School on Superconductivity

Editors: N. H. Andersen and K. Mortensen
Physics Department

Risø National Laboratory, DK-4000 Roskilde, Denmark
December 1988

DK 89C0171 - DK 89C0178

Risø-M-2756

SUPERCONDUCTIVITY

D: 8903002164

n 223

Lecture notes of basic courses presented at
1st Topsøe Summer School on Superconductivity

Editors: N.H. Andersen and K. Mortensen
Physics Department

Abstract This report contains lecture notes of the basic lectures presented at the 1st Topsøe Summer School on Superconductivity held at Risø National Laboratory, June 20-24, 1988. The following lecture notes are included: L.M. Falicov: "Superconductivity: Phenomenology", A. Bohr and O. Ulfbeck: "Quantal structure of superconductivity. Gauge angle", G. Aeppli: "Muons, neutrons and superconductivity", N.F. Pedersen: "The Josephson junction", C. Michel: "Physicochemistry of high-T_c superconductors", C. Laverick and J.K. Hulm: "Manufacturing and application of superconducting wires", J. Clarke: "SQUID concepts and systems"

December 1988
Risø National Laboratory, DK-4000 Roskilde, Denmark

ISBN 87-550-1477-1
ISSN 0418-6435

Grafisk Service, Risø 1988

1/2

CONTENTS

LECTURE NOTES OF 1st TOPSØE SUMMER SCHOOL ON SUPERCONDUCTIVITY

Preface

The Topsøe Summer Schools have been initiated by the Danish Research Academy in co-operation with the Haldor Topsøe Corporation in an attempt to stimulate the recruitment of young scientists. The Topsøe Summer Schools will be organized in co-operation with Danish universities and research institutes.

The 1st Topsøe Summer School on Superconductivity was organized by and held at Risø National Laboratory, June 20-24, 1988. Superconductivity is a basic disciplin in solid state physics and may as such be justified as a topic for a summer school. It is obvious, however, that the recent discovery of high temperature ceramic superconductors has stimulated the interest for this field of research both on a basic scientific level and with respect to applications. Two major questions appear: What is the origin of superconductivity in high temperature ceramic superconductors, and to what extend will the overwhelming expectations of their technological applications come true? Many scientists in basic and applied physics and chemistry will inevitably face these questions for quite some time in the future. With this in mind SUPERCONDUCTIVITY became a natural choice of topic for the 1st Topsøe Summer School. Future Topsøe Summer Schools comprise: "Physics of small storage rings" to be held at the Institute of Physics, University of Århus, 1989, and "Applied mathematically advanced computer models" in 1990.

The format of the School was basic lectures on superconductivity in the mornings and practical experiments in the afternoons, except for one day which was devoted to: "Workshop on Ceramic Superconductors". During the workshop review lectures, summarizing the evolution and current understanding, as well as presentations of the most recent experimental and theoretical advances in the study of the high temperature superconductors were given, and the participants had the opportunity to present their own work during a poster session.

The basic course on superconductivity comprised the following lectures:

G. Aeppli, AT&T Bell Laboratories:	**Muons, Neutrons and Superconductivity.**
K. Beckgaard, Univ. of Copenhagen:	**Superconducting Molecular Solids.**
J. Clarke, Berkeley:	**SQUID - Magnetometers.**
L.M. Falicov, Berkeley	**Superconductivity: Phenomenology.**
C. Laverick, Private Company:	**Manufacture and Application of Superconducting Wires.**
C. Michel, University of Caen:	**Physiochemistry of High-T_c Superconductors.**
N.F. Pedersen, Technical Univ. of Denmark:	**The Josephson Effect.**
O. Ulfbeck, Niels Bohr Institute:	**Quantal Structure of Superconductivity.**

The workshop lectures included:

S. Amelinckx, University of Antwerp:	**The Study of High-T_c Superconductors by Means of High Resolution Electron Microscopy and Electron Diffraction.**
D.J. Bishop, AT&T Bell Laboratories:	**Ultrasound and Torsional Oscillator Measurements on Superconductors.**
L.M. Falicov, Berkeley:	**Models for High-T_c Superconductivity.**
J.D. Jorgensen, Argonne National Laboratory:	**Noval Structural Properties of High-T_c Superconductors.**
H.R. Ott, ETH, Zurich:	**Some Low Temperature Properties of High-T_c Superpconductors.**
P.H. Wu, Nanjing University:	**High-Tc Superconducting Devices for High Frequency Applications: New Chances and New Challenges.**

The experimental exercises dealt with:

Synthesis and Characterization
Neutron Diffraction
Transport- and Magnetic Properties
Josephson Effects

Organization and guidance of experimental exercises were performed by:

J. Als-Nielsen, Risø National Laboratory
N. Hessel Andersen, Risø National Laboratory
J.B. Bilde-Sørensen, Risø National Laboratory
K.N. Clausen, Risø National Laboratory
C. Schelde Jacobsen, Technical University of Denmark
C. Thune Jacobsen, University of Copenhagen
I. Johannsen, University of Copenhagen
W. Kofoed, Risø National Laboratory
J. Gutzon Larsen, Haldor Topsøe Corporation
B. Lebech, Risø National Laboratory
M.T. Levinsen, University of Copenhagen
M. Nielsen, Risø National Laboratory

The present set of notes cover most of the lectures given on the basal courses on superconductivity. They intend to give the students a reference to the lectures presented at the School and more generally to the literature on superconductivity. It is the hope that they may serve as guide and inspiration for further studies of the basic properties of superconductivity and the many possible applications of superconducting materials and devices.

Preliminary notes for all the lectures, essentially based on the lecturers's viewgraphs, were distributed during the School. These and the guides to the experimental exercises are available on request.

The organizing committee of the School was:

J. Als-Nielsen, Risø National Laboratory
N. Hessel Andersen (head), Risø National Laboratory
J. Bøttiger, Århus University
N. Falsig Pedersen, Technical University of Denmark
J.K. Kjems, Risø National Laboratory
M.T. Levinsen, Copenhagen University
K. Mortensen, Risø National Laboratory
M. Nielsen, Risø National Laboratory
H. Topsøe, Haldor Topsøe Corporation

Secretary of the School was:

G. Olesen, Risø National Laboratory
assisted by: K. Kjøller and B. Laursen, Risø National Laboratory

On behalf of the organizing committee we would like to thank the lecturers for the inspiring lectures they presented and thereby gave decisive contributions for a successful School. Special thanks are expressed to the lecturers on the basic courses who have taken the time to prepare these lecture notes..

Risø, December 1988

N. Hessel Andersen and K. Mortensen
Editors

CHAPTER 1

SUPERCONDUCTIVITY: PHENOMENOLOGY

L. M. Falicov

Department of Physics,
University of California,
Berkeley, California, 94720,
U.S.A.

and

Materials and Chemical Sciences Division,
Lawrence Berkeley Laboratory
Berkeley, California, 94720,
U.S.A.

ABSTRACT

I.- THE SUPERCONDUCTING STATE.

(a) The superconducting transition temperature; (b) Zero resistivity; (c) The Meissner effect; (d) The isotope effect; (e) Microwave and optical properties; (f) The superconducting energy gap.

II.- THE GINZBURG-LANDAU EQUATIONS.

(a) The coherence length; (b) The penetration depth; (c) Flux quantization; (d) Magnetic-field dependence of the energy gap; (e) Quantum interference phenomena; (f) The Josephson effect.

August 2, 1988

SUPERCONDUCTIVITY: PHENOMENOLOGY

L. M. Falicov

Department of Physics,
University of California,
Berkeley, California, 94720,
U.S.A.

and

Materials and Chemical Sciences Division,
Lawrence Berkeley Laboratory
Berkeley, California, 94720,
U.S.A.

I. THE SUPERCONDUCTING STATE.

IA. Background Information.

SUPERCONDUCTIVITY is a phase, a state of matter (in the sense that ice and steam are phases of water and diamond and graphite are phases of pure carbon) observed *only* in some solids, mostly metals [1-3].

The SUPERCONDUCTING STATE has several characteristic properties:

1.- When it exists for a given substance, it exists only at temperatures below a so-called TRANSITION TEMPERATURE, T_c, and in general down to the absolute zero of the temperature scale ($0\,K = -273.15\ \ C$).

2.- It exhibits *d.c.* ZERO RESISTIVITY, i.e. infinite conductivity for zero-frequency measurements (an effect discovered in mercury by Kamerlingh Onnes in 1911),

$$\rho(\omega = 0; T < T_c) = 0 \ . \qquad (1)$$

3.- It exhibits, for weak magnetic fields, perfect DIAMAGNETISM, i.e. its magnetic susceptibility in Gaussian units is given by

$$\chi_M = - (1/4\pi) \;. \tag{2}$$

which means that magnetic flux lines are completely expelled from the superconductor and that there is a force pushing superconductors away from magnetic fields. This effect, known as the MEISSNER EFFECT, was discovered by Meissner and Ochsenfeld in 1933.

4.- There is a minimum energy value – called an ENERGY GAP [4] – for exciting *electronically* the system away from its state of lowest energy (the so-called ground state). This energy gap

$$E_G = 2|\Delta| \;, \tag{3}$$

was conjectured theoretically by F. London in 1935, deduced from thermodynamic data in 1946, observed by infrared measurements in 1957 and by electron tunneling in 1960.

Infrared absorption measurements in 1937, down to frequencies of the order of 10^{14} cycles per second showed no differences between the normal and superconducting phases. Microwave measurements by H. London in 1940 gave no appreciable absorption of electromagnetic radiation by superconductors up to a frequency of 10^{9} cycles per second. These two experiments together gave upper and lower bounds to the superconducting energy gap.

In 1957 Glover and Tinkham were successful in reaching the far infrared region of the electromagnetic spectrum and observed, for lead, a sudden drop in the absorption as the frequency was decreased.

In 1960 Giaever discovered that the current/voltage characteristics of sandwiches consisting of a superconductor and either another superconductor or a normal metal, separated by a thin oxide insulating layer were nonlinear, and that the non-linearity could be easily interpreted in terms of an energy gap in the spectrum of the superconductor(s).

5.- There is a surprising dependence on the transition temperature, T_c, on the isotopic mass of the atomic nuclei of the superconductor. (It is surprising that a phase which is electric and magnetic in nature, and therefore caused by the *electrons*, depends in any fashion on nuclear parameters, in particular the mass of the *nuclei*.) This is the so-called ISOTOPE EFFECT, was discovered in 1950, and establishes that

$$M^{\alpha} \cdot T_c = constant \ , \tag{4}$$

where M is the nuclear mass and, for various metals, the exponent α takes the values:

0.485 for Pb, 0.415 for Sn, 0.150 for Ti, 0.065 for Ru, and -0.015 for Ir.

6.- In addition to the effect of high temperatures, superconductivity can be destroyed (with a return to the normal state) by either a large enough electric current $I > I_c$, or a large enough magnetic field $H > H_{c2}$. (It should be mentioned that in some superconductors, the so-called type II superconductors, for intermediate field strengths $H_{c1} < H < H_{c2}$, the magnetic flux lines partially penetrate the superconductor but do not destroy the superconducting state.) The quantities I_c, H_{c1}, and H_{c2}, are called the CRITICAL CURRENT, and the first and second CRITICAL MAGNETIC FIELDS, respectively.

7.- Superconductivity is a MACROSCOPIC QUANTUM PHENOMENON, with amplitudes and phases associated with the energy gap parameter Δ. Therefore interference and diffraction effects can be achieved, in particular the JOSEPHSON EFFECT [3]. These effects can be fruitfully employed in processing, storing, and retrieving information, i.e. in computer technology.

IB. Theory.

The currently, universally accepted theory of superconductivity, known as the BCS THEORY was formulated [5] by Bardeen, Cooper and Schrieffer in 1957. The theory in its most general form states that, if metallic mobile electrons interact ATTRACTIVELY with each other, then they will condense into a ground state with:

(1) an energy gap in the excitation spectrum;

(2) zero resistivity;

(3) the Meissner effect; and

(4) a phase transition to the normal metallic state at a transition temperature T_c.

There is an important issue to resolve. How can two electrons – which are charged particles with identical negative charges, and therefore experience a strong Coulomb-force repulsion – attract one another? The answer is: by polarizing the crystal lattice. [An instructive simile is the attraction that two billiard balls experience when placed on a rubber membrane: one billiard ball falls readily into the depression caused by the other ball, hence it is attracted by the other ball.] Since the polarization of the crystal lattice depends on the mass of the nuclei which form it, the strength of the electron-electron attraction, which is caused by the lattice polarization, depends the mass of the nuclei, i.e. there is an ISOTOPE EFFECT.

The BCS theory yields, in general, an integral equation for the energy gap parameter Δ, and another integral equation for the transition temperature T_c. These integral equations depend on the electronic structure of the metal, and on the details of the attractive interaction between the electrons. As an example of their theory, Bardeen, Cooper and Schrieffer introduced a very simple model, the so-called BCS MODEL, for which the integral equations can be analytically solved, and that yields

$$\Delta = 1.76\, k\, T_c = 2\hbar\, \omega_D \exp[-1/NV] \quad , \tag{5}$$

where k is Boltzmann's constant, ω_D is the vibration (Debye) frequency of the lattice, N is the number of available electronic states per unit energy in the solid (density of states at the Fermi level), and V is the strength of the attractive (lattice mediated) electron-electron interaction. This formula gives an isotope effect because ω_D, a lattice frequency, depends on the nuclear mass [it is proportional to $M^{-1/2}$].

This simple BCS model gives a good idea of how the BCS theory works: the transition temperature can be increased (i) by increasing ω_D, (ii) by increasing N, or (iii) by increasing V. [It should be remarked that the influence of both N and V on T_c is much more dramatic than the simple proportionality of T_c and ω_D.] According to formula (5) there is no maximum transition temperature; T_c can be increased without limit by finding solids with larger and larger N, V, and ω_D.

In fact formula (5) is not accurate: it is only a simple model. A very good and accurate theory, based on the BCS theory, was developed by Eliashberg and McMillan [6] which, starting from precise experimental information about the crystal lattice vibrations, could accurately -- by numerical methods -- calculate the gap parameter Δ and the transition temperature T_c. The main results of this theory are presented in the Appendix. With a precision of a few percent, the equations yield excellent results for the transition temperature T_c and the isotope effect exponent α in several well studied cases, mostly transition metals. Numerical experiments performed with the Eliashberg-McMillan equations produced, for sensible input of lattice vibration spectra, superconducting transition temperatures which never exceeded 40 K. Therefore, although no rigorous limit was established for a MAXIMUM SUPERCONDUCTING TRANSITION TEMPERATURE, the belief among most specialists was that such an upper bound existed, and that it was in the range of 30 K to 40 K.

IC. History of the Highest Superconducting Transition Temperatures.

The Table below shows the history of the experimentally found highest superconducting transition temperatures:

YEAR	T_c [K]	SUBSTANCE	Notes and References.
1911	4.2	Hg	[1]
~ 1913	7.2	Pb	
1933	9.5	Nb	
1941	16.0	NbN	
1953	17.1	V_3Si	
1960	18.05	Nb_3Sn	
1969	20.8	$NbAlGe$	
1973	23.2	Nb_3Ge	[7]
1986	~ 30	$La-Ba-Cu-O$	[8,9]
1988	~ 30	$Ba-K-Bi-O$	highest T_c superconductor without Cu [10]
1986	39	$La-Sr-Cu-O$	[11]
1987	~ 92	$RE-Ba-Cu-O$	RE = various rare earths [12,13].
1988	~ 105	$Bi-Sr-Ca-Cu-O$	[14]
1988	125	$Tl-Ca-Ba-Cu-O$	[15,16]
1987	~ 230	$RE-Ba-Cu-O$	not reproducible, unstable! [17]

As can be seen, from 1911 to 1973 the increase in maximum observed transition temperatures was a more-or-less linear function of about 0.3 K per year. No temperature was found to violate the (wrongly believed) upper bound.

For the sake of comparison it should be remembered that liquid helium boils at 4.5 K, liquid hydrogen at 20.7 K, liquid neon at 27.2 K, and liquid nitrogen (i.e. liquid air) at 77.4 K. These are the most commonly used refrigerants, and any technology based on superconductivity will have its running costs determined, almost exclusively, by the refrigeration costs. The discovery of superconducting Nb_3Ge in 1973 was considered a major breakthrough, since for the first time the liquid-hydrogen barrier was crossed. Needless to say the events of the last two years can be considered, by any standards, fantastic: first the liquid-neon barrier was broken; soon thereafter the liquid-air temperature was surpassed; and -- if the elusive and unstable very high temperatures reported [17] but easily lost, are both confirmed and stabilized -- it seems that the dream of room-temperature superconductivity is now within accessible reach.

II.- THE GINZBURG-LANDAU EQUATIONS.

IIA. General formulation.

In 1950 Ginzburg and Landau[4,18-23] (GL) proposed a phenomenological theory of superconductivity, which was independent of the microscopic aspects of the phenomenon. The theory was quantum-mechanical, in the sense that included coherent, macroscopic quantum effects. It was a pioneering theory which, independently of the mechanisms responsible for superconductivity, is still valid today. It contains such diverse phenomena as magnetic-field penetration depths, coherence lengths, magnetic-field flux quantization, magnetic-field dependence of the energy gap (order parameter), and the Josephson effect. It can be applied to all superconductors, as well as to superfluid ^{3}He, and has become the prototype theory to study a whole class of phenomena related to second-order phase transitions.

The GL theory introduces a complex order parameter ψ which is allowed to vary in space. Originally GL interpreted ψ as an amplitude, and $|\psi|^2$ as the density of the "superconducting" electrons (they envisioned a superconductor as two interpenetrating electron fluids, the non-dissipative, non-resistive "superconducting" electron fluid, and the dissipative, resistive "normal" electron fluid). In 1959, however, Gor'kov[24,25] proved, using his own formulation of the BCS theory, that for temperatures below and close to T_c, equations identical to those of GL could be obtained, and that the GL parameters ψ could be interpreted (except for a trivial constant of proportionality) as the BCS energy-gap parameter Δ.

The starting point of the GL theory is the introduction of a magnetic Helmholtz free energy F_{SH} for the superconductor, derived from plausibility arguments

$$F_{SH} = \int_{superconductor} d^3r \left[F_{N0} + \Delta F(|\psi|^2) + (1/2m)\left|-i\hbar\nabla\psi - (e*/c)\mathbf{A}\psi\right|^2 + (1/8\pi)H^2(\mathbf{r})\right] . \tag{6}$$

Here F_{N0} is the free-energy density of the normal state in the absence of a magnetic field; ΔF is the difference of free-energy densities between the superconducting and the normal states (also in the absence of a field) and is a function of $|\psi|^2$. The third term is the gauge invariant "superconducting kinetic energy", and the last term is the magnetic field energy in the superconductor. The vector potential is $\mathbf{A}$, $\mathbf{H}$ is the magnetic field, and $e*$ is an effective charge, known now to be the charge of a a "Cooper pair"

$$e* = 2e \ . \tag{7}$$

All terms in (6) are functions of the position $\mathbf{r}$, and change with the magnitude and direction of the magnetic field.

Because the proper variables of the magnetic Helmholtz free energy are the temperature T and the magnetization $\mathbf{M}$, where

$$\mathbf{M} = (1/4\pi) \int_{all\ space} d^3r \left[\mathbf{H}(\mathbf{r}) - \mathbf{H}_0\right] , \tag{8}$$

$$\mathbf{H}_0 = applied \ \ magnetic \ \ field \ ,$$

F_{SH} is not continuous at the critical fields. The function which is continuous at H_{c1} and H_{c2}, and whose proper variables are T and $\mathbf{H}_0$, is the Gibbs free energy G_{SH}, given by

$$G_{SH} = F_{SH} - \mathbf{M}\cdot\mathbf{H}_0 \ . \tag{9}$$

Substitution of (6) and (8) into (9) yields

$$G_{SH} = G_{NH} + \int_{superconductor} d^3r \left[\Delta F(|\psi|^2) + (1/2m)\left|-i\hbar\nabla\psi - (e*/c)\mathbf{A}\psi\right|^2\right] + (1/8\pi) \int_{all\ space} d^3r \left[\mathbf{H}(\mathbf{r}) - \mathbf{H}_0\right]^2 , \tag{10}$$

where

$$G_{NH} = \int_{superconductor} d^3r \left[F_{N0} + H_0^2 / 8\pi \right] .$$

It should be noted that the last term in (10) is to be integrated over *the whole space* (both in the superconductor and outside). Minimization of G with respect to the four functions ψ and **A** [or equivalently ψ and **H**] yields the famous GL equations:

$$\nabla^2 \mathbf{A} = \frac{ie^*\hbar}{mc} \left[\psi^* \nabla \psi - \psi \nabla \psi^* \right] + \frac{4\pi e^{*2}}{mc^2} |\psi|^2 \mathbf{A} \ , \tag{11}$$

$$\nabla \times \mathbf{A} = \mathbf{H}_0 \ \ \textit{on surface} \ , \tag{12}$$

$$\frac{\partial \Delta F}{\partial \psi^*} + \frac{1}{2m} \left[-i\hbar \nabla - \frac{e^*}{c} \mathbf{A} \right]^2 \psi = 0 \ , \tag{13}$$

$$\left[i\hbar \nabla \psi + \frac{e^*}{c} \mathbf{A} \psi \right]_{perpendicular} = 0 \ , \tag{14}$$

where the London gauge

$$\nabla \cdot \mathbf{A} = 0$$

has been chosen.

IIB. Penetration Length and Coherence Length.

In singly connected samples with no penetration of the magnetic flux into the bulk superconductor, the phase of ψ can be chosen so that ψ is real throughout the sample. In particular for a one-dimensional, singly connected problem, with quantities varying along the x-axis, and with magnetic field and vector potential given by

$$\mathbf{H} = [\, 0 \, , 0 \, , H(x) \,] \ ,$$

$$\mathbf{A} = [\, 0 \, , A(x) \, , 0 \,] \ ,$$

the equations (11)-(14) become

$$(d^2A\ /\ dx^2) = (4\pi e*^2/mc^2)\ \psi^2 A\ , \tag{15}$$

$$(dA\ /\ dx) = H_0 \quad on\ surface\ , \tag{16}$$

$$\frac{\partial \Delta F}{\partial \psi} + \frac{e*^2}{mc^2}A^2\psi = \frac{\hbar^2}{m}\frac{d^2\psi}{dx^2}\ , \tag{17}$$

$$(d\psi\ /\ dx) = 0 \quad on\ surface\ . \tag{18}$$

For the free-energy difference ΔF, the original GL derivation used a power-series expansion in $|\psi|^2$, and neglected all terms higher than the second. That expansion is still commonly used, and is known to be valid for superconductors at temperatures close to T_c:

$$\Delta F = \frac{H_{cb}^2}{8\pi}\left[-2\left[\frac{\psi}{\psi_T}\right]^2 + \left[\frac{\psi}{\psi_T}\right]^4\right]\ , \tag{19}$$

where H_{cb} is the thermodynamic bulk critical field, and ψ_T is the equilibrium value of ψ in the bulk, at temperature T, in the absence of a magnetic field.

One of the simplest and most instructive cases to solve is that of the superconducting half-space, with a constant magnetic field H_0 applied parallel to the surface at $x = 0$. Integration of (15)-(19), under the assumption of small changes in ψ near the surface, yields for $x > 0$

$$\frac{\psi(x, H_0)}{\psi_T} = 1 - \frac{\kappa_o}{(2-\kappa_o^2)\sqrt{8}}\left[\frac{H_0}{H_{cb}}\right]^2\left[e^{-\frac{\sqrt{2}\kappa_o x}{\lambda_L}} - \tfrac{1}{2}\kappa_o\ e^{-\frac{2x}{\lambda_L}}\right]\ , \tag{20}$$

and

$$H(x) \simeq H_0 \exp\left(-x/\lambda_L\right)\ , \tag{21}$$

where λ_L, which governs the decay of the magnetic field into the superconductor, is the London penetration depth

$$\lambda_L^2 = \frac{mc^2}{4\pi e*^2\,\psi_T^2}\ , \tag{22}$$

and κ_o is a dimensionless constant

$$\kappa_o = (\sqrt{2}e*\ /\ \hbar c)\ \lambda_L^2 H_{cb}\ . \tag{23}$$

Two remarks are necessary at this point. First, there are two length scales in the problem: (i) the decay length for magnetic fields, λ_T, and (ii) the decay length, $(\lambda_L / \sqrt{2}\kappa_o)$, for the order parameter ψ, given by the first exponent in (20). Second, Gor'kov has shown[24,25] that

$$\kappa_o = 0.96\, \lambda_L\, \xi_o^{-1} \;, \tag{24}$$

where ξ_o is Pippard's electromagnetic coherence length[26,27], now known to be related to the energy gap parameter

$$\xi_o = \hbar\, v_F / \Delta \tag{25}$$

(v_F is the Fermi velocity of the electrons in the metal). Values of κ_0 are small (< 0.707) for the soft, type I superconductors [0.01 for Al; 0.3 for Pb], whereas it takes large values (> 0.707) for the hard, type II superconductors [~ 8 for V; extremely large for the new, high T_c materials].

A type I superconductor excludes a magnetic field from its bulk completely. If the magnetic field is increased there is a value, H_c for which the superconductivity is suddenly destroyed, the system returns to the normal state, and the magnetic field penetrates the specimen completely. A type II superconductor excludes the field completely up to a value H_{c1}. Above H_{c1} the field is partially excluded, although the specimen remains superconducting and exhibits zero resistivity. At a higher field, H_{c2}, the flux penetrates completely, superconductivity is destroyed and the specimen returns to its normal state.

IIC. Flux quantization.

In many applications (thin specimens, weak magnetic fields, etc.), the order parameter ψ can be considered to have a constant magnitude $n^{1/2}$, although its phase $\theta(r)$ can vary appreciably in space,

$$\psi = n^{1/2}\, e^{i\theta(r)} \;. \tag{26}$$

From standard quantum-mechanical arguments the electrical supercurrent is given in this case by the usual formula

$$\mathbf{j} = \frac{1}{2m}\left[\psi^* \left[-i\hbar\nabla - \frac{e^*}{c}\mathbf{A}\right]\psi + \psi\left[i\hbar\nabla - \frac{e^*}{c}\mathbf{A}\right]\psi^*\right] = \frac{ne^*}{m}\left[\hbar\nabla\theta - \frac{e^*}{c}\mathbf{A}\right] . \tag{27}$$

Deep inside any superconductor the electric current is zero and, therefore, from (27) one obtains

$$e^* \mathbf{A} \approx \hbar c \ \nabla\theta \ . \tag{28}$$

In a multiply connected sample one can find a closed path C which encircles a non-superconducting region where there may be a magnetic field. Line integration of (28) over that path, use of Stokes theorem and knowledge that ψ must be single-valued yields

$$\int_{closed\ C} \mathbf{A} \cdot d\mathbf{s} = \int_{area\ C} \nabla\times\mathbf{A} \cdot d\boldsymbol{\sigma} = \int_{area\ C} \mathbf{H} \cdot d\boldsymbol{\sigma} = \Phi$$

$$= \frac{\hbar c}{e^*} \int_{closed\ C} \nabla\theta \cdot d\mathbf{s} = \frac{\hbar c}{e^*} \cdot 2\pi\nu \ , \tag{29}$$

where Φ is the magnetic-field flux, and ν is an arbitrary integer. In other words (29) can be written

$$\Phi = \nu \ \Phi_0 \ = \ \nu \ \cdot \ 2.0678 \times 10^{-7} \ gauss \ cm^2 \ , \tag{30}$$

i.e. if a closed path without currents can be established deep inside a multiply connected superconductor, then the magnetic-field flux encircled by that path is quantized in units of Φ_0.

IID. Phase-current relationship; the Josephson effect.

From the GL equations it can be easily seen that the order parameter ψ has an indeterminate *arbitrary*, *constant* phase. In a given superconductor (called 1) its phase θ_1 is completely arbitrary. If, however, there is nearby a second superconductor (called 2), which is *weakly* connected to the first one, although both phases, θ_1 and θ_2, are indeterminate by the *same* additive constant, the *phase difference* between the two,

$$\delta = \theta_2 - \theta_1 \ ,$$

is an observable meaningful quantity. As can be seen from (27) a change if θ over space is responsible for the existence of a supercurrent. Similarly[3,28] a phase difference between two weakly coupled, spatially close superconductors produces a current flow between them given by

$$J = J_0 \ \sin\delta \ , \tag{31}$$

where J_0, a constant, describes the maximum possible current which may flow between the the two specimens. Equation (31) is Josephson's famous *d.c.* equation relating current and phase difference. It is implicit in the GL equations and applies to any system with a macroscopic, quantum-mechanical, complex order parameter. It is the consequence[28] of the standard quantum mechanical uncertainty relation between particle number and wave-function phase.

IIE. Magnetic-field dependence of the energy gap.

Detailed solution of (15)-(19) for thin films[4] clearly exhibit a field dependence of the *amplitude* of the order parameter $|\psi|$ on applied magnetic fields H_0. As the field is increased the value of $|\psi|$ decreases, and there is a value H_f for which it goes (either continuously or discontinuously) to zero and the film becomes normal. It is found that H_f depends on H_{cb}, d and the London penetration depth (22), and that the $|\psi|$ transition to zero at H_f is discontinuous if

$$d / \lambda_L > \sqrt{5} \; .$$

These results, and many others obtained from the solution of the GL equations for a variety of geometries and situations, have been confirmed by superconducting tunnelling experiments.

IIF. Quantum interference phenomena.

Finally the facts that

(i) the order parameter ψ is complex; (ii) ψ must be single valued; (iii) the magnetic field **H** couples to it in a gauge invariant form and therefore is directly related to the phase θ of ψ; and (iv) the GL equations are non linear;

result in an enormous wealth of interference and diffraction effects which can be fruitfully used in designing interesting electronic devices[29,30]. It can be said that, in mastering the science of superconductivity, scientists have promoted quantum mechanics to the macroscopic, everyday-use level.

APPENDIX

The integral equations for the normal and pairing self-energies of a superconductor are

$$\xi(\omega) = [1 - Z(\omega)]\,\omega = \int_{\Delta_0}^{\infty} d\omega' \,\mathrm{Re}\left[\frac{\omega'}{(\omega'^2 - \Delta'^2)^{1/2}}\right] \times \int d\omega_q\, \alpha^2(\omega_q)\, F(\omega_q)\, [D_q(\omega' + \omega) - D_q(\omega' - \omega)] \quad , \qquad (31)$$

$$\phi(\omega) = \int_{\Delta_0}^{\omega_c} d\omega' \,\mathrm{Re}\left[\frac{\Delta'}{(\omega'^2 - \Delta'^2)^{1/2}}\right] \times \left\{\int d\omega_q\, \alpha^2(\omega_q)\, F(\omega_q)\, [D_q(\omega' + \omega) + D_q(\omega' - \omega)] - \mu^*\right\}, \qquad (32)$$

where $D_q(\omega) = (\omega + \omega_q - i0^+)^{-1}$, $\Delta(\omega) = \phi(\omega)/Z(\omega)$, and $\Delta_0 = \Delta(\Delta_0)$. $F(\omega)$ is the phonon density of states

$$F(\omega) = \sum_{\lambda} \int \frac{d^3q}{(2\pi)^3}\, \delta(\omega - \omega_{q\lambda}) \quad , \qquad (33)$$

and $\alpha^2(\omega)$ is an effective electron-phonon coupling function for phonons of energy ω:

$$\alpha^2(\omega)\, F(\omega) = \int_S \frac{d^2p}{v_F} \int_{S'} \frac{d^2p'}{(2\pi)^3 v_F'} \sum_{\lambda} g^2_{pp'\lambda}\, \delta(\omega - \omega_{p-p'\lambda}) \Big/ \int_S \frac{d^2p}{v_F}, \qquad (34)$$

where $g^2_{pp'\lambda}$ is the dressed electron-phonon matrix element, $\omega_{q\lambda}$ is the phonon energy for polarization λ and wave number q (reduced to the first zone), and v_F , is the Fermi velocity. The two surface integrations are performed over the Fermi surface.

In order to solve these equations, the necessary input consists of two numbers, the electron Coulomb interaction pseudopotential μ^* , and the cut-off ω , and the electron-phonon coupling function $\alpha^2(\omega)\, F(\omega)$.

ACKNOWLEDGMENT

This research was supported, in part, at the Lawrence Berkeley Laboratory by the Director, Office of Energy Research, Office of Basic Energy Sciences, Materials Sciences Division, U.S. Department of Energy under Contract No. DE-AC03-76SF00098.

REFERENCES

1 C. Kittel, *Introduction to Solid State Physics*, 5th edition (Wiley, New York, 1976), Chapter 12.

2 M. Tinkham, *Introduction to Superconductivity* (McGraw-Hill, New York, 1975).

3 J. Clarke, Amer. J. Phys. 38, 1071 (1970)

4 D. H. Douglass, Jr., and L. M. Falicov, in *Progress in Low Temperature Physics*, edited by C. J. Gorter (North-Holland, Amsterdam, 1964), volume 4, p 97.

5 J. Bardeen, L. N. Cooper, and J. R. Schrieffer, Phys. Rev. 106, 162 (1957); 108, 1175 (1957).

6 For a comprehensive review of this complex subject, see the various articles in *Superconductivity*, two volumes edited by R. D. Parks (Dekker, New York, 1969).

7 See the review in Science 183, 293 (1974).

8 J. G. Bednorz and K. A. Muller, Z. Phys. B - Condensed Matter 64, 189 (1986).

9 C. W. Chu, P. H. Hor, R. L. Meng, L. Gao, Z. J. Huang, and Y. Q. Wang, Phys. Rev. Lett. 58, 405 (1987).

10 R. J. Cava, B. Batlogg, J. J. Krajewski, R. Farrow, L. W. Rupp Jr., A. E. White, K. Sjort, W. F. Peck, and T Kometani, Nature 332, 814 (1988)

11 R. J. Cava, R. B. van Dover, B. Batlogg, and E. A. Rietman, Phys. Rev. Lett. 58, 408 (1987).

12 M. K. Wu, J. R. Ashburn, C. J. Tong, P. H. Hor, R. L. Meng, L. Gao, Z. J. Huang, Y. Q. Wang, and C. W. Chu, Phys. Rev. Lett. 58, 908 (1987).

13 See the article *Superconductivity seen above the boiling point of nitrogen*, in *Search and discovery*, Physics Today, April 1987, p 17.

14 M. Maeda, Y. Tanaka, M. Fukutomi, and T. Asano, Jpn. J. App. Phys., Pt 2, 27, 209 (1988)

15 Z. Z. Sheng and A. M. Hermann, Nature 332, 138 (1988).

16 S. S. S. P. Parkin, V. Y. Lee, E. M. Engler, A. I. Nazzal, T. C. Huang, G. Gorman, R. Savoy, and R. Beyers, Phys. Rev. Lett. 60, 2539 (1988).

17 C. Y. Huang, L. J. Dries, P. H. Hor, R. L. Meng, C. W. Chu, and R. B. Frankel, Nature 328, 403 (1987).

18 V. L. Ginzburg and L. D. Landau, Zhur. Eksp. Teor. Fiz. SSSR 20, 1064 (1950).

19 V. L. Ginzburg, Dokl. Akad. Nauk SSSR 83, 385 (1952).

20 V. L. Ginzburg, Nuovo Cim. 2, 1234 (1955).

21 V. L. Ginzburg, Zhur. Eksp. Teor. Fiz. SSSR 29, 748 (1955) [Soviet Phys. JETP 2, 589 (1955)].

22 V. L. Ginzburg, Dokl. Akad. Nauk SSSR 110, 358 (1956) [Soviet Phys. Dokl. 3, 102 (1956)].

23 V. L. Ginzburg, Zhur. Eksp. Teor. Fiz. SSSR 34, 113 (1958) [Soviet Phys. JETP 7, 78 (1958)].

24 L. P. Gor'kov, Zhur. Eksp. Teor. Fiz. SSSR 36, 1918 (1959) [Soviet Phys. JETP 9, 1364 (1959)].

25 L. P. Gor'kov, Zhur. Eksp. Teor. Fiz. SSSR 37, 1407 (1959) [Soviet Phys. JETP 10, 998 (1959)].

26 A. B. Pippard, Proc. Roy. Soc. (London) A203, 210 (1950).

27 A. B. Pippard, Proc. Roy. Soc. (London) A216, 547 (1953).

28 Aa. Bohr and O. Ulfbeck, *Quantal structure of superconductivity. Gauge angle.*, lectures presented in this Summer School.

29 J. Clarke, *SQUID-Magnetometers*, lectures presented in this Summer School.

30 N. Falsig Pedersen, *The Josephson Effect*, lectures presented in this Summer School.

CHAPTER 2

Quantal structure of superconductivity. Gauge angle

Aage Bohr Ole Ulfbeck
The Niels Bohr Institute

Two Lectures Prepared for 1st Topsøe Summer School on Superconductivity
June 1988

1 Intrinsic motion of superconductor

- **Pair field**
    - **Degrees of freedom**
    - **Interaction. Pair force**
    - **Pairspin**
    - **Polarization of pairspin. Pair field**
- **Pair correlation**
    - **Eigenstates of individual pairspin**
    - **Ground state of total system**
    - **Excitations. Quasiparticles**
- **Self-consistency. Phase transition**
    - **Ground state**
    - **Critical temperature**

2 Gauge angle as dynamical variable

- **Rotation in gauge space**
    - **Angle conjugate to particle number**
    - **Spontaneous symmetry breaking**
    - **Dynamics of gauge angle**
    - **Supercurrent in Josephson junctions**
- **Superflow**
    - **Gauge angle as velocity potential**
    - **Winding number**
- **Local gauge invariance**
    - **Electromagnetic potentials and coupling to particles**
    - **Supercurrent. Spontaneous breaking of gauge invariance**
    - **Impermeability of superconductor to magnetic field**

The superconducting phase of the electron fluid arises through an instability of the fermi surface due to a weak, effective interaction between pairs of electrons close to the fermi surface[1]. The instability leads to the formation of a static mean field, the pair field, which acts by adding and removing pairs of particles. The pair field thus constitutes a deformation in a new dimension, by which the symmetry associated with particle number conservation is spontaneously broken. The first lecture deals with simple aspects of the electron matter in the presence of the pair field (intrinsic motion).

The deformation defines a direction angle, the gauge angle, conjugate to particle number, and the system thereby acquires the ability to rotate collectively in the new dimension. Moreover, the spatial variation of the gauge angle, by which local gauge invariance is spontaneously broken, manifests itself in the supercurrent. The second lecture addresses some general features of the collective degrees of freedom of the superconducting material, illustrating the effect of the symmetry breaking[2].

1 Intrinsic motion of superconductor

- Pair field
- Pair correlation
- Self-consistency. Phase transition

In normal metals, the metallic electrons form a fermi liquid characterized by a long mean free path. Our starting point is therefore the quantal states $|\nu\rangle$ of the individual particles in the mean field from the ions and electrons. For definiteness, we may think of the quantum numbers ν as momentum and spin component $\nu = (\vec{p}, \sigma)$, as in a homogeneous medium. The ground state (T=0 Kelvin) of the metallic electrons then forms a fermi sphere, in which all single-particle orbits are occupied up to the fermi surface, with momentum p_F and energy ϵ_F. The detailed structure of the single-particle orbits, related to the symmetries of the mean potential, is not of significance for the following, but it is assumed that the mean potential respects time reversal symmetry, as is the case for a lattice without magnetic ions. The $\mathcal{T}$-symmetry entails that the orbitals ν, no matter how complex their spatial structure, occur in degenerate time reversed pairs, denoted by $|\nu\rangle$ and $|\bar{\nu}\rangle$, respectively. Such orbitals, though orthogonal, follow each other closely in space, with complex conjugate amplitudes for opposite spin components, in the point $\vec{r}$. For any mean field with $\mathcal{T}$-symmetry, the ground state of the metallic electrons can therefore be described as a pairwise filling of orbitals ν and $\bar{\nu}$, up to the last filled orbit ν_F, with energy ϵ_F. Such a picture tacitly assumes that all components of the mean field commute with particle number. However, mean fields of a more general character, changing particle number, can be accomodated in the quantal description in a straightforward manner. The formation of such a mean field underlies the following discussion.

---

[1] The lectures deal with the theory of superconductivity developed by J. Bardeen, L.N. Cooper, J.R. Schrieffer, Phys. Rev. **108** 1175 (1957).

[2] The lectures attempt to describe general concepts that have been developed in the description of superconductivity and which are of broad significance to quantum physics.

1.1 Pair field

- Degrees of freedom
- Interaction. Pair force
- Pairspin
- Polarization of pairspin. Pair field

1.1.1 Degrees of freedom

The ground state of the uncorrelated system consists of filled pairs of orbits $|\nu\bar{\nu}\rangle$ that are invariant under time reversal symmetry. This symmetry is maintained in the correlated state describing the superconducting electron fluid. In this state, the time reversed partners ν and $\bar{\nu}$ always occur together; either both orbitals are occupied, or both are empty. Such a state characterized by a pairwise occupancy of time reversed orbits is referred to as a pair correlation.

The dynamical variables describing the pair correlation are the occupation numbers of the pair of orbitals $\nu\bar{\nu}$, with eigenvalues 1 and 0,

$$n(\nu\bar{\nu}) = \begin{cases} 1 & |n(\nu\bar{\nu}) = 1\rangle = |\nu\bar{\nu}\rangle \\ 0 & |n(\nu\bar{\nu}) = 0\rangle = |0\rangle \end{cases} \tag{1}$$

and the Hamiltonian for the uncorrelated system is

$$H_0' = \sum_{\nu>0} 2\epsilon'(\nu)n(\nu\bar{\nu}) \qquad \epsilon'(\nu) = \epsilon(\nu) - \mu \tag{2}$$

where the single-particle energies $\epsilon'(\nu)$ are measured from the fermi surface, also referred to as the chemical potential μ. The notation $\nu > 0$ indicates that the summation is over pairs, each pair counted once. (The states $|\nu\bar{\nu}\rangle$ are invariant under T, since $T^2|\nu\rangle = |\bar{\bar{\nu}}\rangle = -|\nu\rangle$, for a state of a single fermion, and since the two-particle states are antisymmetric under exchange of particles, $|\nu\bar{\nu}\rangle = -|\bar{\nu}\nu\rangle$).

1.1.2 Interaction. Pair force

In the space of pairwise occupied orbits, the interaction that is reponsible for the pair correlation acts by transferring two particles from one pair of time reversed orbits to another. This transfer is performed by the quantal operators $a^\dagger(\nu), a(\nu)$ that add and remove a particle from the orbit ν (creation and annihilation operators). Thus the product

$$a^\dagger(\bar{\nu}_2)a^\dagger(\nu_2)a(\nu_1)a(\bar{\nu}_1) \tag{3}$$

gives the transition

$$\nu_1\bar{\nu}_1 \rightarrow \nu_2\bar{\nu}_2 \tag{4}$$

The matrix element for this process can depend on ν_1 and ν_2, but since each $\nu\bar{\nu}$ pair is acted upon by a large number of pairs in a region around the fermi surface, the forces are represented by an effective attractive interaction with average matrix element G,

$$V_p = -G \sum_{\nu_1>0\,\nu_2>0} a^\dagger(\bar{\nu}_2)a^\dagger(\nu_2)a(\nu_1)a(\bar{\nu}_1) \qquad (G > 0) \tag{5}$$

which acts in the neighbourhood of the fermi surface.

1.1.3 Pairspin

The $n(\nu\bar{\nu})$ degree of freedom acts on the states $|\nu\bar{\nu}\rangle$ and $|0\rangle$ that can be viewed as basis vectors in a two-dimensional space,

$$|\nu\bar{\nu}\rangle = a^\dagger(\bar{\nu})a^\dagger(\nu)|0\rangle \rightarrow \begin{pmatrix} 1 \\ 0 \end{pmatrix} \qquad |0\rangle = a(\nu)a(\bar{\nu})|\nu\bar{\nu}\rangle \rightarrow \begin{pmatrix} 0 \\ 1 \end{pmatrix} \tag{6}$$

Any operator in this space, such as pair addition or removal and the number operator, can be expressed as linear combinations of Pauli matrices

$$\begin{aligned} a^\dagger(\bar{\nu})a^\dagger(\nu) &= \begin{pmatrix} 0 & 1 \\ 0 & 0 \end{pmatrix} = \frac{1}{2}(\sigma_x(\nu) + i\sigma_y(\nu)) = s_+(\nu) \\ a(\nu)a(\bar{\nu}) &= s_-(\nu) \qquad\qquad \vec{\sigma} = 2\vec{s} \qquad s_\pm = s_x \pm is_y \\ n(\nu\bar{\nu}) &= \begin{pmatrix} 1 & 0 \\ 0 & 0 \end{pmatrix} = \frac{1}{2}(1 + \sigma_z(\nu)) \end{aligned} \tag{7}$$

Thus, by the introduction of operators $\vec{s}(\nu)$, referred to as pairspins[3], the pair correlated fermi liquid appears in the guise of a system of interacting spins, one for each $\nu\bar{\nu}$, and the total Hamiltonian takes the form (see (2) and (5))

$$H' = H'_0 + V_p \tag{8}$$

with

$$H'_0 = \sum_{\nu>0} \epsilon'(\nu)(1 + \sigma_z(\nu)) \tag{9}$$

and

$$\begin{aligned} V_p &= -G \sum_{\nu_1>0\,\nu_2>0} s_+(\nu_2)s_-(\nu_1) \\ &= -G \sum_{\nu_1>0\,\nu_2>0} \vec{s}_\perp(\nu_2)\cdot\vec{s}_\perp(\nu_1) \qquad (\vec{s}_\perp = (s_x, s_y)) \end{aligned} \tag{10}$$

The transverse pairspin $\vec{s}_\perp$ has components s_x and s_y, perpendicular to the z-axis. The last expression (10) ignores commutators for $\nu_1 = \nu_2$, since the number of these terms is negligible compared to those with $\nu_1 \neq \nu_2$, when many pairspins contribute to the interaction.

From (7), it follows that the total pairspin in the z-direction is equivalent to the number operator,

$$\begin{aligned} S_z &= \sum_{\nu>0} s_z(\nu) \\ &= \sum_{\nu>0}(n(\nu\bar{\nu}) - \frac{1}{2}) \\ &= \frac{1}{2}(\mathcal{N} - \mathcal{N}_0) \end{aligned} \tag{11}$$

where $\mathcal{N}_0$ is a constant depending on the single-particle space included. The axial symmetry of H'_0 and V_p in pairspin space, which implies that these operators commute with S_z, therefore expresses particle number conservation.

---

[3] The description of the pair correlated phase in terms of spin variables (quasi spin) was introduced by P.W. Anderson, Phys. Rev. 112 1900 (1958). With the rapid rise in the use of spin-like quantities, it seems appropriate to use the more specific term pairspin in the present context.

1.1.4 Polarization of pairspin. Pair field

The interaction V_p is a spin-spin coupling, which seeks to align the transverse components of the pairspins. Were it not for H_0', all spins would line up in the same direction, perpendicular to the $\hat{z}$-axis. The single-particle energy H_0' counteracts this alignment. Indeed, H_0' plays the role of a magnetic energy, which tends to align the spins in the $\hat{z}$-direction, or opposite to it, with a strength that increases with distance from the fermi surface. Thus, for sufficiently large $|\epsilon'|$, the single-particle energy H_0' dominates. But close to the fermi surface, V_p is the overriding effect, and a large transverse pairspin is formed

$$\vec{S}_\perp = \sum_{\nu>0} \vec{s}_\perp(\nu) \tag{12}$$

Whereas any single pairspin in this sum has large quantal fluctuations, the total pairspin can have a well defined magnitude and orientation, since the fluctuations of the constituent pairspins add quadratically.

The interaction (10) can be written

$$V_p = -G\vec{S}_\perp \cdot \sum_{\nu>0} \vec{s}_\perp(\nu) \tag{13}$$

and the emergence of a collective transverse pairspin $\vec{S}_\perp$ therefore produces a mean field acting on the individual pairspins. The analysis proceeds in two steps

a We first assume a value for the magnitude of $\vec{S}_\perp$ and chose an orientation, in the x-direction. The pair interaction is then replaced by a mean field, the pair field, of strength Δ,

$$\begin{aligned} V_p \longrightarrow U_p &= -G\langle S_x\rangle \sum_{\nu>0} s_x(\nu)\cdot 2 \\ &= -\Delta \sum_{\nu>0} \sigma_x(\nu) \qquad (\sigma_x = 2s_x) \\ \Delta &\equiv G\langle S_x\rangle \qquad 0 = G\langle S_y\rangle \end{aligned} \tag{14}$$

(where a factor 2 takes into account that each product of different pairspins occurs twice in (10)). The pairspins thus move independently of each other in a total field consisting of H_0' and the pair field U_p produced by all the other pairs together. This motion of the particles with respect to the orientation of the pairfield is referred to as intrinsic motion (section 1.2).

b For the intrinsic motion in the assumed field, the mean polarization $\langle \vec{S}_\perp \rangle$ is evaluated. Symmetry ensures that the direction of the polarization coincides with that of the mean field (x-axis). Self-consistency requires that the magnitude of the induced polarization is equal to the assumed value $\frac{\Delta}{G}$, and this condition connects the strength Δ with the matrix element G (section 1.3).

With the formation of the pair field, a transverse direction in pairspin space is singled out. This orientation angle is a dynamical variable for the collective motion (topic for the second lecture).

1.2 Pair correlation

- **Eigenstates of individual pairspin**
- **Gound state of total system**
- **Excitations. Quasiparticles**

1.2.1 Eigenstates of individual pairspin

When the pairspin interaction V_p is replaced by the mean field $\mathcal{U}_p$, the total Hamiltonian is a sum over the individual pairspins

$$H' = \sum_{\nu>0} h'(\nu) \tag{15}$$

with (see (9) and (14))

$$h' \;=\; \epsilon' + \epsilon'\sigma_z - \Delta\sigma_x \tag{16}$$

describing a pairspin acted upon by a field with components $(\Delta, -\epsilon')$ in the x- and z-directions (see Fig.1). The Hamiltonian (16) is diagonalized in terms of the component

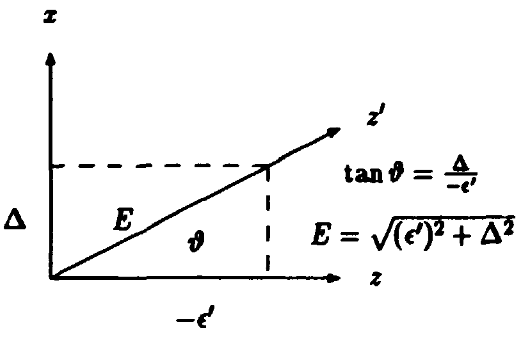

Figure 1: Direction of pairspin in zx-plane
The figure is drawn for $\epsilon' < 0$ (Deep below the fermi surface the $\hat{z}$- and $\hat{z}'$- axes coincide).

$\sigma_{z'}$ in the direction of the field

$$\begin{aligned} h' &= \epsilon' - E\sigma_{z'} \qquad E = ((\epsilon')^2 + \Delta^2)^{\frac{1}{2}} \\ \sigma_{z'} &= \sigma_z \cos\vartheta + \sigma_x \sin\vartheta \\ \cos\vartheta &= -\frac{\epsilon'}{E} \qquad \sin\vartheta = \frac{\Delta}{E} \end{aligned} \tag{17}$$

In the ground state $|\hat{0}\rangle$, the pairspin is therefore polarized in the direction of $\hat{z}'$,

$$\begin{aligned} |\hat{0}\rangle &= |\sigma_{z'} = 1\rangle = u|\sigma_z = -1\rangle + v|\sigma_z = +1\rangle \\ u &= \sin\frac{\vartheta}{2} \qquad v = \cos\frac{\vartheta}{2} \end{aligned} \tag{18}$$

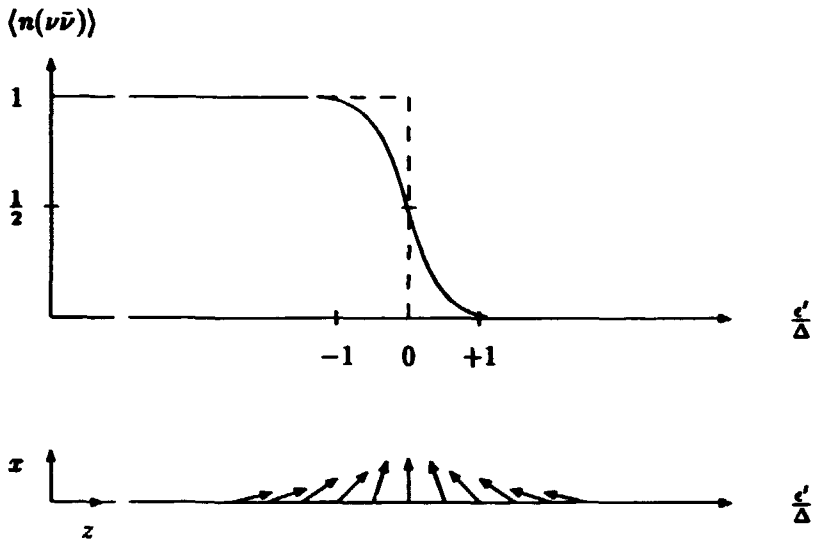

Figure 2: Pairspin polarisation

The figure illustrates the occupancy $\langle n(\nu\bar{\nu})\rangle$ (upper) and the pairspin polarisation $\langle\vec{\sigma}(\nu)\rangle$ (lower), as a function of single-particle energy. The polarization is in the xz-plane, with the directions of axes indicated to the left in the figure.

with amplitudes u and v for pairspin down and up, respectively. For the state (18), the mean value of the polarization vector is

$$\langle\sigma_x\rangle = \sin\vartheta = 2uv = \frac{\Delta}{E} \qquad \langle\sigma_z\rangle = \cos\vartheta = v^2 - u^2 = \frac{-\epsilon'}{E} \tag{19}$$

and the occupancy is

$$\langle n(\nu\bar{\nu})\rangle = \frac{1}{2}\langle 1 + \sigma_z(\nu)\rangle = \frac{1}{2}(1 - \frac{\epsilon'(\nu)}{E(\nu)}) \tag{20}$$

The instability of the fermi surface associated with the transverse polarization is shown in Fig.2. The ground state (18) of the individual pairspin is a superposition of spin up and down and therefore not axially symmetric. Indeed, the transverse polarization - which inherently breaks this symmetry - arises from the superposition.

However, spin up and spin down is but a way of describing the states $|\nu\bar{\nu}\rangle$ and $|0\rangle$, and the ground state

$$\begin{aligned} |\hat{0}\rangle &= u(\nu)|0\rangle + v(\nu)|\nu\bar{\nu}\rangle \\ &= (\,u(\nu) + v(\nu)a^\dagger(\bar{\nu})a^\dagger(\nu)\,)|0\rangle \end{aligned} \tag{21}$$

is thus a superposition of states with zero and two particles. This superposition, which entails indeterminacy in particle number, is produced by the pairfield (see (7) and (14)),

$$\begin{aligned} \mathcal{U}_p &= -\Delta \sum_{\nu>0} a^\dagger(\bar{\nu})a^\dagger(\nu) + a(\nu)a(\bar{\nu}) \\ \Delta &= G\sum_{\nu>0}\langle a^\dagger(\bar{\nu})a^\dagger(\nu)\rangle \; (= G\sum_{\nu>0}\langle a(\nu)a(\bar{\nu})\rangle) \end{aligned} \tag{22}$$

which adds and removes particles.

1.2.2 Ground state of total system

Since the $\nu\bar{\nu}$ channels are independent in the mean field approximation, the ground state for the entire system is a product

$$|\mathrm{v}=0\rangle = \prod_{\nu>0}(u(\nu) + v(\nu)a^\dagger(\bar{\nu})a^\dagger(\nu))|0\rangle \tag{23}$$

where v is the quantum number representing the number of excitations (quasiparticles, see 1.2.3), which has the value zero in the ground state. The $|\mathrm{v}=0\rangle$ state (23) is a superposition of states with different particle numbers. Due to the independence of the different $\nu\bar{\nu}$ channels, the fluctuations in total particle number for the state (23) is, however, very small compared to the number of particles participating in the pair correlation, assumed to be large.

In the ground state, the energy of each pairspin is $\epsilon' - E$ (see (17)). However, since the total pair field energy (14) counts the pairspin interaction twice, the total energy is given by

$$\begin{aligned} \mathcal{E}' &= \sum_{\nu>0} \epsilon'(\nu) - E(\nu) + \Delta\langle s_x(\nu)\rangle \\ &= \sum_{\nu>0} \epsilon'(\nu) - E(\nu) + \frac{\Delta^2}{2E(\nu)} \end{aligned} \tag{24}$$

by means of (19). An evaluation of the sum gives

$$\mathcal{E}' = \mathcal{E}'_0 + \mathcal{E}_{cor} \tag{25}$$

where

$$\mathcal{E}'_0 = \sum_{\nu>0\ \epsilon'<0} 2\epsilon'(\nu) \tag{26}$$

is the energy of the uncorrelated system, and where

$$\mathcal{E}_{cor} = -\frac{1}{2}\rho(\epsilon_F)\Delta^2 \tag{27}$$

is the correlation energy, expressed in terms of the density $\rho(\epsilon_F)$ of $\nu\bar{\nu}$ states per unit energy, at the fermi surface. The correlation energy arises primarily from orbits in a region of order Δ around the fermi surface, in which there are $\sim \rho(\epsilon_F)\Delta$ pairspins, each contributing a binding energy $\sim \Delta$.

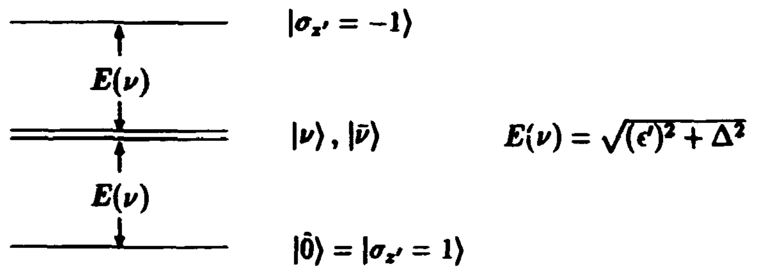

Figure 3: Excitation energy of states $|\nu\rangle$, $|\bar{\nu}\rangle$ and $|\sigma_{x'} = -1\rangle$

1.2.3 Excitations. Quasiparticles

The total space connected with the orbits ν and $\bar{\nu}$ contains in addition to $|0\rangle$ and $|\nu\bar{\nu}\rangle$ the two single-particle states $|\nu\rangle$ and $|\bar{\nu}\rangle$. These states are annihilated by the pair field, which only connects the states $|0\rangle$ and $|\nu\bar{\nu}\rangle$,

$$\mathcal{U}_p|\nu\rangle = 0 \qquad (\nu \leftrightarrow \bar{\nu}) \tag{28}$$

The single-particle states are therefore stationary

$$h'(\nu)|\nu\rangle = \epsilon'(\nu)|\nu\rangle \qquad (\nu \leftrightarrow \bar{\nu}) \tag{29}$$

with energy exceeding that of the ground state by $E(\nu)$ (see (17) and Fig.3). The excitation spectrum thus has a gap Δ.

The state $|\nu\rangle$ arises from the ground state (21) by adding a particle to the empty state $|0\rangle$ or removing one from the doubly occupied state $|\nu\bar{\nu}\rangle$. The excitation is referred to as a quasiparticle and can be created from the pair correlated ground state by the operators

$$\begin{aligned} \alpha^{\dagger}(\nu) &= u(\nu)a^{\dagger}(\nu) + v(\nu)a(\bar{\nu}) \\ \alpha^{\dagger}(\bar{\nu}) &= u(\nu)a^{\dagger}(\bar{\nu}) - v(\nu)a(\nu) \end{aligned} \tag{30}$$

which involve linear combinations of creation and annihilation operators $a^{\dagger}$ and a. (The expression for $\alpha^{\dagger}(\bar{\nu})$ takes into account that $\mathcal{T}^2 = -1$, for a state of a single fermion). In terms of the quasiparticle variables $\alpha^{\dagger}, \alpha$, the Hamiltonian $h'(\nu)$ has the diagonal form

$$h'(\nu) = \epsilon'(\nu) - E(\nu) + E(\nu)(\alpha^{\dagger}(\nu)\alpha(\nu) + \alpha^{\dagger}(\bar{\nu})\alpha(\bar{\nu})) \tag{31}$$

where the operators $\alpha(\nu)$ and $\alpha(\bar{\nu})$ remove quasiparticles and therefore give zero, when acting on the quasiparticle vacuum ($|\hat{0}\rangle$ or $|\mathrm{v} = 0\rangle$). Thus, the total Hamiltonian H' describes a system of independent quasiparticles.

In tunnelling between a normal metal and a superconductor, a quasiparticle excitation is created in the superconductor by addition or removal of a particle. The current therefore has a voltage threshold $eV = \Delta$, corresponding to the minimum quasiparticle energy.

1.3 Self-consistency. Phase transition

- Ground state
- Critical temperature

1.3.1 Ground state

The pair field with strength Δ produces the v = 0 state,

$$\mathit{Pairfield}\ U_p \longrightarrow \mathit{State}\ |\mathrm{v}=0\rangle \qquad (32)$$

and self-consistency therefore requires

$$\mathit{State}\ |\mathrm{v}=0\rangle \longrightarrow \mathit{Pairfield}\ U_p \qquad (33)$$

Thus, the transverse polarizations $\langle s_x(\nu)\rangle$ of the individual pairspins must add up to $\frac{\Delta}{G}$ (see (14) and (19))

$$\begin{aligned} \Delta &= G\langle \mathrm{v}=0|S_x|\mathrm{v}=0\rangle \\ &= G\sum_{\nu>0}\frac{\Delta}{2E(\nu)} \qquad E=((\epsilon')^2+\Delta^2)^{\frac{1}{2}} \end{aligned} \qquad (34)$$

which determines Δ as a function of G, for the single-particle spectrum considered. In a model with constant G in an interval $|\epsilon'| < S$ around the fermi surface, the self-consistency relation (34) gives

$$\begin{aligned} 1 &= G\sum_{\nu>0}\frac{1}{2E(\nu)} \\ &= G\rho(\epsilon_F)\int_{-S}^{S}\frac{d\epsilon'}{2\sqrt{(\epsilon')^2+\Delta^2}} \\ &= G\rho(\epsilon_F)\log\frac{2S}{\Delta} \end{aligned} \qquad (35)$$

where the last equation assumes $S \gg \Delta$. The relationship (35) shows that the fermi surface is unstable for arbitrary small attractive interactions. The effective value of G needed to produce a given pair field depends on the space of single-particle states, characterized by S.

1.3.2 Critical temperature

When quasiparticles are excited, thermally or by external fields, the pairspin polarization is diminished,

$$\begin{aligned} \Delta(\mathrm{v}) &= G\langle \mathrm{v}|S_x|\mathrm{v}\rangle \\ 1 &= G\sum_{\nu>0}\frac{1}{2E(\nu)}(1-n_q(\nu)-n_q(\bar{\nu})) \end{aligned} \qquad (36)$$

where $n_q(\nu)$ is the number of quasi particles in the orbit ν ($n_q = 0$ or 1). Thus, if a single quasi particle is present in the $\nu, \bar{\nu}$ space ($n_q(\nu) + n_q(\bar{\nu}) = 1$), the pair field cannot exploit this space, and there is no contribution to $\Delta(\mathrm{v})$. The doubly excited state $n_q(\nu) = n_q(\bar{\nu}) = 1$ has $\sigma_{x'} = -1$, and contributes negatively to $\Delta(\mathrm{v})$.

The self-consistency relation (36) gives the pair field parameter as a function of temperature, when thermal averages are introduced for n_q. Subtracting (35) from (36) one obtains

$$\log \frac{\Delta}{\Delta(T)} = 2\int_0^\infty \frac{d\epsilon'}{E} \frac{1}{1+e^{\frac{E}{kT}}} \qquad \langle n_q(\nu) \rangle = (1+e^{\frac{E}{kT}})^{-1} \tag{37}$$

for $\Delta(T)$, which vanishes for

$$kT_c \simeq \frac{\Delta}{1.76} \tag{38}$$

For this critical temperature, the pair correlation disappears, by a second order phase transition.

2 Gauge angle as dynamical variable

- Rotation in gauge space
- Superflow
- Local gauge invariance

The pair correlation is characterized by the collective pairspin $\vec{S}_\perp$, which points in a transverse direction in pairspin space. The symmetry axis in this space (the z-axis) is referred to as the gauge axis. The pairspin polarization may rotate collectively about the gauge axis, and the azimuthal angle of $\vec{S}_\perp$ with respect to this axis is therefore a dynamical variable [4]. The second lecture touches on the following aspects of the collective motion
a The relative rotational frequency of two superconductors as observed in a Josephson junction.
b The superflow connected with a spatial variation of the gauge angle
c The coupling of the supercurrent to the magnetic field, associated with the spontaneous breaking of gauge invariance.

2.1 Rotation in gauge space

- Angle conjugate to particle number
- Spontaneous symmetry breaking
- Dynamics of gauge angle
- Supercurrent in Josephson junctions

2.1.1 Angle conjugate to particle number

The total pairspin angular momentum S_z in the direction of the gauge axis is related to particle number by (11). Thus, the gauge angle ϕ, defined as half the azimuthal angle of $\vec{S}_\perp$ (see Fig.4), is conjugate to particle number

$$[\mathcal{N}, \phi] = -i \tag{39}$$

This relation - which applies to any pair of angle and angular momentum variables - expresses $\mathcal{N}$ as generator of infinitesimal rotations about the gauge axis. A finite rotation through an angle χ (c-number) is represented by

$$\mathcal{G}(\chi) = e^{-i\mathcal{N}\chi} \tag{40}$$

which produces a shift

$$\mathcal{G}(\chi)\phi\mathcal{G}^{-1}(\chi) = \phi - \chi \tag{41}$$

of the gauge angle.

For a state with a definite value of $\mathcal{N}$, the angle ϕ is completely indeterminate. (The probability $|\langle\phi|\mathcal{N}\rangle|^2$ is independent of ϕ). However, the superposition of components with

---

[4] This angle is referred to as the phase angle of the order parameter associated with the pair field. We here use the more specific notation gauge angle for a variable conjugate to particle number.

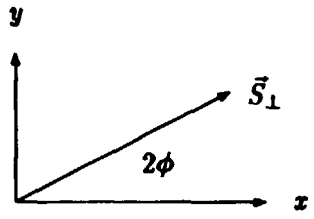

Figure 4: Transverse polarization $\vec{S}_\perp$ with azimuthal angle 2ϕ

The angle ϕ, conjugate to particle number, is referred to as the gauge angle.

different particle number produces states in which the gauge angle emerges from indeterminacy. Thus, a state with a sharpness of orientation $\Delta\phi$ contains components within a range $\Delta\mathcal{N}$, where

$$\Delta\mathcal{N}\Delta\phi \gtrsim 1 \tag{42}$$

expresses the complementary relationship between $\mathcal{N}$ and ϕ.

2.1.2 Spontaneous symmetry breaking

The static pair field constitutes a deformation that defines an orientation relative to the gauge axis. Through this deformation, the system spontaneously breaks away from axial symmetry, and the indeterminacy in the number of particles in a pair correlated state is an inherent feature of this symmetry breaking (see (42)). The static deformation introduces a collective degree of freedom ϕ and gives the system the ability to rotate as a whole around the gauge axis. When there are no external forces depending on the orientation ϕ, the total Hamiltonian describing collective as well as intrinsic motion has axial symmetry and hence conserves particle number.

Symmetry breaking with features akin to those associated with the formation of a pair field occurs in nuclei for which the shell structure leads to a non spherical equilibrium shape with a deformed mean potential. This deformation defines an orientation in space and thus constitutes a spontaneous breaking of rotational symmetry, associated with an indeterminate angular momentum for the nucleonic motion in the deformed potential. The orientation angles of a deformed nucleus are collective variables that manifest themselves in the rotational spectra. The intrinsic excitations associated with the individual nucleons in the deformed potential is the counterpart of the quasiparticle excitations in the pair field. (Nuclei may also deform relatively to a gauge axis. Such nuclei possess a static pair field, which adds and removes pairs of nucleons in time reversed orbits. This deformation is reflected in sequences of quantal states with different particle numbers, associated with rotational motion around the gauge axis) [5].

---

[5] For a discussion of nuclear deformations, see e.g. A. Bohr and Ben R. Mottelson, Nuclear Structure Vol. 2, W.A. Benjamin (1975)

2.1.3 Dynamics of gauge angle

The total energy H as a function of $\mathcal{N}$ and ϕ, for a fixed internal state, gives the equations of motion

$$\begin{aligned} \dot{\mathcal{N}} &= \tfrac{i}{\hbar}[H,\mathcal{N}] = -\tfrac{1}{\hbar}\tfrac{\partial H}{\partial \phi} \\ \dot{\phi} &= \tfrac{i}{\hbar}[H,\phi] = \tfrac{1}{\hbar}\tfrac{\partial H}{\partial \mathcal{N}} \end{aligned} \qquad H = H_{col}(\mathcal{N},\phi) \tag{43}$$

When large numbers of particles contribute to the formation of the pair field ($\mathcal{N} \gg 1$), the uncertainty relation (42) is compatible with

$$\Delta\phi \ll 1 \qquad \frac{\Delta\mathcal{N}}{\mathcal{N}} \ll 1 \tag{44}$$

The gauge angle can then appear as a classical quantity.

If the system can turn freely around the gauge axis, unaffected by external forces, H is independent of ϕ, and the particle number is a constant of motion. The second equation (43) shows that ϕ rotates with frequency

$$\dot{\phi} = \frac{\mu}{\hbar} \tag{45}$$

where

$$\mu = \frac{\partial H}{\partial \mathcal{N}} \tag{46}$$

is the chemical potential (energy per added particle, for fixed internal (pair correlated) state).

The identification of μ with the rotational frequency is implicit in the description of the pair correlation by the Hamiltonian (see (8) and (2))

$$H' = H - \mu\mathcal{N} \tag{47}$$

The last term can be associated with a transformation to a rotating reference system in which ϕ is stationary

$$\begin{aligned} (\dot{\phi})' &\equiv \frac{i}{\hbar}[H',\phi] \\ &= \frac{i}{\hbar}[H,\phi] - \frac{i}{\hbar}\mu[\mathcal{N},\phi] \\ &= \dot{\phi} - \frac{\mu}{\hbar} = 0 \end{aligned} \tag{48}$$

(The added energy $-\mu\mathcal{N}$ is analogous to the Coriolis term $-\hbar\vec{\omega}_{rot}\vec{I}$ in the Hamiltonian describing motion of particles, with total angular momentum $\vec{I}$, in a reference frame rotating with frequency $\vec{\omega}_{rot}$. Such a term acts, for example, in the intrinsic motion of rotating nuclei).

The chemical potential contains a term $-e\varphi$, where φ is the electrostatic potential, assumed to be constant over the conductor. Since the absolute value of φ can be chosen arbitrarily (gauge invariance), the rotational frequency $\dot{\phi}$ for a single superconductor has the same arbitrariness. However, the intrinsic motion (quasiparticle excitations) depends only on the energy differences $\epsilon'(\nu) = \epsilon(\nu) - \mu$, which are independent of the choice of potential.

While there is no reference frame for the gauge angle of an isolated superconductor, the gauge angle of one conductor may be referred to that of another.

2.1.4 Supercurrent in Josephson junctions

A coupling between gauge angles arises if two conductors are connected by a weak link (Josephson junction). Due to the indeterminacy in the occupation numbers for the $\nu\bar{\nu}$ channels in either conductor, a correlated electron pair (superposition of many $\nu\bar{\nu}$ channels) may tunnel from the v = 0 state in one conductor and merge into the v = 0 state for the other. No quasiparticles are exited, and the transfer of electrons is therefore referred to as a supercurrent.

An interaction, which links the states $|\nu_1\bar{\nu}_1\rangle$ and $|\nu_2\bar{\nu}_2\rangle$ in the two conductors, can be expressed as (see (5) and (7))

$$\begin{aligned} H_W &= \sum_{\nu_1,\nu_2} W(\nu_1\nu_2)a^\dagger(\bar{\nu}_2)a^\dagger(\nu_2)a(\nu_1)a(\bar{\nu}_1) + \textit{Hermitian conjugate} \qquad (49) \\ &= \sum_{\nu_1,\nu_2} W(\nu_1\nu_2)s_+(\nu_2)s_-(\nu_1) + \mathcal{H}.c \end{aligned}$$

in terms of the matrix elements $W(\nu_1\nu_2)$ for the transfer of a pair of particles. If ϕ_1 and ϕ_2 are the gauge angles on the two sides of the junction, the mean azimuthal orientations of the pairspins are $2\phi_1$ and $2\phi_2$, respectively (see Fig.4). The components $s_\pm(\nu_{1,2})$ thus have the phase factors $e^{\pm i2\phi_{1,2}}$ (see (7)), and the interaction energy, averaged over the intrinsic motion, is therefore of the form

$$H_W = -W_0 \cos 2\phi \qquad \phi = \phi_2 - \phi_1 \qquad (50)$$

where W_0 is a constant energy characteristic of the junction. (A phase in $W(\nu_1\nu_2)$ leads to a shift in the phase of (50), which is not of significance for the following).

The coupling (50) implies a time variation of $\mathcal{N}_{1,2}$, which gives the current

$$\begin{aligned} \mathcal{J}(=\mathcal{J}(1\rightarrow 2)) &= -e\dot{\mathcal{N}}_2 = e\dot{\mathcal{N}}_1 \qquad (-e = \textit{electron charge}) \qquad (51) \\ &= e\frac{i}{\hbar}[H_W,\mathcal{N}_1] \\ &= -\frac{e}{\hbar}\frac{\partial H_W}{\partial\phi_1} \end{aligned}$$

or

$$\mathcal{J} = \mathcal{J}_0 \sin 2\phi \qquad \mathcal{J}_0 = \frac{2e}{\hbar}W_0 \qquad (52)$$

Thus, by means of a constant external current $\mathcal{J}(< \mathcal{J}_0)$, the relative orientation of the gauge angles can be adjusted to take on any value.

If the conductors are kept at a constant potential difference $V(= \varphi_2 - \varphi_1)$, an energy eV per electron is associated with the tunnelling,

$$H_V = -\frac{1}{2}eV(\mathcal{N}_2 - \mathcal{N}_1) \qquad (53)$$

This energy difference forces the gauge angles to rotate with different angular velocities,

$$\begin{aligned} \dot{\phi} &= \frac{i}{\hbar}[H_V,\phi] \qquad (54) \\ &= -\frac{eV}{\hbar} \qquad (\dot{\phi} = \dot{\phi}_2 - \dot{\phi}_1) \end{aligned}$$

and an alternating current results

$$\mathcal{J} = -\mathcal{J}_0 \sin\omega(t - t_0) \qquad \omega = -2\dot{\phi} = \frac{2eV}{\hbar} \qquad \mathcal{J}_0 = \frac{2e}{\hbar}W_0 \tag{55}$$

The frequency of this current is universally related to the voltage (the work associated with the passage of an electron across the junction) and is independent of the characteristics of the junction.

In the above discussion, ϕ was treated as a classical quantity with a definite value. Quantal fluctuations in gauge angle and particle number reveal themselves in the quantized oscillations of the junction in the potential (50). (The kinetic energy of oscillation arises from the voltage generated by the transfer of charge, inversely proportional to the capacity of the junction).

2.2 Superflow

- Gauge angle as velocity potential
- Winding number

The rotations considered thus far refer to a gauge axis common to the entire superconductor and therefore generate a global (or overall) change of the state. The pair correlated system, however, is capable of distortions in which the gauge angle $\phi(\vec{r})$ changes slowly as a function of space, with the magnitude Δ of the deformation staying constant. The variation of $\phi(\vec{r})$ is associated with a collective flow of the electron fluid. The consequence of local gauge invariance for the superflow (coupling to the magnetic field) is considered in section 2.3.

2.2.1 Gauge angle as velocity potential

The degree of freedom associated with a spatial variation of $\phi(\vec{r})$ involves a local gauge axis for each point in space. The global rotation (40) thus develops into local rotations $\chi(\vec{r})$ generated by the local particle number (density) $\rho(\vec{r})$. The total rotation operator, which contains a factor for each point in space, is therefore

$$\mathcal{G}(\chi) \;=\; e^{-i\int d^3r\rho(\vec{r})\chi(\vec{r})} \tag{56}$$

which is a functional of $\chi(\vec{r})$ and changes the local gauge angle in analogy to (41),

$$\mathcal{G}(\chi)\,\phi(\vec{r})\,\mathcal{G}^{-1}(\chi) = \phi(\vec{r}) - \chi(\vec{r}) \tag{57}$$

(The transformation (56) rotates the local pairspin by an angle $2\chi(\vec{r})$ about the gauge axis and multiplies the quantal operators $a^\dagger$ by the phase factor $e^{-i\chi(\vec{r})}$).

The expression (56) shows that the sites of the rotation axes are the particle co-ordinates, which are left invariant by the local rotations

$$\mathcal{G}(\chi)\vec{r}_k\mathcal{G}^{-1}(\chi) \;=\; \vec{r}_k \tag{58}$$

Thus, if $\rho(\vec{r})$ is expressed as a sum of delta functions for each particle, the gauge operator (56) can be written

$$\mathcal{G}(\chi) = e^{-i\sum_k \chi(\vec{r}_k)} \qquad \rho(\vec{r}) = \sum_k \delta(\vec{r} - \vec{r}_k) \tag{59}$$

which is a function of the particle co-ordinates, hence commuting with $\vec{r}_k$. By contrast, the particle momentum $\vec{p}_k$, which connects neighbouring points, has the transformation

$$\mathcal{G}(\chi)\vec{p}_k\mathcal{G}^{-1}(\chi) = \vec{p}_k + \hbar\vec{\nabla}_k\chi(\vec{r}_k) \tag{60}$$

which registers the change in rotation angle $\chi(\vec{r})$ between infinitesimally separated gauge axes.

The increment $\hbar\vec{\nabla}\chi$ of the particle momenta associated with the shift of the gauge angle from ϕ to $\phi - \chi$ shows that a state, in which the local gauge angle varies from point to point, carries a momentum current

$$\vec{i}_p = -n\hbar\vec{\nabla}\phi \tag{61}$$

The parameter n is referred to as the density of superconducting electrons (and is temperature dependent, see below). The local velocity is

$$\vec{u}(\vec{r}) = -\frac{\hbar}{m}\vec{\nabla}\phi(\vec{r}) \tag{62}$$

and the gauge angle thus appears as the velocity potential of a collective flow superposed on the pair correlated intrinsic motion. The superflow is undamped, because the internal degrees of freedom are frozen, by the energy gap.

The pair correlation is built out of single particle states in a narrow momentum interval $\delta p \sim \frac{\Delta}{v_F}$ around the fermi surface, and the corresponding spatial extension is characterized by the parameter

$$\xi = \frac{\hbar v_F}{\Delta} \tag{63}$$

referred to as the coherence length. The distortion of the intrinsic motion produced by $\phi(\vec{r})$ is relatively small, if $\phi(\vec{r})$ is approximately constant over distances comparable with ξ.

The quasi particle excitations have the energy E (see Fig. 3), when described in a co-ordinate system moving with the local velocity $\vec{u}$ of the superflow. In the fixed co-ordinate system of the lattice, a quasi particle with momentum $\vec{p}$ has the energy $E + \vec{p}\vec{u}$, to first order in $\vec{u}$, as follows from a Galilean transformation. Thus, when the fluid is in thermal equilibrium with the lattice, more quasi particles move against the flow, than in the direction of the flow (see (37)). This reduction in the momentum carried by the flow implies that the density n of superconducting electrons in (61) is a decreasing function of temperature, which vanishes for $T = T_c$.

The gauge rotation (56) is not a symmetry operation, since it produces a distortion of the electron system resulting in an increase in the energy, through the kinetic energy of the flow. With the incorporation of local gauge invariance, however, the rotation (56) becomes part of more extensive symmetry operation, which links the superflow to the magnetic vector potential (see section 2.3.2).

2.2.2 Winding number

The line integral

$$\int_1^2 \vec{u}(\vec{r})\cdot d\vec{r} = -\frac{\hbar}{m}(\phi(\vec{r}_2)-\phi(\vec{r}_1)) \qquad (64)$$

measures the change of ϕ between two points. For a closed loop, this change must be a multiple ν of π, since 2ϕ is the orientation of the local pairspin polarization $\vec{S}_\perp(\vec{r})$, which has a well defined direction at each point in space,

$$\oint \vec{\nabla}\phi\cdot d\vec{s} = \pi\,\nu \qquad \nu = 0, \pm 1, \pm 2, \ldots \qquad (65)$$

The integer ν, which gives the number of revolutions of the pairspin polarization along the loop, is referred to as the winding number.

The loop integral has the same value for curves that can be continuously deformed into each other. Thus, for a singly connected domain, the winding number is zero for any loop. For doubly connected domains, such as the interior of a torus, the flow is characterized by a single winding number. More generally, the flow possesses a set of winding numbers for the topologically distinct loops.

For a stationary flow, the continuity equation requires the divergence of $\vec{u}(\vec{r})$ to vanish. The velocity potential $\phi(\vec{r})$ therefore satisfies

$$\nabla^2\phi(\vec{r}) = 0 \qquad (66)$$

which, together with the winding number and the boundary condition for the flow through the surface

$$-\frac{\hbar}{m}\frac{\partial\phi}{\partial n} = u_n \qquad (67)$$

completely specifies $\phi(\vec{r})$. Thus, for a singly connected specimen with no currents flowing to and from the system, the gauge angle is a constant throughout the conductor.

The winding number ν is a measure of the circulation per particle, and can be expressed in terms of the action integral (see (62) and (65))

$$\nu = -\frac{2}{h}\oint \vec{p}_u\cdot d\vec{s} \qquad \vec{p}_u = m\vec{u} \qquad (h = 2\pi\hbar) \qquad (68)$$

For example, in cylindrical symmetry, the action is the angular momentum, and the flow carries the total angular momentum $\frac{1}{2}\hbar\mathcal{N}\nu$. The condition (65) is therefore a quantization in macroscopic scale, and states with different winding numbers ν constitute different phases of the pair correlated substance. Hence, the quantity ν can only be altered by disrupting the coherence of the pair correlation in the multiply connected domain, by passing a section of the substance through an uncorrelated phase.

2.3 Local gauge invariance

- Electromagnetic potentials and coupling to particles
- Supercurrent. Spontaneous breaking of gauge invariance
- Impermeability of superconductor to magnetic field

The local gauge rotations, which act on the electrons through (56), are part of a more comprehensive symmetry operation. Thus, the quantal states acquire invariance under local gauge transformations, when the relationship between the dynamical variables is modified in a manner that involves interactions between particles. For the case of gauge rotations around an axis, the extended symmetry- referred to as local gauge invariance- introduces the electromagnetic field and prescribes the equations of motion of particles and field (Maxwell and Lorentz equations).

The electrodynamic potentials have orientation with respect to the local gauge axis and are therefore indeterminate in a gauge invariant state. In a superconductor, however, the spontaneous breaking of local gauge symmetry associated with the formation of the pair field provides a reference for the potentials. The relative orientation of potential and pair correlation manifests itself in the supercurrent. The connection between field and current gives mass to the photon, and a static magnetic field therefore cannot penetrate into the superconductor.

2.3.1 Electromagnetic potentials and coupling to particles

In a description that recognizes local gauge rotations as a conserved symmetry, the invariance (58) of the particle position implies that also the velocity is a gauge invariant quantity. However, the momentum is affected by a local operation (see (60)), and this difference between momentum and velocity introduces a new degree of freedom $\vec{A}(\vec{r})$, the vector potential, which for $\vec{r} = \vec{r}_k$ satisfies

$$m\dot{\vec{r}}_k = \vec{p}_k + \frac{e}{c}\vec{A}(\vec{r}_k) \qquad (-e\ =\ \textit{electron charge}) \tag{69}$$

where e is a coupling constant (the elementary unit of charge), and where the velocity of light is introduced to give the field $\vec{A}$ the dimension of charge $\times\ L^{-1}$. The gauge invariance of the velocity $\dot{\vec{r}}_k$ implies that the vector potential has the gauge transformation

$$\mathcal{G}(\chi)\vec{A}(\vec{r})\mathcal{G}^{-1}(\chi) \ = \ \vec{A}(\vec{r}) - \frac{\hbar c}{e}\vec{\nabla}\chi(\vec{r}) \tag{70}$$

in which case the displacement (60) of $\vec{p}$ cancels that of $\vec{A}$.

The transformation (70) requires the total gauge operator $\mathcal{G}(\chi)$ to act on the degrees of freedom of the field, as well as on the particles through (56). (The field operator that is conjugate to $\vec{A}(\vec{r})$ and produces the shift (70) is the electric field $\vec{\mathcal{E}}(\vec{r})$, and the generator of $\mathcal{G}(\chi)$ therefore has a term proportional to $\vec{\nabla}\vec{\mathcal{E}}$).

Local gauge symmetry for the system as a whole is obtained in quantal states that are invariant under gauge transformations affecting particles and field at the same time. By this invariance, the field is anchored in the particles (through Maxwell's equation $\vec{\nabla}\vec{\mathcal{E}} = 4\pi\rho$, and the corresponding equation for the current).

The relation (69) connects spatial components of four-vectors, and the analogous relation for the time components introduces the scalar potential φ and gives the equation of motion for the particles in the electromagnetic field ($\frac{1}{2}mv_k^2 = E+e\varphi(\vec{r}_k)$ or $H = \frac{1}{2m}(\vec{p}+\frac{e}{c}\vec{A})^2-e\varphi$).

The gauge shift (70) can be exhibited as a rotation of an angular variable about the local gauge axis. Thus, a vector field $\vec{A}(\vec{r})$, assumed to vanish at infinity, is determined by its divergence $\vec{\nabla}\cdot\vec{A}$ and rotation $\vec{\nabla}\times\vec{A}$ and can therefore be uniquely divided into transverse and longitudinal components

$$\vec{A} = \vec{A}^{tr} + \vec{A}^{l} \qquad \vec{\nabla}\cdot\vec{A}^{tr} = 0 \quad \vec{\nabla}\times\vec{A}^{l} = 0 \tag{71}$$

also assumed to vanish at infinity. These components can be expressed as integrals of $\vec{A}$ over all space. The transverse part of $\vec{A}$, determined by $\vec{\nabla}\times\vec{A}$ is unaffected by the gauge transformation (70), and the longitudinal part can be expressed as a gradient

$$\vec{A}^{l} = \frac{\hbar c}{e}\vec{\nabla}\phi_A \tag{72}$$

where ϕ_A is dimensionless and has the transformation (see (70))

$$\mathcal{G}(\chi)\phi_A(\vec{r})\mathcal{G}^{-1}(\chi) = \phi_A(\vec{r}) - \chi(\vec{r}) \tag{73}$$

Thus, $\phi_A(\vec{r})$ can be viewed as an angular variable, which gives the direction of the vector potential with respect to the gauge axis.

Any quantity, such as the vector potential $\vec{A}(\vec{r})$, that is affected by gauge transformations (gauge dependent quantity), is indeterminate in a state that is invariant under gauge transformations. The gauge dependence of $\vec{A}(\vec{r})$ is carried by the field angle $\phi_A(\vec{r})$, which - as an azimuth with respect to the gauge axis - is completely indeterminate in a rotationally invariant state.

In classical electrodynamics, gauge invariance appeared as a freedom in the choice of electromagnetic potentials in the description of the physical phenomena. In the quantal description, this freedom can be viewed as an indeterminacy of the potentials in a gauge invariant state. The standard description of gauge transformations, which is taken over from classical physics, is expressed by

$$\vec{A} \rightarrow \vec{A} + \vec{\nabla}\Theta \qquad \Theta = -\frac{\hbar c}{e}\chi \tag{74}$$

with a function Θ of dimension charge. The quantity Θ is connected with the rotation angle χ by a relation in which Planck's constant enters, and the interpretation of gauge symmetry as a rotational invariance for particles and field was therefore outside the scope of classical physics.

2.3.2 Supercurrent. Spontaneous breaking of gauge invariance

The superconducting phase is distinguished from ordinary matter by the deformation, which defines a gauge angle $\phi(\vec{r})$ for the electron system. The emergence of this angle has a profound effect on the electrodynamic properties of the superconductor. Thus, the link (69) between particles and field implies that the superflow with momentum density (61) carries the electric current

$$\begin{aligned}\vec{\imath} &= -\frac{e}{m}\vec{\imath}_p - \frac{ne^2}{mc}\vec{A} \\ &= \frac{ne\hbar}{m}\vec{\nabla}\phi - \frac{ne^2}{mc}\vec{A}\end{aligned} \tag{75}$$

Like the particle velocity, the current (75) is invariant under combined gauge transformations of particles and field (see (57) and (70)). The relation (75), involving the vector potential, is specific to the superconductor, for which the indeterminacy in $\vec{A}(\vec{r})$ can be compensated by a corresponding indeterminacy in $\phi(\vec{r})$, so that the resulting current can have a definite value. In (75), as in (61), the effective density n of superconducting electrons is a decreasing function of temperature, which vanishes at the transition to the normal state.

The local relation (75) between current and vector potential assumes fields that are approximately constant over distances comparable with the coherence length ξ, which characterizes the non-locality of the pair correlation (see (63)). When $\vec{A}$ varies more rapidly, the internal degrees of freedom come into play (virtual quasiparticle excitations), and the induced current is smaller than (75) (by a factor $\sim (q\xi)^{-1}$ for a wave number q large compared with ξ^{-1}). A similar effect arises from impurities that cause a finite mean free path for the electrons. However, the deformation in the superconductor with orientation $\phi(\vec{r})$ continues to manifest itself in a linear, though non-local, relation between vector potential and current.

In the gauge invariant description of field together with particles, the formation of the pair correlation in the superconductor acquires the character of a spontaneous symmetry breaking, like that of the global symmetries considered in section 2.1.2. This symmetry breaking introduces an orientation $\phi(\vec{r})$, which provides a reference (intrinsic frame) for the direction $\phi_A(\vec{r})$ of the vector potential; inversely, the orientation of the field (externally or internally produced) can act as a reference for the direction of the pair field. In the gauge invariant state for the total system, any azimuthal angle, such as $\phi(\vec{r})$ or $\phi_A(\vec{r})$, is completely indeterminate, but relative angles can have definite values.

The orientation of vector potential with respect to pair correlation manifests itself in the supercurrent (75). If $\vec{A}$ is decomposed into longitudinal and transverse parts (see (71) and (72)), the current takes the form

$$\begin{aligned}\vec{\imath} &= \frac{ne\hbar}{m}(\vec{\nabla}\phi - \frac{e}{\hbar c}\vec{A}) \\ &= \frac{ne\hbar}{m}\vec{\nabla}(\phi - \phi_A) - \frac{ne^2}{mc}\vec{A}^{tr}\end{aligned} \tag{76}$$

The first term is the superflow (61), in which the orientation $\phi(\vec{r})$ is referred to the direction of $\phi_A(\vec{r})$. This term brings in the longitudinal part of $\vec{A}$ and is therefore complemented by the second term, since only the total field has a local significance.

2.3.3 Impermeability of superconductor to magnetic field

The connection (75) between current and vector potential modifies the propagation of the electromagnetic field in the superconductor. Thus, a magnetic field generates a current with a local circulation,

$$\vec{\nabla} \times \vec{\imath} = -\frac{ne^2}{mc}\vec{\mathcal{H}} \qquad \vec{\mathcal{H}} = \vec{\nabla} \times \vec{A} \tag{77}$$

and this current, in turn, generates a magnetic field

$$\vec{\nabla} \times \vec{\mathcal{H}} = \frac{4\pi}{c}\vec{\imath} \tag{78}$$

by Maxwell's equation for stationary fields.

For given boundary conditions, specified by external magnetic fields and by currents flowing in and out of the conductor, the equations (77) and (78) uniquely determine the current and magnetic field, for a singly connected domain. The equation for $\vec{\mathcal{H}}$, obtained by elimination of $\vec{\imath}$,

$$\vec{\nabla}^2\vec{\mathcal{H}} - \frac{1}{\lambda^2}\vec{\mathcal{H}} = 0 \qquad \lambda^2 = \frac{mc^2}{4\pi ne^2} \tag{79}$$

$$(\vec{\nabla} \times (\vec{\nabla} \times \vec{\mathcal{H}}) = \vec{\nabla}(\vec{\nabla} \cdot \vec{\mathcal{H}}) - \vec{\nabla}^2\vec{\mathcal{H}} \qquad \vec{\nabla} \cdot \vec{\mathcal{H}} = 0)$$

describes a field that decays exponentially in the superconductor, with a characteristic length λ (London length). The same equation is obtained for the current $\vec{\imath}$.

Thus, for a superconductor of linear dimensions R large compared with λ, the field and current are confined to a surface region of thickness λ. The current flowing in this region shields the interior of the superconductor from the magnetic field (Meissner effect). In the opposite limit ($R \ll \lambda$), the screening effect is small, and the current is the potential flow considered in section 2.2.

If the parameter λ, or the mean free path for scattering, is smaller than the coherence length, the current (77), induced by the magnetic field, is reduced (see 2.3.2), and the effective penetration depth is correspondingly increased. The values of these parameters can vary over a wide range, depending on material, temperature, and other parameters.

For doubly connected regions, the field equations (77) and (78) are supplemented by the topological condition (65) for the winding number, which gives the relation (see (75))

$$\oint \vec{\imath} \cdot d\vec{s} = \frac{ne\hbar}{m}\pi\nu - \frac{ne^2}{mc}\Phi \qquad \Phi = \oint \vec{A} \cdot d\vec{s} = \int \vec{\mathcal{H}} \cdot d\vec{f} \tag{80}$$

where Φ is the magnetic flux passing through the loop. If the dimensions of the conductor are large compared with the penetration depth, the current is confined to the surface region, and the integral (80) therefore vanishes along any integration path confined to the interior of the conductor. For such a loop, it follows from (80) that the enclosed flux is quantized

$$\Phi = \nu\Phi_0 \qquad \Phi_0 = \frac{hc}{2e}\nu \qquad \nu = 0 \pm 1, \pm 2 \ldots \tag{81}$$

in units of the flux quantum Φ_0. However, in contrast to the underlying quantization of circulation, which is of general validity, flux quantization only holds in the limit of complete screening.

The linear field equation (79) describes photons, which have a mass

$$m_\gamma = \frac{\hbar}{\lambda c} \tag{82}$$

when propagating in the superconductor. (For time dependent fields, the addition of the displacement current $\frac{1}{c}\dot{\vec{\mathcal{E}}}$ to (78), combined with the induction law $\vec{\nabla} \times \vec{\mathcal{E}} = -\frac{1}{c}\dot{\vec{\mathcal{H}}}$, gives the extra term $-\frac{1}{c^2}\ddot{\vec{\mathcal{H}}}$ in (79)). The static magnetic field may thus be viewed as a zero frequency condensate of these massive photons.

A methamorphosis of massless gauge bosons, similar to that occurring in the superconductor, arises in the unification of the weak and electromagnetic interactions. This extended local gauge symmetry involves rotations about four different axes and introduces four massless gauge fields. The symmetry is spontaneously broken by a static deformation of a field, referred to as the Higgs field, which plays the role of the pair field (Δ, ϕ). The orientation (in gauge space) of the Higgs field thus provides a frame of reference for the gauge fields, and the propagation of the gauge fields is thereby modified in such a manner that three of the bosons become massive ($W^{\pm}, Z$ particles). The fourth (the photon) is blind to the deformation and remains massless - until it encounters a superconductor. (There is little evidence so far concerning the structure of matter underlying the orientation in gauge space attributed to the Higgs field).

The pair correlated ground state is based upon invariance under time reversal $\mathcal{T}$ (see 1.1.1). However, the collective flow and the magnetic field are odd under $\mathcal{T}$, and therefore subject the intrinsic motion to forces that violate time reversal symmetry, hence acting differently on the conjugate single-particle states ν and $\bar{\nu}$. When the current and magnetic field reach critical values - for which the time reversal violating single-particle energies are comparable with Δ - the pair correlated phase becomes unstable.

CHAPTER 3

MUONS, NEUTRONS AND SUPERCONDUCTIVITY

G. Aeppli
AT&T Bell Laboratories
Murray Hill NJ 07974
and
Physics Dept.
Risø National Laboratory
DK-4000 Roskilde, Denmark

Abstract

The principles of the neutron scattering and muon spin relaxation (µSR) techniques and their applications to studies of superconductors are described briefly. µSR and neutron scattering work on magnetic correlations in superconductors and materials directly related to superconductors are reviewed.

I. Introduction

Magnetic correlations are central to the phenomenon of superconductivity, as can be seen from examining the BCS (pairing) wavefunction. Furthermore, some of the essential macroscopic properties, such as the Meissner-Ochsenfeld effect, of superconductors are magnetic. Consequently, magnetic probes are of considerable value for examining superconductors. In the present lecture, we discuss two probes of microscopic magnetism, namely neutron scattering and muon spin relaxation (μSR), whose roots are in nuclear and particle physics but which have proven themselves as useful tools in condensed matter physics. We first describe the neutron scattering technique and its application to determining the microscopic and macroscopic properties of superconductors after which we do the same for μSR. The final section of these notes is devoted to a brief survey of the interplay between microscopic magnetic correlations and superconductivity (1), as determined by neutron scattering and μSR.

II. Magnetic Neutron Scattering

Various textbooks give thorough introductions to neutron scattering (1). What is important here is that the magnetic cross-section is directly proportional to the Fourier transform (in space and time) of the two-spin correlation function:

$$\frac{\partial^2\sigma}{\partial\Omega\partial E} = \left|\frac{\gamma e^2}{m_e c^2}\right|^2 \frac{|\mathbf{k}_f|}{|\mathbf{k}_i|} |\tfrac{1}{2} g f(\mathbf{Q})|^2 \times \frac{1}{\hbar} \sum_{\alpha,\beta} (\delta_{\alpha\beta} - \hat{Q}_\alpha \hat{Q}_\beta) S^{\alpha\beta}(Q,\omega) \times \exp(-2W(\mathbf{Q})) \tag{1}$$

where

$$S^{\alpha\beta}(\mathbf{Q},\omega) = \frac{1}{2\pi}\int dt \exp(-i\omega t) \times \sum_{m,n} \exp[i\mathbf{Q}\cdot(\mathbf{r}_m - \mathbf{r}_n)] \times \langle S_m^\alpha(t) S_n^\beta(0)\rangle . \tag{2}$$

In Eq. (1), $\mathbf{k}_i$ and $\mathbf{k}_f$ denote the wave vectors of the ingoing and outgoing neutrons, respectively; $\mathbf{Q} = \mathbf{k}_f - \mathbf{k}_i$, $\hat{\mathbf{Q}} = \mathbf{Q}/|\mathbf{Q}|$, $f(\mathbf{Q})$ refers to the atomic form factor of the magnetic species, and $\exp(-2W(Q))$ is the Debye-Waller factor; in Eq. (2), $\mathbf{r}_m$ represents the positions of the spins $\mathbf{S}_m$. The angle brackets ($<\cdots>$) refer to a thermal (statistical) average. The correlation function is a sum of contributions due to dynamic (oscillatory and relaxational) processes and the equilibrium arrangement of the spins;

$$S^{\alpha\beta}(\mathbf{Q},\omega) = \frac{1}{\pi}(1 - \exp - \beta\hbar\omega)^{-1} \chi''_{\alpha\beta}(\mathbf{Q},\omega) + S^{\alpha\beta}(\mathbf{Q})\delta(\omega) \tag{3}$$

$\chi_{\alpha\beta}''(Q,\omega)$ is the imaginary part of the generalized magnetic susceptibility due (via the fluctuation-dissipation theorem) to the spin dynamics. $S^{\alpha\beta}(Q)$ is the static (infinite-time) two-spin correlation function.

We first discuss $S^{\alpha\beta}(Q)$, which is defined as:

$$S^{\alpha\beta}(Q) = \sum_{m,n} \exp[i\mathbf{Q}\cdot(\mathbf{r}_m - \mathbf{r}_n)] \langle S^{\alpha}_m(t=\infty) S^{\beta}_n(t=0)\rangle . \tag{4}$$

If the spins S_n are aligned ferromagnetically, for example along the z axis, $S^{\alpha\beta}(Q)$ vanishes except when $\alpha = \beta = z$, in which case it is directly proportional to the Fourier transform $\rho(Q)$ of the pair-correlation function for the magnetic ions:

$$S^{zz}(Q) = |\langle S^z\rangle|^2 \sum_{m,n} \exp[i\mathbf{Q}\cdot(\mathbf{r}_m - \mathbf{r}_n)] = |\langle S^z\rangle|^2 \rho(Q). \tag{5}$$

For a crystalline system, $\rho(Q)$ is a sum of δ functions centered at reciprocal-lattice points and vanishes elsewhere. Of course, this result is only a consequence of Fourier's theorem, and does not depend on the origin of the ferromagnetic alignment. In particular, it can be due either to spontaneous order of the type found in, for example, Fe below its Curie point, or, which will be of greater interest to us below, to an external magnetic field applied to the sample.

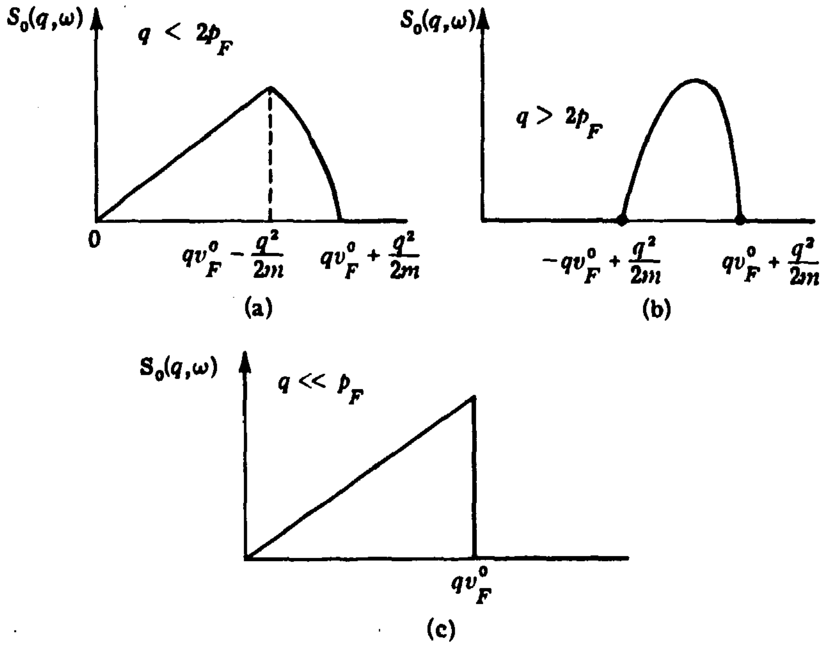

Fig. 1. Dynamical correlation function $S_0(Q,\omega)$ for non-interacting Fermi liquid. From ref. 2.

For a simple ordered antiferromagnet, the magnetic unit cell is generally larger than the nuclear cell, and $S^{zz}(Q)$ will be a sum of δ functions centered at the reciprocal lattice points corresponding to the enlarged (magnetic) unit cell. Note that this means that for most antiferromagnets, new Bragg peaks appear in neutron diffraction spectra, while for ferromagnets the magnetic peaks appear at nuclear Bragg points; the onset of a ferromagnetic phase is usually signalled by an increase in intensity of a pre-existing nuclear reflection.

The dynamic response $\chi_{\alpha\beta}(Q,\omega)$ is due to magnetic relaxation processes which are due to interactions among the electronic moments themselves (category I) and between the electronic moments and charge fluctuations (category II) and lattice vibrations (category III) in the solid. Spin waves in magnetically ordered materials are examples of processes in category I, while decays of magnetic correlations in mixed valence materials (such as $CePd_3$) belong to category II. For a non-interacting Fermi liquid with a spherical Fermi surface, $\chi''(Q,\omega)$ is a Lindhard function due to intraband transitions (2); it is shown in Fig. (1). Note that $\chi''(Q,\omega)$ is gapless for all $Q < 2k_f$, this corresponds to the production of electron hole pairs with arbitrarily small energy. Furthermore, $\chi''(Q,\omega)$ has a Q-dependent maximum at Qv_f (for small Q) where v_f is the Fermi velocity.

III. Magnetic Neutron Scattering from Superconductors

As described above, neutron scattering is a direct probe of magnetic correlations in solids. The two distinct magnetic manifestations of superconductivity are related to the two magnetic lengths associated with superconductors, namely the penetration depth λ and the pair coherence length ξ^3. λ owes its existence to the special connection between electric current and magnetic vector potential in a charged superfluid (known as the London equation) combined with Maxwell's equations.. For superfluids such as ^3He, composed of Fermions without charge, $\lambda = \infty$. The finite value of λ is responsible for many macroscopic properties of superconducting solids, notably the Meissner effect and flux lattices in type I and II materials, respectively.

ξ corresponds roughly to the typical separation of paired electrons. Because the pairs in conventional S-wave superconductors consist of electrons with opposite spin, on distance scales large compared to ξ, the magnetic moments of the conduction electrons are effectively hidden.

Magnetic neutron scattering experiments performed on superconductors to date have been devoted to three issues. The first two are ramifications of the two respective magnetic lengths, ξ and λ. The corresponding measurements could in principle (but not in practice) be performed for any superconductor. The third theme is the interplay of magnetism and superconductivity as demonstrated by exploration of phase diagrams (with e.g. composition, magnetic field, pressure, and temperature as variables) containing both superconducting and magnetic regimes. The next two sections briefly survey the first two categories of studies, while Chapter V of these notes summarizes neutron scattering as well as µSR results relevant to the third theme.

A. Flux exclusion, λ, and "macroscopic" phenomena

(i) Observation of Flux Lattices

The Abrikosov lattice is an ordered array of vortices, each admitting one quantum of magnetic flux. Therefore, there is a modulated magnetic field in the solid. For neutron diffraction, the situation is exactly as for the ordered antiferromagnet (as discussed in section II above), and corresponding superlattices are expected. Thus, neutron scattering is a direct, in-situ method for measuring the properties of flux lattices. Extensive neutron studies of equilibrium and non-equilibrium effects in conventional superconductors such as Nb have been performed[4]. On the other hand, attempts to study high-T_c materials in similar fashion have at the time of writing, failed.

(ii) Measurements of λ

For scattering angles sufficiently close to grazing, neutrons are subject to total external reflection of the type also found for photons (light, X-rays....). By measuring reflectivities as a function of scattering angle and/or wavelength, it is possible to extract detailed information concerning the reflecting interface. In particular, polarized neutrons can be used to measure gradients in magnetization density associated with a type I superconductor (or type II material with $H < H_{c1}$) in a magnetic field. This gradient is directly related to λ, and has been measured successfully for polished single crystals of Nb. Because of the sensitivity of the technique to surface imperfections, work on sintered powders of $YBa_2Cu_3O_{7-\delta}$ has been less successful in the sense of yielding results for λ roughly one order of magnitude smaller than those obtained by all other means[5].

B. Bound singlet formation in the superconducting state (ξ)

In a conventional (s-wave) superconductor, electron pairs are singlets with respect to their spin degrees of freedom. This implies that the spin susceptibility, χ_s, but not the orbital susceptibility, χ_o, vanishes in the superconducting state. In a classic experiment using polarized neutron diffraction in an external field, Shull and Wedgwood[6] showed this to be the case for V_3Si. The basic idea is to polarize the superconductor well within its flux lattice regime (where the lattice constant $d \approx (\phi/H_{exp})^{1/2} \ll \lambda$) and to measure the uniform magnetic contribution to the Bragg scattering by measuring the difference between the scattering intensities with neutron spins polarized parallel and antiparallel to the applied field:

$$A \sim (f_M + f_N)^2 - (f_M - f_N)^2 = 4 f_M f_N \,, \tag{6}$$

where f_N and f_M are the nuclear and magnetic scattering lengths, respectively. Since $f_M \sim \chi f(Q)$ where χ is the net susceptibility and $f(Q)$ is the magnetic formfactor, the temperature dependence of χ can be monitored. Note that since nuclear scattering lengths are known with considerable precision, $\chi f(Q)$ is readily established in absolute units and can be compared directly to calculations with not even an adjustable scale factor. Fig. 2 shows the results. Note that as predicted, χ is reduced only by χ_s, with the orbital susceptibility χ_o surviving in the ordered state.

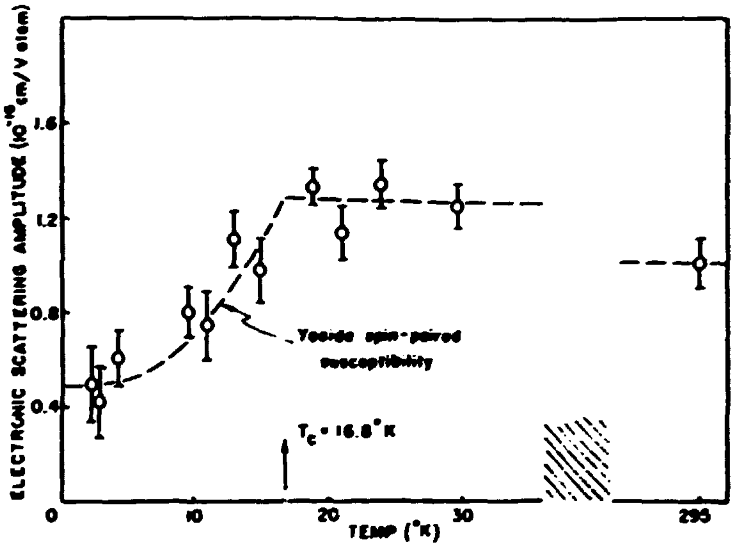

Figure 2. Temperature dependence of the electronic scattering amplitude of the (210) Bragg reflection of V_3Si through the superconducting transformation. The spin component is suppressed at low temperature, leaving only the orbital component. χ_s as calculated by Yosida is matched to the data. From ref. 6.

References for Chapters I-III

1. See, e.g. S.W. Lovesey, **Theory of neutron scattering from condensed matter, Vols I & II**, Clarendon Press, Oxford (1984).
2. D. Pines and P. Nozières, **Quantum Liquids**, Benjamin, NY (1966).
3. An introduction to these concepts is by P.G. DeGennes, **Superconductivity of Metals and Alloys**, Benjamin, NY (1966).
4. The pioneering work was by D. Cribier, B. Janot, L.M. Rao, and B. Farnoux, Phys. Lett. 9, 106 (1964).
5. See R. Felici et al., Nature 329, 503 (1987) and references therein.
6. C.G. Shull and F.A. Wedgwood, Phys. Rev. Lett. 16, 513 (1966).

IV. Muon spin relaxation

(based on ref. 2)

Like neutron experiments, muon spin relaxation measurements fall into categories relating to macroscopic and microscopic magnetism. In this chapter, we give a brief introduction to the technique and then describe its application to studies of the magnetic penetration depth. Use of the technique for surveying magnetism of materials related to superconductors will be reviewed below.

A. Brief introduction to μSR[1]

In time-differential μSR experiments, muons with known initial spin polarization are stopped one at a time in a sample, where they decay via a parity-violating process emitting positrons preferentially along their final polarization. The relevant processes in the generation and subsequent decay of the muons (generally positive) are as follows:

$$p + p \rightarrow \begin{cases} \pi^+ + d \\ \pi^+ + n + p \\ \pi^+ + \pi^- + p + p \end{cases} \tag{7}$$

$$\pi^+ \rightarrow \mu^+ + \nu_\mu \tag{8}$$

$$\mu^+ \rightarrow e^+ + \nu_e + \bar{\nu}_\mu \tag{9}$$

The proton-proton collision of (7) is produced by the acceleration (by e.g., a cyclotron) of protrons into a fixed target. The pion (π^+) and muon (μ^+) rest masses and lifetimes are 139.6 MeV, 105.7 MeV, 2.6×10^{-8} s, and 2.2×10^{-6} s, respectively. Data are collected as a function of time t after arrival of the individual muons in the sample by counting the numbers $N_+(t)$ and $N_-(t)$ of positrons emitted in the directions parallel and antiparallel to the incident muon spin. Typically, more than 10^6 muon decays are timed to yield suitable $N_+(t)$ and $N_-(t)$ histograms. The resulting ratio, $[N_+(t)-N_-(t)]/[N_+(t)+N_-(t)]$, is proportional to the time-dependent polarization of the muon ensemble. A magnetic field can be applied either parallel (longitudinal) or perpendicular (transverse) to the initial muon polarization, yielding, respectively, a T_1-type relaxation function $G_{zz}(t)$ or a T_2-like relaxation envelope $G_{xx}(t)$ modulating a precessing muon decay asymmetry, just as for the free induction decay in NMR[7]. Of course, the muon precession observed in the presence of either an external or internal field is simply Larmor precession where the frequency $\omega = \gamma_\mu H$, and $\gamma_\mu = 2\pi\times135.5$ MHz/T is the gyromagnetic ratio of the muon. External fields are generally applied for studies of the response to external fields, while internal fields arise in systems with frozen magnetic moments.

B. Measurements of the magnetic penetration depth

Instead of giving a survey of the vast literature on this subject, we simply describe one such measurement[2], which was performed on $La_{1.85}Sr_{0.15}CuO_4$, with a superconducting transition at $T_c = 37$ K.

Fig. 3 shows the transverse-field (TF) μSR precession signals for a field of 80 G at room temperature and at 10 K after zero-field cooling (ZFC). The enhanced relaxation rate at 10 K is obvious. The solid lines are the results of fits made to a Gaussian relaxation function, $G_{xx}(t) = \exp-(\Lambda t)^2$, which corresponds to a Gaussian distribution of internal fields. The low field in these spectra is convenient for illustrative purposes, but for measurements of λ, we used an external field $H_{ext} = 4$ kG, which is well above H_{c1} ($\simeq 150$ G at 10 K, from other measurements) and well below H_{c2} for $T < 35$ K. Fig. 4 displays the muon depolarization rate Λ as a function of increasing temperature after cooling in an external field of 4 kG. Above $T_c = 37$ K, the fitted Λ, which is due to static nuclear dipole relaxation, is small $[0.102(2)\times10^6\,s^{-1}]$; below T_c, Λ increases by an order of magnitude indicating that the internal field becomes more inhomogeneous as the superconducting state is entered. NMR[3] and μSR[4] experiments on other type-II superconductors have revealed the same effect, due to the vortex lattices formed when the external field penetrates the materials. The mean square inhomogeneity in the field sampled by the muons in μSR or nuclear spins in NMR is[5], for fields H with

$$H_{c1} \ll H \ll H_{c2}, \quad \langle|\Delta H|^2\rangle = 0.00371\, \phi_0^2 \lambda^{-4} \tag{1}$$

where λ is the London penetration depth and ϕ is the magnetic flux quantum, 2.068×10^{-7} G cm^2.

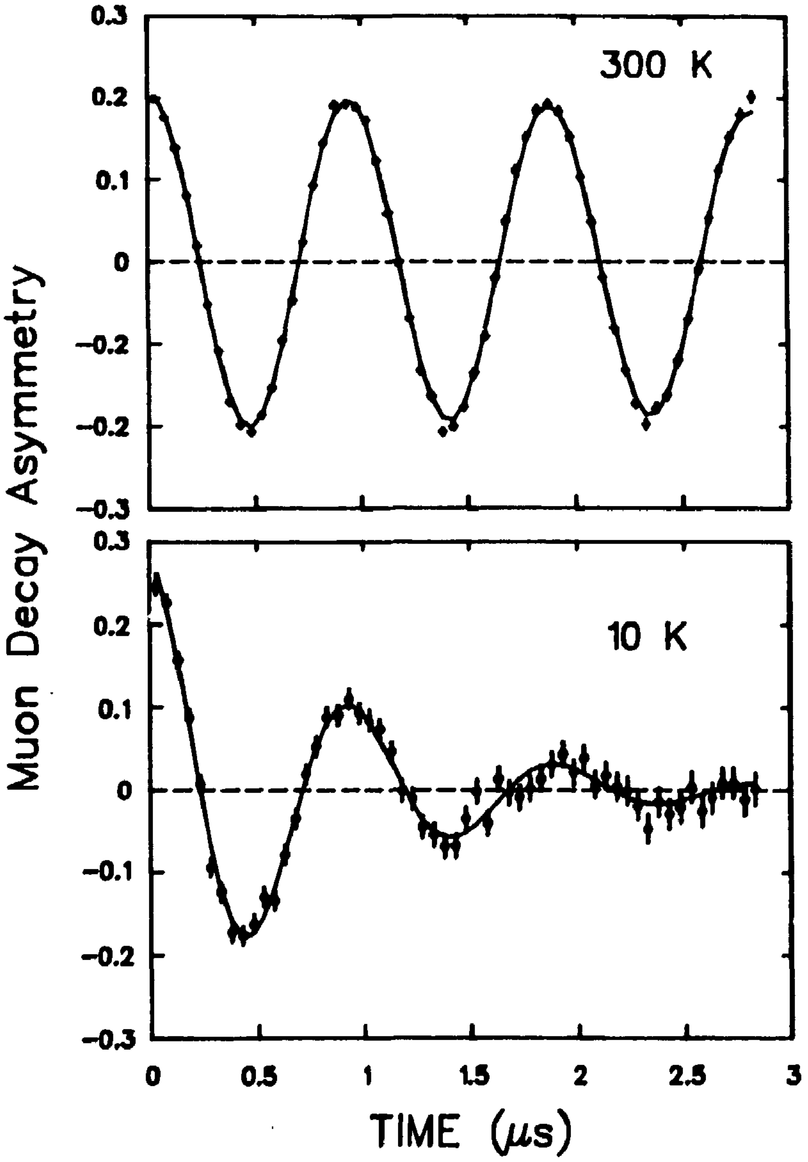

Fig. 3. Muon-spin-relaxation signal in a transverse field of 80 G for T above and below $T_c = 37$ K. The 10 K data were obtained after cooling in a 4 kG field.

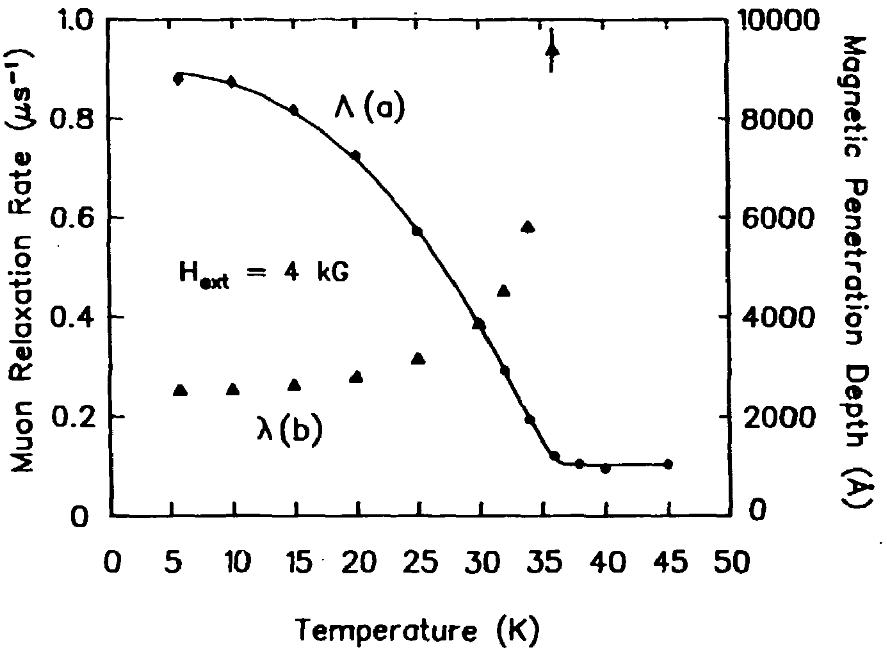

Fig. 4. Temperature dependence of (a) (circles) the Gaussian relaxation rate Λ obtained for a transverse field $H_{ext}=4$ kG after cooling in zero applied field; and (b) (triangles) the magnetic penetration depth λ inferred from Λ using Eq. 1 after correcting for a fixed nuclear dipolar relaxation rate $\Lambda_0=0.102(2)\times10^6\ s^{-1}$, assumed to add in quadrature with the depolarization rate due to the vortex lattice. The solid curve is a guide to the eye.

Because $\Lambda\sqrt{2} = \gamma_\mu <|\Delta H|^2>^{1/2}$, Eq. (2) implies that λ can be extracted from μSR data. In particular, for high fields, $d \ll \lambda$ and Eq. (2) becomes $\Lambda(\mu s^{-1}) \approx [2025/\lambda(\text{Å})]^2$. For $La_{1.85}Sr_{0.15}CuO_4$, the corresponding value for λ at 6 K is 2150 Å, which is comparable to those of A15 compounds such as Nb_3Sn and V_3Si. In type-II superconductors, the London formula gives an approximate value for λ,

$$\lambda = \left[\frac{m^*c^2}{4\pi n_s e^2}\right]^{1/2} = \left[\frac{m^*/m_e}{4\pi n_s r_e}\right]^{1/2}, \tag{2}$$

where $r_e = e^2/mc^2 = 2.82\times10^{-5}$ Å is the classical radius of the electron, m^* is the effective carrier mass, and n_s is the superfluid density, which for ordinary superconductors at $T = 0$, is identical to the carrier density (n) for $T > T_c$. The Sommerfeld constant can also be expressed in terms of m^* and n,

$$\gamma = k_B^2(\pi/3)^{2/3}m^*n^{1/3}/\hbar^2, \tag{3}$$

for a three-dimensional (isotropic) electron gas and

$$\gamma = k_B^2(\pi/3)m^*/(\hbar^2\Delta) \tag{4}$$

for a stack of two-dimensional systems with spacing Δ between them. In the two-dimensional case, m^* is a strong function of angle θ between the electron propagation direction and the basal planes: $m^*(\theta = 0) = m^*_{ab}$, while $m^*(\theta = 90^\circ) = \infty$. This implies that λ is also strongly angle-dependent (see eq. (2)), with the result that for a powder, eq. (1) must be modified to read:

$$<|\Delta H|^2> = 0.0085\,\phi_o^2\lambda_{ab}^{-4} \tag{5}$$

Recent measurements[7] on single crystals of $YBa_2Cu_3O_{7-\delta}$ strongly indicate the two-dimensional nature of the carrier liquid in high-T_c copper oxide superconductors, which makes Eqs (4) and (5) more appropriate than (1) and (3). We can solve Eqs. (3) and (4), using the measured values of λ_{ab} and γ ($\approx$ 6 mJ/mole K^2), to obtain a small n, 0.4×10^{22} carriers/cm^3 ($\simeq$ 0.3 carriers/formula unit), and a sizable m^*/m_e of 4. We emphasize that our values for n and m^*/m_e are merely estimates based on Eqs. (2), (4) and (5); it remains to be seen whether the uncorrected London formula is valid for samples such as ours.

Fig. 4(b) shows the temperature dependence of λ computed from Λ and Eq. (2). Attempts to fit the present data to the form,

$$\lambda(T) = \lambda(0)[1-(T/T_c)^4]^{1/2}\ , \tag{6}$$

which generally describes the behavior of ordinary superconductors as well as $YBa_2Cu_3O_7$[8], failed. The failure can be due to inhomogeneities, which lead to a distribution of T_c's or to the pressed powder's granularity, which causes percolation, finite size, and weak link effects. We note also that when the electronic mean free path ℓ becomes comparable to ξ_0, which might well be the case for $La_{1.85}Sr_{0.15}CuO_4$, the standard expressions, Eqs. (3) and (5), for $\lambda(0)$ and $\lambda(T)$ become invalid.

References for Chapter IV

1. An introductory text is A. Schenck, **Muon Spin Rotation Spectroscopy, Principles and Applications in Solid State Physics** (Hilger, Bristol, 1985).
2. G. Aeppli et al., Phys. Rev. B **35**, 7129 (1987).
3. P. Pincus et al., Phys. Lett. **13**, 21 (1964).
4. A.T. Fiory et al., Phys. Rev. Lett. **33**, 969 (1974); Y.J. Uemura et al., Hyperfine Interact. **31**, 413 (1986).
5. E.H. Brandt, Phys. Rev. B **37**, 2349 (1988).
6. W. Barford and J. Gunn, preprint (1988).
7. D. Harshman et al., preprint (1988).
8. D. Harshman et al., Phys. Rev. B **36**, 2386 (1987).

V. Magnetic Fluctuations and Order in Materials Related to Superconductors

(from ref. 18)

A. Introduction

There are by now three classes of superconductors with potentially unconventional pairing mechanisms. For all three, namely the heavy fermion systems, the cuprous oxides, and the organic superconductors, magnetic fluctuations have been proposed as the source of the pairing. While examination of the magnetic fluctuations in these systems will not necessarily provide direct and unambiguous proof that magnetic fluctuations are responsible for superconductivity, it should, at the very least, prove useful in the sense that the study of phonons in conventional superconductors has been useful. In the present chapter, we give a brief overview of work on the magnetic fluctuations and order in various heavy fermion and copper oxide systems.

B. Heavy Fermion Systems

Antiferromagnetic correlations have been found in all heavy fermion compounds of which large single crystals are available. The list of such compounds includes superconducting UPt_3[1], antiferromagnetic U_2Zn_{17}[2], and paramagnetic $CeCu_6$[3]. For example, Fig. 5 shows data collected for UPt_3, in directions parallel to a* (in the basal planes) through the (0,0,1.05) and (0,0,2.05) points in reciprocal space. In addition to sharp phonon scattering, indicated by the dashed lines, there is diffuse magnetic scattering which peaks near (0,0,1) and (±1,0,2). This implies that the U moments, when fluctuating at the rate corresponding to 8 meV, are antiferromagnetically correlated with respect to their nearest neighbors. More recent work[4,5] shows that at much smaller energy scales ($\hbar\omega \leq 1$ meV), there are diffuse scattering maxima at $Q = (\pm 1/2,0,1)$, reciprocal lattice points where relatively strong magnetic Bragg reflections occur in $(U_{1-x}Th_x)Pt_3$ and $U(Pt_{1-x}Pd_x)_3$[6]. A greater surprise was that all of the nominally pure single crystals of UPt_3 examined[4] displayed magnetic order below 5 K, with the same wavevector but also with a greatly reduced ordered moment ($(0.02 \pm 0.01)\mu_B$/U ion). Previous muon spin relaxation (μSR) measurements had suggested the presence of magnetic order in polycrystalline UPt_3[7]. The onset of the ordering is close to the hitherto unexplained maxima in the temperature derivative of the resistivity and magnetoresistance of pure UPt_3[8].

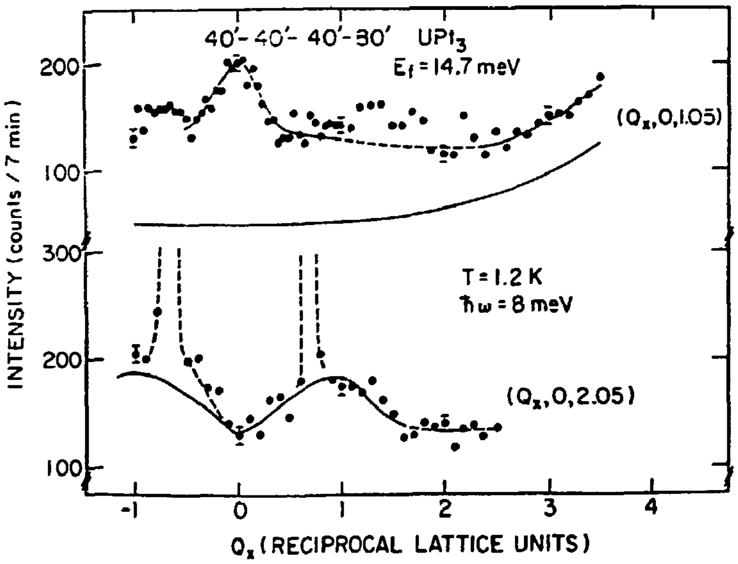

Fig. 5. Constant$-\hbar\omega$ scans for UPt_3 carried out at the thermal beam H7 of Brookhaven national Laboratory.

It is quite clear that the antiferromagnetic fluctuations revealed by neutron scattering from UPt_3 coexist with superconductivity. Furthermore, theoretical work[9] shows that such fluctuations are of the correct type to yield the peculiar superconductivity of UPt_3. However, until recently, no direct evidence for coupling of magnetic and superconducting order parameters has been found. It is therefore satisfying that our newest experiments[4] show that the magnetic order parameter actually decreases below the superconducting T_c, a result which indicates such a coupling *whether or not the magnetic order is stabilized by defects or impurities.*

C. $La_{2-x}Sr_xCuO_4$

Shortly after the discovery of (relatively) high-T_c superconductivity in $La_{2-x}(Sr,Ba)_xCuO_4$, many groups[11] reexamined the question of magnetic order in the parent compound, La_2CuO_4. Neutron diffraction work[12] confirmed that La_2CuO_4 is indeed an antiferromagnet. Furthermore, both bulk and neutron data indicate that the ordered moment and Néel temperature depend strongly on oxygen deficiency and dopant concentration, x. In particular, for $x \geq 0.06$, magnetic order is absent. Inelastic neutron scattering measurements on nearly stoichiometric La_2CuO_4[13], and the isostructural analog, La_2NiO_4[14], reveal strong two-dimensional correlations above the three-dimensional Néel temperature, T_N. Furthermore, two-dimensional fluctuations (spin waves) reduce the three-dimensionally ordered moments. While readily observed by neutron scattering these fluctuations are not visible by the muon spin relaxation (μSR) technique for $x \approx 0$[15,16]. On the other hand, both inelastic neutron scattering[17] and μSR[15] performed on sintered powders with the optimal composition ($x \approx 0.15$) for superconductivity failed to reveal magnetic fluctuations. However, for samples with low but non-zero Néel temperatures, magnetic fluctuations are visible even by μSR. We conclude that the effective exchange coupling, J_{eff}, is greatly reduced on introduction of charge carriers. Well beyond the impurity concentration at which J_{eff} and T_N are reduced to zero, the magnetic fluctuations could simply have an energy scale of order the bandwidth, W, for the charge carriers, which would make their detection by thermal neutron scattering difficult. Clearly, neutron scattering studies of large single crystals are required to firmly establish whether magnetic correlations exist in the superconducting systems. We close by noting that for $La_{2-x}Sr_xCuO_4$, it seems that J_{eff}/W becomes small very rapidly as x is increased and the best superconducting properties achieved. In contrast, for heavy fermion systems, superconducting and otherwise, J_{eff}/W is always of order unity.

References to Chapter V

1. G. Aeppli, A.I. Goldman, G. Shirane, E. Bucher and M.-Ch. Lux-Steiner, Phys. Rev. Lett. **58** (1987) 808; A.I. Goldman, G. Shirane, G. Aeppli, E. Bucher and J. Hufnagl, preprint (1987).
2. D.E. Cox. G. Shirane, S.M. Shapiro, G. Aeppli, Z. Fisk, J.L. Smith, J. Kjems and H.R. Ott, Phys. Rev. B **33** (1986) 3614; C. Broholm, J.K. Kjems, G. Aeppli, Z. Fisk, J.L. Smith, S.M. Shapiro, G. Shirane and H. R. Ott, Phys. Rev. Lett. **58** (1987) 917.
3. G. Aeppli, H. Yoshizawa, Y. Endoh, E. Bucher, F. Hufnagl, Y. Onuki and T. Komatsubara, Phys. Rev. Lett. **57** (1986) 122; L.P. Regnault, W.A.C. Erkelens, J. Rossat-Mignod, J. Flouquet, E. Walker, D. Jaccard, A. Amato and B. Hennion, J. Magn. Magn. Mat. **63 & 64** (1987) 289.
4. C. Broholm, J. Kjems, G. Aeppli, E. Bucher and W.J.L. Buyers, in: Proc. Torino Meeting on Magnetic Excitations and Fluctuations II (Springer, Heidelberg (1987); G. Aeppli, E. Bucher, C. Broholm, J. Kjems, J. Baumann and J. Hufnagl, Phys. Rev. Lett. **60**, 615 (1988); C. Broholm, D. Bishop, G. Aeppli, and E. Bucher, unpublished (1988).
5. P. Frings, B. Renker and C. Vettier, preprint (1987).
6. P. Frings, B. Renker and C. Vettier, J. Magn. Magn. Mat. **63-64** (1986) 6561.
7. R. Heffner, paper presented at International Conference on Valence Fluctuations (Bangalore, 1987).
8. A. de Visser, Ph.D. thesis (University of Amsterdam, 1986).
9. N. Miyake, S. Schmitt-Rink and C.M. Varma, Phys. Rev. B **34** (1986) 6554; M.T. Béal-Monod, C. Bourbonnais and V.J. Emery, Phys. Rev. B **34** (1986) 7716.
10. J.G. Bednorz and K.A. Muller, Z. Phys. B **64** (1986) 189; S. Uchida, II. Tagaki, K. Kitazawa and S. Tanaka, Jap. J. Appl. Phys. Lett. **26**, L1 (1986); C.W. Chu, P.H. Hor, R.L. Meng, L. Gao, Z.J. Huang and Y.Q. Wang, Phys. Rev. Lett. **58** (1987) 405: R.J. Cava, R.B. van Dover, B. Batlogg and E.A. Rietman, Phys. Rev. Lett. **58** (1987) 408.
11. L.F. Schneemeyer, J.V. Waszcak, E.A. Rietman and R.J. Cava, Phys. Rev. B **35** (1987) 8421: Y. Yamaguchi, II. Yamauchi, M. Dhashi, II. Yamamoto, N. Shimoda, N. Kikuchi and Y. Syono, Jpn. J. Appl. Phys. Part 2, L447 (1987); R.L. Greene, H. Maletta, T.S. Plaskett, J.G. Bednorz and K.A. Miller, Solid State Comm. **63** (1987) 379.
12. See, e.g., D. Vaknin, S.K. Sinha, D.E. Moncton, D.C. Johnston, J. Newsam, C. Safinya and H. King, Phys. Rev. Lett. **58** (1987) 2807.

13. G. Shirane, Y. Endoh, R.J. Birgeneau, M.A. Kastner, Y. Hidaka, M. Oda, M. Suzuki and T. Marakami, Phys. Rev. Lett. 57 (1987) 1611.
14. G. Aeppli and D. Buttrey, Phys. Rev. Lett. 61, 203 (1988).
15. D. Harshman, G. Aeppli, G. Espinosa, J. Remeika, E. Ansaldo, T. Risaman, D. Williams, D. Noakes, B. Ellman, and T. Rosenbaum, Phys. Rev. B 38, 852 (1988).
16. Y.J. Uemura, W.J. Kossler, X. H. Yu, J.R. Kempton, H. E. Shone, D. Opie, C.E. Stronach, D.C. Johnston, M.S. Alvarez and D.P. Goshorn, preprint (1987).
17. B. Yang, G. Shirane, D. Johnson, R. Cava and G. Aeppli, unpublished.
18. G. Aeppli, in **Proceedings of Yamada Conference on Correlated Electron Systems** (Sendai, 1987).

Acknowledgements

The author is grateful to D. Bishop, C. Broholm, E. Bucher, D. Buttrey, J. Kjems, G. Shirane, A. Goldman, B. Yang, D. Johnson, R. Cava, D. Harshman, G. Espinosa, J. Remeika, J.H. Brewer, T. Riseman, D. Williams, S. Dodds, E.J. Ansaldo and D.R. Noakes for the fruitful collaborations which led to the results briefly surveyed in these notes. Work at Brookhaven was supported by the division of Materials Sciences, U.S. Department of Energy under contract DE-AC02-76CH00016. The author also thanks Risø National Laboratory (Denmark) and TRIUMF (Canada) for their hospitality.

CHAPTER 4

D: 8903002202

The Josephson Junction.

N.F. Pedersen
Physics Laboratory I
The Technical University of Denmark
DK-2800 Lyngby, Denmark

Abstract.

The basic equations for the Josephson junction are derived in a simple way. We discuss the properties of such junctions under various circumstances - including the effects of damping and capacitance - according to the shunted junction model. Also the effects of an external rf bias current are discussed; this leads to a definition of the various characterizing frequencies and to the appearence of many new phenomena. rf-applications such as SIS-mixers and parametric amplifiers will be mentioned. The introduction of spatial dimensions leads to problems concerning cavity exitations and solitons. Finally conditions for the appearence of chaos in Josephson junctions will be discussed.

1. Introduction.

The following description concentrates on the properties of superconducting Josephson junctions, in particular the unique nonlinear properties that has so much promise for useful applications. Although we largely think in terms of the "old" superconductors simply because the corresponding thin film Josephson junctions are well characterized, we expect most of the following to hold also for the new high T_C ceramic superconductors if and when high quality thin film Josephson junctions become available; modifications may occur, of course, because of changed parameters.
The basic physics of superconductivity ("old" and "new") has been discussed by others at this conference and will not be dealt with in any detail here. Section 2 gives an account of the properties of the (autonomous) Josephson junction. Section 3 deals with the magnetic field dependence, while section 4 introduces the topic of external pumping with time varying signals, i.e. rf properties. Section 5 deals very briefly with the temperature dependence of the Josephson effect. Section 6 deals with the Josephson junction in external circuits, in particular a cavity, while section 7 discusses the properties of a long Josephson junction, i.e. cavity exitations and solitons on a Josephson transmission line. Finally section 8 discusses the chaos that often appears in the case of very large pumping signals. The paper is summarized in section 9.

2. The autonomous Josephson junction.

The basic properties of superconductors have been discussed by others at this conference [1,2]. Here I will concentrate on the properties of Josephson junctions with special emphasis on the non-linear behaviour.

A Josephson junction consists of two weakly coupled superconductors as shown in Fig. 1a. The superconductors are so close that the wavefunction of the left superconductor, ψ_L, is having an overlap with the superconductor to the right and vice versa. A rigorous derivation of the properties of such a structure was first given by Josephson [3]. However a very simple and elegant argument by Feynman [4] reproduces the essentials of the original derivation, and gives the necessary weak coupling between the two sides. It leads to a tunneling pair current that may be expressed as $I_0 \sin\phi$, where ϕ is the difference between the phases of the superconducting wavefunctions on either side of the barrier and I_0 is the maximum pair current. Allowing also for a shunt resistance R carrying a normal electron current (V/R), and a capacitance C carrying a capacitive current C(dV/dt), one obtains a total current I_{dc}

$$C dV/dt + V/R + I_0 \sin\phi = I_{dc} \qquad (1a)$$

The argument by Feynman also reproduces Josephson's result for the time rate of change of the phase difference, as

$$d\phi/dt = 2eV/\hbar, \qquad (1b)$$

where $\hbar$ is Planck's constant and e is the electron charge.

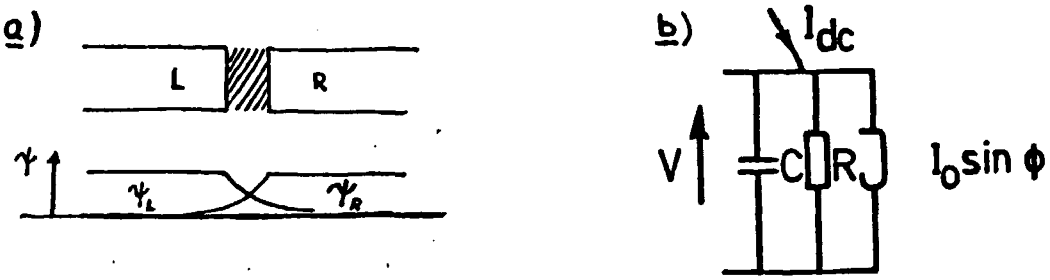

Fig. 1 (a) Schematic drawing of a Josephson junction. Left and right superconductors and wave functions.
(b) Equivalent diagram for a small Josephson junction.

Eq. (1b) is the famous Josephson frequency to voltage relation and Eq. (1a) is Kirchoffs law applied to the Josephson junction equivalent circuit shown in Fig. 1b.

This current-driven Josephson junction is the most widely investigated Josephson junction system; a description may be found for example in one of the good recent books on the subject [5,6], or in a more classic text on superconductivity [7]. The equation for the Josephson junction also describes other important physical systems, such as the synchronous motor, the phased-locked loop, pinned charge density waves, and the damped driven pendulum.

In a Josephson junction the tunneling currents are from two different kinds of charge carriers, Cooper pairs and normal electrons. The unique non-linear properties are due to the Cooper pair current, or supercurrent, as it is often called. With time normalized to the reciprocal of the socalled plasma frequency, $\omega_o^{-1} = (\hbar C/2eIo)^{1/2}$, and current normalized to the critical current I_o, Eqs. (1a,1b) may be simplified to the dimensionless equation, [5,6]

$$\phi_{tt} + \alpha\phi_t + \sin\phi = \eta \tag{2a}$$

$$v = \phi_t \tag{2b}$$

The plasma frequency, ω_o, is a natural oscillation frequency for the Josephson junction, corresponding to the pendulum frequency in a pendulum. β_c - the (dimensionless) Mc-Cumber parameter - is given by $\beta_c = 2eR^2I_oC/\hbar$, and the damping parameter α is given by $(1/\sqrt{\beta_c})$. η is the normalized (to I_o) dc bias current, and v is the voltage normalized to $\hbar\omega_o/2e$.

The dynamical behaviour of Eq. (2a,2b) may be described in the following way. For η (current) below one, a time independent solution $\phi = \arcsin\eta$ and voltage $v = 0$ is possible. For very large values of η the average voltage $\langle v\rangle$ is determined by the resistance (the average of the capacitive current is zero, and the average value of the supercurrent is less than one) i.e. $\eta \approx \alpha \langle\phi_t\rangle$. If we chose another normalizing frequency, the socalled characteristic frequency $\omega_c = 2eRI_o/\hbar$, and normalize the time to $1/\omega_c$ and the voltage to RI_o, we may obtain a convenient plot of a series of I-V curves with β_c as a parameter [5,6]. These are shown in Fig. 2a. We notice that for high damping, $\beta_c = 0$, the I-$\langle v\rangle$ curve is single valued. For $\beta_c > 0$ hysteresis occurs i.e. for $\eta_c < \eta < 1$ a zero-voltage solution coexist with a solution at a finite voltage. The threshold bias value η_c is a function of the damping parameter, which is shown in Fig.2b.

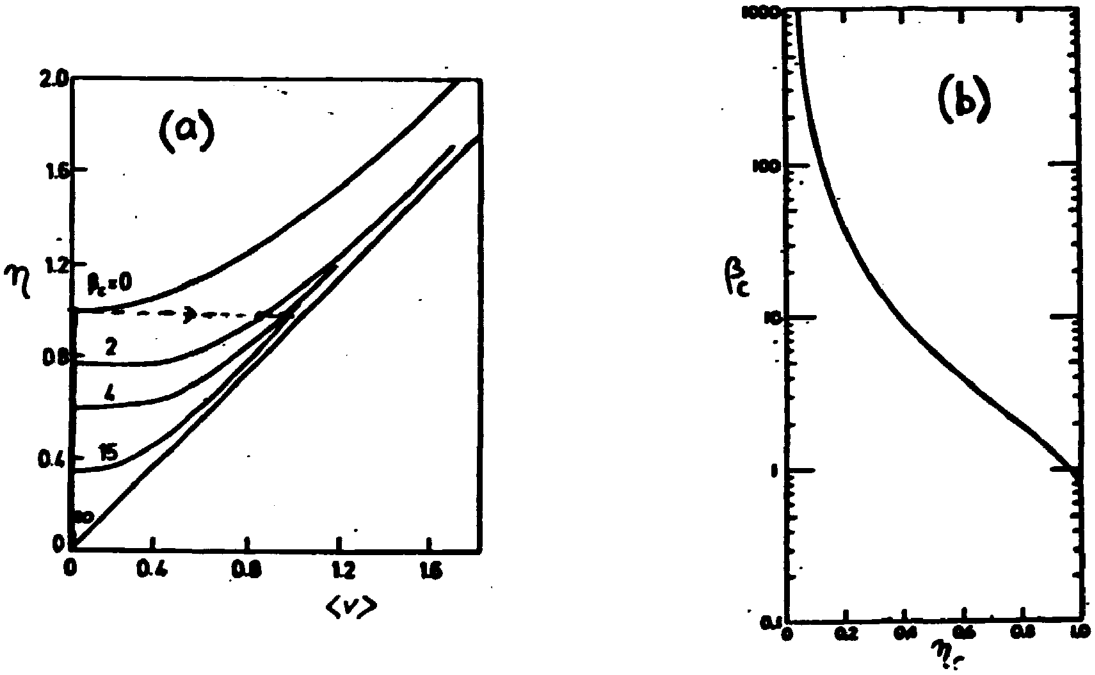

Fig. 2 (a) IV curves for the shunted junction model
(b) The McCumber curve

The details of the dynamical behaviour of this socalled shunted junction model may be found in [5,6]; it is the most important and widely used Josephson junction model. It should be mentioned that no general analytical solution to the model exists; however the qualitative behaviour, approximation formulas, and numerical calculations are described in great detail in the literature.

3. Magnetic field dependence.

If a magnetic field is applied to the Josephson junction parallel to the plane of the barrier, a spatial dependence of the phase is introduced [7,5,6]. The phase ϕ varies linearly with distance x perpendicular to the magnetic field H in the plane of the barrier, and the pair current becomes spatially dependent

$$J(x) = J_1 \sin (2\pi d/\Phi_0 \, H\cdot x + \phi_0) \qquad (3)$$

Here J denotes the current density and Φ_o, the magnetic flux quantum, is given by $\Phi_o = h/2e = 2.064\times10^{-15}$ Vs. d is the magnetic thickness of the junction, $d = 2\lambda_L + t$ where λ_L is the socalled London penetration depth, and t is the oxide thickness. This spatial dependence of the pair current gives a total current that is an oscillating function of the magnetic field, as may be seen by integrating the current density, Eq. (3) over the junction dimensions [5,6,7].

4. rf properties of the Josephson junction.

If we apply a time varying bias current $I = I_{rf} \sin\omega t$ in Eg. (1a) we may quite generally assume that to some approximation the voltage has the same fundamental frequency; accordingly we may write

$$V = V_o + V_{rf}\cdot\sin(\omega t + \gamma) \qquad (4)$$

where V_o, V_{rf} and the phase γ has to be determined. From Eq. (1b) this leads to a phase ϕ (t) of the form

$$\phi(t) = (2eV_o/\hbar)\cdot t + \phi_1 \sin(\omega t + \gamma) + \phi_o \qquad (5)$$

which gives a supercurrent of the form

$$I = I_o \sin\phi = I_o \sin(\omega_J t + \phi_1 \sin\omega t + \phi_o) \qquad (6)$$

where ϕ_1 and ϕ_o has to be determined, and the Josephson frequency ω_J is given by $\omega_J = 2eV_o/\hbar$. The evaluation of the double sine in Eq. (6) gives rise to the socalled rf-induced steps in the IV-curve, the amplitude of which depends on the applied rf power as Bessel functions. Fig. 3 shows schematically an example of an IV curve with such rf-induced steps at a spacing $\Delta v = \hbar\omega/2e$.

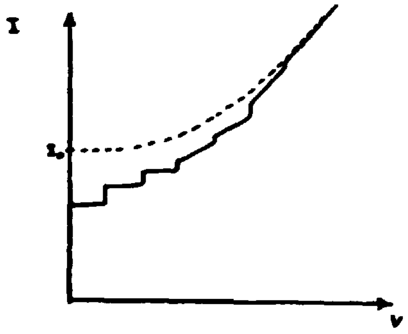

Fig. 3 rf induced steps in the IV-curve (schematic draving).

A very important topic within Josephson junctions is the rf-applications. Such applications include millimeter wave sources and low noise SIS mixers, detectors and parametric amplifiers for the millimeter wave region. For the latter applications the pump power levels are moderate and below the threshold for chaos, (though often not very far below) for best performance. In the section on chaos we will consider the situation when the pump strength is above the threshold.

5. Temperature dependence.

Near T=0 all electrons are paired, and the supercurrent has its maximum value. The number of pairs - and hence the superconducting properties - disappear in a gradual way as the transition temperatur T_C is approached. For the 'old' superconductors the temperature dependence is discussed in detail in [5,6,7]. For the 'new' superconductors there are no well established theory yet, although experiments show the same gradual transition as for the 'old' superconductors.

6. The Josephson junction with external circuits.

For the purpose of the present section we will write Eq. (2a,b) as a set of two coupled first order equations.

$$\dot{\phi} = v \tag{7a}$$

$$\dot{v} = \eta - \alpha v - \sin\phi - i_s \tag{7b}$$

where we have introduced i_s for the interaction with the external circuit (see Fig. 4a). Eqs. (7a,7b) is a set of coupled first order differential equations, that with $i_s = 0$ describes the autonomous junction. For a Josephson junction interacting with external circuits ($i_s > 0$) additional equations describing those circuits are necessesary. An example is a Josephson junction coupled to a cavity. Its equivalent diagram is shown in Fig. 4a; with time normalized to the inverse plasma frequency $\omega_0^{-1} = (\hbar C/2eI_0)^{\frac{1}{2}}$ it is described by Eqs. (7a,7b) for the basic Josephson junction together with

$$\dot{i}_s = (v - (\omega_C/\omega_0)(r'/R)i_s)/\beta_L \tag{8}$$

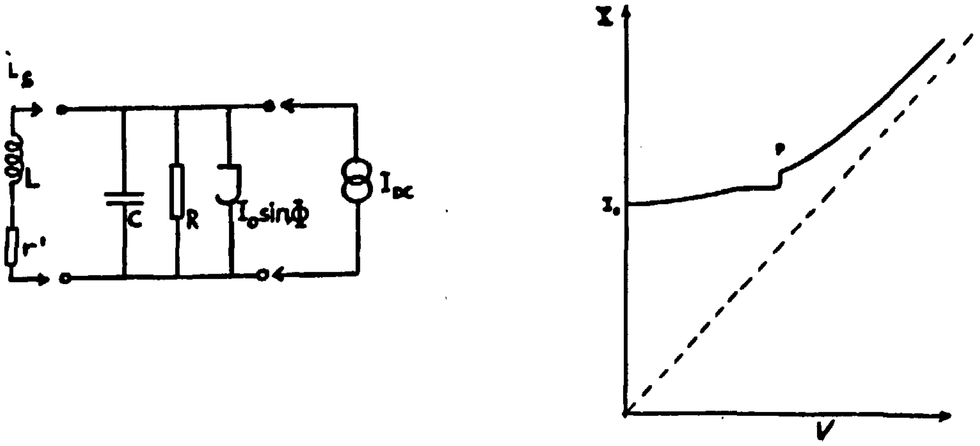

Fig. 4 Josephson junction coupled to a cavity.
(a) The equivalent diagram
(b) The IV-curve with a cavity induced step near P.

for the series resonance circuit. Here r' is the resistance of the series resonance circuit, r is the same resistance normalized to the junction shunt resistance R and $\beta_L = 2eLI_O/\hbar$ [8].

The qualitative behaviour of a junction coupled to a cavity is the following [5,6]. A Josephson junction with a dc voltage V_O oscillates at a frequency which is given by $\omega_J = 2eV_O/\hbar$. When that frequency is in the vicinity of the cavity resonance frequency, a non-linear interaction with frequency locking may occur. For strong locking the oscillation frequency is determined by the cavity frequency. When the frequency is only sligthly detuned from resonance, the system may oscillate at the cavity frequency for some time and then shift to the "Josephson frequency" for some time - before going back to the cavity frequency, and so on. The motion becomes intermittent [5,6,8]. The IV-curve of such a system is shown qualitatively in Fig. 4b. The detailed dynamical behaviour of the system, Eq. (7a,7b,8) is described for example in [8].

7. Long Josephson junctions: Spatial dependence.

Already in the previous section, the cavity mode involves a spatial variation of the phase, although it is not explicitly visible in the lumped element equivalent circuit diagram.

In the weakly non-linear limit the spatial variations may form in such a way that an integral number of half wavelengths appear across the junction. This gives rise to the cavity modes that may be seen directly in the IV-curve (cf. Fig. 4b and section 6). Since a magnetic field changes the spatial variation (section 3) many of the cavity modes can be exited by a magnetic field [5,6].

In the following we will consider the highly non-linear limit when a large spatial variation of the pair phase difference is allowed. We may then get a new type of excitation called a soliton, which is a localized 2π variation of the phase that may move like a particle under external driving. Indeed the very long Josephson junction, or the Josephson transmission line (JTL) is one of the physical systems where soliton propagation is accessible for direct experimental measurements [9,10]. For the purpose of this presentation it suffices to note that the physical manifestation of the soliton is a fluxon, i.e. a quantum of magnetic flux $\Phi_o = h/2e = 2.064 \times 10^{-15}$ Vs. Moving fluxons in the Josephson transmission lines manifest themselves as the socalled zero field steps (ZFS) in the dc current-voltage characteristic of the Josephson junction - somewhat similar in appearence to the cavity step discussed in the previous section. Figure 5a shows the equivalent diagram for a JTL and Fig. 5b shows the geometry of a long junction of the socalled overlap type. The physical origin of the inductance L' shown in Fig. 5a is Cooper pair currents within the London penetration layer of thickness λ_L (Fig. 5b) . A possible resistance, R', due to a flow of normal electrons in the

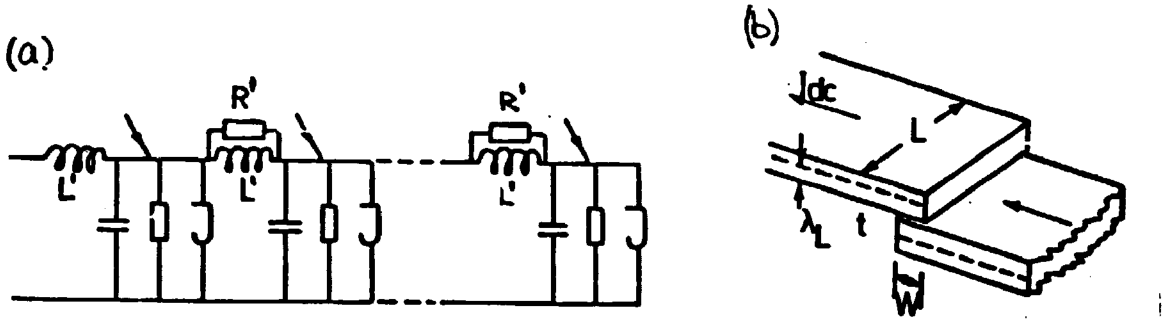

Fig. 5 (a) Equivalent diagram for a Josephson transmission line.
(b) Schematic drawing of the junction geometry.

same layer is also shown. Taking all these circuit elements into account, the wave equation for the JTL may be written as an extension of Eq. (2)

$$-\phi_{xx} + \phi_{tt} + \sin\phi = \eta - \alpha\phi_t + \beta\phi_{xxt} \qquad (9)$$

with (normalized) voltage $v = \phi_t$ (as in Eq. 2b) and (normalized) current $i = -\phi_x$. The additional normalisations used are as follows: Length is measured in units of the socalled Josephson penetration depth $\lambda_J = \sqrt{(\hbar/2de\mu_0 J)}$. The damping parameter β is given by $\beta = L'\omega_0/R'$, J is the current density and d is the magnetic thickness of the junction, $d = 2\lambda_L + t$. The junction length, L, is assumed large, and the width, W, is assumed small compared to the Josephson penetration depth. Finally velocities become normalized to the velocity of light in the barrier, c, given by $c = c\sqrt{t/d}$, where c is the velocity of ligth in vacuum. The expression for c reflects the fact that electric fields exist only across the tunneling barrier of thickness, t, whereas magnetic fields exist both in the barrier and the penetration layers (see Fig. 5b). For typical experimental junctions ("old" superconductors) c is a few percent of c.

7a. Perturbation calculation for the infinite line.

Soliton Dynamics.

The methods and ideas in this section are largely based on the work of McLaughlin and Scott [9]. With the rigth hand side equal to zero, Eq. (9) is the sine-Gordon equation. The loss and bias terms on the rigth hand side are considered as a perturbation to the sine-Gordon equation. The unperturbed sine-Gordon equation has the well known analytical single soliton solution [9].

$$\phi = 4\tan^{-1}\exp\theta \qquad (10)$$

where $\theta = (x-ut)\gamma(u)$ and $\gamma(u) = 1/\sqrt{(1-u^2)}$ is the Lorentz factor. The solution gives rise to a 2π phaseshift over a length of a few λ_J, and its derivative ϕ_t represents a voltage pulse. Note that the form of the solution - a traveling wave in the parameter $\theta = \gamma(u)(x-ut)$ - is a consequence of the Lorentz invariance of the sine-Gordon equation. The sine-Gordon soliton behaves very much like a relativistic particle with energy, H, and momentum, P, given by

$$H = 8\gamma(u) \quad , \qquad P = 8u\gamma(u) \tag{11}$$

With the normalisations used here the rest mass of the soliton is 8. In Eq. (10) the velocity u is a free parameter. As shown in [9] the perturbation terms are included by assuming a solution of the same form as that in Eq. (10), but with u to be determined by a power balance equation. Requiring either the Hamiltonian or the momentum to be independent of time one finds the velocity (momentum) to be determined by [9,10,11]

$$\pi\eta/4 = u\gamma(u)(\alpha + \beta/(3(1 - u^2))) \tag{12}$$

As is clear from Eq. (12) the velocity is determined by a balance between the losses represented by α and β and the energy input represented by the bias term η. In most of what follows we will assume $\beta = 0$ and take only shunt losses into account. In that case the velocity may be found explicitly as

$$u = 1/\sqrt{(1 + (4\alpha/\pi\eta)^2)} \quad , \tag{13}$$

Because Eqs. (12,13) are derived by a perturbational approach, they are not expected to be valid if the perturbing terms are large, i.e. if the bias term approaches one and/or the system is heavily damped. Various corrections applicable to that situation have been considered in [12].

7b. Soliton experiments: dc IV-curves.

The overlap JTL.

In the overlap junction (Fig. 5b) the bias current is uniformly distributed over the junction length, and $\eta = I_0/JWL$ may be assumed in Eq. (9). Due to the moving fluxon, the mechanism of which is described below, a phaseshift of 2π takes place in a time interval l/u, where l is the (normalized) length of the junction. This in turn gives rise to a (normalized) dc voltage, v given by

$$v = (2\pi/l)u \tag{14}$$

The overlap junction has boundary conditions requiring that no currents flow out at the ends, i.e.

$$\phi_x(0,t) = \phi_x(l,t) = 0 \tag{15}$$

It may be shown that this boundary condition is mathematically equivalent to a soliton antisoliton collision, that may be treated analytically within the framework of perturbation theory [10,13]. The collision gives rise to an energy loss and a phaseshift that changes sligthly the average velocity from that of the infinite line.

Fig. 6a shows a numerical simulation of a collision between a soliton and an anti-soliton on a Josephson transmission line.

In the I-V-curve the moving soliton gives rise to the so-called zero field steps (ZFS). The mechanism for the first

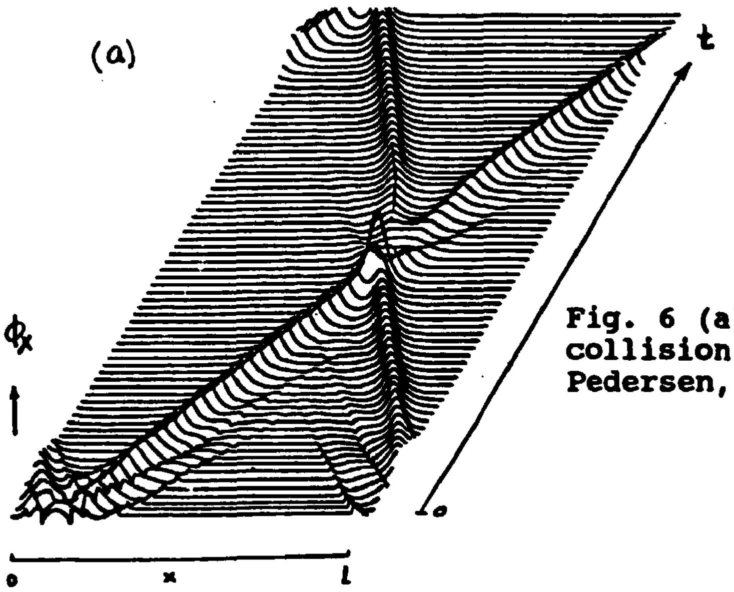

Fig. 6 (a) Soliton-antisoliton collision (A. Davidson and N.F. Pedersen, unpublished)

ZFS, n = 1, is that a fluxon moves along the junction and is reflected at the boundary as an antifluxon. Since the reflection at x = 1, is equivalent to a collision with a virtual antifluxon at x = 1, the problem may be treated in the framework of perturbation theory for the phaseshift and the energy loss. If the junction length, 1, is very large, the details at the boundaries play only a minor role, and the voltage of the first step is given by Eq. (14). Thus for example Pedersen and Welner [11] were able to completely neglect the effects of collisions in a comparison between experimental soliton ZFS on a very long overlap junction (1 = 45) and perturbation theory. Fig. 6b shows an example of one of their experimental curves. If the junction length is smaller (for example of the order 5 - 10), the energy loss and the phaseshift will give rise to corrections [13].

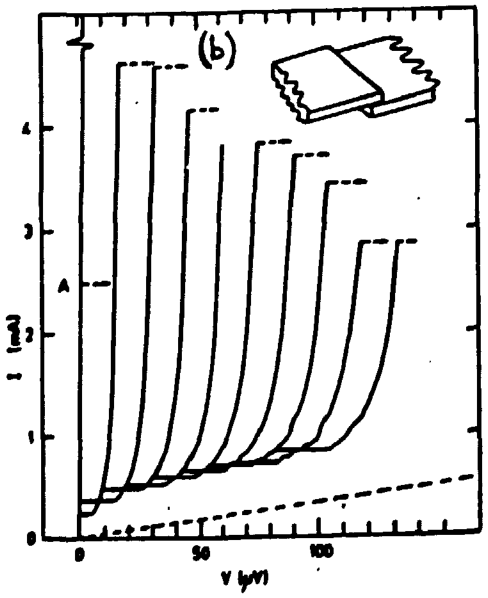

Fig. 6 (b) Experimental zero field steps of a long overlap junction. (From ref. 11).

7c. Direct sampling measurement of the soliton waveform.

The smallness of the flux quantum, $\Phi_0 \approx 2\times 10^{-15}$ Vs, gives some rather difficult specifications on the bandwidth and sensitivity of the amplifiers to be used. Most of the experimental work has been performed in Japan. A very nice method for the experimental verification of Josephson junction solitons is to take advantage of the properties of Josephson junction electronics. In [14] Josephson pulse generator and a Josephson sampling circuit was fabricated directly on the same substrate as the JTL; a time resolution of less than 10 ps and a current sensitivity of a few μA was obtained. They also investigated fluxon dynamics [15] by evaporating a resistor (of length a few μm) on top of the JTL. By means of a control current supplied to the resistor it was found that a fluxon could be accelerated, made to pause, or even reverse its direction of propagation. Details of the reflection at an open boundary (section 7b) [16] and in particular of the fluxon antifluxon collision [17] has been revealed by direct measurement with on-chip Josephson electronics. In that way most of the expected dynamical behaviour of the solution has been confirmed in direct measurements. It is now feasible to talk about Josephson soliton electronics.

Solitons on the JTL may very well have technical applications. Three possible candidates for applications that have emerged are microwave oscillators and amplifiers, digital information processing, and analog amplifiers.

8. Chaos in Josephson junctions.

Another non-linear signature appearing quite often in Josephson junctions is chaos - together with its accompagnying bifurcations. In fact, quite often the Josephson junction is used as a model system for chaos in numerical simulations. A particular feature of chaos in Josephson junctions is that the effect of thermal noise and the effect of deterministic noise (chaos) are both very important for the experiments. The interplay between those two sources of noise is at best very complicated, and at worst makes it impossible to interpret experiments. This has led to new theoretical and numerical work on the non-linear interaction between thermal and deterministic noise.

8a. Deterministic chaos in the Josephson junction.

The most widely investigated Josephson junction system is the rf-driven Josephson junction for which the equation may be obtained by adding a term $I_{rf}\sin\omega t$ to Eq. (1a), i. e. in normalized units ($\Omega = \omega/\omega_0$)

$$\phi_{tt} + \alpha\phi_t + \sin\phi = \eta_0 + \eta_1 \sin\Omega t \qquad (16)$$

This equation is the same as the one discussed in section 4; here however the value of the rf drive is typically larger than when rf applications are considered.

Since analytical solutions do not exist, one has to do numerical simulations in the four dimensional parameter space of α, η_0, η_1, and Ω [18-23]. A particularly thorough investigation of the parameter space was done in [23].

Typically the system has been investigated numerically in the η_1 - Ω plane for a fixed damping parameter α, a plot which more or less has become a standard for such systems [18-20].

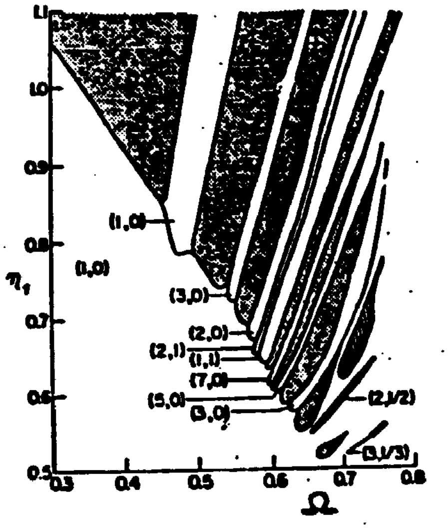

Fig. 7. Characterization of solutions in the Ω-η_1 plane. β_C= 25, η_0 = 0. Crosshatched region: chaos. Hatched region: complicated periodic. Indexing (p,q) corresponds to the pth subharmonic on the qth rf induced step. (From ref. 19).

Fig. 7 shows such a plot with its complicated mapping of different dynamical behaviour. Note that for $\omega > \omega_0$, i.e. $\Omega > 1$ the threshold rises dramatically because the capacitor shorts out the applied rf-current. For $\omega < 1/RC$, i.e. $\Omega < 1/\sqrt{\beta_C}$, the system is able to adiabatically follow the rf-current, and chaos only occur if $\eta_1 > 1$. For $\omega \approx \omega_0$, the threshold for chaos is lowest.

Another method of a somewhat computational nature is to use electronic analogs simulating the Josephson equation. Such systems have the advantage of being very fast, and poincare sections and bifurcation diagrams may be readily displayed [20,24]. The disadvantage is the limited precision and resolution, and the drift of analog electronic circuits.

8b. Experiments on real Josephson junction.

Common to all the experimental results is that they are not nearly as spectacular as the numerical simulations. The main reason is that thermal noise, which is most often not taken into account in simulations, has a major effect on the outcome of the experiments. This is because the energy levels in the thermal oscillations may very well be of the same order of magnitude as the intrinsic energy levels in the Josephson junction and complicated non-linear interactions occur.

Thermal effects may produce not only quantitative changes but also qualitative and quite dramatic changes. Two examples will be given below.

dc observation of chaos.

Before the term chaos was connected to Josephson junctions, researchers sometimes noted very irregular and erratic IV curves in samples subject to strong applied rf signals. In many cases such junctions were discarded because of assumed defects during fabrication.

It is now known that such irregular IV curves may be a signature of chaos. Examples of such irregular behaviour, in particular the loss of phaselock on an rf induced step has been published in several cases [25-27].

By comparing such experimentally obtained, irregular IV curves to numerically obtained ones, one has in principle the simplest experiment on chaos [25]. A numerical calculation of the IV-curve without noise will show a lot of complicated fine structure with many different phaselocked steps that exist only over a very small region of bias current. Small amounts of thermal noise will soften those steps to a smooth curve. An example of such a dc experiment is illustrated in Fig. 8, which shows an experimentally obtained IV curve [27] with loss of phaselock on the rf induced step. Also shown in the figure is the spectrum of half harmonic generation as measured with a sensitive microwave spectrometer. Note that these experimental curves, which contain two period doubling bifurcations and a chaotic region on a rf-induced step, can be considered as a standard example of the period doubling route to chaos.

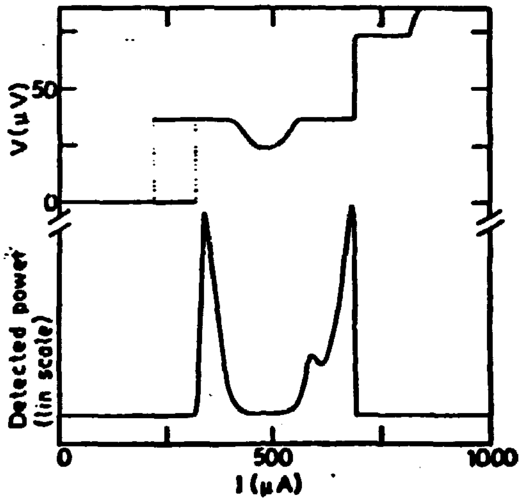

Fig. 8. Experimental, microwave irradiated IV-curve and the corresponding spectrum of half harmonic generation. f = 17.6 GHz, T = 3.54K. (From ref. 27).

Chaos and parametric amplification.

The externally pumped Josephson junction parametric amplifier is basically governed by Eq. (16). For such Josephson junction parametric amplifiers low noise temperatures have been in some cases, however, more often experiments showed considerable excess noise [28]. For experimentalists the observed noise rise has been a major puzzle. A large number of theoretical and numerical papers [29] have dealt with the problem. The conclusion is that the very large noise temperatures cannot be explained by traditional noise sources such as Johnson noise, shot noise, or quantum noise. Hubermann et al. [18] first suggested that chaos was the origin of the excess noise. This suggestion was further substantiated in ref. 19.

More recently a sligthly different type of Josephson junction parametric amplifier was investigated [30]; for this amplifier it was concluded that the large noise cannot arise from deterministic chaos alone: The observed noise rise required the presence of thermal noise. They suggested that the noise rise was due to thermally induced hopping between a bias point that would be stable in the absence of thermal noise and an unstable point. The observation demonstrates the importance of thermal noise in modeling chaos in Josephson junction systems. As much as 10^6 K of noise temperature may be obtained by such thermally induced hopping.

9. Conclusion.

This paper has discussed mainly the non-linear properties of Josephson junctions, that has so much promise for both applications and continued research on fundamental problems. The problems we have dealt with have all been defined on the basis of the old superconductors. The future work involving the new high T_c superconductors will most likely have to deal not only with the same type of problems with changed parameters, but also with completely new non-linear phenomena for example due to anisotropy. It may be safely predicted that a lot of interesting non-linear physics lies ahead.

References.

1. L. Falicov. This conference.
2. O. Ulfbæk. This conference.
3. B.D. Josephson, Phys. Lett. **1**, 251 (1962)
4. R.P. Feynman, R.B. Leighton, and M. Sands, The Feynman lectures on physics, Vol. III, Addison-Wesley, 1965, Chapt. 21.
5. A. Barone and G. Paterno, Physics and Applications of the Josephson Effect, New York: Wiley-Interscience, 1982.
6. K.K. Likharev, Dynamics of Josephson junctions and Circuits. Gordon and Breach, New York (1986).
7. M. Tinkham, Introduction to superconductivity, McGraw-Hill, New York 1975.
8. R.F. Miracki, M.H. Devoret, and J. Clarke, Phys. Rev. **A31**, 2509 (1985)
9. D.W.McLaughlin and A.C.Scott, Phys.Rev.A18, 1652 (1978)
10. N.F. Pedersen in " Solitons in Action" MPCMS, Eds. A.A. Maraduddin and V.H. Agranovich, North Holland, 1986. p469.
11. N.F. Pedersen and D. Welner, Phys.Rev.B29, 2551 (1984)
12. M. Buttiker and H. Thomas, Phys. Rev. **A37**, 235 (1988)
    M. Buttiker and R. Landauer, Nonlinear Phenomena at Phase Transitions and Instabilities, (Plenum Publishing Corp.), 1982, p.111
13. N.F. Pedersen, M.R. Samuelsen, and D. Welner, Phys.Rev.B30, 4057 (1984)

14. S. Sakai, H. Akoh, and H. Hayakawa, Jap. Journ. of App. Phys. 22, L479 (1983).

15. H. Akoh, S. Sakai, A. Yagi, and H. Haykawa, IEEE Trans. Magn. MAG-21, 737 (1985).

16. H. Akoh, S. Sakai, and S. Takada, Phys. Rev. B35, 5357 (1987)

17. A. Fujimaki, K. Nakajima and Y. Sawada, Phys. Rev. Lett. 59, 2895 (1987)

[18] B.A. Huberman, J.P. Crutchfield, and N.H. Packard, Appl. Phys. Lett. 37, 750 (1980)

[19] N.F. Pedersen and A. Davidson, Appl. Phys. Lett. 39, 830 (1981)

[20] D. D'Humieres, M.R. Beasley, B.A. Huberman, and A. Libchaber, Phys. Rev. A26, 3483 (1982)

[21] R.L. Kautz, J. Appl. Phys. 52, 3528 (1981)
M. Octavio, Phys. Rev. B29, 1231 (1984)
Kazuo Sakai and Yoshihiro Yamaguchi, Phys. Rev. B30, 1219 (1984)

[22] R.L. Kautz, J. Appl. Phys. 52, 6241 (1981)

[23] R.L. Kautz and R. Monaco, J. Appl. Phys. 57, 875 (1985)

[24] M. Cirillo and N.F. Pedersen, Phys.Lett. 90A, 150 (1982)
W.J. Yeh and Y.H. Kao, Appl. Phys. Lett. 42, 299 (1983)
H. Seifert, Phys. Lett. 98A, 213 (1983)
Da-Ren He, W.J. Yeh and Y.H. Kao, Phys. Rev. B31, 1359 (1985)
V.K. Kornev, K.Yu. Platov and K.K. Likharev, IEEE Trans. Magn. MAG-21, 586 (1985)

[25] D.C. Cronemeyer, C.C. Chi, A. Davidson, and N.F. Pedersen Phys. Rev. B31, 2667 (1985)

[26] K. Okuyama, H.J. Hartfuss, and K.H. Gundlach, J. Low Temp. Phys. 44, 283 (1981)

[27] N.F. Pedersen, O.H. Sørensen, B. Dueholm, and J. Mygind, J. Low Temp. Phys. 38, 1 (1980)

[28] R.Y.Chiao, M.J. Feldman, D.W. Peterson, B.A. Tucker, and M.T. Levinsen, Future trends in superconductive electronics, AIP Conference Proceedings 44, 259 (1978)

[29] For references on this see e.g. N. F. Pedersen in SQUID 80, edited by H.D. Hahlbohm and H. Lubbig (de Gruyter, Berlin, 1980), p739.

[30] R.F. Miracky and J. Clarke, Appl. Phys. Lett. 43, 508 (1983)

CHAPTER 5

PHYSICOCHEMISTRY OF HIGH Tc SUPERCONDUCTORS

Claude MICHEL

Laboratoire CRISMAT - ISMRa - Bld du Maréchal Juin - F-14032 CAEN Cédex

The main direction for research of superconducting oxides lays in investigating non stoichiometric oxides involving transition or post transition metal ions, characterized by a mixed-valence. This idea is supported by the existence of three families of superconductors A_xWO_3 (A = K, Rb, Cs, Tl), $LiTi_2O_4$ and $BaPb_{1-x}Bi_xO_3$ which are characterized by :

- A_xWO_3 : Tc ≃ 0.6-6.7 K, mixed-valence W(V) - W(VI)
- $LiTi_2O_4$: Tc ≃ 13.7 K, mixed-valence Ti(III) - Ti(IV)
- $BaPb_{1-x}Bi_xO_3$: Tc ≃ 13 K, mixed-valence Bi(III) - Bi(V)

In all these oxides the individual mixed-valence ions cannot be identified since the electrons are delocalized in a conduction band which results either from the overlapping of the orbitals of metallic and oxygen atoms or from the direct overlapping of the orbitals of the metallic atoms. A well known example is that of the metallic oxygen tungsten bronzes Na_xWO_3 of perovskite structure. In these oxides, the conduction band is the π^* band which results from the overlapping of the tungsten $5d_{t_{2g}}$ orbitals with the $2p\pi$ oxygen orbitals (Fig. 1).

The superconductivity discovered by Muller in the copper oxides is in agreement with this point of view since copper exhibits theorically two oxidation states simultaneously, Cu(II)- Cu(III). However the surprising feature is in the high value of the critical temperature of those oxides : Tc≃30-40 K in the Ba-La-Cu-O and Sr-La-Cu-O systems, TC≃90 K in the Y-Ba-Cu-O system and related, Tc≃22K and 80-110 K in bismuth compounds and Tc≃60-125 K in superconductors with thallium. For the theorists, these high values of the critical temperature is attributed in addition of the mixed-valence of copper, to the low dimensionality of their structures. So it may be an interesting way for the comprehension of the superconductivity in these compounds, to analyse their crystal chemistry in relation with the superconducting properties.

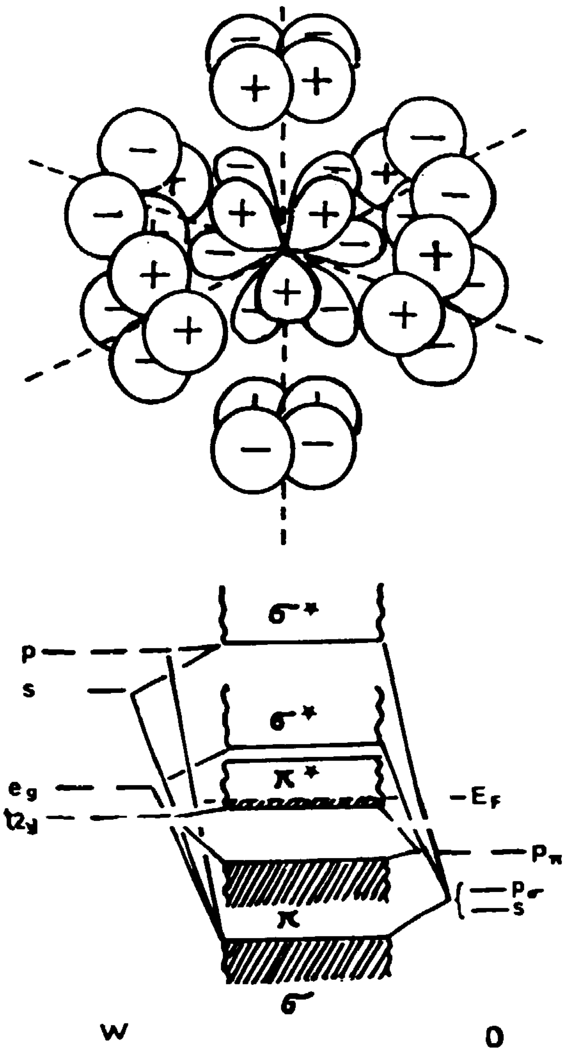

Fig. 1- Perspective view of the tungsten $5d_{t_{2g}}$ orbitals and $2p\pi$ oxygen orbitals, and band diagram for the metallic perovskite Na_xWO_3.

I) MIXED-VALENCE OF COPPER

a) Stabilization of Cu(III)

Contrary to its neighbourgs of the first transition period such as iron and nickel, for which higher oxidation states Fe(IV) and Ni(III) can easily stabilized in oxides, copper is not commonly observed in its highest oxidation states, Cu(III). Only a few ternary copper oxides $A_mCu_nO_t$ containing trivalent copper can be prepared under 1 atm oxygen pressure or high oxygen pressure according to the nature of the A element, for example some A elements, such as alkaline earths : barium, calcium or strontium allow the formation of Cu(III) in air. But the ability of copper to be oxidized into the three-valent state also depends upon the structure. It can be observed that among the oxides of the systems A-Cu-O and A-Ln-Cu-O (A = Ba, Ca, Sr, Ln = lanthanides and Yttrium), only those related to the perovskite exhibit the mixed-valence. For example, in the system Y-Ba-Cu-O, the oxides Y_2BaCuO_5 ("the green phase") and $YBa_2Cu_3O_{7-\delta}$ exhibit only Cu(II) and mixed-valence of copper respectively. In the first one, divalent copper ions are surrounded by five oxygens in a distorted pyramidal configuration (Fig. 2), and are isolated in the structure, whereas the second one is an oxygen deficient perovskite (Fig.7). The reason of this difference can be explained in terms of anionic vacancies. To stabilize Cu(III) at a rather low oxygen pressure, the host lattice of the structure must be able to present a great number of oxygen vacancies favourable for the intercalation of oxygen. In this respect, the very flexible perovskite framework is a potential candidate. This phenomenon is enhanced in the case of copper perovskites by the ability of copper to take several coordinations : square planar, square pyramidal, tetrahedral and octahedral.

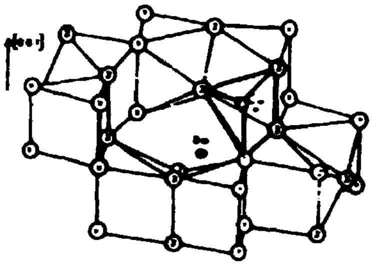

Fig. 2 - Part of the structure of Y_2BaCuO_5 showing copper in square pyramidal coordination.

The study of the electrical properties of the mixed-valence copper oxides shows that they are all p type conductors due to the presence of Cu(III). This valence must be considered as formal and does not imply the existence of a $3d^8$ configuration for copper. The recent study of the copper L_3 edge by X ray absorption spectroscopy of La_2CuO_4, $La_{1.85}Sr_{0.15}CuO_{4-y}$ and $YBa_2Cu_3O_{7-\delta}$ is most compatible with a $3d^9$ ligand hole state leading to holes delocalized a conduction band mainly built up from 2p oxygen orbitals. The $3d^9$ ligand hole state is also often noted (Cu^{2+}- O^-).

b) Determination of the mean oxidation state of copper

As it will be discussed latter, the mean oxydation state of copper, i.e. the "Cu(III)" content, is a very important parameter which must be known with accuracy to be related with the superconducting properties. It can be determined by chemical or thermogravimetric analyses :

- chemical analysis

It is a iodometric titration. In an acidic solution and in the presence of an excess of I^- ions, copper ions lead to the following reaction :

$$Cu^{n+} + nI^- \rightarrow CuI + (\frac{n-1}{2})I_2$$

$$\text{or } (Cu - O)^{p+} + (2+p)I^- \rightarrow CuI + \frac{(p+1)}{2} I_2$$

Any Cu^+ in the sample will precipitate out as CuI, without generating any neutral iodine. All species oxidized beyong Cu^+ will react to yeld a quantity of iodine directly proportional to the degree of oxidation greater than Cu^+. This quantity can be accurately determined by titrating with a sodium thiosulfate solution and using starch as an indicator.

- thermogravimetrie analysis

The oxydation state of copper is directly related to the oxygen content of the samples which can be determined by measuring the weight loss with a sensitive thermobalance, when the oxides are heated in a reducing atmosphere. For superconductors with lanthanides or Yttrium, only copper is reduced. For $YBa_2Cu_3O_{7-\delta}$, the reaction can be written :

$$YBa_2Cu_3O_{7-\delta} \rightarrow 1/2\ Y_2O_3 + 2BaO + 3Cu + (3,5-\delta)H_2O$$

The temperature of the end of the reduction is dependant on the nature of the oxide (Fig. 3)).

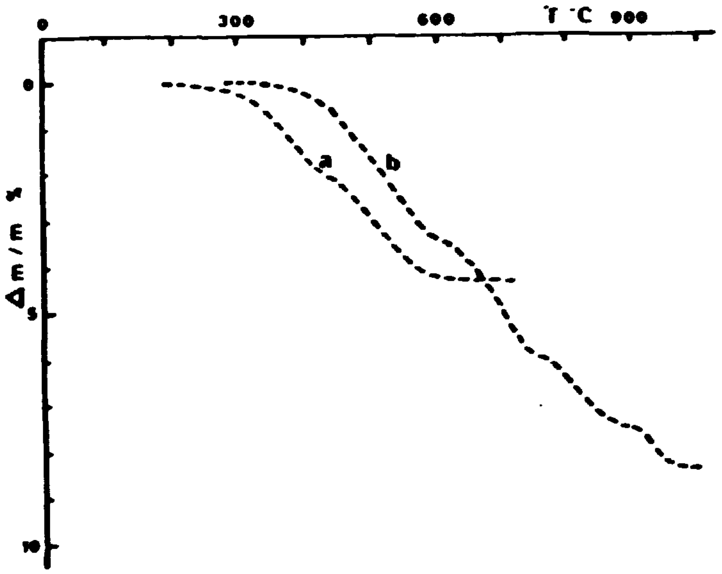

Fig. 3 - TGA curves for $La_{1.85}Sr_{0.15}CuO_{4-y}$ (a) and $YBa_2Cu_3O_7$ (b) under reducing atmosphere.

II) SYNTHESIS OF COPPER OXIDES

Usually, the mixed-valence copper oxides are synthesized at high temperature by Solid state reaction between oxides , peroxides or carbonates . The procedure depends on the nature of the reactants. For the actually known superconductors, it can be summarized as follow :

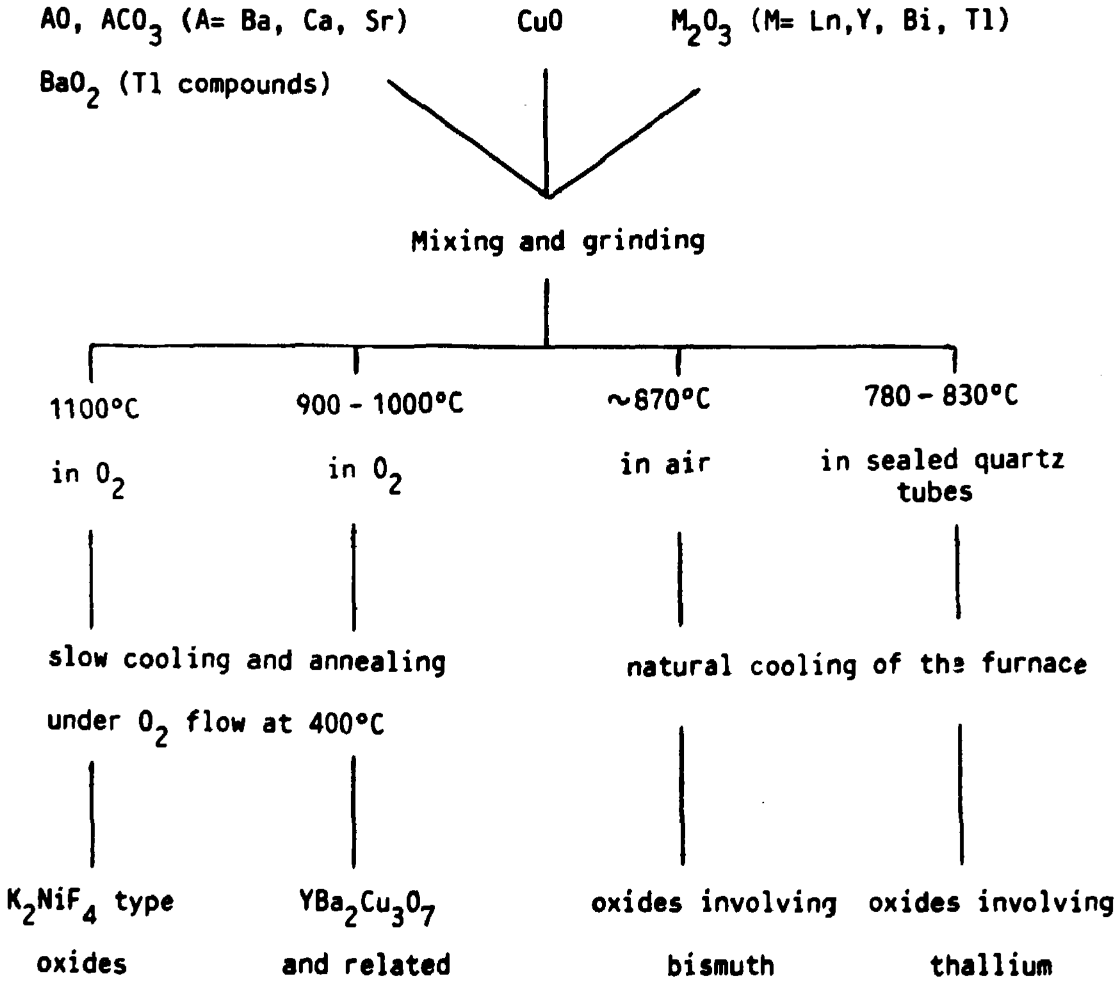

Variations in the procedure of preparation of samples can induce variations in the superconducting properties as it will be shown in sections III and VI.

II) STRUCTURE AND ELECTRICAL PROPERTIES OF MIXED-VALENCE COPPER OXIDES RELATED TO THE PEROVSKITE

Among the mixed-valence copper oxides related to the perovskite, two classes can be distinguished:

- oxygen deficient perovskites
- intergrowths of the oxygen deficient perovskite structure and of the sodium chloride-type structure.

Recalls on structural determinations

The localization of oxygen vacancies in the structures of these oxides is important, so most of the structural studies have been undertaken using neutron diffraction.
Why is the neutron diffraction better than the X ray diffraction ?

In every expression for the intensity of the beam of X-rays (or neutrons) diffracted in any given direction from a crystal (or powder) a factor F occurs, the structure factor which is a measure of the composite wave due to the combined scattering of all the atoms in the units cell in the given direction. It depends on:

- the nature of the scattering material
- the arrangement of the scattering material
- the direction of the scattering

For X ray : $F_{hkl} = \Sigma f_n \exp 2\pi i(hx_n + ky_n + lz_n)$

fn is the scattering power of the element n, it is dependent on its electronic structure and on the hkl direction. It varies from 1 (hydrogen) to about 100 (Actinides). So it is clear that the influence of oxygen ($f = 10$) with regerd to "heavy" metal ions like La^{3+} or Ba^{2+} ($f = 54$) or Bi^{3+} ($f = 80$) is very weak in the structure factor calculations (Fig. 4).

For neutrons diffraction : $F_{hkl} = \Sigma b_n \exp 2\pi i(hx_n + ky_n + lz_n)$

bn is called the neutrons scattering length of the element n, it depends on its nucleus and it is independant of the hkl direction. For all elements of the periodic table, bn varies only in a ratio 3 or 4, and for example the oxygen scattering length is greater than the barium one (Fig. 4).

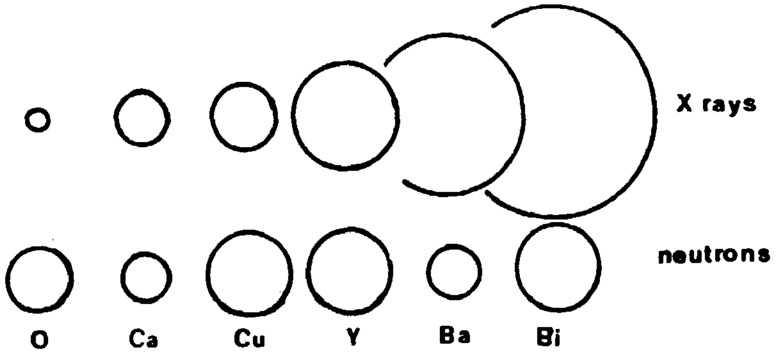

Fig. 4 - The visibilities of some elements involved in high Tc superconductors for X rays and neutrons. The radii of the circles are proportional to the scattering amplitude.

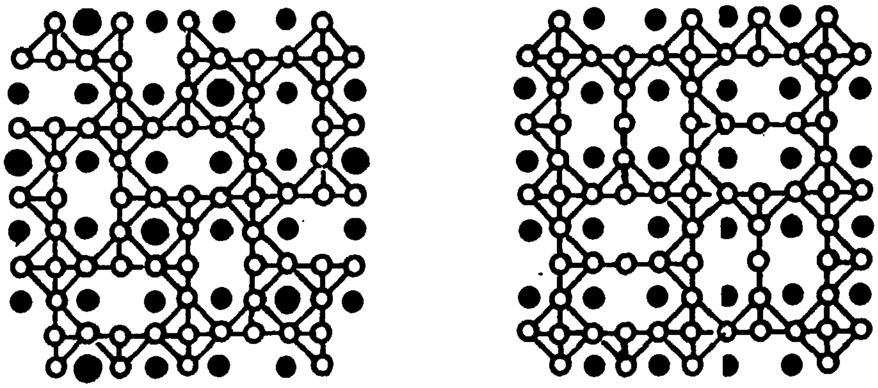

$La_4 Ba Cu_5 O_{13+\delta}$ $La_{8-x} Sr_x Cu_8 O_{20-\varepsilon}$

Fig. 5 - Projection onto (001) of the structure of the oxides $BaLa_4Cu_5O_{13}$ and $La_{8-x}Sr_xCu_8O_{20}$.

A Oxygen deficient perovskites

Ordered deficient perovskites can be generated by elimination of rows of oxygen atoms in an ordered manner in the perovskite framework. This is the case in the tetragonal oxides $La_4BaCu_5O_{13}$ and $La_{8-x}Sr_xCu_8O_{20}$ ($1.3 \leqslant x \leqslant 1.9$) which were synthesized in Caen (fig.5). Their host lattice is built up either from CuO_6 octahedra and CuO_5 pyramids, or CuO_6 octahedra, CuO_5 pyramids and CuO_4 square planar groups and forms tunnels running along $\vec{c}$. These structures are deduced from that of the stoichiometric perovskite by elimination of rows of oxygen atoms along the [001] direction. In the compound with barium, ordering between barium (in the perovskite cages) and lanthanum (in the tunnels) is observed. It is clear that in this oxide, the ordering of these cations is favoured by their different sizes and is related to the ordering of the oxygen vacancies. The amount of Cu(III) is about 40 % and 15 % in the barium and strontium oxide respectively. Both exhibit metallic behaviour (fig.6), but no sign of superconductivity was observed likely owing to the three-dimensional character of their structure. The importance of the bidimensional character of the structure in superconductivity has been outlined by several authors, in particular in France by Labbé and Bock. It is confirmed by the structure of the superconductor YBa_2Cu3O_7.

Superconductivity in the system YBaCuO was discovered by Chu and the superconductivity phase YBa_2Cu3O_7 (33 % Cu III), called "123" was isolated almost simultaneously by several labs. The symmetry of this oxide is orthorhombic and its structure is built up from triple layers of corner-sharing CuO_5 pyramids and CuO_4 square planar groups (fig.7), it can be deduced from the stoichiometric perovskite by ordered elimination of rows of oxygen atoms parallel to the [010] direction. The triple layers can be described as formed of two single $[CuO_{2.5}]_\infty$ layers of CuO_5 pyramids surrounding one $[CuO_2]_\infty$ layer of CuO_4 square planar groups. The latter layer forms planes parallel to b. Once again, yttrium and barium atoms are ordered forming planes parallel to the (001) plane of the orthorhombic cell. This ordering of the cations is also likely to be the origin of the oxygen vacancies, since the cohesion between the triple layers is only ensured by yttrium ions. In this structure, yttrium ions can be replaced by almost all the elements of the rare-earth series. All the samples are superconductors with a Tc of about 90 K (Fig.8), except $LaBa_2Cu3O7$ which exhibits a lower Tc (75 K) . Superconducting properties can be influenced by the thermal treatment as shown in (Fig.8), they will be intensively discussed in section VI.

Although closely related to the previous oxides $Ba_{1.5}La_{1.5}Cu_3O_{7+\delta}$ differs by its symmetry which is tetragonal and results in a random distribution of the oxygen atoms situated at the same level as the copper ions of the CuO4 groups. This difference can be due to the fact that inside the

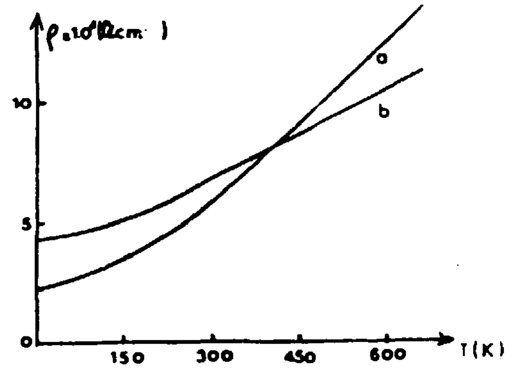

Fig. 6 - ρ= f(T) for $La_{6.4}Sr_{1.6}Cu_8O_{20}$ (a) and $BaLa_4Cu_5O_{13}$ (b).

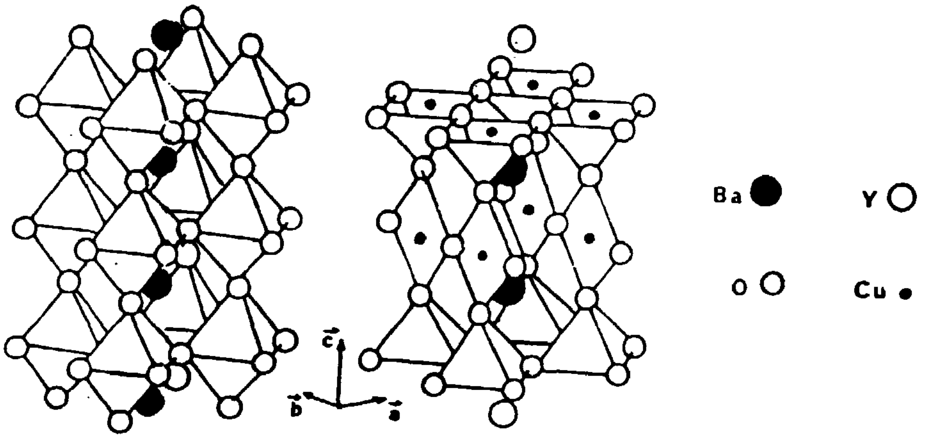

Fig. 7 - Structure of the stoichiometric perovskite and of the superconductor $YBa_2Cu_3O_7$.

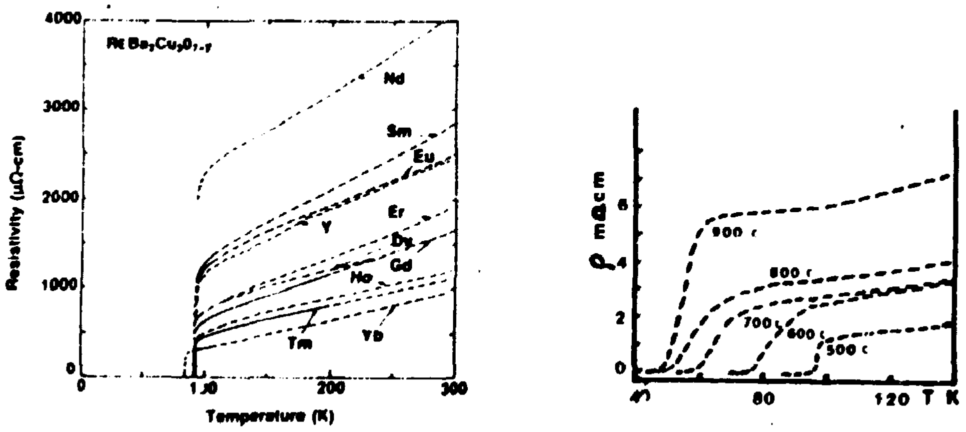

Fig. 8 - ρ = f(T) for the superconductors $REBa_2Cu_3O_{7-\delta}$ (RE = lanthanides and yttrium) and influence of the thermal treatment upon the superconducting properties of $YBa_2Cu_3O_{7-\delta}$.

triple layers, barium ions are partly replaced by lanthanum ions. The electrical properties of this oxide are very sensitive to the thermal treatment which influences the δ value (Fig. 9). We can observe a smooth transition from a semiconductive behaviour to a semimetallic behaviour, but never superconductivity was observed. This difference could be partly explained by high resolution electron microscopy. This study which was carried out in Caen shows effectively that this oxide appears more as a juxtaposition of microphases whose composition may vary rather than a single phase (Fig. 10).

B Intergrowths of oxygen deficient perovskites and "AO" sodium chloride type structure

A way to create anisotropy in the physical properties of perovskites and especially in their electron transport properties is to realize an intergrowth with another structure. In this respect the sodium chloride-type structure of SrO is an interesting candidate since both structures exhibit a bidimensional accord along (001) (Fig. 11).
Before 1987, only two families were known : $La_{2-x}A_xCuO_{4-x/2+\delta}$ and $La_{2-x}A_{1+x}Cu_2O_{6-x/2+\delta}$, but with the recent discovery of superconductivity in the systems Bi-Sr-Cu-O, Bi-Sr-Ca-Cu-O and Tl-Ba-Ca-Cu-O, the number of families is greatly increased. All the compounds corresponding to such intergrowths can be described with the same formula :

$$(AO)_n(A'CuO_{3-y})_m$$

($1 \leq n \leq 3$, $1 \leq m \leq 3$) where n and m correspond to the multiplicity of the sodium chloride-layers and of the oxygen deficient perovskite type layers respectively. The n value depends on the nature of the A elements.

1) Oxides involving lanthanum

$n = 1$, $m = 1$: the oxides $La_{2-x}A_xCuO_{4-x/2+\delta}$

The structure is known as the K_2NiF_4-type structure (Fig. 11). These oxides can be synthesized for A = Ba,Ca,Sr. The homogeneity range depends on the nature of the A cation : narrow for calcium and barium ($0 \leq x \leq 0.2$) and rather wide for strontium ($0 \leq x \leq 1.33$) whose size is similar to that of lanthanum. In those oxides, the SrO-type layers are stoichiometric, whereas the oxygen vacancies are distributed in the basal plane of the octahedra of the single perovskite layer.

In the $La_{2-x}Sr_xCuO_{4-x/2+\delta}$ the physicochemistry is complex ; it has been extensively studied in Caen (Nguyen et al.). For samples prepared in air without annealing, three domains of composition can be distinguished :
$0 \leq x \leq 0.1$
The cell symmetry is orthorhombic, δ (consequently the ratio $Cu(III)/Cu_{total}$) and the number of oxygen vacancies are weak. Oxygen interca-

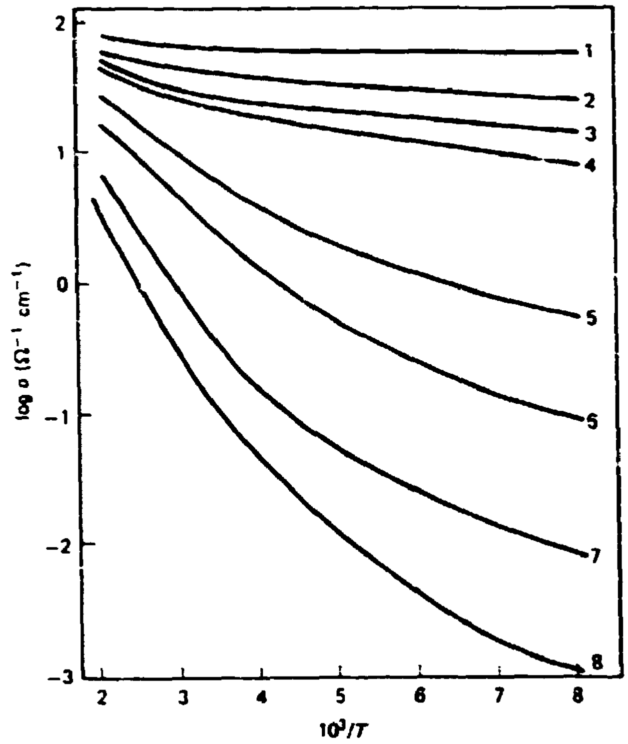

Fig. 9 - σ = f(1/T) for some δ values of the oxides $Ba_{1.5}La_{1.5}Cu_3O_{7+\delta}$: 1) 0.22; 2) 0.19; 3) 0.17, 4) 0.15; 5) 0.12; 6) 0.10; 7) 0.05; 8) 0.02.

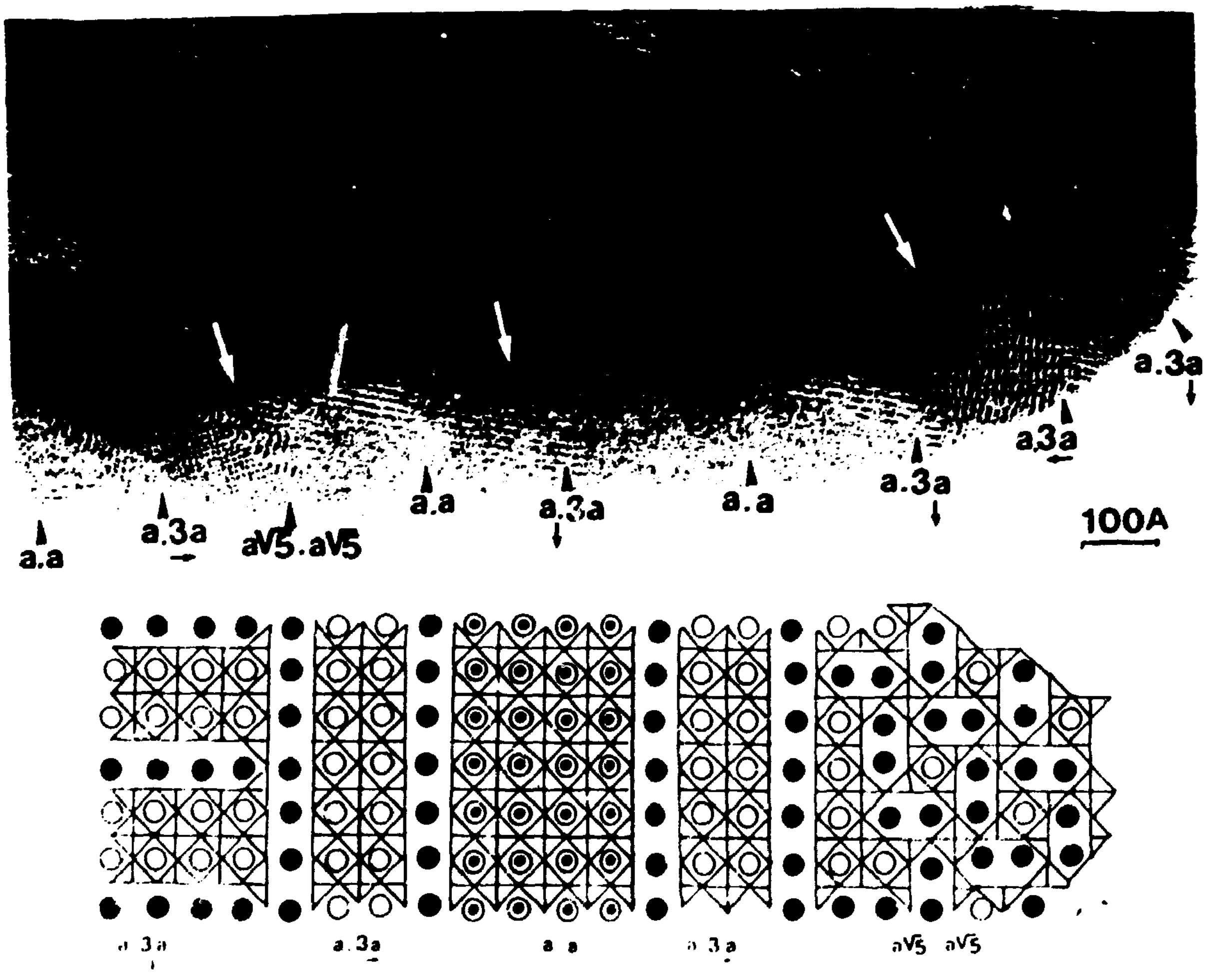

Fig. 10 - High resolution image of an array of small domains and models.

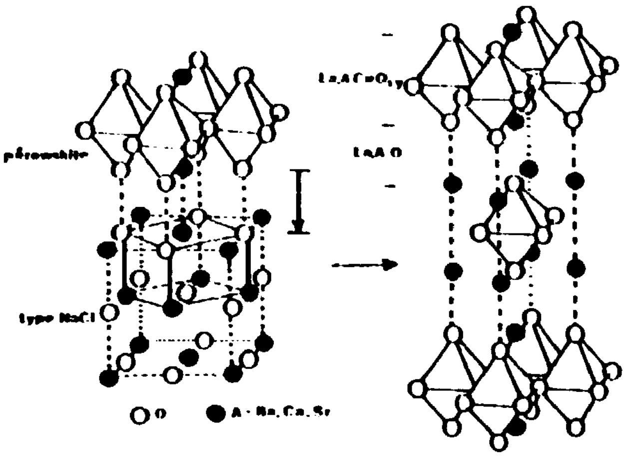

Fig. 11 - Structure of the oxides $La_{2-x}A_xCuO_{4-x/2+\delta}$ resulting from the intergrowth of perovskite and sodium chloride structures.

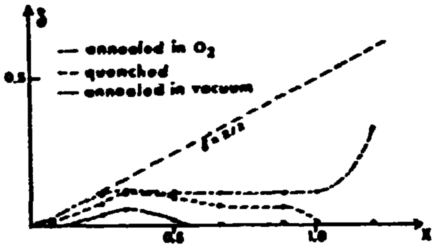

Fig. 12 - δ = f(x) for various thermal treatments.

lation is possible allowing the stoichiometry to be reached.

$0.1 < x < 1$

The cell symmetry is tetragonal. δ reaches a maximum at about $x = 0.3$ ($Cu(III)/Cu_{tot} \simeq 25\%$). Oxygen is easily intercalated, but the stoichiometry is not easily reached (the number of oxygen vacancies increases as x increases).

$1 < x \leq 1.33$

No mixed-valence is observed. Superstructures appear due to the ordering of the oxygen vacancies.

The curves $\delta = f(x)$ for different thermal treatments and $\sigma = f(1/T)$ for some x values (quenched samples) are plotted in Fig. 12 and Fig. 13 respectively.

Superconductivity is only observed in a narrow range of composition ($0.06 \lesssim x \lesssim 0.3$) with a maximum of Tc ($\simeq$ 40 K) for $x = 0.15$ as shown in Fig. 14 (Tarascon's data). For some authors the appearence of this property can be related to the transition orthorhombic-tetragonal and the Tc value to the temperature where this transition occurs (Fig. 14). However La_2CuO_4 whose symmetry is orthorhombic at room temperature and was claimed to be a semiconductor or an insulator at low temperature, can be prepared as a superconductor (see section IV). As for $YBa_2Cu_3O_7$, the superconducting properties of these oxides are dependant of the thermal treatment (Fig. 15).

The nature of the A element seems to have an influence on the value of the critical temperature since Ba^{+2} and Ca^{+2} which are respectively smaller and bigger cations than La^{+3} lead ,for the same x value, to lower Tc than Sr^{+2} which is about of the same size than lanthanum.

$n = 1$, $m = 2$: the oxydes $La_{2-x}A_{1+x}Cu_2O_{6-x/2+\delta}$

They have only been synthesized for strontium ($0 \leq x \leq 0.14$) and calcium ($x = 0.1$) (Nguyen et al.). The cell is tetragonal and the oxygen vacancies can be numerous as shown for example for $La_2SrCu_2O_6$, involving only Cu(II), whose double oxygen deficient perovskite layer $[LaSrCu_2O_5]_\infty$ is only formed of corner-sharing CuO_5 pyramids (Fig. 16). No superconctivity was observed in this series in spite of the bidimensional character of the structure.

2) Oxides involving Bismuth.

The first sign of superconductivity in the system Bi-Sr-Cu-O (Tc $\simeq$ 22 K) was discovered in Caen one year ago. The study of the system Bi-Ca-Sr-Cu-O allows Maeda et al., then Chu et al. and Politis to give evidence of superconductivity in the range 80-110 K for the composition $Bi_2Sr_{3-x}Ca_xCu_2O_8$ with $x \simeq 1$ (Fig. 17).

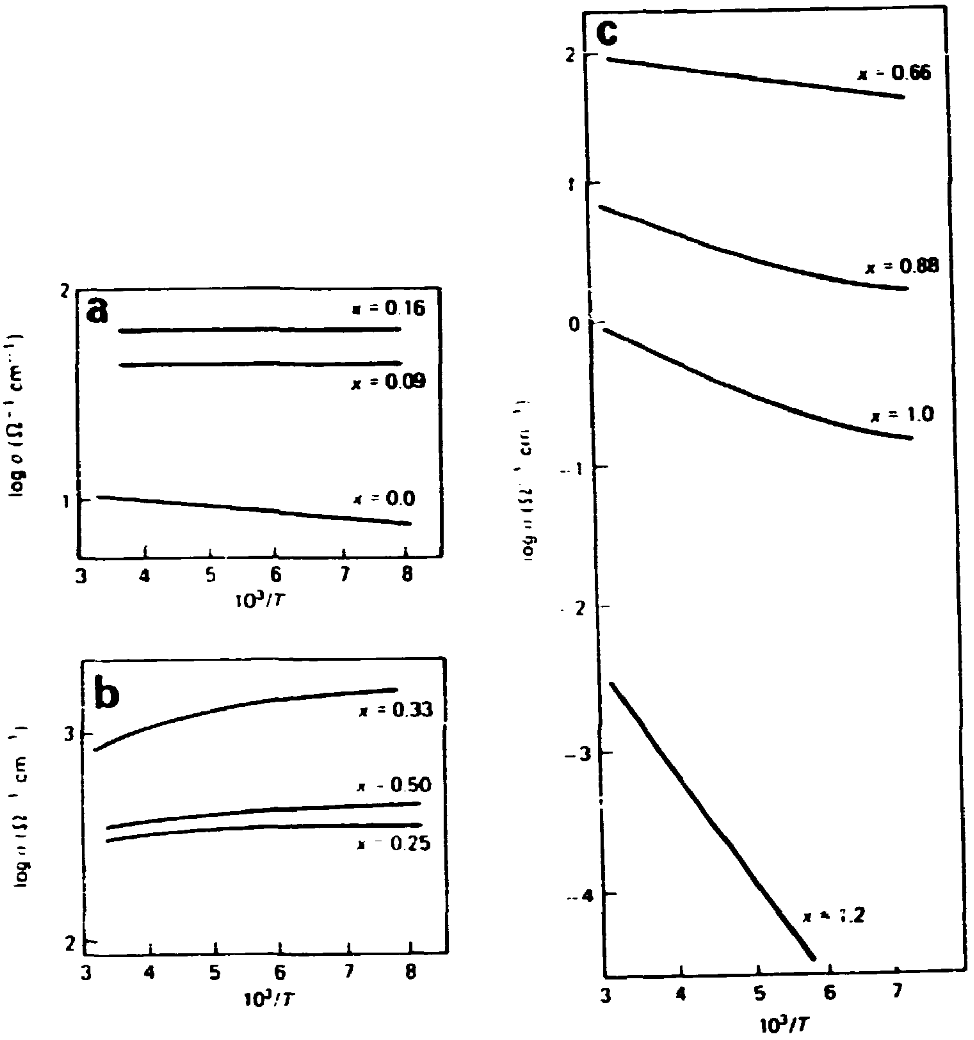

Fig.13 - σ = f(1/T) for different x values (quenched samples).

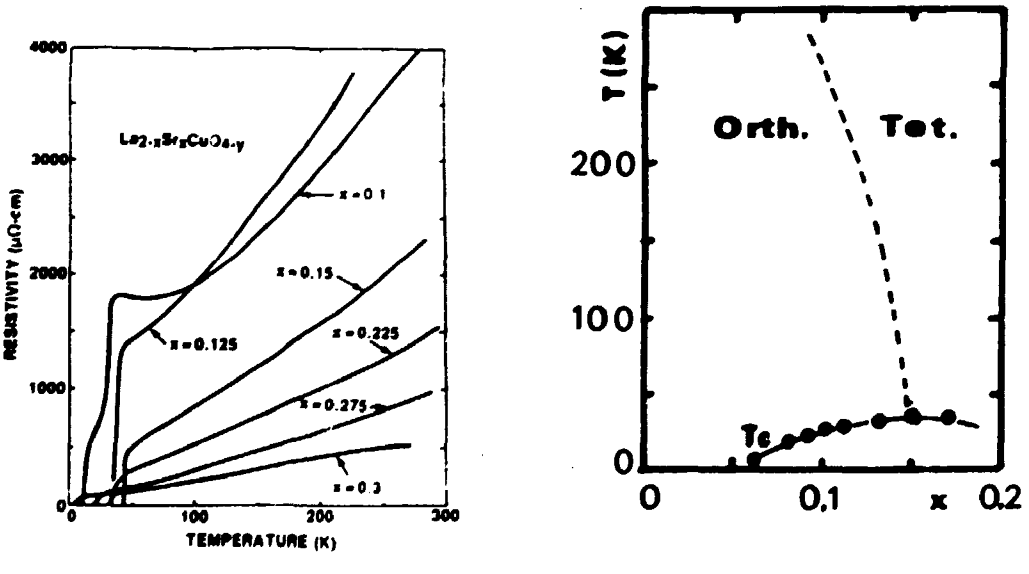

Fig. 14 - ρ = f(T) for different x values (Tarascon et al.) (a), and Tc = f(x) and temperature of transition vs x (Kang et al.) (b).

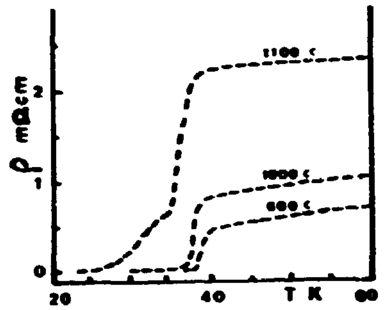

Fig. 15 - Influence of the thermal treatment on the superconducting properties of $La_{1.84}Sr_{0.16}CuO_{4-y}$ (Fueki et al.)

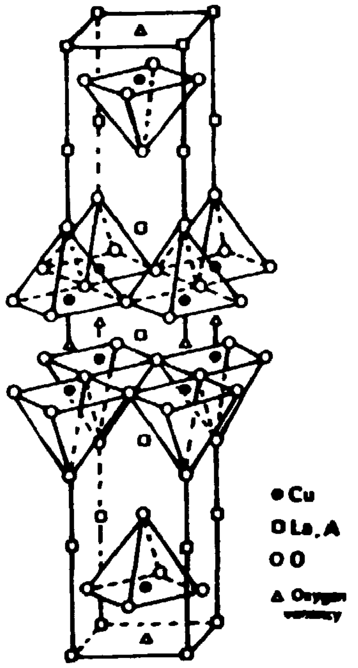

Fig. 16 - Structure of $La_2SrCu_2O_6$.

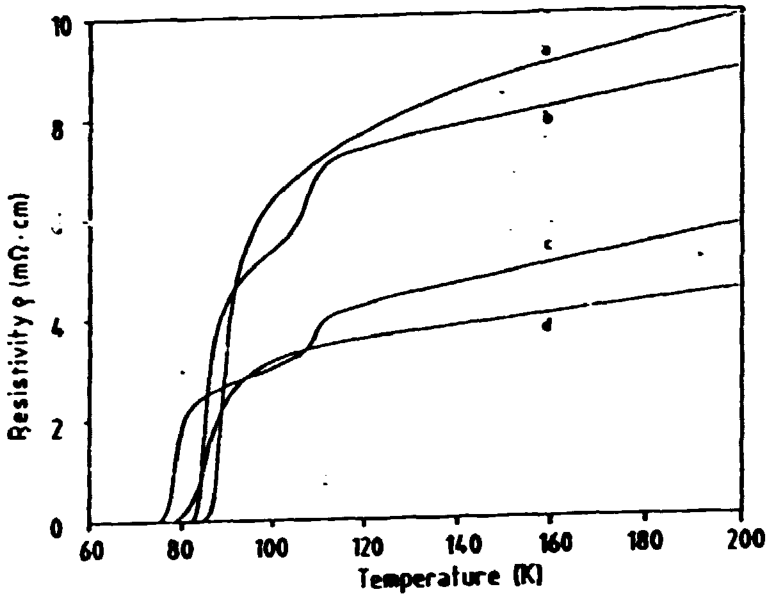

Fig. 17 - ρ = f(T) for oxides in the system Bi-Sr-Ca-Cu-O.

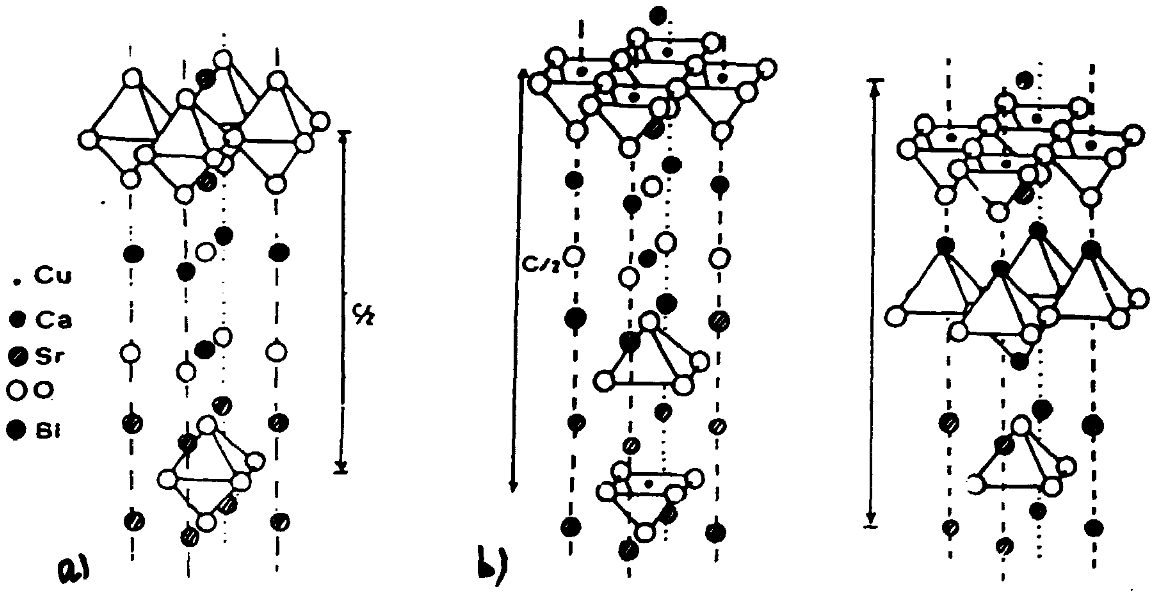

Fig. 18 - Structure of $Bi_2Sr_2CuO_6$ (a) and $Bi_2Sr_2CaCu_2O_8$ for Tarascon's and Sleight's models (b).

n = 3, m = 1 : The oxide $Bi_2Sr_2CuO_6$

This oxide is also called "2201". Its structure (Fig. 18) results in an intergrowth between a single perovskite layer and a triple "AO" layer built up from one SrO layer and a double "bismuth-oxygen layer".

n = 3, m = 2 : the oxide $Bi_2Sr_2CaCu_2O_8$

In this oxide which is called "2212", the triple "AO" layer is the same as in the previous oxyde. The double oxygen deficient perovskite layer $[SrCaCu_2O_5]_\infty$ is like that in $La_2SrCu_2O_6$. The cohesion between the two corner-sharing CuO_5 pyramid layers is ensured by a calcium plane (Fig. 18).

The cell symmetry of these two oxides is orthorhombic and superstructures are observed along the b axis owing to the nature of the "bismuth-oxygen" layers which is actually not known with accuracy in spite of single crystal structural studies. Tarascon proposes for $Bi_2Sr_2CaCu_2O_8$ a double distorted rock salt-type layer $((BiO)_2)$; Sleight observes a splitting of the bismuth positions and proposes a Bi_2O_2 layer as in the Aurivillius phases, and von Schnering proposes a double (BiO_{2-y}) layer like the CuO_2 layer of the perovskites. High electron microscopy (Fig. 19) suggests from careful simulations of the images that the "bismuth-oxygen" layers are rather distorted NaCl-type layers than Aurivillius-type or perovskite-type layers. The oxygen content of these layers is also unknown, this can result in the mica-like nature of the crystals (Fig. 20) which makes the structural study difficult. The mica-like character is due to weak intersheet Bi-O bonds : the distance between adjacent bismuth sheets is unusually long (3.25 Å) compared to the Aurivillius phases (2.7 Å).

3) Oxides involving thallium

Superconductivity in mixed-valence copper oxides involving thallium, barium and calcium was recently discovered by Sheng et al. Actually five compounds are known whose Tc are in the range 60-125 K. The curves $\rho = f(T)$ are given in fig. 21 for the three first known compositions. The cell symmetry of those oxides is tetragonal. Most of the structures have been determined by powder X rays diffraction, so the positions of the oxygen atoms were not determined with accuracy. However, the help of high resolution microscopy allows the sequences of planes along the c axis to be determined, like the nature of the TlO layers which are distorted sodium chloride type layers.

n = 3, m = 1 : the oxide $Tl_2Ba_2CuO_6$ (or "2201")

Its structure is like that of $Bi_2Sr_2CuO_6$ where bismuth and strontium are replaced by thallium and barium respectively (Fig. 22). The critical temperature is found to be at about 85 K (Fig. 21).

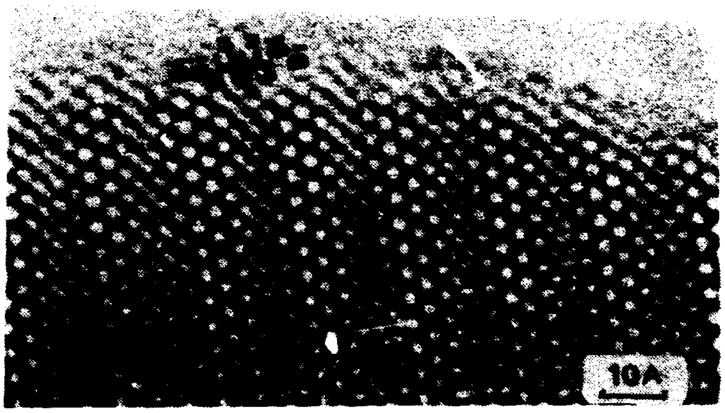

Fig. 19 - HREM image of the "2212" bismuth superconductor showing the sequence ...Bi-Bi-Sr-Cu-Ca-Cu-Sr-Bi-....

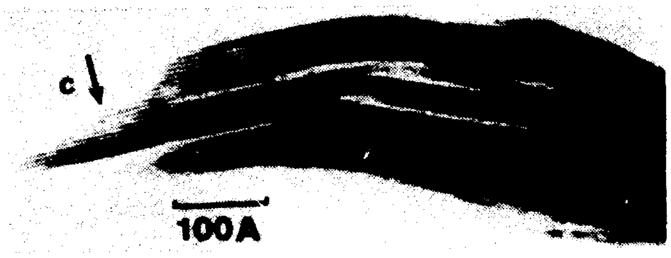

Fig. 20 - Electron mocroscopy image showing the lamellar character of the bismuth superconductors

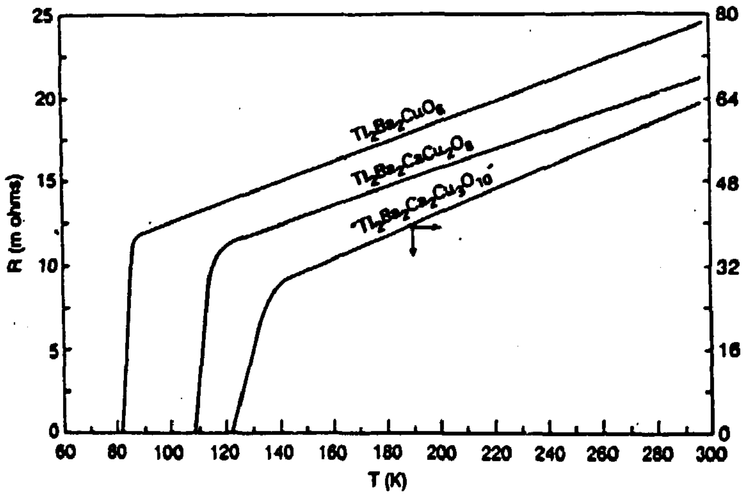

Fig. 21 - ρ = f(T) for some thallium superconductors.

n = 3, m = 2 : the oxide $Tl_2Ba_2CaCu_2O_8$ (or "2212")

Its Tc is 107 K (Fig. 21). The structure is similar to that of the bismuth oxide involving the same n and m values (Fig. 22).

n = 3, m = 3 : the oxide $Tl_2Ba_2Ca_2Cu_3O_{10}$ (or "2223")

The structure differs from the previous one by the presence of a triple oxygen deficient perovskite layer $[BaCa_2\ Cu_3\ O_6\ ]_\infty$ built up from $[CuO_4]_\infty$ single layer of corner-sharing CuO_4 square planar groups sandwiched by two $[CuO_{2.5}]_\infty$ single layers of corner-sharing CuO_5 pyramids. The cohesion is ensured by two calcium planes (Fig. 22). To explain the superconducting properties of this oxide (Tc = 125 K), the formation of Cu(III) must be considered, this involves the presence of "extra" oxygen atoms in the calcium planes.

The presence of defects in the plane stacking, observed in the HREM images (Fig. 23), allowed us to synthesize two other superconducting oxides involving only a distorted rock salt-type bilayer built up from one TlO single layer and one BaO single layer (Fig. 24).

n = 2, m = 2 : the oxide $TlBa_2CaCu_3O_7$ (or "1212")

Its structure differs from the "2212" by the bilayer $(TlO)_2$ which is replaced here by a single layer (TlO) (Fig. 24). Superconductivity is observed at about 60 Kelvins.

n = 2, m = 3 : the oxide $TlBa_2Ca_2Cu_3O_{10-y}$ (or "1223")

It exhibits a superconductivity behaviour with Tc ≃ 120 K. Its structure results in the stacking of a triple oxygen deficient perovskite layer with a bilayer of sodium chloride type (one BaO layer and one TlO layer) (Fig. 24).

The structure of the superconductors $(AO)_n(A'CuO_{3-y})m$ are summarized in (Fig. 25).

IV SUPERCONDUCTIVITY IN La_2CuO_4 TYPE OXIDES

1/ La_2CuO_4

Up to February 1987, La_2CuO_4 was claimed to be a semiconductor or an insulator at low temperature. A recent study we carried out in Caen in collaboration with CRTBT in Grenoble (Tournier *et al.*) and LPCS in Bordeaux (Etourneau *et al.*) clearly shows for the first time that La_2CuO_4 can be prepared as superconductor with a T_c = 37 K (Fig. 26 a) by just working at

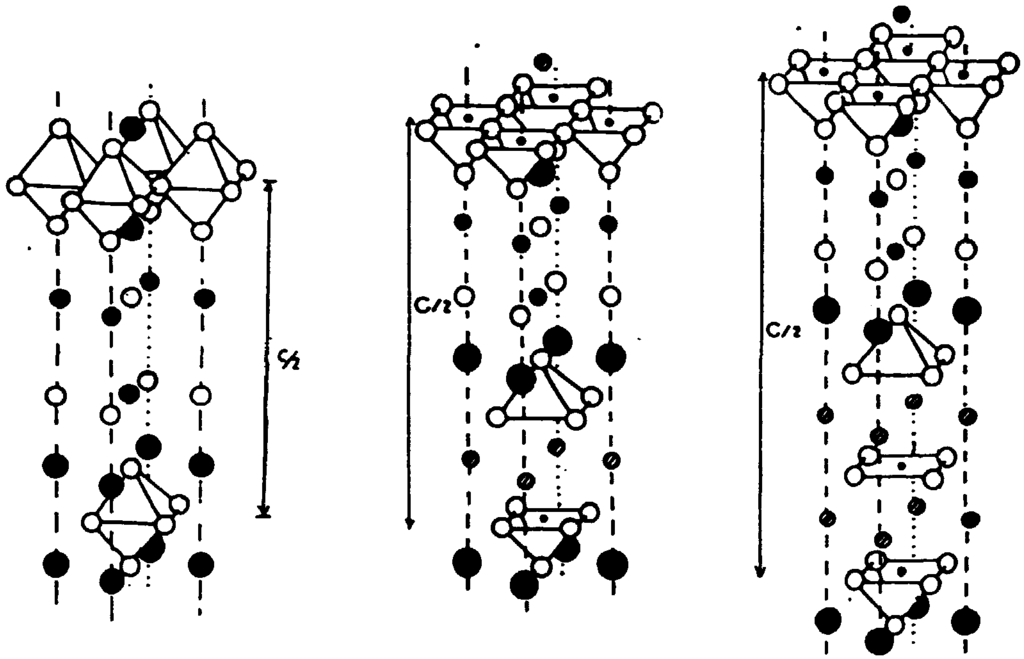

Fig. 22 - Structures of the thallium superconductors : "2201", "2212" and "2223".

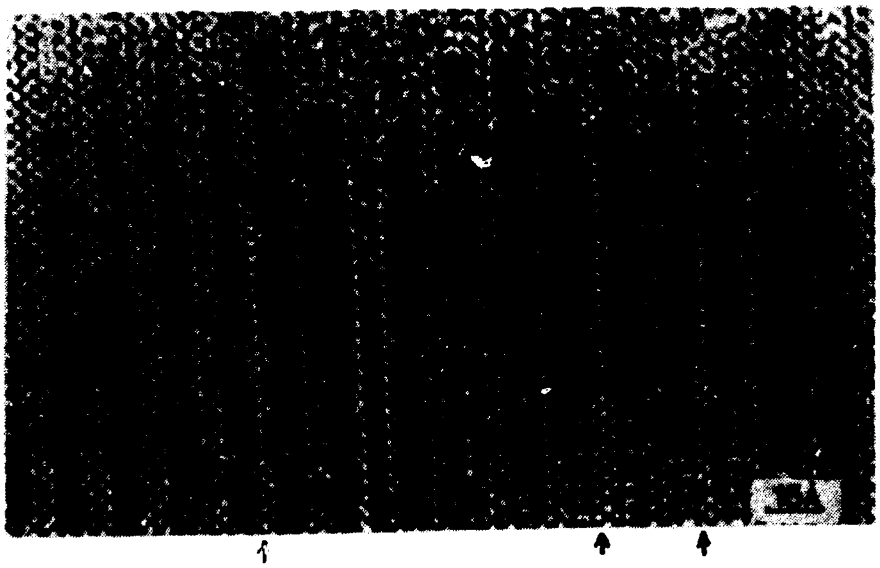

Fig. 23 - HREM image of the "2212" oxide showing defects in the stacking of the AO layers

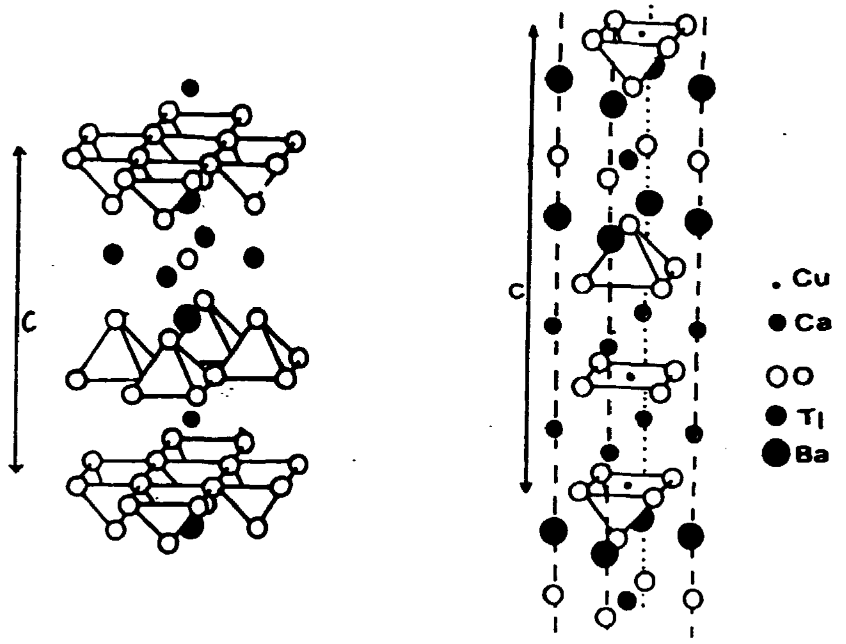

Fig. 24 - Strutures of the thallium superconductors "1212" and " 1223".

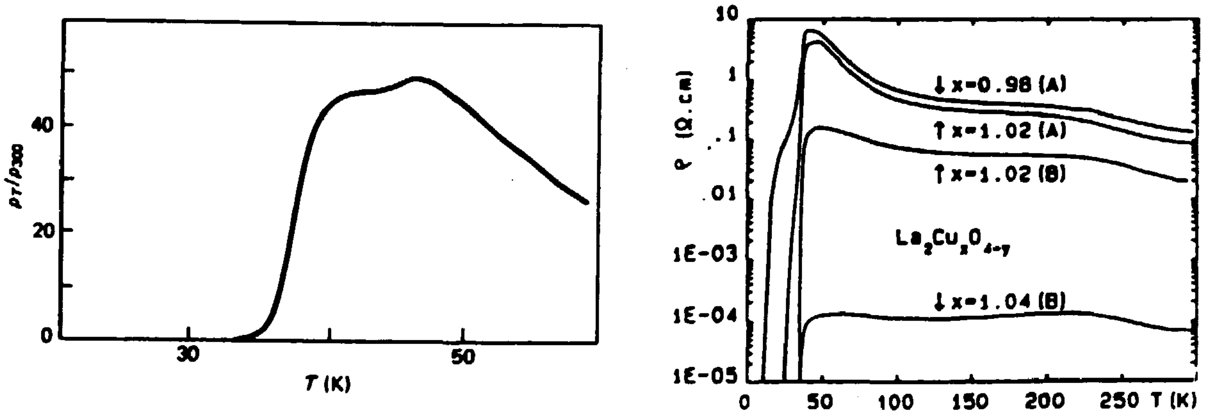

Fig. 26 - ρ = f(T) for La_2CuO_4 and $La_2Cu_xO_4$ (A: annealing at 450°C under pO_2= 1b; B: annealing at 900°C under pO_2 = 500b)

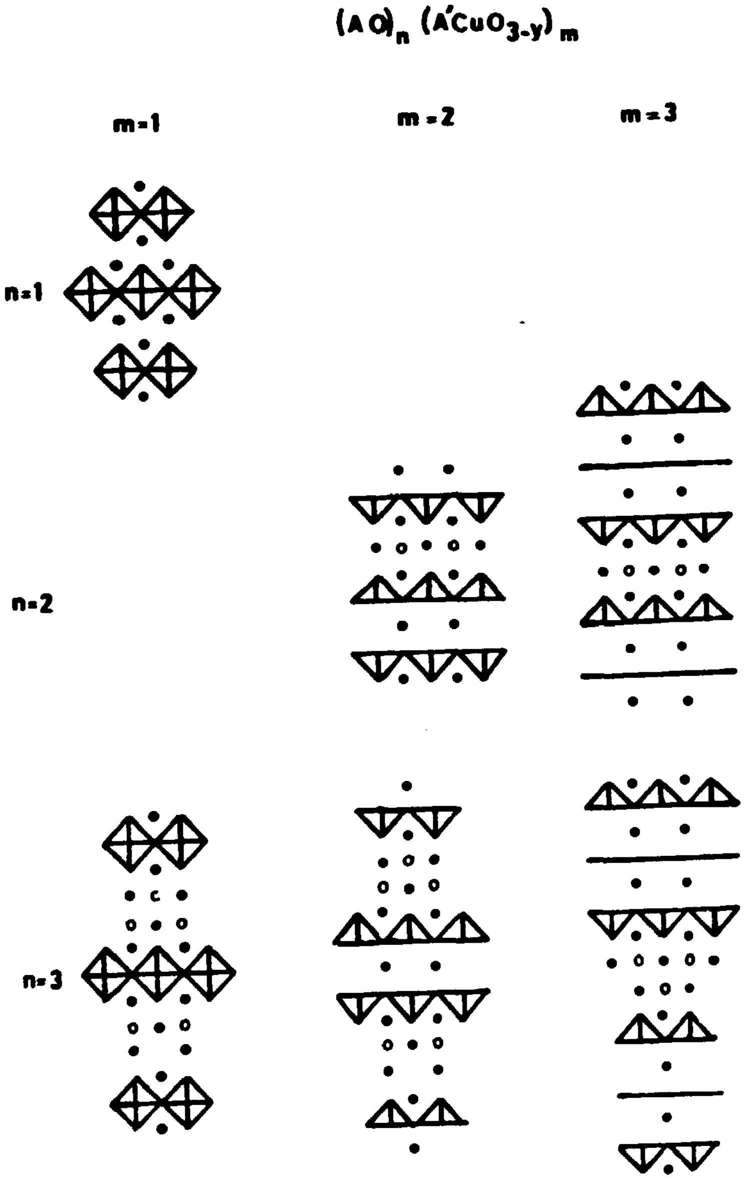

Fig. 25 - Structures of high Tc superconductors resulting from intergrowths between perovskite and sodium chloride-type structure.

higher oxygen pressure or by introducing an excess of copper oxide : the Meissner effect study shows a bulk conductivity without any ambiguity. This can be explained by the fact that semi-conducting stoichiometric La_2CuO_4 prepared in air contains only Cu(II), but exhibits Schottky defects according to the formulation $La_{2-2\varepsilon}Cu_{1-\varepsilon}O_{4-4\varepsilon}$. Annealing this compound under a higher oxygen pressure allows oxygen to be fixed on the anionic vacant sites leading to the limit formula $La_{2-2\varepsilon}Cu^{II,III}_{1-\varepsilon}O_4$, which is characterized by the mixed-valence of copper necessary for superconductivity. In the same way, an excess of copper oxide, favours the formation not only of lanthanum vacancies but of anionic vacancies according to the hypothetical non superconducting oxide $La_{2-\delta}Cu^{II}O_{4-3\delta/2}$; the latter can easily be oxidized under an oxygen flow, owing to its excess of anionic vacancies, leading to the mixed-valence $La_{2-\delta}Cu^{II,III}O_4$.
An excess of lanthanum favours also the superconducting state, leading again to the mixed-valence in agreement with the limit formulation $La_2Cu^{II,III}_{1-\varepsilon}O_4$. However in this latter case the critical temperature decreases drastically, likely owing to the presence of vacancies on the copper sites. (Fig. 26 b)

2/ Introduction of bismuth in the $La_{2-x}Sr_xCuO_{4-y}$ oxides

Lanthanides and yttrium as well as alkaline earth ions are not directly involved in the superconducting properties of the copper oxides. Lanthanides and yttrium are very useful ions because of their rather high charge and their big size compared to copper, allowing the charge balance to be satisfied. Bi (III) owing to its similar size to the lanthanides cations can replace these cations. This hypothesis was recently confirmed in Caen by synthesis of the K_2NiF_4-type $La_{2-x}Bi_{x'}Sr_{x-x'}CuO_{4-y}$, and especially by study of the compound $La_{1.7}Bi_{0.1}Sr_{0.2}CuO_{4-y}$, which was found to be a superconductor at 42 K (cf. 38 K for $La_{1.85}Sr_{0.15}CuO_{4-y}$) (Fig. 27). However, annealing under oxygen flow breaks the superconductivity. This is probably due to the partial oxidation of Bi (III) into Bi (V), so that a synthesis in air without annealing is sufficient for the synthesis of the best superconductor.

V DEFECTS IN $YBa_2Cu_3O_7$

The study of the superconductor $YBa_2Cu_3O_{7-\delta}$ ($\delta \simeq 0$) is a good example to show the complexity of the physicochemistry of these oxides and that perfect crystals do not exist even in carefully synthesized samples. The crystals are twinned and many oriented domains are observed ; moreover, different defects involving deviation from oxygen stoichiometry are observed.

Microtwinning

$YBa_2Cu_3O_7$ is orthorhombic, by heating it looses oxygen to finally give the tetragonal semiconductor $YBa_2Cu_3O_6$.

All the crystals the orthorhombic form are twinned, due to the orthorhombic-tetragonal transformation which takes place at 750°C. The twin boundaries, which are parallel either to (110) or to (110), can be parallel or quasi-perpendicular. Such a phenomenon results from a change in the vacancy ordering in the core of the matrix without any large displacement of the cations in the host lattice.

Through such boundaries, the chains O-Cu-O are not broken but zig-zag in the $[CuO_2]_\infty$ layer of the matrix. Several models can be proposed which show the change of orientation of the CuO_4 planes from one domain to the next (Fig. 28 + 29).

It should be noted that these twinning domains are in fact small, the distance between the boundaries ranging from 500 to 1000 Å. They also lead to a change of oxygen content at the boundary enabling the mixed-valence Cu(III)- Cu(II) to be modified in a local way, as well as the structure.

Oriented domains (Fig. 30)

A second type of domain forming slices perpendicular to the *c* axis, is often observed. They correspond to a change of orientation of the $CuO_2]_\infty$layers from the triple layer of polyhedra to the adjacent one, forming 'oriented' slices perpendicular to the *c* axis ; they are, thus, characterized by a junction involving the juxtaposition of two different parameters 'a' and 'b' at the boundary.

Extended defects

Three sorts of extended defects can be mainly distinguished :

1/Oxygen overstoichiometry (Fig. 31)

Such defects whose size ranges from 30 to some hundred Å are characterized by a progressive change of contrast, which could be interpreted from the image simulation by the intercalation of additional oxygen between the CuO_4 planes belonging to the $[CuO_2]_\infty$ layers, leading to the formation of CuO_6 octahedra, i.e. tending to the formation of the $YBa_2Cu_3O_8$ structure.

2/Oxygen substoichiometry (Fig. 32).

A variation of the spacing of the ion spots appears in regions of about 10-20 Å diameter. Such a phenomenon can be interpreted by the formation of a double row of edge-sharing CuO_4 groups similar to that encountered

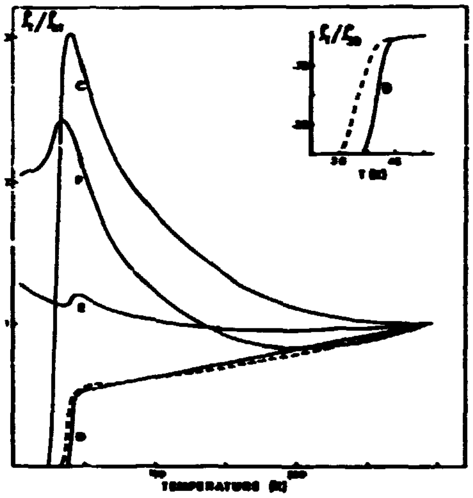

Fig. 27 - ρ/ρ_{300K} = f(T) for the oxide $La_{1.7}Bi_{0.1}Sr_{0.2}CuO_{4-y}$ (C: annealed in air, D: quenched in air, E: annealed in O_2, F: synthesized and annealed in O_2)

Fig. 28 - Low resolution images showing twinning domains.

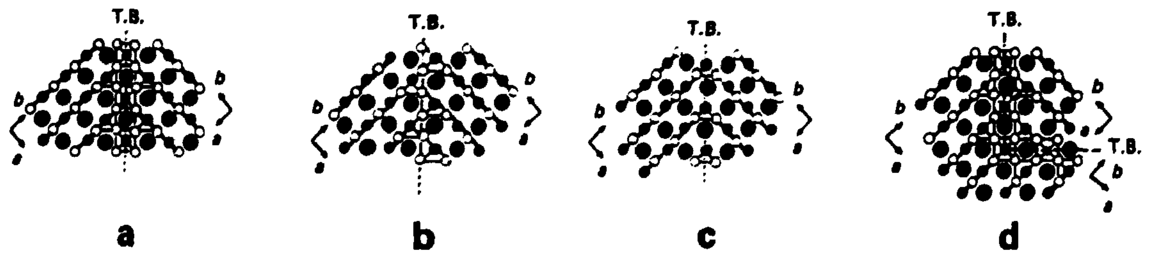

Fig. 29 - Idealized models of junction between twinning domains.

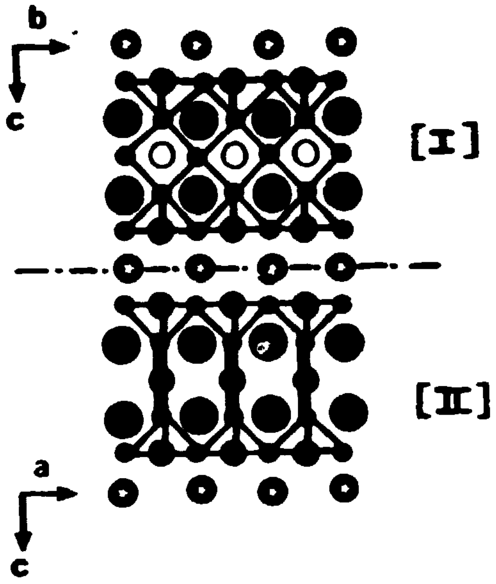

Fig. 30 - Idealized drawing of junction between two oriented domains.

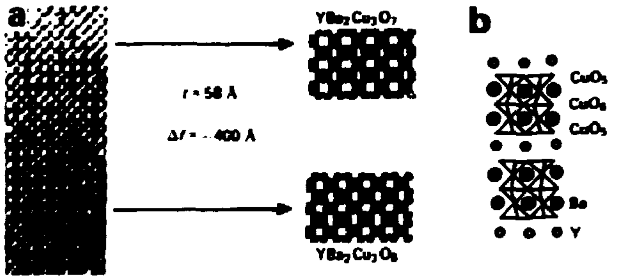

Fig. 31 - (a) HREM [001] image of a region of oxygen overstoichiometry and calculated [001] images for $YBa_2Cu_3O_7$ and $YBa_2Cu_3O_8$, (b) idealized structure of $YBa_2Cu_3O_8$.

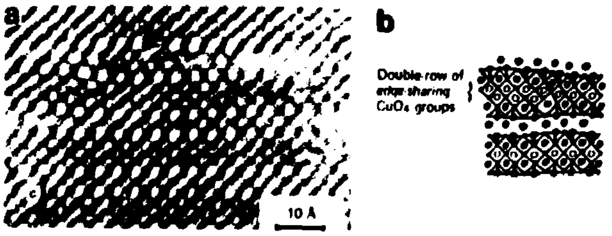

Fig. 32 - (a) HREM [100] image of the defect (arrow); (b) model of the defect

in the $SrCuO_2$ type structure.

3/Change of Y - Ba cations ordering (Fig. 33)

These defects, whose dimensions are similar to the previous ones, are characterized by a c/3 shifting of the fringes ; they can easily be interpreted by a reversal of one barium and one yttrium layer from one part of the defect to the other, while one barium layer remains unchanged through the defect.

VI OXYGEN NON STOICHIOMETRY IN $YBa_2Cu_3O_{7-\delta}$

The mixed-valence of copper is absolutely necessary for superconductivity. Thus the oxygen non-stoichiometry will play an important role in the superconductivity of these oxides. Orthorhombic $YBa_2Cu_3O_7$ looses oxygen by heating (Fig. 34) to finally give the tetragonal oxide $YBa_2Cu_3O_6$ whose structure is represented on fig. 37. The orthorhombic form of the oxides $YBa_2Cu_3O_{7-\delta}$ disappears for $\delta \simeq 0.6$ (Fig. 35). Only the orthorhombic oxides are superconductors. They give a good example of the dramatic influence of the oxygen content upon the critical temperature (Fig. 36). Although all the results do not coincide from one author to the other, due to the method of synthethis and also to the accuracy in the determination of the oxygen content, it is well established that Tc decreases drastically from 92 K for $\delta = 0$, to 22 K for $\delta = 0.6$, value beyond which superconductivity disappears, as shown for example by the results obtained by Tarascon et al., Monod et al., Cava et al. and Tokumoto et al.

Only consideration of electroneutrality leads to consider two domains :

$0 < \delta < 0.5$ involving Cu(II) and Cu(III)
$0.5 < \delta < 1$ involving Cu(I) and Cu(II)

Thus the second domain should not exhibit any superconductivity owing to the absence of the mixed-valence Cu(III)-Cu(II). However we have to take into consideration the coordination of copper. From the chemical point of view it is indeed well-known that Cu(II) or Cu (III) can only take coordinations greater than 3, whereas Cu(I) takes only the linear twofold coordination in oxides.

A model based on the continuous transition from the $YBa_2Cu_3O_7$ structure to the $YBa_2Cu_3O_6$ structure (Fig. 37) can be proposed. In order to respect the coordination of copper the different compositions corresponding to $0 < \delta < 1$ will be described as disorded intergrowths of the "O_7" and "O_6" structures.

In this model the pyramidal layers [$CuO_{2.5}$] remain untouched whereas $[CuO_2]_\infty$ rows of CuO_4 square planar groups alternate with $[CuO]_\infty$ rows of Cu^IO_2 groups either in the same layer (Fig. 38a) or from one layer to the next (Fig. 38b). Longitudinal intergrowths of CuO_4 square planar groups and CuO_2 groups within a same chain can also be considered (Fig.

Fig. 33 - Variation of the Y-Ba ordering: (a) HREM image, (b) idealized model

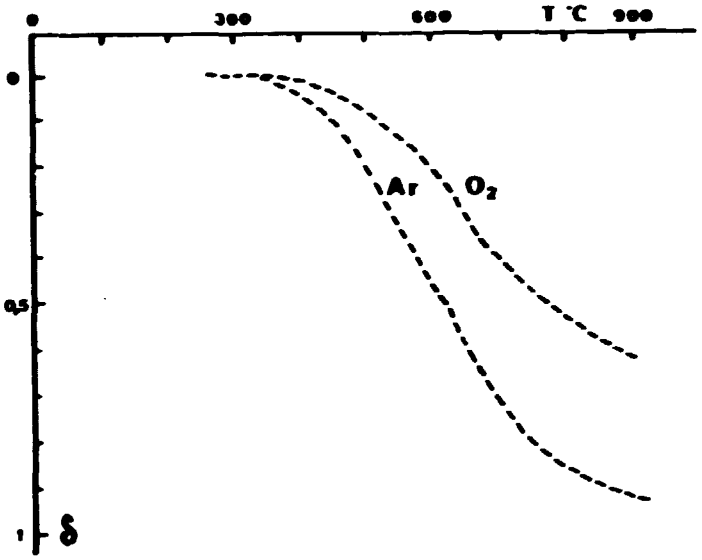

Fig. 34 - TG curves showing the behaviour of $YBa_2Cu_3O_7$ heated in O_2 and Ar atmosphere.

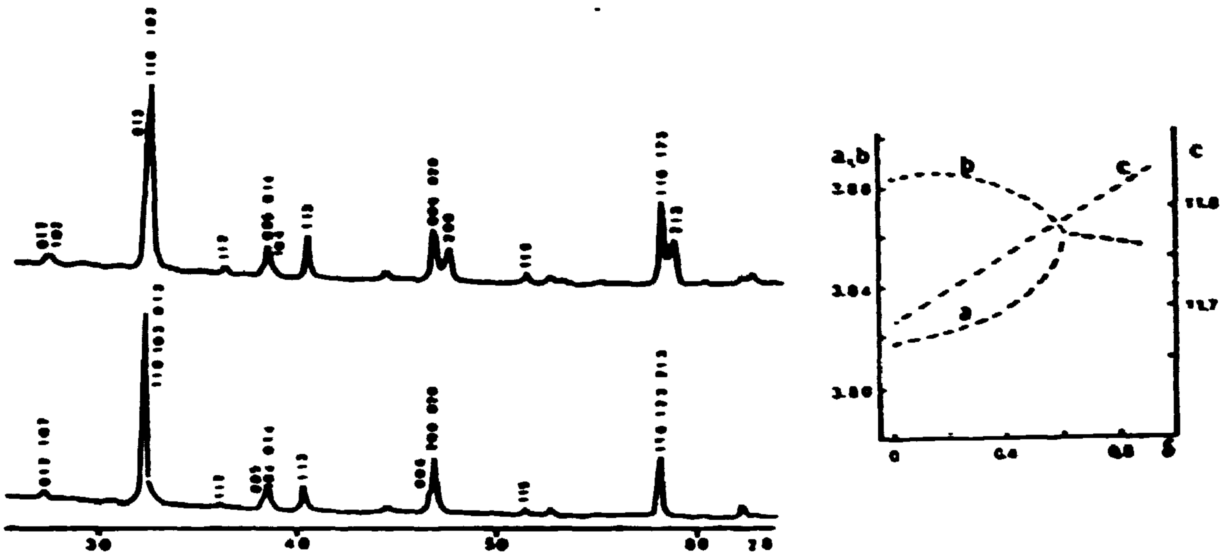

Fig. 35 - X rays patterns of the orthorhombic and tetragonal forms of the oxides $YBa_2Cu_3O_{7-\delta}$ and evolution of the cell parameters vs δ

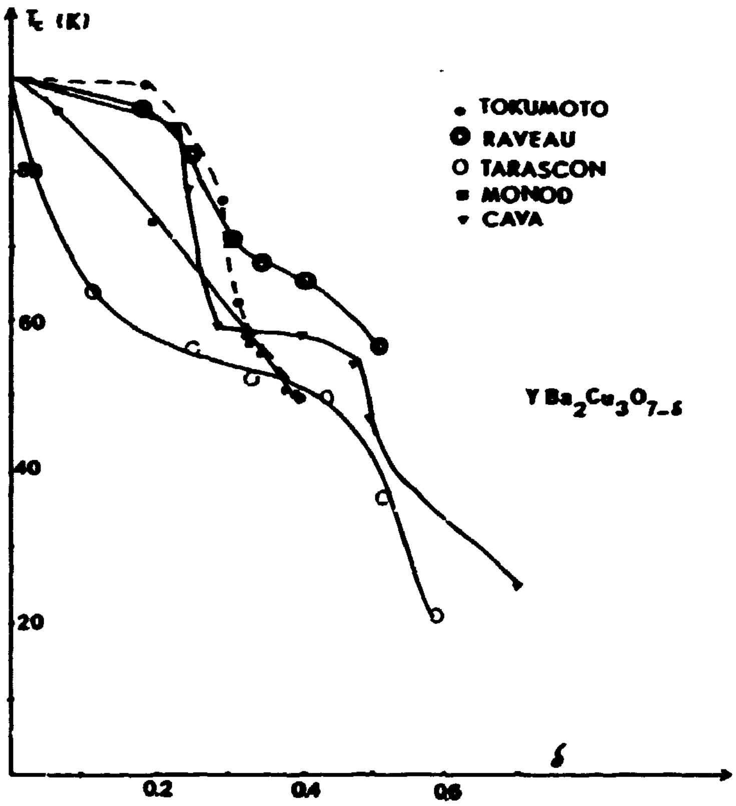

Fig. 36 - Variation of Tc vs δ from different authors.

38c).

This structural model which is characterized by a partial disproportionation of Cu(II) into Cu(III) and Cu(I) leads to the formulation

$$YBa_2[Cu^{II}_2Cu^{III}O_7]_{1-\delta}[Cu^{II}_2Cu^{I}O_6]_\delta$$

It is supported by the observations by X-ray absorption of noticeable amounts of Cu(I) in all the domain $0 < \delta < 1$ simultaneously with Cu $3d^9\underline{L}$ (Baudelet et al. ; Oyanadgi et al.).

The examination of this formulation shows that the Cu(III) content is much greater than that deduced from the knowledge of δ. Using this formulation, Tc increases approximatively continuously as the ratio $[Cu(III)/Cu_{total}]$ increases for Monod's data, whereas the plateaus observed by different authors could be due to an ordering of the oxygen vacancies which is not yet really elucidated (Fig. 39).

This prominent influence of the $[Cu(III)/Cu_{TOT}]$ ratio upon the Tc value is confirmed by the study of the oxides $La_{2-x}Sr_xCuO_{4-y}$. In this case no disproportionation of Cu(II) into Cu(III) and Cu(I) needs to be considered since the oxygen deficiency does not introduce for copper a coordination smaller than four. From the data obtained by Kang et al. it can be established that there is no discontinuity in the evolution of Tc versus the $Cu(III)/Cu_{tot}$ ratio. In the same way pure orthorhombic $La_{1.95}CuO_4$ prepared under high oxygen pressure (Tournier et al.), which exhibits bulk superconductivity below 37 K, corresponds to a $[Cu(III)/Cu_{TOT}]$ ratio close to that observed for $La_{1.85}Sr_{0.15}CuO_4$ in agreement with the similar values of Tc for these two compounds.

VIII SUBSTITUTIONS IN $YBa_2Cu_3O_{7-\delta}$

Many studies have been carried out these last months in order to determine the influence of doping upon the superconducting properties of these phases (Tarascon et al., Tsurumi et al.) (Fig. 8). This confirms the very weak influence of the interleaved rare-earth ions upon superconductivity of these materials. On the opposite, Takita has shown that Tc decreases dramatically as barium is partially replaced by rare-earth ions in the oxides $Ln_{1+x}Ba_{2-x}Cu_3O_{7-\delta}$ (Ln = La, Nd, Sm, Eu). This variation is accompanied by a decrease of the orthorhombic distortion leading to a tetragonal symmetry around x = 0.20 for Nd which composition remains superconductive (Tc = 60K). The lack of data concerning the oxygen content does not allow to decide here whether the decrease of Tc is due to the introduction of rare- earth ions in the barium sites or to a simple decrease of the $[Cu(III)/Cu_{TOT}]$ratio.

Several studies of the replacement of copper by different metallic elements have shown that only a progressive decrease of Tc was observed even for magnetic ions such as iron (Fig. 40) Maeno et al., Oseroff et al.). Here again the lack of data concerning the oxygen content makes dif-

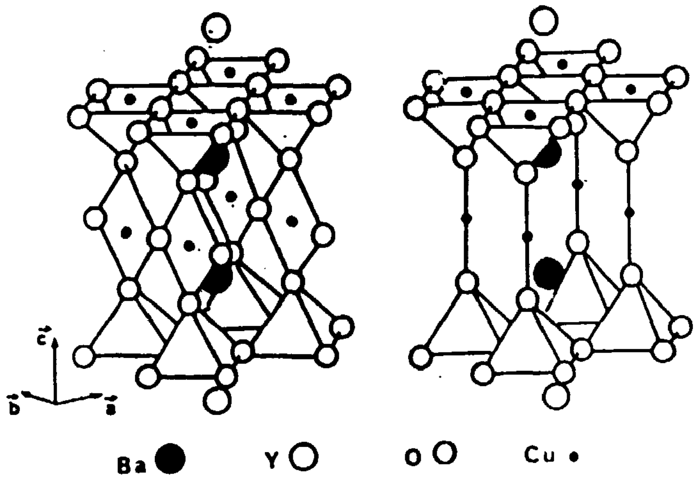

Fig. 37 - Structure of the superconductor $YBa_2Cu_3O_7$ and of the semiconductor $Yba_2Cu_3O_6$.

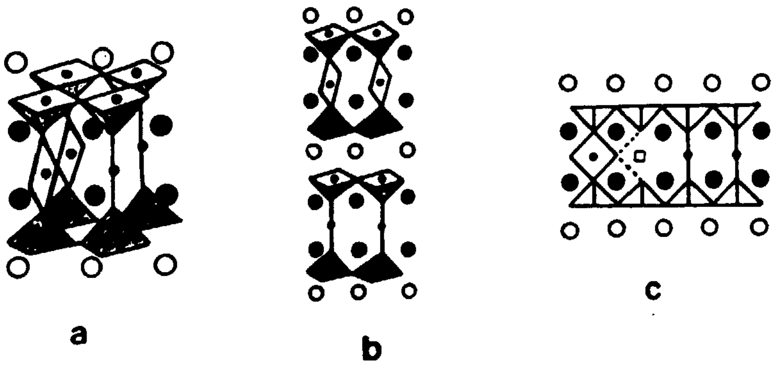

Fig. 38 - Hypothetical models of intergrowths between "O_7" and "O_6" structures.

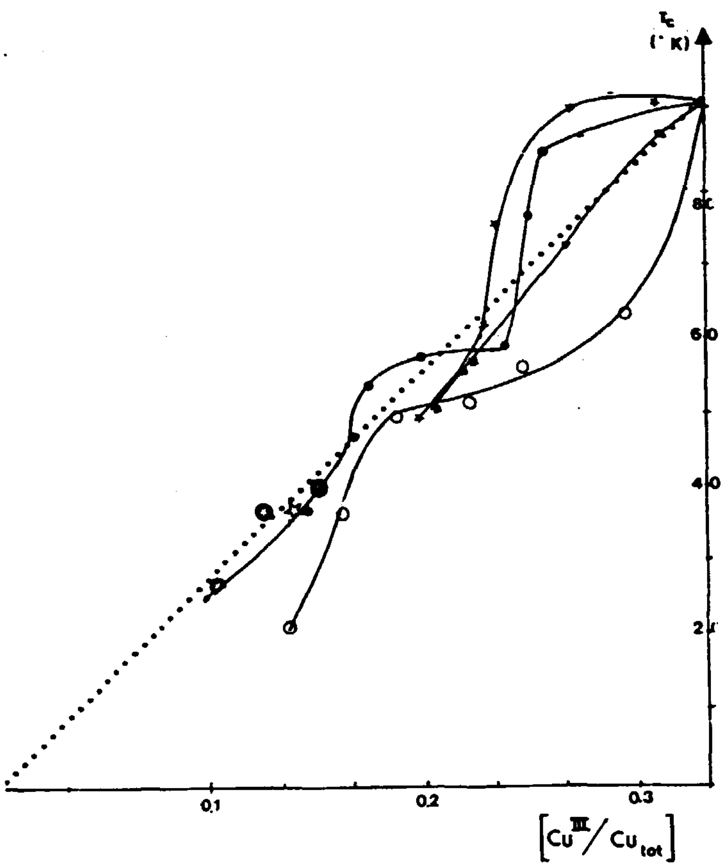

Fig. 39 - Variation of Tc vs $Cu(III)/Cu_{tot}$.

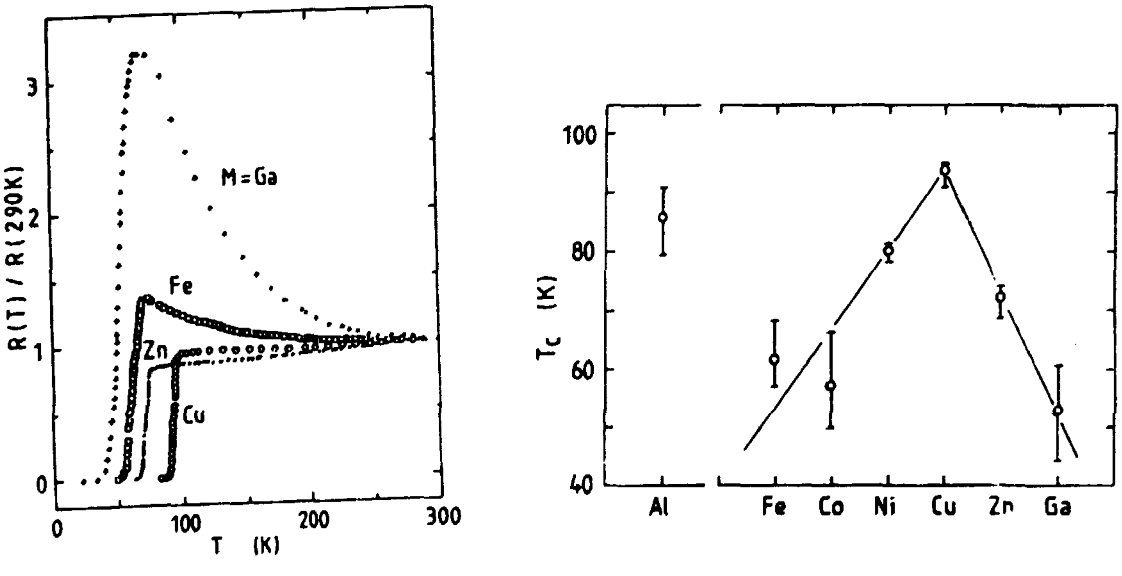

Fig. 40 - Superconducting properties of the oxides $YBa_2Cu_{2.9}M_{0.1}O_{7-\delta}$.

ficult the chemical interpretation of these results.

More complete results have however been obtained for the oxides $YBa_2Cu_{3-x}Fe_xO_7$. They showed that Tc of these oxides decreases continuously as x increases from 92K for x = 0 to about 37K for x = 0.36. The recent structure determination of the oxide $YBa_2Cu_{2.85}Fe_{0.15}O_7$ shows that this oxide is a superconductor (Tc = 70K) in spite of its tetragonal symmetry and that iron is distributed in a preferential way between the pyramidal sites (0.05 Fe) and the oxygen deficient octahedra (0.1 Fe). The systematic study of these oxides by Deslandes et al. confirms the superconductive character of the tetragonal form for x ranging from 0.15 (Tc = 70K) to 0.35 (Tc = 30K) and shows from the analysis of oxygen that δ remains close to 0.00 ± 0.02 (Fig. 41). The Mössbauer study of these compounds shows that the Fe(IV) is present but in small amount compared to Fe(III). From these results the curve of Tc vs the ratio $[Cu(III)]/[(Cu+Fe_{TOT}]$ can be plotted assuming the approximate formulation $YBa_2[Cu^{II}Cu^{III}_{1-x}Fe^{III}_x]O_7$ (Fig. 42). It can be seen that this curve is near to that established for the pure oxide $YBa_2Cu_3O_{7-\delta}$ using Monod's data. The small difference between the two curves may partly be due to the presence of Fe(IV) which was not taken into consideration in our calculation. These results confirm the prominent role of the $[Cu(III)/Cu_{TOT}]$ ratio in the superconductivity of these oxides.

VII CONCLUSION

The physicochemistry of the high Tc superconductors is very complex and a great number of phenomena are not yet well understood as well as in the oxides involving lanthanides and yttrium as in those involving bismuth and thallium. The understanding of these phenomena may open a way for the preparation of superconductors with higher Tc.

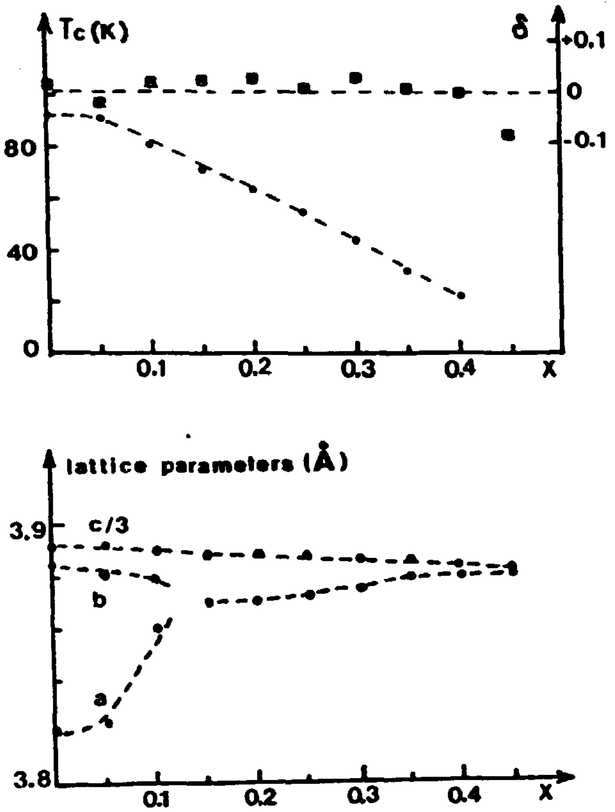

Fig. 41 - Variation vs x of Tc and δ (a), and of the cell parameters (b) for the oxides $YBa_2Cu_{3-x}Fe_xO_{7-\delta}$.

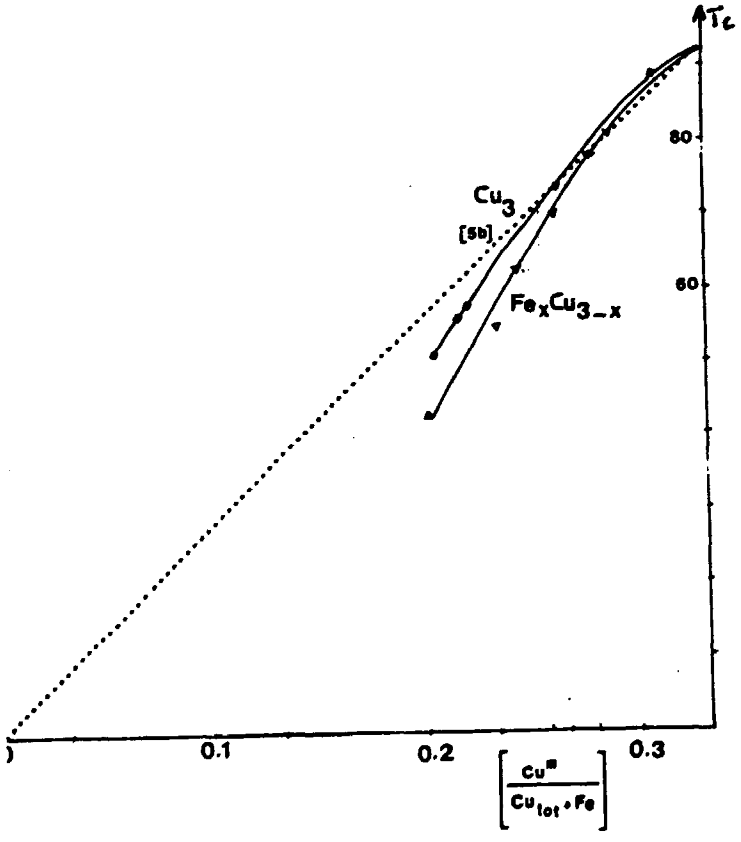

Fig. 42 - Tc vs $Cu(III)/(Cu+Fe)_{tot}$.

SOME OF THE CITED LITTERATURE

Baudet F. et al., Z. Phys. B,69 (1988) p.141.

Cava R.J.et al., Nature, 329 (1987) p.423.

Chu C.W. et al., Phys. Rev. Lett., 58 (1987) p.911; Phys. Rev. Lett., 60 (1988) p.1174.

Eserof S.B. et al., Novel Superconductivity, S.A. Wolf Ed., (1987) p.679.

Kang W. et al., J. Phys. Fr., 48 (1987) p.1181.

Maeda H. et al., Jpn. J. Appl. Phys., 27 (1988) L209, L548.

Maeno Y. et al., Novel Superconductivity, S.A. Wolf Ed., (1987) p.1073.

Magneli A., Arkiv Chemi, 1 (1949) p.213.

Michel C. et al., J. Solid State Chem., 37 (1981) p.151; Rev. Chim. Miner.,21 (1984) p.407; Mat. Res. Bull., 20 (1985) p.667; J. Solid State Chem., 68 (1987) p.143; C. R. Acad. Sci., 304 II (1987) p.1059; Z. Phys. B, 68 (1987) P.421.

Müller K. A. et al., Z. Phys. B, 64 (1986) p.189.

Monod P. et al., J. Phys. Fr., 48 (1987) p.1367.

Nguyen N. et al., J. Solid State Chem., 39 (1981) p.120; J. Phys. Chem. Solids, 44 (1983) p.389.

Oyanagi H. et al., Jpn. J. Appl. Phys., 26 (1987) L649.

Politis C., Appl. Phys., A45 (1988) p.261.

Roth G. et al., Z. Phys. B, 69 (1987) p.53; Z. Phys. B, 71 (1988) p.43.

Sheng Z.Z. et al., Nature, 332 (1988) p.55; Phys. Rev. Lett., 60 (1988) p.937; Appl. Phys. Lett., 52 (19888) p.1738.

Sleight A.W. et al., Science, 239 (1988) p.1015; Nature, 332 (1988) p.420..

Tarascon J.M. et al., Phys. Rev. B, 35 (1987) p.7245; Science, 235 (1987) p.1373; Phys. Rev. B, 37 (1988) p.9382.

Tokumoto M. et al., Jpn. J. Appl. Phys., 26 (1987) L1566.

Tournier R. et al., C. R. Acad. Sci., 304 II (1987) p.1097; Physica B, 46 (1987) p.307.

Tsurumi S. et al., Jpn. J. Appl. Phys., 26 (1987) L1865.

Von Schnering H.G. et al., Angew. Chem., 27 (1988) p.574.

CHAPTER 6

D: 8903002229

MANUFACTURING AND APPLICATION OF SUPERCONDUCTING WIRES

Charles Laverick
16, Roslyn Court
Patchogue NY 11772

and

John K. Hulm
Westinghouse R&D Center
Pittsburgh PA 15235

ABSTRACT

The discovery of materials which exhibit superconductivity up to 125 Kelvin is a major scientific event and may lead to an extension of the range of superconductor application beyond that which has so far been attained in over 25 years of effort. Some reports suggest that superconductivity may exist even at room temperature or beyond: an exciting prospect which could revolutionize electrotechnology as we know it.

The new superconductors offer the prospect of operation up to the temperature of boiling liquid nitrogen at atmospheric pressure (77 K) as opposed to the temperature region around 4.2 K. This could lead to cheaper and simpler refrigeration.

It may be that the new superconductors will be used in applications which we have not as yet conceived or that the true value of the discovery will lie in our enhanced understanding of the nature of the solid state. Only time will tell.

In this paper, some of the characteristics of the new materials bearing on their utilization are examined and some of the principal barriers to application are assessed. Some of the promises and successes in applying superconductors over the past 28 years are discussed and the implications of the new discoveries from the point of view of application considered.

THE LOW TEMPERATURE SUPERCONDUCTORS: APPLICATIONS - PAST & PRESENT

INTRODUCTION

The story of superconductivity begins with the discovery and liquefaction of helium, since a liquid helium environment was essential for the early superconductors.

HELIUM DISCOVERIES:

1868 - IN THE SUN; 1895 - IN THE EARTH'S ATMOSPHERE;

1905 - IN KANSAS NATURAL GAS; 1908 - HELIUM LIQUEFIED.

1911 - SUPERCONDUCTIVITY DISCOVERED IN MERCURY

Soon after the discovery of superconductivity in 1911 it was recognized that many elements were superconductors, but that they were too limited in magnetic field and current to be of practical use. In the fifty years to 1961 the physics of superconductivity came to be understood, but its practical application remained elusive. Important milestones on the road to practicality were the discovery of superconductivity in niobium zirconium in 1953 and in niobium tin in 1954 by Hulm and Mathias, but they failed to check the current carrying capacity of these materials in magnetic fields: this was left to Kunzler et al. in 1960.

The search for practical superconducting magnets was advanced in 1965 by G.B. Yntema who reported on the operation of a 7 kG superconducting coil using cold worked niobium wire. Five years later, in 1960, S.H. Autler reported on the operation of a similar magnet up to 10 kG using an iron yoke. This was the first coil to show that superconducting windings could be used successfully in an iron magnet.

In 1961 the group at Bell Laboratories (Kunzler et al) was asked to develop a compact liquid helium cooled magnet to operate in conjunction with a maser. They first operated a coil wound with cold worked molybdenum rhenium wire to 15 kG but in the same year were also successful in developing niobium tin wire which produced even higher fields without loss: the practical potential of superconductivity had gained a new lease on life. Within weeks, at an MIT conference on high magnetic fields, several workers reported on the successful construction and operation of superconducting magnets wound from the new materials. These included small bore niobium tin (Kunzler et al. > 7T) and niobium zirconium solenoids (Hulm et al., 5.5T and Hake et al., 5.9T). In the same year, commercial quantities of these materials were being produced in wire and tape form and researchers world-wide began the task of producing useful superconducting magnets.

Table 1: PRINCIPAL SUPERCONDUCTOR APPLICATIONS

CURRENT

COMMERCIAL AND INDUSTRIAL USES

MAGNETIC RESONANCE IMAGING
MR SPECTROSCOPY
GYROTRONS
R&D MAGNETS
SEPARATORS
MAGNETIC SHIELDING

PHYSICS MACHINES AND DEVICES

HIGH ENERGY COLLIDERS
SMALLER MACHINES
RADIO FREQUENCY CAVITIES
DETECTOR MAGNETS

POTENTIAL

ELECTRIC UTILITIES

POWER TRANSMISSION
ENERGY STORAGE
ROTATING MACHINERY
TRANSFORMERS
CURRENT LIMITERS

ENERGY CONVERTERS

MAGNETIC FUSION
MAGNETOHYDRODYNAMICS

TRANSPORTATION

HIGH SPEED TRAINS
SHIP PROPULSION

ELECTRONIC APPLICATIONS

COMPUTERS AND LOGIC DEVICES

Semiconducting - Superconducting Hybrids
ie. superconducting bus connectors @ 77K
save space, reduce power loss,
increase switching speed

Semiconducting memory with Superconducting Logic

SQUIDS - SUPERCONDUCTING QUANTUM INTERFERENCE DEVICES

Very sensitive magnetic field and voltage measurement
Medical diagnostics, geophysics, submarine detection

RADIATION DETECTORS: Microwave and far infra-red

ANALOGUE SIGNAL PROCESSORS

MAGNETIC SHIELDING

VOLTAGE STANDARD

The low temperature superconductors have been used in electronics and in high power or magnet applications (see Table 1). However this paper concentrates on the high current and magnet applications. Some of the highlights in such applications throughout the years are listed in Table 2. thus illustrating the long history of technological advance in applied superconductivity. Development of the technology has been a continuing world-wide effort, with free and open communication at the many national and international conferences devoted to this topic.

TABLE 2 - SOME HIGHLIGHTS: SUPERCONDUCTORS and APPLICATIONS

1960-61	**THE NEW HIGH FIELD, SUPERCONDUCTORS**
1963-65	SMALL BORE 10T COILS: WESTINGHOUSE, GE, RCA THE BROOKHAVEN 14T SIGMA MAGNET
1964 -	THE ARGONNE HELIUM BUBBLE CHAMBER MAGNET SYSTEM
1966 -	THE AVCO DEMO MHD STABLE, SADDLE COIL
1966-74	DEMONSTRATION MOTORS AND GENERATORS
1968 -	THE ARGONNE 3.7m BUBBLE CHAMBER MAGNET
1973-74	MAGLEV TRAIN DEMONSTRATIONS IN GERMANY & JAPAN
1976 -	US/ MHD COIL INSTALLED IN THE U-25 CHANNEL, MOSCOW
1978 -	SC TOKAMAK T-7 OPERATIONAL IN MOSCOW
1983 -	FERMILAB SC ENERGY DOUBLER OPERATES AT 512 GeV BNL DEMONSTRATION SC TRANSMISSION LINE OPERATES
1984 -	FERMILAB DOUBLER OPERATES AT 800 GeV
1985 -	FIRST TESTS OF THE FERMILAB COLLIDER AT 1.6 TeV
1986 -	ANL/ATLAS HEAVY ION, SC LINAC OPERATES; SC FUSION SYSTEMS - MFTF-B & LCT IN US; TORE SUPRA, FRANCE; TRIAM-1M, JAPAN; OPERATED
	--
1986 -	**HIGH TEMPERATURE SUPERCONDUCTIVITY (HTSC) HT 37 K!!.**
1987 -	**HIGH TEMPERATURE SUPERCONDUCTIVITY AT 90 K & ABOVE**
1988 -	**MORE HTSC's at 125 K+ & at 30 K (isotropic).**

Many factors contributed to the development of superconductor technology following the 1961 advances. By this time a whole infra-structure was in place and there was a need for this advanced technology. Kamerlingh Onnes could not have carried out such developments in his time because the infra-structure did not exist and there was little perceived need for such high technology.

Among the factors necessary for superconductor development was the growth of big science during and after World War II and the development of a large scientifically literate sub-group in the general population. In addition, the peace was followed very soon afterwards by an arms race, the establishment of the large National Laboratories and the development of the H-bomb, rockets, Sputnik and later satellites beginning in 1957. These developments required a large scale liquid hydrogen technology and large quantities of helium. Thus large scale cryogenics and liquid hydrogen technology dominated the 1950's and the advent of the high field superconductors coincided with the beginning of the age of plentiful helium, an established cryogenic technology and the need for very large physics machines. All the factors were in place at the right time.

The successful reduction to practice which followed led to applied superconductivity as a new engineering technology in all the advanced industrial countries in less than a decade. However its fields of application in everyday life were severely limited, being principally in physics and research.

BRIEF HISTORY

Early Conductors and Magnet Problems

The first niobium tin conductors were prepared by winding a tube of niobium containing a mixture of niobium and tin powders around the coil form and creating the niobium tin 'in situ' by reacting the mixture at high temperature for several hours. The insulation between turns and layers had to withstand this heat treatment. By comparison, the niobium zirconium and niobium titanium were extruded wires which only needed to be cooled below their critical temperatures to become superconducting. Niobium titanium quickly became the work horse of the field because of its superior ductility in spite of its low upper critical temperature and an upper critical field well below that of niobium tin. Later niobium tin conductors were in the form of tapes formed from the vapor deposition of the niobium and tin from their chlorides and these quickly found a niche in the market for the highest field research magnets: a position they still occupy today.

It was soon found that it was not so easy to make superconducting magnets as it had first appeared. Many problems appeared when coils were wound and energised. They were labelled as coil 'effects'. Typical was the 20 amp. catastrophe: it seemed that no matter what was tried the limit of coil current appeared to be 20A. As coils were made larger, the maximum attainable coil currents appeared to drop: this was the large coil effect. One published theory concluded that at a limiting size, the coil current would be zero. Again, there was the proximity effect: when two or more coils were placed near each other, the operating currents were lower than those attainable by either coil at the same field level. It was also found that the wire operating currents were drastically reduced and erratic if there was the slightest motion of the wire. All these effects had to be overcome if reliable engineered magnets were to be constructed.

A further set of problems involved operating coils. Well below the short sample characteristics of the wires themselves, the coils would switch quickly to the normally conducting state, discharging so violently that they were frequently damaged beyond repair. This phenomenon was, and still is, known as quenching. Techniques for removing this stored energy in a harmless way were devised and are used in many installations today.

In 1962 and 1963 I was able to duplicate all these coil effects in simple hairpins of wire energized in a magnetic field and to extend the work to large numbers of small coils fabricated in different ways and wound with different conductors. The upshot of this work was a set of simple rules for making reliable coils. These were; hold the conductor securely, cool it well, and shunt it with as much good normally conducting material as the application permits. In order to gain mechanical strength, improve the amount of shunting provided for each wire and use operating currents of adequate intensity for larger magnet systems, the superconductors were cabled and it was found that even in large coils the inhibiting earlier coil effects could be eliminated.

Using these techniques, a helium bubble chamber magnet was constructed and operated in Argonne National Laboratory in late 1964, following a series of successful tests of component parts of the system. Constraints imposed by the bubble chamber enclosure prohibited the use of large volumes of copper shunting, but the outer coils could be operated with stable normally conducting regions in the windings.

Shortly afterwards, in late 1964, Stekly and Kantrowitz operated a small coil wound with a strip conductor containing nine 0.25mm diameter, parallel NbZr wires rolled in a 12x1mm cross-section copper strip (19/1 Cu/SC ratio) and this was fully stable. While these developments continued, the early commercial organizations were not idle and in 1963 and 1964 a series of small, technologically significant coils operating at or slightly in excess of 10T were built by RCA, GE and Westinghouse, using their respective commercially developed, in-house superconductors and by W. Sampson of Brookhaven National Laboratory who used niobium-tin tape. The path to very high field technology was opened and there were several technological options available.

Bubble chamber development for this first superconducting detector had paralleled the magnet development and by early 1966 the bubble chamber was installed on the experimental floor of the Argonne 12.5 Gev proton synchrotron. A successful series of experiments was carried out, during which the magnet was completely trouble free and this success was followed immediately by plans to build a series of very large bubble chambers in Argonne, Brookhaven and CERN laboratories. The age of the superconducting magnet had arrived.

All these very large coils used the fully stable conductor concept, although the first three, at Argonne, Brookhaven and CERN (The European Center for Nuclear Research) used the parallel conductor configuration in copper, as opposed to the cables which had been so successful in the first small, high field chamber. This had the disadvantage that eddy currents induced in the conductor by magnetic field gradients take days or even months to die down, resulting in gradual field changes in the magnet after a change in current or a charge or discharge. Argonne was lucky in this respect because the use of a 1600 ton iron yoke eliminated the field gradients in the coils.

In all, four such large magnets were built, and all were successful. Three were used in bubble chambers and one in a CERN experiment known as the Omega experiment. This latter magnet was unique because it was the first use of a conductor in which the helium flowed through the windings, thus simulating the construction of a conventional water cooled coil. This allowed for a rigid winding structure with good insulation.

Finally a fifth magnet was commissioned for the Fermi National Accelerator Laboratory and also operated successfully. In this latter case there was a return to the cable concept developed by C. Laverick, the cable being soldered in a groove in the stabilizing strip, so overcoming the eddy current effects during field change which hampered the operation of the earlier magnets without iron yokes. Each coil was an improvement on its predecessor both in design and operating field and each was wound with stablized conductor with large amounts of copper.

The success of these physics coils stimulated development in fusion and magnetohydrodynamic development programs and in the development of very high current density, relatively high field coils for use in high energy particle beam transport systems for the large accelerator installations. Most recently, these efforts have resulted in a series of successes in magnet design and demonstration for a large range of projects.

Throughout the years following this earlier work, techniques in conductor manufacture improved. Cables were supplanted by twisted multistrand conductors consisting of fine superconducting filaments co-extruded in matrixes of copper or aluminum. In some cases these multistrand conductors were cabled for higher strength and current carrying capacity. On this foundation a small, but mature world wide superconductor industry has grown and there is hope for a bright future for the further application of this technology.

HIGH TEMPERATURE SUPERCONDUCTORS

Over two years have passed since the discovery of the high temperature perovskite superconductors. As with the early low temperature materials, there are now several families of the new materials with large numbers in each group and often, many variations of each compound. Almost all the early materials have found no practical use, and for the present, this is true of the new materials. The properties of the new materials and their various classifications have been exhaustively discussed in the present school.

We have the lanthanum series with Tc around 35 K, the 1-2-3 series, of which Yttrium Barium Copper Oxide with a Tc around 95 K can be considered the model compound of the class, the Bismuth or Thallium Strontium Calcium Copper Oxide series, with Tc's up to 130 K and, even more recently, Barium Potassium Bismuth Oxide at a Tc of 30 K, which some claim to be istropic. Thus we have the possibility of operating superconductors in liquid nitrogen at 77K instead of in helium at around 4.2K, with the subsequent promise of ease of use, lower cost and simplification in magnet system design - if practical conductors can be produced. It remains to be seen if this promise can be fulfilled. A more important by-product of the discovery may turn out to be our enhanced understanding of the solid state and applications as yet unforseen today.

In the past two years, much has been learned about the new materials and techniques for processing them. However they retain the disadvantage of being anisotropic in current carrying capacity. Even organic superconductivity has received a recent boost with the announcement by K. Oshima et al. (U of Tokyo) of superconductivity in a deuterated organic salt at 10.4K, the highest so far for an organic system.

There have been many unsubstantiated claims for even higher temperature superconductors approaching or exceeding room temperature. These could be the first glimpses of a new electrical phenomena or type of metal, rather than superconductivity: other possibilities include misinterpretations of the phenomena or errors in measurement. However all these advances within two years testify to the dynamic state of a new physics and materials science which may have profound technological significance in the years ahead. Adding to the excitement are rapid advances in materials processing and in the understanding of the structure of many of these new materials.

Unlike the alloy superconductors, the transitions for the new ceramics are broad. In this rapidly evolving new field there is enough broad similarity in characteristics between the various ceramic families to justify considering the older materials (of last year!) for the purpose of examing the problems involved in their practical application: the mechanical and electrical problems are similar. Some of these characteristics are

As is well known, the current carrying capacity and operating field limit for superconductors falls rapidly as the critical temperature is approached. The model 1-2-3 material has the formula $YBa_2Cu_3O_7$. It is possible to replace the Yttrium with almost every member of the rare earth series without affecting T_c. The normal state resistivity just above the onset of superconductivity for these materials is over 500 micro-ohm cm: a factor of about fifty times that for niobium tin.

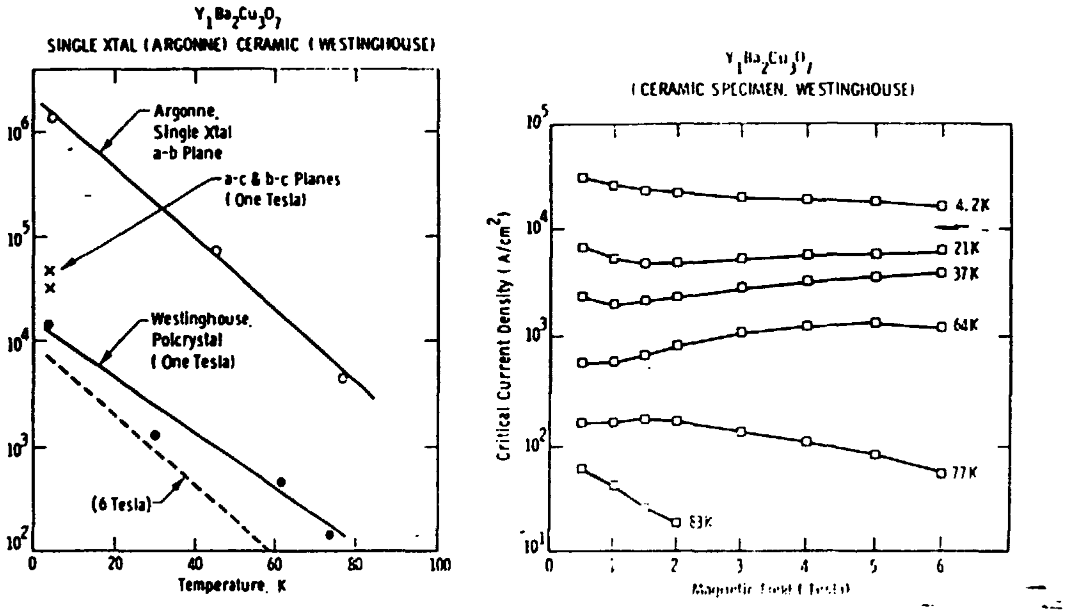

Figure 1a.

Figure 1b.

Figure 1: a) Variation of Jc A/cm^2 with temperature for single crystal and bulk Y/Ba/CuO specimens. b) Variation of Jc with magnetic field for a bulk specimen at various temperatures.

In figure 1a, the critical current densities for bulk ceramic and single crystal specimens are compared and those for the bulk material are orders of magnitude lower. The single crystal measurements also reveal a large anisotropy in J_c. This is of the order of 10^6 A/cm^2 in the a-b plane at 4.2 K and a factor of 30 lower in the c-a and c-b planes. Even for the favorable a-b direction of current flow, J_c falls off very steeply with increasing temperature, falling by two orders of magnitude between 4 K and 77 K. The same behavior is observed in the bulk ceramic specimen of figure 1a and is very different from that of the low temperature materials where the dependence upon T/T_c is commonly linear.

The model compound has a very high, upper critical field near T_c, and is much superior in this respect to earlier lanthanum type (40 K) compounds and to Nb_3Sn. This gives ample field margin for application to magnet and power equipment. However, critical current density (J_c) is another matter. The measured J_c is reasonably high at 4 K but falls off steeply with increasing temperature and is unacceptably low (about 100 A/cm^2) at liquid nitrogen temperature; the desired goal for operation (fig.1b). The low temperature superconductors in current use are operated at or near the temperature of boiling liquid helium at atmospheric pressure (4.2 K). Their critical current densities are orders of magnitude higher than the bulk ceramics, but not so different from the values observed by measurement of single crystals.

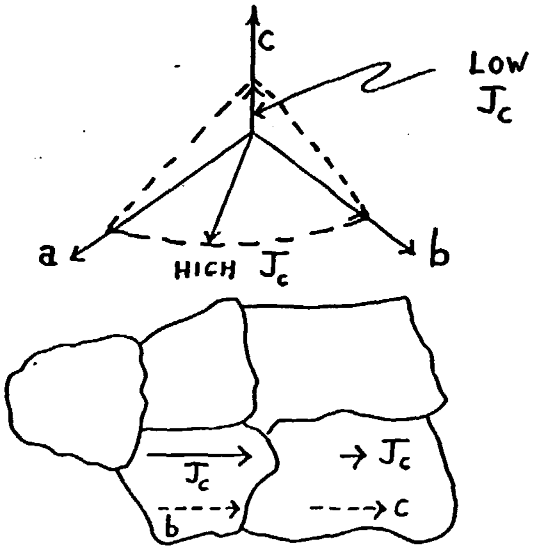

Fig. 2a
Anisotropy in 1-2-3 bulk specimens

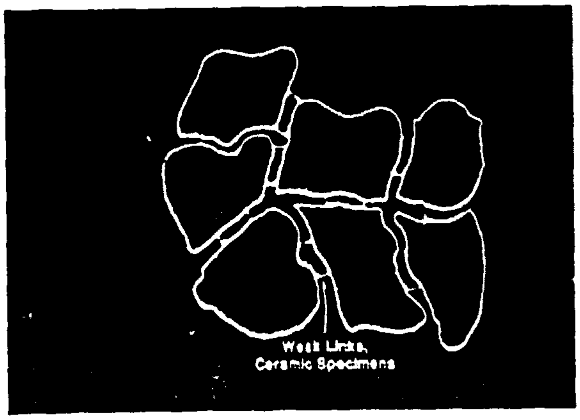

Fig. 2b
Weak links limit current as field is applied

The probable connection of the crystalline anisotropy to the low critical current density in bulk ceramic material is illustrated in Figure 2a, in which we show that grains oriented close to the worst (c-plane) direction of current flow will dominate the electrical behavior of the material. We consider this to be a basic materials problem which is a make or break factor for applications. A possible solution might be to develop a grain orientation process as has been done with transformer cores for years. More unlikely, would be the attempt to produce single crystal conductors.

A further problem is highlighted in Figure 2b, where superconducting weak links between grains are illustrated. These intergranular regions are superconducting in zero field but are driven normal in very low fields of the order of 100 gauss, producing a low average resistivity in what otherwise would be a perfect superconductor. These regions cannot be tolerated in most applications and it remains questionable if they can be eliminated by suitable processing.

BARRIERS TO APPLICATION

It can be seen from the preceding discussion that the new ceramic materials are not yet suited for applications requiring high magnetic fields and current densities in large conductors: much work lies ahead! Anisotropic effects have to be mitigated or overcome. The weak links reducing J_c in high magnetic fields have to be reduced or eliminated. Techniques to reduce deterioration in the materials in various ambient atmospheres have to be developed. Radiation sensitivity has to be improved for applications such as fusion magnets and possibly accelerator magnets. High quality electrical contacts are necessary to transfer current to the conductors at minimum heat input. Information on AC characteristics is needed.

Present day conductors are composites containing hundreds to thousands of fine superconducting filaments embedded in normal metal. This improves performance in varying magnetic fields, reduces hysteresis and magnetization effects, and enhances strain tolerance, flexibility and thermal characteristics. A typical example is the inner cabled conductor of the two layer Superconducting SuperCollider dipole windings, which contains 23 transposed, compacted strands of multifilamentary niobium titanium in a copper matrix. In many applications, it will be necessary to produce similar conductor types using the new ceramics. Practical conductor manufacturing techniques need to be developed and proven.

Operation at liquid nitrogen temperature offers the possibility of simpler and cheaper refrigeration systems. However, composite conductors capable of operating safely at these temperatures are needed. Advantages of higher temperature operation are the increased enthalpy of materials such as copper compared with 4.2 K operation. Disadvantages are the increased resistivity and decreased thermal conductivity at the higher temperature. However the specifications for reinforcing materials are less stringent at the higher temperature. Careful engineering is needed to develop optimum conductors for each application.

We next consider the progress that has been made in the last twenty five years or more in applying the low temperature superconductors.

COMMERCIAL APPLICATIONS:
and
PROSPECTS FOR BOTH HIGH & LOW TEMPERATURE SUPERCONDUCTORS

Magnetic Resonance

Magnetic Resonance Imaging (MRI), which began to reach the market in 1982 is the most important commercial application of superconductors to date. It is an offshoot of Nuclear Magnetic Resonance (NMR) which was first discovered in 1946 and developed into the most important tool for studying the structure and dynamics of molecules. The availability of superconducting magnets at reasonable prices, together with advances in computer techniques, has led to the expanded use of this technique in spectroscopy.

Most major manufacturers of NMR equipment now offer a wide range of systems of differing bore sizes and magnetic field intensities to meet a wide range of applications. Larger sizes were later used for whole body spin imaging of small animals and, with this success, were extended to human beings, thus necessitating increases in bore size. In industry, NMR equipment is used for fast, non-destructive studies of materials in all states of aggregation, without mechanical or electrical contact with the sample.

About 1300 MRI systems are in use world-wide for medical diagnostics. The medical community removed the "nuclear" description of the technique to make it more attractive to patients. The market distribution is estimated to be: USA - 60%; Europe - 20%; Japan - 15% and the rest of the world - 5%. By the year 1998 about 6000 systems may be needed world wide, if the present rate of increase is maintained. Most of these systems operate in the region of 0.5T but many installations operate at both higher and lower magnetic fields. At magnetic fields of 1.5T and above, the systems can be used for non-invasive spectroscopy (MRS) and used for in-vivo study and treatment of disease. Together, these two techniques are in the forefront of the ongoing revolution in medicine.

Potential Impact of the New Superconductors

System cost depends upon magnetic field intensity, increasing with increasing field because more ampere turns are needed at the higher fields and hence more superconductor is needed. In a 2T system, manufacturers magnet cost is about 45% of system cost of which 27% is the superconducting coil, and 18% is the cryogenic enclosure. Eliminating the cryostat completely would thus save about 18% and this would be the target saving at present if room temperature superconductors were available at a competitive price. Operation at liquid nitrogen temperatures would require a cheaper cryostat and the savings would be around 10%. Cryogen operating costs account for 3% of total operating costs where

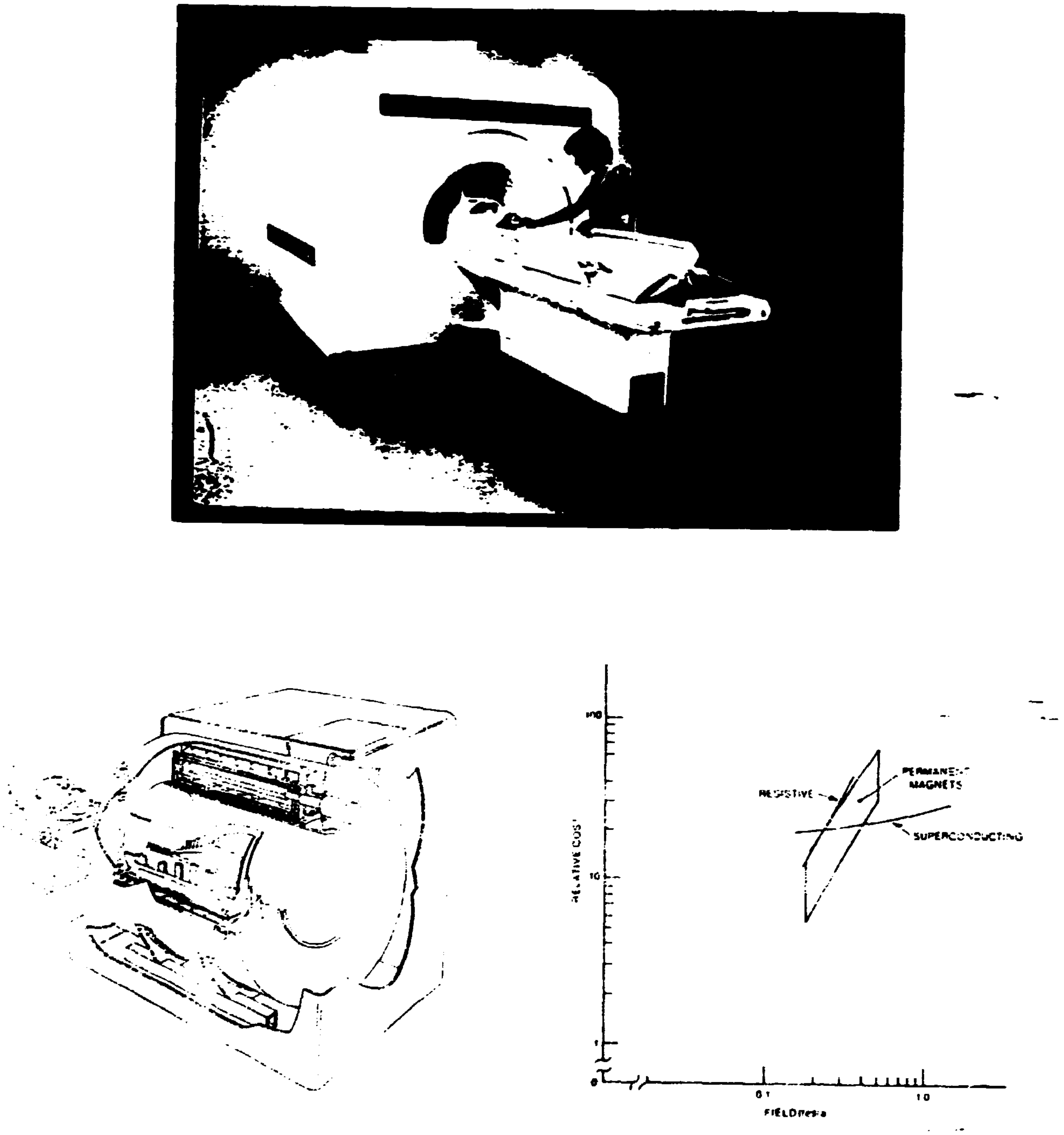

Figure 3. Magnetic Resonance Imaging (MR) is Revolutionizing Medical Diagnostics.a) An MRI Magnet System in a Clinical Setting. b) MRI Magnet Schematic showing the Coil, Support Structure and Cryogenic Enclosure.c) Cost Comparisons for Superconducting, Resistive and Permanent Magnet Systems.

helium liquifiers are not used and thus for nitrogen cooling maybe these costs would drop to 1% of total operating costs. It is estimated that halving magnet cost would reduce cost/scan by about 12%, so that elimination of the cryostat would be a 10% reduction and use of a liquid nitrogen system about half this. The use of nitrogen cooling could thus result in some saving in cost which may or may not be passed on to the patient and to some simplifying of cryostat design. We can expect cost reductions as manufacturing techniques improve. Thus the differential costs between low temperature and hypothetical high temperature systems may decrease with time.

Other Commercial Uses

Compared with the market for MRI systems, the other commercial uses are very small. Even MRS is principally in the clinical experimental stage at present, in spite of its promise. It will take time to develop the expertise to analyse its output on a routine basis and pass this expertise to the medical community at large.

Gyrotrons

Gyrotrons are devices for producing high power microwaves at millimeter wavelengths. A gyrotron is a microwave source that derives its power output from the interaction of a relativistic electron beam with the microwave field. The frequency is determined by the relativistic electron frequency of the electron rather than by the resonant cavity as in a klystron. A gyrotron operating at 120 GHz (2.5 mm) requires a field of 4.8T and this field is produced using superconducting magnets. The slope of the magnetic field at the cathode has to be controlled as well as producing the central field and one split pair coil system is used for each purpose, making four coils in all. Typical sizes are 50mm internal diameter and 18mm length for main coils.
These devices are being produced in many countries for use in high power millimeter rf systems such as radar or for plasma heating in fusion experiments

R&D Magnets

R&D magnets are of all types, from those used in the fusion test facilities of various countries to test large Tokamak and mirror coils, to the smaller versions used to generate very high or moderate fields. Superconducting magnets are to be found in all types of laboratory around the world as essential investigative tools. Until recently, the record was held by the Institute of Metals in Japan with the Tachikawa 18T system, which they hope to operate at 20T. This composite system has an inner bore of 30mm, an od of 630mm and length of 680mm. The three concentric coils use different winding materials, the outer uses niobium tin, the intermediate uses niobium titanium tin and the inner uses two different types of vanadium gallium conductor, surface diffusion and 'in situ' processed tapes.

More recently a 24 mm bore, cryogenically stabe 19.3T system was operated at KfK Karlsruhe. As with the Japanese, the aim is 20 T. The system consists of 5 nested coils operating in liquid helium at 1.8 K. An NbTi magnet generates a background field of 11T and insert magnets of Nb_3Sn multifilamentary wire which was first layer wound and then reacted to form the Nb_3Sn to develop the incremental field. The innermost coil was wound from a ternary conductor of $(NbTi)_3Sn$ and operated at a average current density of 96 A/mm^2 and a current density in the superconductor of 314 A/mm^2.

Magnetic Separators

Developmental magnetic separators have been operated for years but it has taken time to develop industrial interest in their possibilities. This now seems to be taking place and test units have been installed and operated in industrial settings in several countries. In addition to the advantages of very high fields and field gradients for many separation problems, even the more routine separations where conventional magnets would suffice, are being considered. The argument has to do with cost, rather than technical merit and very high field operation. In some ongoing clay processing plants it is contended that superconducting coils would save as much as $100,000/year in operating costs over their conventional counterparts

In all these commercial applications, the idea of nitrogen cooled (77 K) superconductors or room temperature superconductors is appealing but each application must be studied separately if, and when, the practical conductors become available. Until that time, low temperature technology will continue to be used and improved.

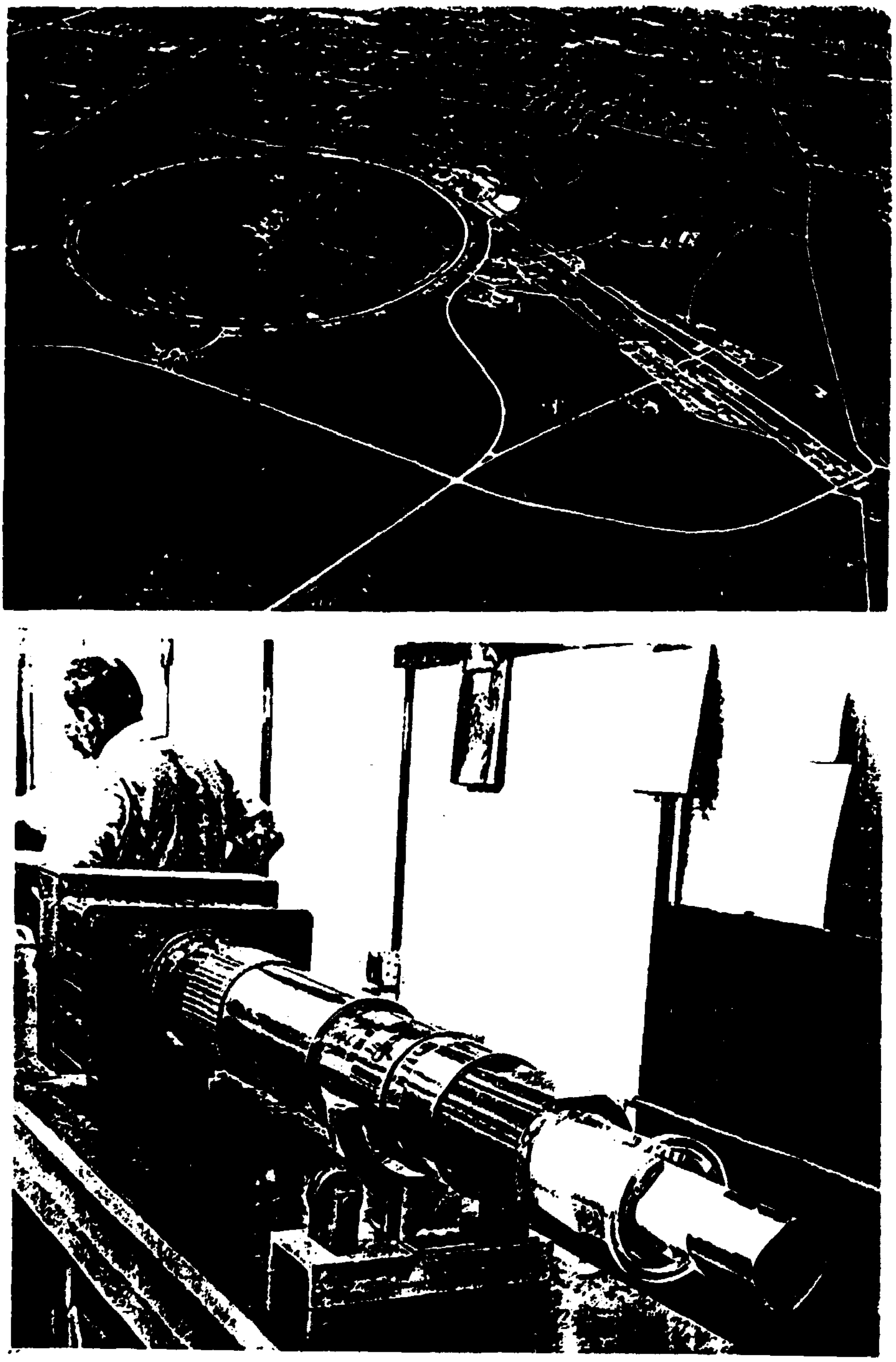

Figure 4 The world's first superconducting proton synchrotron and colliding accelerator: The Fermi National Accelerator Laboratory Tevatron. Above - the 6 km main ring accelerates protons to 900 GeV prior to collision with 900 GeV anti-protons. Below: A view of the superconducting 3.8T dipole magnet of the main ring

PHYSICS MACHINES

High energy physicists were quick to take advantage of the technical superiority of superconducting magnets over conventional water cooled copper electromagnets in large accelerator installations and to estimate the large cost savings involved in their use. The best example of this to date, is the Fermilab Tevatron in which contra-rotating beams of protons and anti-protons are accelerated to almost 1 TeV each before being interleaved so that their interactions may be studied as some of the particles in each beam collide with each other. The 6 km circumference main superconducting ring of the machine contains about one thousand bending and focussing magnets and an equal number of shim coils to adjust the magnetic field profile as needed for the main coils. First operated as a fixed target machine in 1983 and as a collider in 1986, the machine has demonstrated that superconducting magnet technology is reliable and economic. As a consequence, several other large machines are in design or construction at this time, all relying on superconducting magnet technology as an essential ingredient.

The largest of the big machines so far proposed, and possibly the last using this technology, is the Superconducting Super Collider whose 80 km circumference main ring will contain about ten thousand dipoles and quadrupoles and an equal number of trim coils. The 40mm bore, 17 meter long, 6.6T dipole magnets operate at a current of 6500 amperes and a temperature of 4.35K and have an equivalent magnetic length of 16.6m. The windings consist of two layers of multifilamentary, keystoned, transposed, niobium titanium cable containing 23 strands in the inner layer and 30 strands in the outer layer. Each strand contains about 6900 6micron diameter filaments. The copper to superconductor ratio for the inner layer is 1.3:1 and for the outer layer, is 1.8:1 although these ratios, filament numbers and diameters, and wire diameters may change as the design progresses. The 33mm internal diameter beam pipe is snugly cradled in the magnet assembly.

The cryogenic system for the SSC consists of 10 units for the collider ring and one for the injector, interconnected for redundancy. Each unit services a cryogenic sector of 8.06km and consists of a refrigeration plant, helium storage and four loops of cryostats. Each refrigerator is sized to operate at 1.5 times the design heat load. The heat loads for each arc cryogenic sector are 12g/s of liquid helium, 3160 watts at 4.15K, 4800 watts at 20K and 38800 watts at 84K. The total helium refrigeration load for the system is 378200watts at 4.15K and the nitrogen load is 106700 watts. The total cryogenic system power is 33.6MW. Approximately 2 million liters of liquid helium storage and 6 million standard cubic feet of helium gas storage at 16 atmospheres is needed, together with a 200 ton/day air separation plant and 380000 gallons of liquid nitrogen storage.

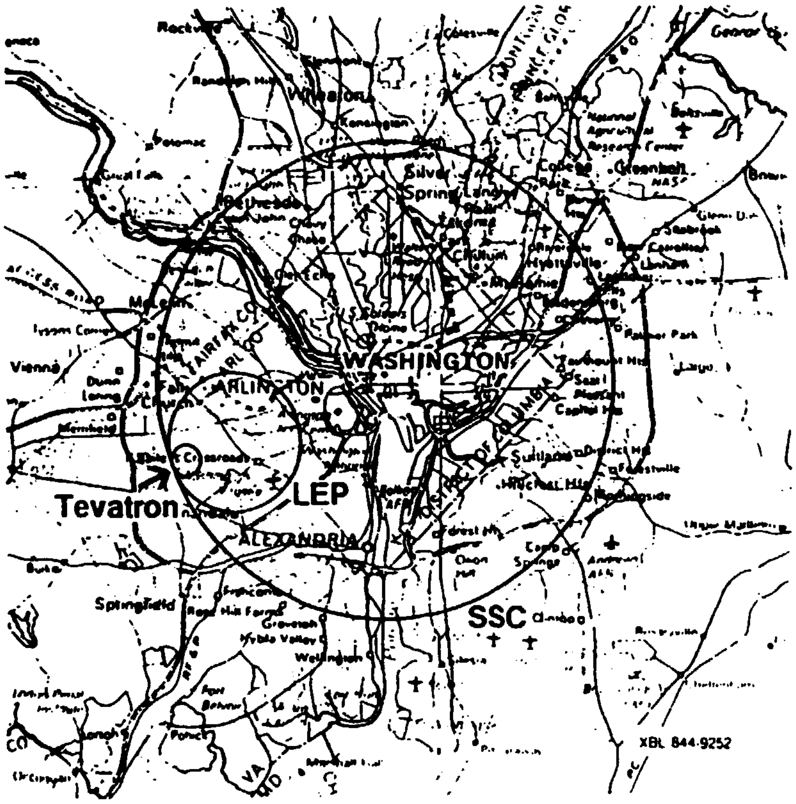

Figure 5. The circumference of the proposed SSC superimposed on a map of the Washington, D.C. Beltway to indicate its proposed size. Also shown are the outlines for LEP, the 16 km circumference Large Electron Proton Collider at CERN, Geneva and the Fermilab Tevatron. The Tevatron is the size of the High Energy Booster of the SSC which will inject 1 TeV protons in opposite directions into the two magnet rings in the main ring for acceleration to 20 TeV in opposite directions before they are induced to interact in the collision halls of the machine.

The machine has not yet had the approval of the US Congress but funding at about \$20M/yr has been allocated for the last four years for conceptual design and prototype magnet construction. The current conductor specification calls for a superconductor current density of 2750A/mm^2 at 5T measured at an effective conductor resistivity of 10^{-14} ohm-m with a strain tolerance of 0.5%. The peak operating field at the conductor is around 7T. This performance level has been reached after an intensive R&D program of conductor improvement over the past few years involving industry, Wisconsin University and the SSC team at the Lawrence Berkeley and Brookhaven National Laboratories.

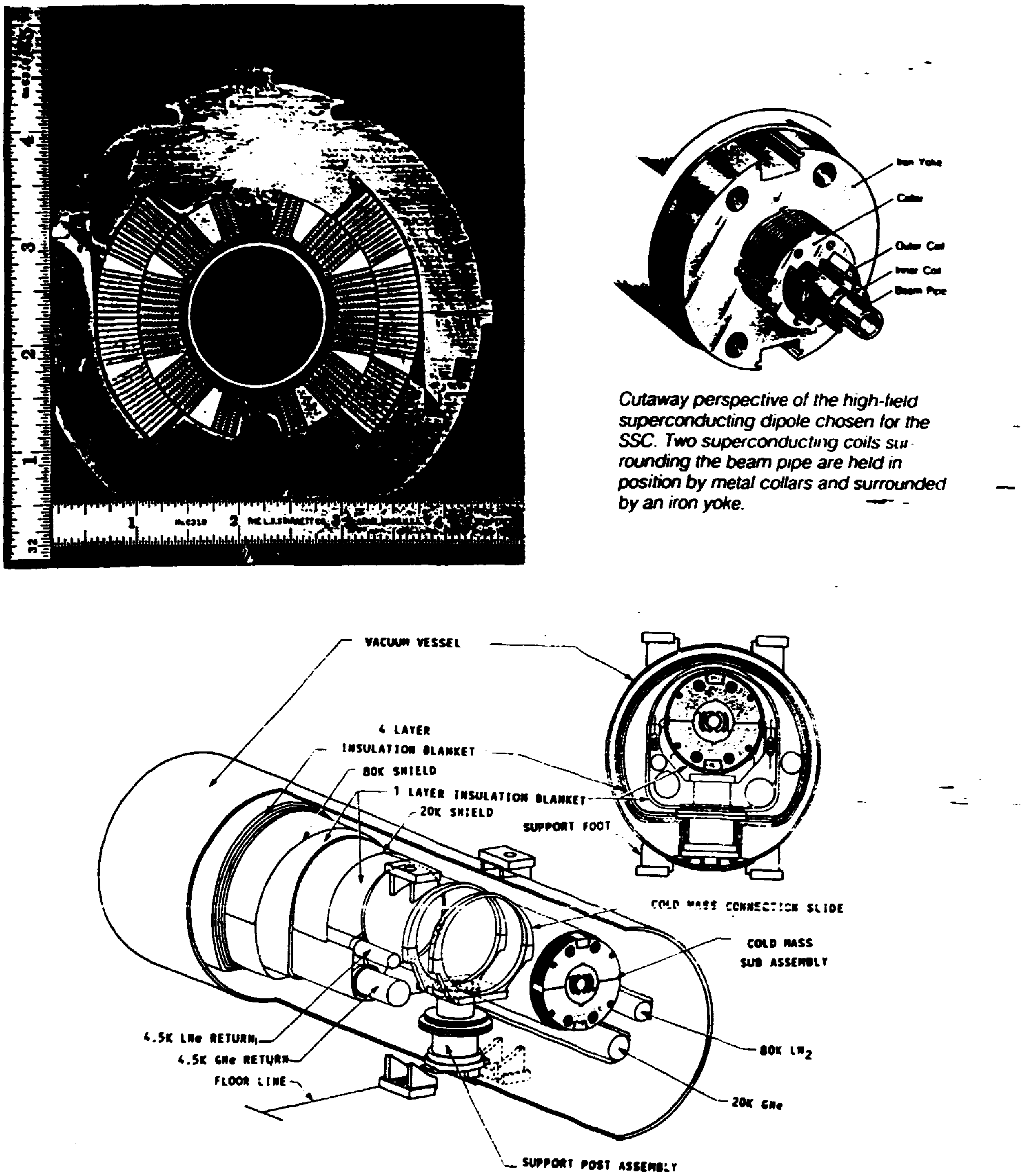

Cutaway perspective of the high-field superconducting dipole chosen for the SSC. Two superconducting coils surrounding the beam pipe are held in position by metal collars and surrounded by an iron yoke.

Figure 6 SSC Dipole Magnet Details: Clockwise from upper left. a) cross section of collared coil assembly showing superconducting cabled two layer windings and restraining collar; b) a cutaway perspective of the 6.6T magnet; c) schematics showing details of magnet and cryostat assembly.

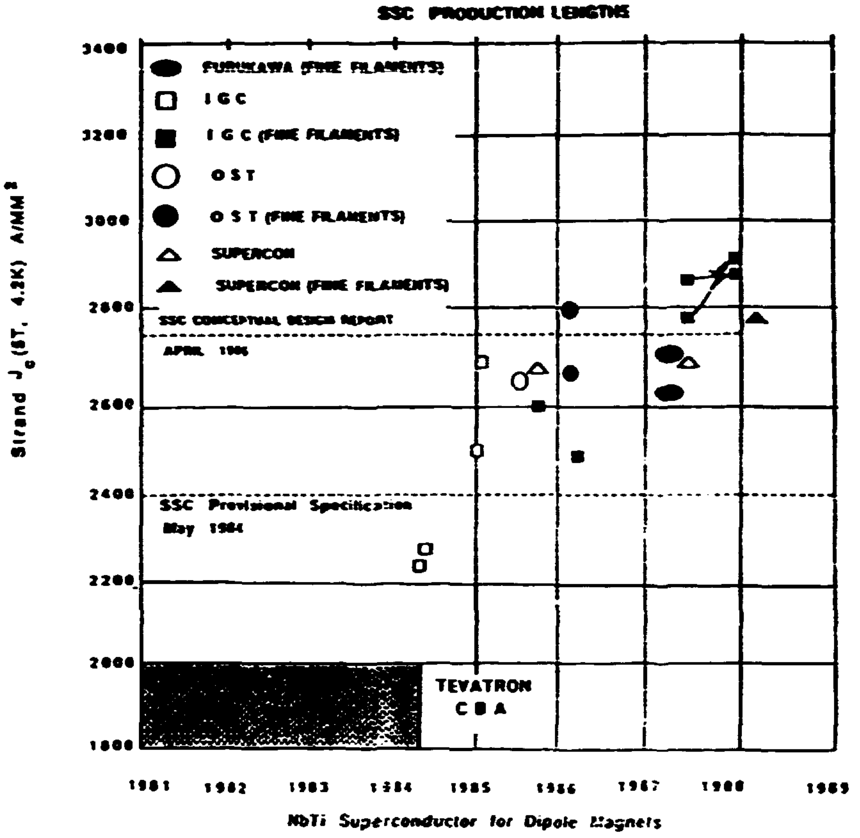

Figure 7 Characteristics of recent production lengths of NbTi mulifilamentary wire for the SSC, showing the change in SSC wire specification with time and the improvements in wire current carrying capacity over the last few years.

The machine, if approved, could be in operation by the mid 1990's and may be expected to be operational for as much as twenty years. Even if some primitive ceramic superconducting wires were produced now with promising current densities at the necessary fields and strain, it would take many years of development to give the degree of confidence and engineering sophistication to make them candidates for such a project, hence it is not likely that they will be used for the SSC. Even after twenty years of application with NbTi conductor an aggressive development program beginning in 1984 to improve conductor performance for the SSC has resulted in spectacular gains and it may be that even further increases may be possible. The idea was to reduce the amount of

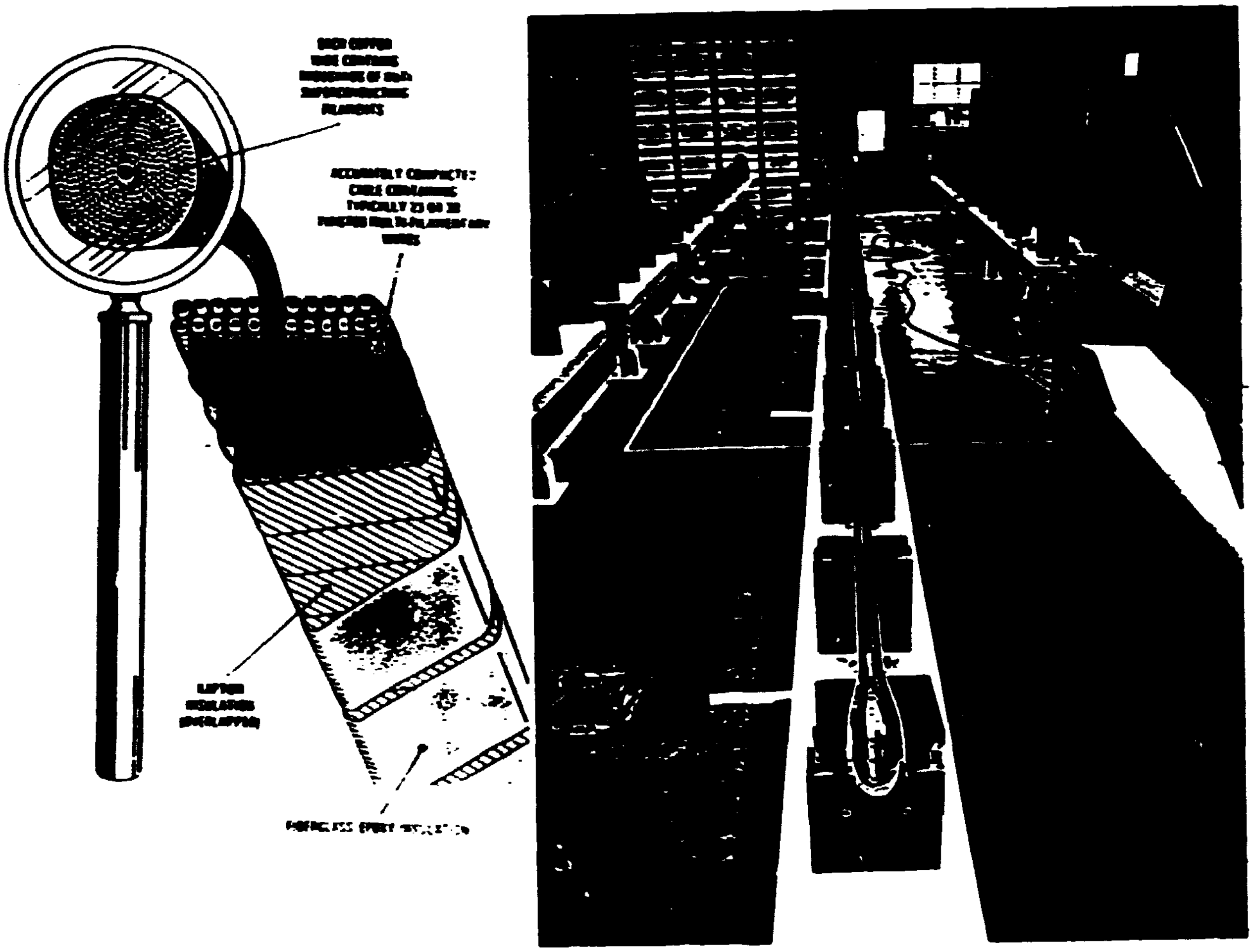

Figure 8. a). SSC magnet multifilamentary wire and transposed, keystoned cable. The Kapton allows slippage with low friction as the coils are energized, hence reducing thermal transients in the conductor and enhancing magnet performance.

b). A 16.6m long SSC inner coil on an assembly work station in Brookhaven Laboratory. The prototype magnets are assembled in Brookhaven and transported the 1600 km by road to Fermilab for assembly in the cryostats and testing.

material needed for the magnets and hence, the cost for the project. All these factors must be taken into account in developing competing ceramic conductors. Again, it is certain that the use of liquid nitrogen cooling would make it necessary to develop a satisfactory vacuum technology to replace the helium cryopumping used to maintain the ultra high vacuum necessary for such a machine. Assuming all problems were satisfactorily solved, it is not clear that cost competitive, technologically equal, ceramic superconductors would result in a cost competitive accelerator complex.

The magnet and materials details for the SSC have been treated at length because they represent some of the most advanced technology to date. Many of the ideas in magnet construction and advances in materials are already being utilized in other devices and systems. The information is also of value to those hoping to develop conductors and devices incorporating the new ceramic materials.

The current crop of large high energy colliders is likely to be the last using this technology. The machines will come on line in the later 1990's and they can probably be expected to operate for as much as twenty years. Linear machines offer promise for future advances in the highest energy accelerators. Experimentalists and machine designers look forward to higher energy machines searching for ever more effects, but many theorists assert that the next interesting energy level is the Grand Unification Energy at which the electromagnetic, electroweak and strong forces coalesce into one force. This is around 10^{12}TeV - a far cry from the 40 TeV centre-of-mass collisions of the SSC. At still higher energies, in the Planck domain there is the further possibility of the unification of this force with gravity.

Smaller machines

Smaller superconducting accelerators for medical and industrial use are also either in operation or under construction, although in many instances, designers are still favoring conventional electromagnets in some recent designs. Compact superconducting synchrotrons for X-ray light sources are in construction in Japan and Europe and under development in the United States: this is a comparatively recent field with widespread applications in science and industry. In particular, a highly competitive area is that using intense monochromatic X-ray beams for lithography in computer chip manufacture. It is anticipated that almost two hundred machines for this purpose alone may be needed in industrial settings by the mid 1990's.

NUCLEAR COLLIDERS

RHIC - THE RELATIVISTIC HEAVY ION COLLIDER

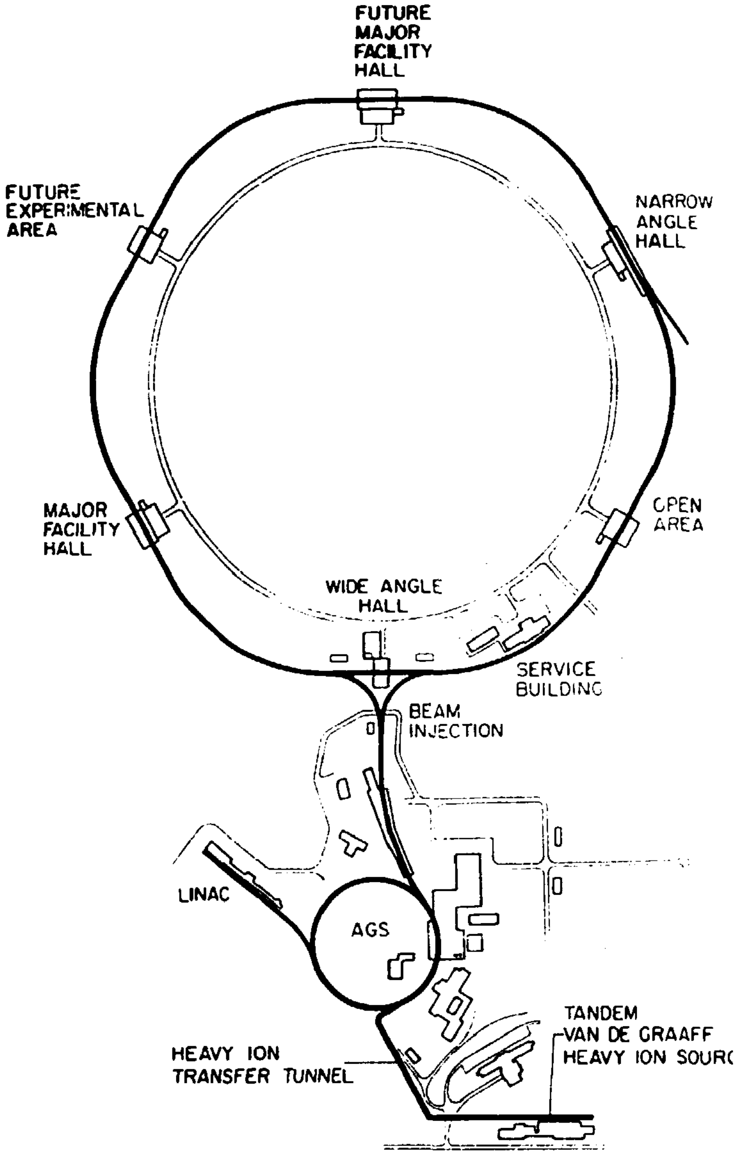

Figure 9. Layout of the BNL/RHIC facility: a complex of accelerators to accelerate and collide beams of heavy ions over the range 7-100 GeV/nucleon for gold and 28.5-250 GeV for protons. The complex will produce and investigate a new form of matter, the quark-gluon plasma, thought to have existed during the first instants of the expansion of the universe.

TABLE 3. General Parameters for the Relativistic Heavy Ion Collider (RHIC)

Number of magnet rings	2
Circumference	3833.87 m
Energy range (each beam)	
Gold	7-100 Gev/nucleon
Protons	28.5-250 Gev
Average luminosity	
Au-Au, 100 Gev/nucleon, 10 hrs	4.4 x 10^{26} $cm^{-2}sec^{-1}$
Number of bunches/ring	57
Number of gold ions/bunch	1.1 x 10^9
Number of crossing points	6
Interaction diamond length	± 27 cm RMS
Free space at crossing point	± 9 m
Filling time	1 min
Acceleration time	1 min

RHIC is being constructed in Brookhaven Laboratory, USA for nuclear physics studies in the high energy boundary area between past nuclear studies and particle physics. The first such experiments with high energy nuclear beams have already been carried out at CERN and Brookhaven using fixed targets using light ions (32 AMU). These experiments have provided the first glimpse of what is expected to be an entirely new regime of physical phemomena: the formation of a new state of matter, the quark-gluon plasma. RHIC is intended to explore this regime at much higher energies and with heavier ions.

Fixed target experiments up to 28(z/A) GeV/amu began at the AGS (the Brookhaven 33 GeV Alternating Gradient Synchrotron) in 1986. A Booster Synchrotron is under construction for completion in 1990 to increase the proton intensity for the high energy physics program and extend the heavy ion mass range to gold nuclei. Given permission to proceed with the final stage of construction, RHIC collider experiments could begin in 1993 with a beam energy of 250 GeV(z/A)/amu per beam in the collider mode.

Ions are produced in the Tandem Van de Graf (see Fig. 9), transported to the Booster Synchrotron pre-injector and then injected into the AGS, which serves as the injector for the main rings of collider magnets. The RHIC system will provide c-m collision energies for gold beams ranging from 1.5+1.5 GeV/nucleon to 100+100 GeV/nucleon (see Table 3). Cryogenic cooling is provided by the refrigerator system originally procured and installed for the colliding beam accelerator (CBA) project which was cancelled some years ago. The system has been modified for use with RHIC. The final collider ring stage for RHIC would be the CBA tunnel which provides for six crossing regions in the main ring for collision experiments. Four experimental halls are already in place.

The principal dipole and superconducting cable parameters are given in Tables 4 and 5 respectively and the cable structure is portrayed in the schematic of figure 10. The single layer, cos theta dipole coils have an i.d. of 8 cm and a yoke length of 9.7 meters and will operate at 3.5T at a design current of 4.56kA. The magnet uses cable of the same type as that developed for the outer layer of the SSC coil. This is a flat, keystoned 30 strand cable of the Rutherford type. The bare cable width is 9.73mm and its average thickness is 1.17mm with a keystone angle of 1.2 degrees. Each wire is 0.65mm in diameter, containing high homogeneity NbTi filaments 5-8 microns in diameter. The copper to superconductor ratio is specified to be 2.25:1 with a superconductor current density at 5T and 4.2K of over 2600 A/mm^2. Pre-stress is applied to the coil directly through the iron yoke through a 5mm thick molded glass-phenolic insulator-spacer surrounding the coil and keyed into the yoke laminations rather than with a non-magnetic collar as in the SSC. A stainless steel shell which is split and welded at the mid-plane takes over compression of the yoke when it is at cryogenic temperature.

The cryostat housing the cold mass consists of a carbon steel vacuum vessel (610mm o.d.), an aluminum heat shield maintained at 55K, blankets of multilayer, aluminumized Mylar, cryogenic headers and the magnet support system. The 24.8kW helium refrigerator for RHIC supplies helium at 2.59K which is returned at 4.19K. A supply pressure of 5,35 atmospheres produces an input helium flow rate of 4154 g/sec at a density of 0.154 g/cm^3 and enthalpy of 7.32 J/g.

Four coils were successfully tested to 4.6T in early 1987 with virtually no training. The arrangement of the cold mass in the cryostat is similar to that used for the SSC design.

Dipole Parameters

B_C, minimum operation	0.24 T
B_0, 100 GeV/amu	3.45 T
Current, 100 GeV/amu	4.56 kA
Inductance	43 mH
Stored energy	490 kJ
Length, effective	9.46 m
Sagitta	47.2 mm
Coil, number of turns	33
Coil, inner radius	40 mm
Iron, outer radius	133.3 mm

Superconducting Cable Parameters

Cu:SC ratio	2.25:1
Wire diameter	0.648 mm
Critical current density	
@5 T, 4.2 K	>2400 A/mm^2
Number of wires in cable	30
Width of cable	9.73 mm
Mid-thickness of cable (bare)	1.17 mm
Keystone angle	1.2°
Filament diameter	5μm

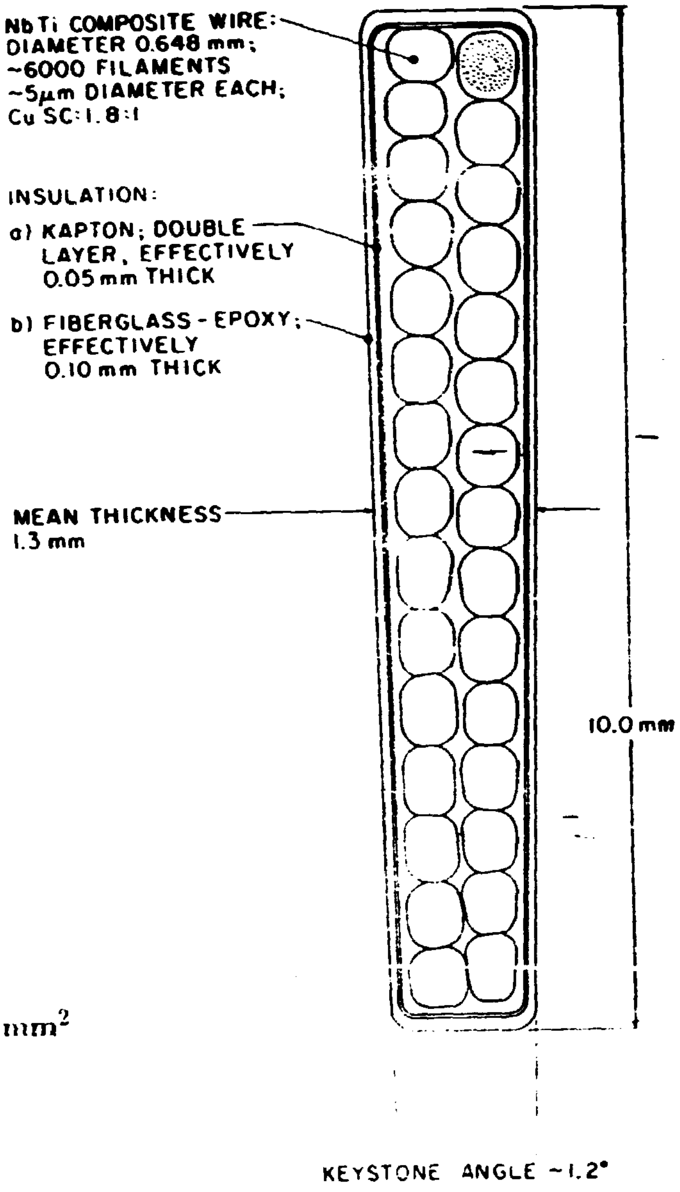

Table 4. Principal Wire and Cable Characteristics for RHIC.

Figure 10. RHIC keystoned cable schematic showing construction detais.

Radio Frequency Cavities

A further developing field of intense importance is that of superconducting radio frequency (rf) cavities where accelerating voltages approaching 10 MeV/meter have been achieved in recent prototypes. In contrast to copper cavities which are usually pulsed to conserve power, these cavities can operate continuously at very low power consumption levels. A superconducting heavy ion linac incorporating superconducting cavities has been in routine operation in Argonne National Laboratory for two years.

Prior to the operation of RHIC, the first priority in the U.S. nuclear physics program is the construction of a 100% duty factor, electron facility to investigate the behavior of the nucleus at higher energies. This can be accomplished by using beams of electrons to penetrate the nucleus to the very short distances where the nucleus can best be described in terms of its fundamental quark and gluon constituents. This research frontier can be reached by accelerators with higher duty factors and higher energies than existing machines. 4 GeV electrons will penetrate this region and be sufficient for studying the production of baryon resonances (excited states of nucleons), heavy mesons and "strange" particles in the nuclear medium. A superconducting electron accelerator known as CEBAF, for Continuous Electron Beam Facility is under construction in Newport News, Virginia, USA to accomplish this goal.

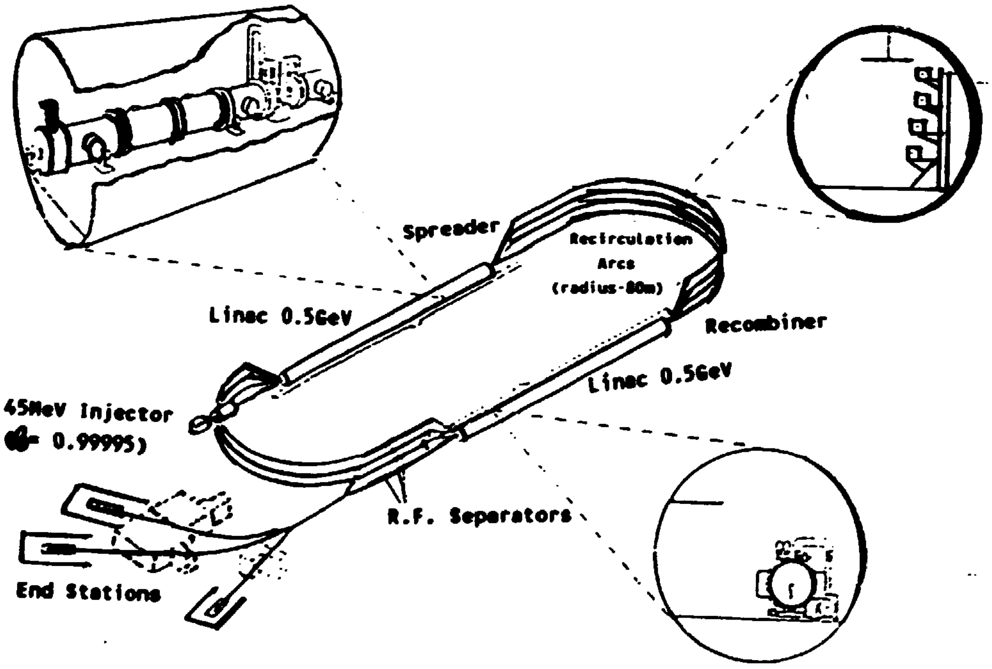

Figure 11. The CEBAF 4 GeV recirulating linac concept in construction at Newport News, USA for nuclear physics research.

CEBAF will provide three separate simultaneous 0.5 to 4 GeV, 200 microamp, continuous electron beams for experiments. The machine has a racetrack configuration with two anti-parallel, 500 MeV, superconducting linac segments connected by beam lines to allow four passes of recirculation. The accelerating structure consists of 1500 MHz, 5-cell superconducting niobium cavities developed at Cornell University. A liquid helium cryogenic system cools the cavities to an operating temperature of 2K. Beam extraction after any three of four passes allows simultaneous delivery of up to three beams of independenty variable currents and different, but correlated energies, to the three experimental areas. Physics operation is scheduled to begin in 1993. Project cost is estimated to be $225 million.

The accelerating structure is arranged in two separate 235m long linac segments comprising the straight sections of the racetrack configuration. Each segment is made up of 25 cryomodules containing 8 cavities per module for a total of 200 cavities per linac segment. Each cavity has an electric length of 0.5m with a design gradient of 5 MeV/m and operates at a temperature of 2K (see Fig. 11). The cavities are five-cell, 1497 MHz elliptical cavities of Cornell design: a shape which yields low peak surface electric fields, a good chemical rinsing geometry and good mechanical rigidity (see Fig 12). A prototype cavity was successfully tested to 6.5 MeV/m and a Q_{res} of $5x10^9$. The linac and rf cavity parameters are listed in Table 5.

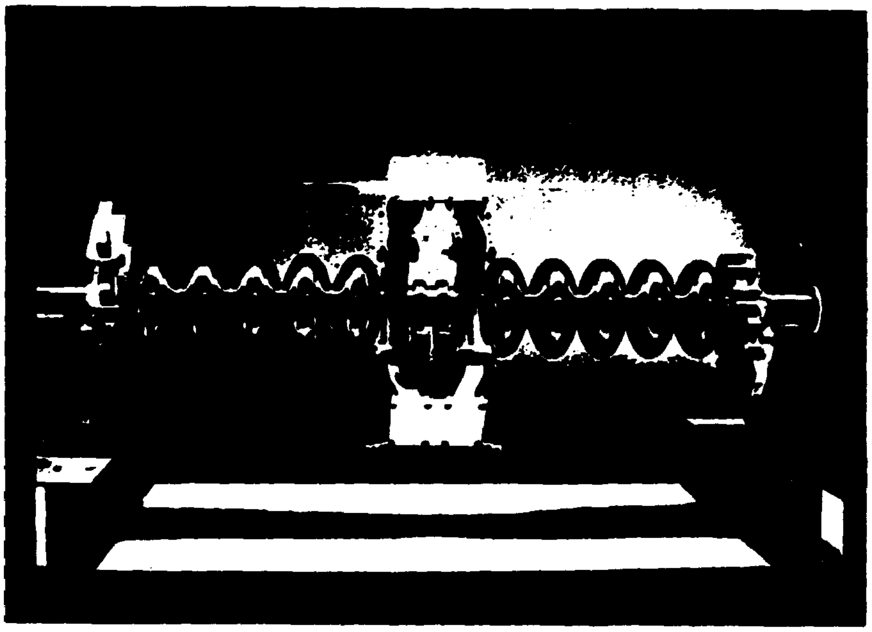

Figure 12. CORNELL/CEBAF 1497 MHz, twin 5 cell, 5 MeV/m rf cavity module.

Table 5: PRINCIPAL CEBAF LINAC AND CAVITY PARAMETERS

LINAC

No. of Passes	4
No. of linac segments	2
Segment length	235m
Max. energy gain/pass	1 GeV
Recirculation time/pass	4.2 microsec
Half cell length	9.4m
No. of cavities/half cell	8
No. of half cells/segment	25

CAVITY

Frequency	1497 MHz
Electric length	0.5m
Design gradient	5 MeV/m

The cryogenic system consists of a 5 kW central helium refrigerator and a transfer line to supply 2.2K, 2.8 atm. helium to the cavity cryostats, 45K helium at 4 atm. to the radiation shields and 4.5K helium at 2.8 atm. to the superconducting magnetic spectrometers in the experimental halls. Total rf load at 2K is 2510W and total 2K heat load is 3310W. The system capacity at 2K is 4800W and the heat load at 45K is 8000W.

Upgrades to superconducting rf cavities are also planned for KEK (TRISTAN), DESY (HERA), and CERN (LEP). Similar cavities are also planned for nuclear physics and free electron laser facilities world wide.

The new ceramic superconductors may have the necessary properties to make them acceptable for the next generation of these machines. Before a judgement can be made, we need to know more about the AC losses in these materials at the frequencies involved. Present cavities use lead or niobium, the latter being superior. A promising candidate is niobium tin which has a much higher upper critical field; however it has yet even to find favor for developmental cavity investigations. The upper critical fields of the new ceramics are even higher and therefore show even more promise from this point of view. However, it remains to be seen what can be accomplished in this area and when. The operating fields in the cavities are low and the supercurrents flow in thin surface layers so the situation favors present day materials where the need for magnet type high field conductors is not present.

The material properties crucial to good performance in rf cavities are rf critical field and minimum achievable surface resistance. High field cavities for application in physics collider machines need to operate at the lowest possible fraction of the transition temperature to achieve lowest loss: hence the benefits of increased transition temperature of the base material are more significant for cavities than for magnets. Cavity accelerating fields are ultimately limited by surface conductor fields alone so the potential benefits of higher field operation offered by the application of the new ceramic superconductors could be spectacular.

The maximum possible accelerating field is, in principle, limited to the 'superheating critical field' which is related to and not very different from, the thermodyamic critical field. Thus niobium has a thermodynamic critical field of 2000 Oersted and has been used to achieve the highest accelerating fields obtained with superconducting rf cavities, about 25 MV/m. The new materials may have thermodynamic critical fields of 10,000 Oe or more, which would increase the accelerating fields by a factor of 5. This would make linear colliders based on such materials leading competitors for collider technology beyond the Superconducting SuperCollider. Significant R&D would be needed to examine the preceding possibility and if the potential is verified, many years of R&D would be needed to exploit it. Superior potential may not be enough! Niobium tin has a higher thermodynamic critical field than niobium, but in spite of being available for over 25 years, it has not so far found use in rf cavities.

In a large superconducting cavity array, the cryogenics represent a much larger fraction of capital and operating costs than in a magnet dominated machine such as a collider. No thorough cost estimates for a state-of-the-art collider based on superconducting rf cavities have yet been made, but it may be that savings of from 5 to 15% of total facility cost may be possible, depending on the operating electric field gradient, at the higher operating temperature.

ELECTRIC UTILITIES

The generation, distribution and use of electric power in a country is an expensive and gigantic undertaking involving the total society. Interruptions in supply are viewed seriously. Superconductors can be used for generation, transmission, storage, transformers, current limiting devices and for potential new energy conversion technologies. All these possibilities have been pursued during the last twenty five years. Some examples are given below for each category.

Studies and development projects on all types of superconducting electric utility equipment have been carried out since the first announcement of the high field, high current superconductors in 1961. In the early years, a limitation was the fact that AC loss in the superconductors was too high for most AC applications. Thus machines with DC rotors were first considered. AC transmission was pioneered by Brookhaven National Laboratory (Forsyth et al.)

Techological advances in the late 1960's included the manufacture of multifilamentary conductors and their application to pulsed magnets. Fast ramp times were demanded for high energy physics devices and energy discharge and storage systems in Controlled Thermonuclear Projects. Studies in the 1970's indicated that very fine superconducting filaments in the matrix, suitably decoupled, may be satisfactory for AC use since the AC losses would be reduced conssiderably. Under the impetus of the accelerator programs, the manufacturing technology continued to improve.

Beginning around 1983 ultra-fine filaments with the desirable diameters (< 1 micrometer) decoupled from each other through the use of cupro-nickel coatings began to be manufactured (Sabrie et al, Alsthom Atlantique). These conductors combine low AC loss, high overall critical current densities and high values of conductor resistivity when the superconductor is driven into the normally conducting state. These properties, if optimally utilized offer the potential for radical improvements in AC equipment design and performance.

TRANSMISSION LINES

Overhead transmission lines are the principal means of moving bulk electrical power from the power plant to the distribution centers because of convenience and cost. In some urban areas this is not possible and the higher priced underground transmission systems are mandated. Usually these underground runs are no more than 25 miles in length at most. At the highest conceivable power levels, superconductors have something to offer and the possibility has been investigated in the world's industrial countries for decades.

In 1973 there were 14 different power cryorestive and superconducting power transmission projects in the United States alone and similar projects in the other industrialized countries. Apart from design studies, all these were abandoned in a few years with the exception of a DOE study for an AC line at Brookhaven National Laboratory which continued through the R&D and test site construction phase in the years 1972-1982 when demonstration tests began and continued through the years 1982-1986 when the project was abandoned after 8 successful runs, the longest of which was 27 days, after it was agreed that technical feasibility had been established.

The 100m long line had a 3 phase rating of 1000MVA, 138kV and an emergency rating of 1500 MVA for 1 hr. It was kept cold for a total time of 2752 hrs during tests and operated at rated voltage or current for 441 hrs., operating up to 330 MVA equivalent, the voltage and current being applied simultaneously but out of phase because no load was available for these high powers. The emergency rating and overvoltage tests were also satisfactory. However, there was no interest in proceeding to the next phase of utility demonstration in the US cable test facility.

Figure 13. The Brookhaven Laboratory 1000 MVA, 138 kV, 100m long Superconducting Transmission Line and Test Site.

In a study for a 60 mile AC transmission line across eastern Pennsylvania in 1976, 16 different tranmission technologies were compared and the superconducting line was among the leading three contenders, but more expensive than an overhead system.

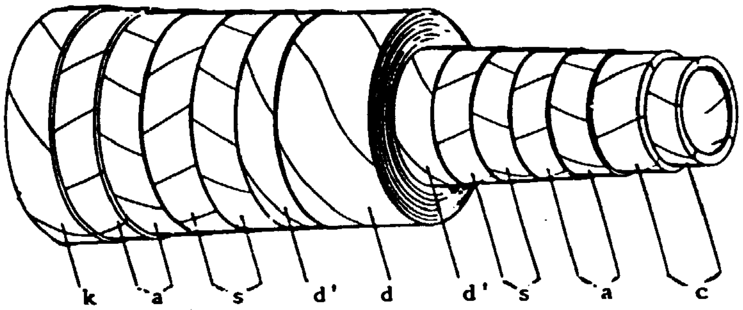

Schematic of cable construction. c, flexible bronze core; a, aluminum stabilizer layers; s, superconductor layers; d, plastic tape insulation; d', dielectric screen k, compression layer

Figure 14. Construction details of the 4100 A flexible conductor used in the BNL superconducting AC transmission line.

Because this line used niobium tin tape operating at 7K for the conductor, and the magnetic fields are low, there is the possibility of developing some type of ceramic type tape conductor for this application if the AC losses can be established as satisfactory. Again the cryogenics are a very small fraction of system cost, other factors being of greater consideration, so the potential saving, if any, would be small.

Energy Storage (SMES)

SMES magnets for utility use would be massive. They must be compared with other installations for electrical energy storage, such as pumped hydro storage from reservoirs, which are land intensive and environmentally insulting, or the use of additional generating capacity as stand by equipment. Base load 1000 MW plants cost as much as $6 billion at present in the U.S.

Superconducting Magnetic Energy Storage Studies have been carried out for over two decades and were first considered in Japan in 1967 because of the high cost of land and the need to use large areas for hydro storage. The chief US proponent has been Prof. Boom of the U. of Wisconsin who has also collaborated in the Japanese studies. The original idea was to compete with other forms of storage such as reservoirs and hydropumping and various other schemes. Clean, relatively compact, efficient storage coils which can be installed underground and which can deliver the stored power to the grid are attractive because they reduce the need for overcapacity in installed base unit power.

The optimum size for such a storage system is around 1 GWhr, based on the idea that about 22 metropolitan regions in the US might have average loads of around 2 GW varying from 1.5 to 2.5 GW through a 24 hr period and that this load could be met with 2 GW of base load plants and 6 GW of storage. While the magnet technology is established, system studies need to be carried out on a relatively large scale. Full size units would cost as much as a power plant and would be very large.

Most recently, due to the political impact of the HTSC publicity and the perceived need for new storage technologies in connection with Star Wars ideas, a design study has been commissioned from two US teams for a 10-30 MWhr system to be installed in the Madison Electric Company System. It is hoped that the study can be completed in two years and that it can be followed by a four year construction period, thus anticipating trial operation around 1993-1995 followed by some years of reliability and performance studies. It is too early in the project for the design details to be fixed.

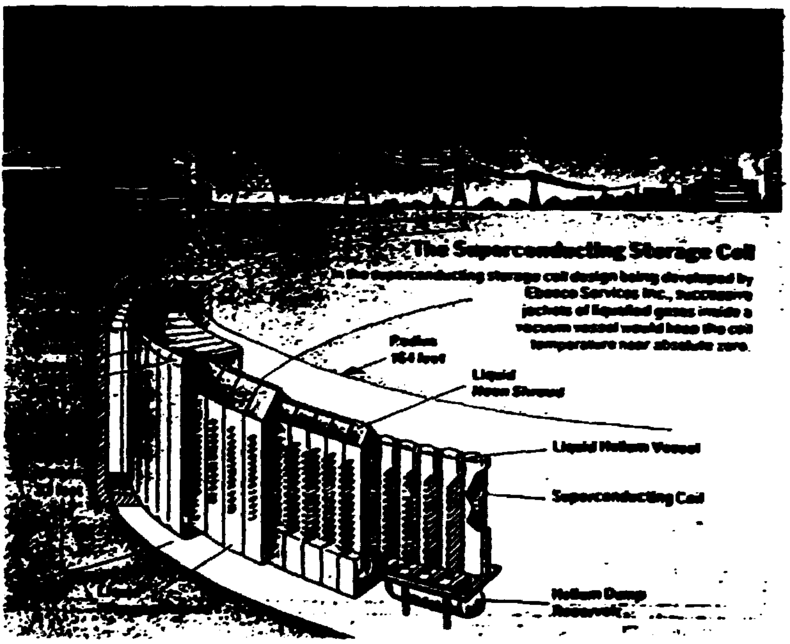

Figure 15. The Wisconsin SMES 10-30 MWhr Storage Study Concept

One of the study concepts envisages a 500 turn, solenoidal magnet, buried in the ground, and supported at its circumference by bedrock. The 50 kA aluminum stabilized conductor would operate at a superconductor current density of $600A/mm_2$ at 5T. The 10m high coil stack would be cooled by liquid helium and use a shrouded liquid neon cooled (27K) intermediate heat shield surrounded by a nitrogen cooled shield. The support structure would transmit the coil loads through the various heat intercepts direct to bedrock at the strata temperature. Energy from the utility system would be converted from AC to DC current by means of a Graetz Bridge system. In spite of its apparent large size, the amount of NbTi superconductor needed for this system is only around 10 tonnes, ie. about 1% of that needed by the SSC.

In considering the possible benefits of high temperature superconductors, we consider the helium related costs of SMES coils. These include helium inventory, helium dump system and thermal shields. Assuming a 1 GWhr unit, the helium related cost would be around 18% of the total. Very small units in the 10 MWhr range would have helium related costs around 50%. Nitrogen cooled superconductors would replace the helium related costs at cost savings approaching the preceding figures. Thus small SMES systems could become feasible at 77K: the question is whether or not these very small units would be of interest to the electric utility companies.

ROTATING MACHINERY

Successful motors and generators have been built for various purposes over the years. Between 1965 and 1986, eighteen superconducting generator models were built and tested in the industrial countries with some success to give evidence of feasibility and to develop basic technology. These included the Federal Republic of Germany, USA, USSR, China, France, Czechoslovakia and Austria. In 1980 Alsthom logged over 5000 hours of testing with a 1m diameter superconducting rotor. 20 MVA machines were tested in Leningrad (1981), and GE USA (1982). A 30 MVA machine was tested by Fuji/Mitsubishi, a 50 MVA machine by Hitachi in 1983 and a 10 MVA machine in MIT in 1985.

Large model rotor projects in Switzerland and Italy were started then discontinued and an EPRI/Westinghouse 300 MVA machine construction project was discontinued when EPRI withdrew the funding. Many large projects have now been discontinued, but some are continuing in the Federal Republic of Germany and the USSR. Siemens, through KFU, continues its development of a superconducting generator and pre-testing of a 300 MVA SC test rotor was scheduled to begin in 1988 with the hope of using this experience to construct an 850MVA SC generator suitable for power plant operation in 1995. Also, Japan has recently announced that a project to develop a large machine to be operational in the mid 1990's will soon begin. In collaboration with Electrosilia, in Leningrad, USSR the USSR Scientific Institute for Electrical Machines will (hopefully !) begin testing a 300 MVA machine this year.

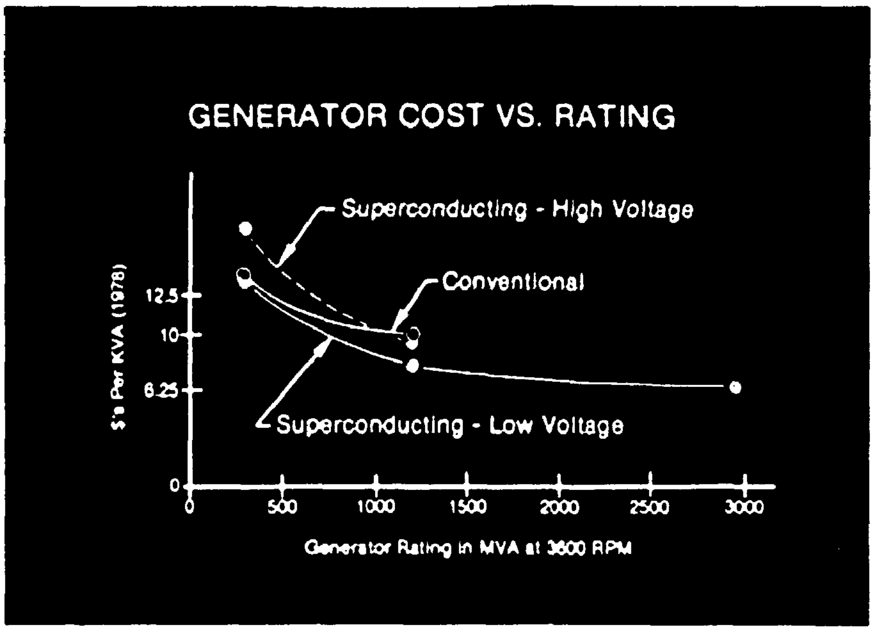

Figure 16 Comparison of estimated costs versus rating for superconducting high voltage, low voltage and conventional generators. Above 1000 MVA the superconducting machines have the advantage but when are they likely to be needed? Can the new ceramic superconductors lower this margin, and if so, when?

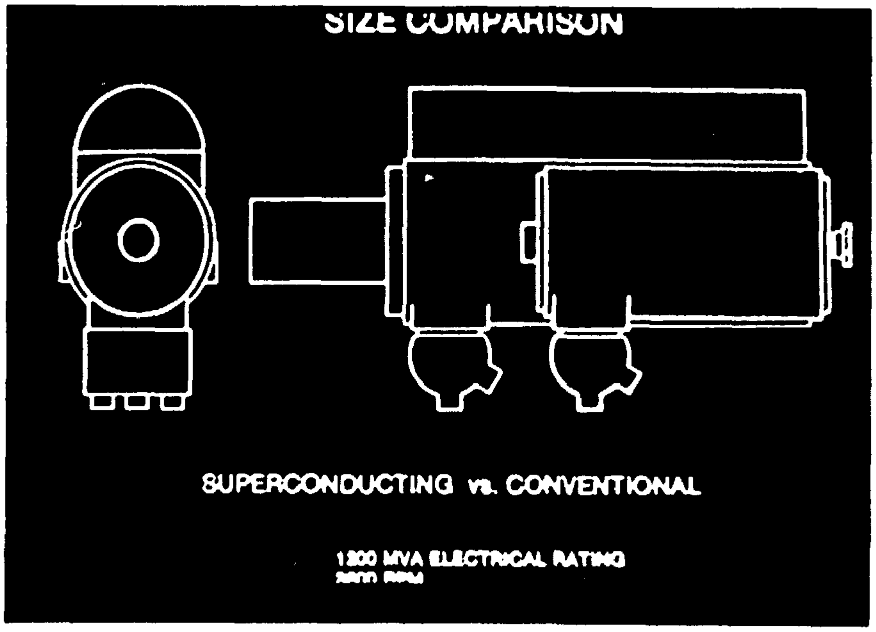

Figure 17 Superconducting machines offer advantages in size and weight over conventional machines at the high power ratings. What can we expect from the new ceramic superconductors?

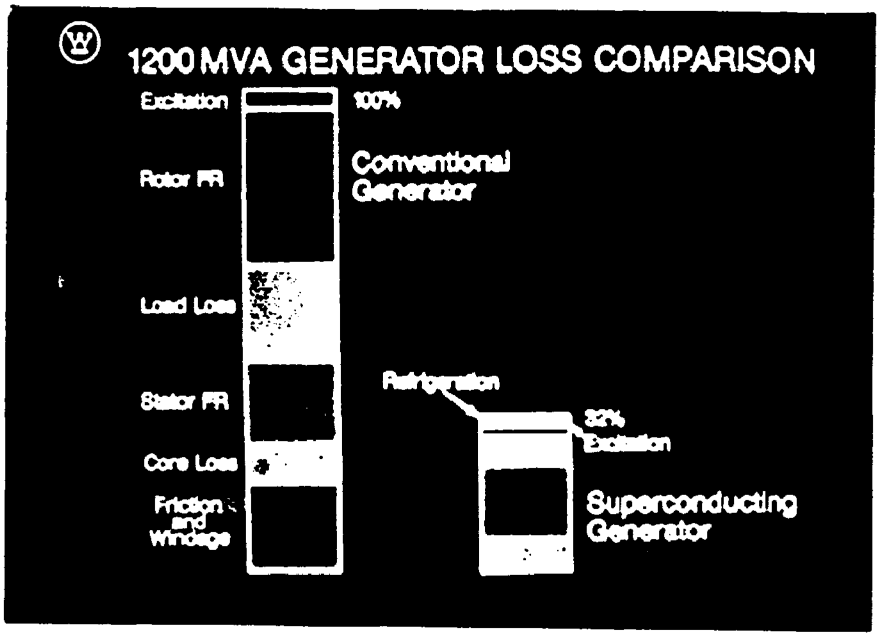

Figure 18 Superconducting 1200 MVA generators are estimated to be more efficient than conventional machines. It can be seen that helium refrigeration is a small component in the comparison.

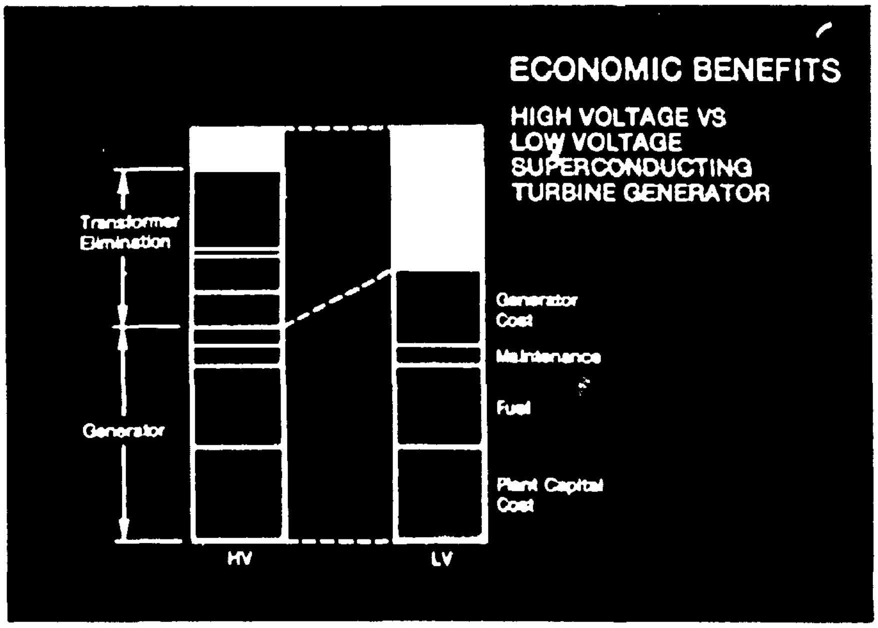

Figure 19 The estimated advantage of a high voltage electric power station superconducting generator is that the transformer is eliminated, thus reducing overall cost.

SC generators offer outstanding technical and economic advantages over conventional machines and the potential for future improvements in SC technology is great. Prototypes of high rating must be built and tested before a mature design and guaranteed reliability can be achieved: these requisites are essential before a machine can be incorporated into the power system. The development costs for such a program far exceed anything committed to date. Gains in efficiency and size over these machines if high temperature superconductors are used are likely to be marginal, but there may be some simplification in refrigeration with improvements in reliability and design.

Transformers

Superconducting transformers were studied in the early 1960's but all concepts seemed to result in excessive AC loss. Conventional transformers are very efficient and a savings of only about 0.2% in efficiency is possible if the AC losses are eliminated. This requires the use of conductors in which the individual superconducting strands in the matrix are fully decoupled and not more than about 0.5 microns in diameter. This was beyond the capability of the technology of the time. In a Westinghouse 1979 study it was also concluded that fault currents would damage the conductor, and hence the transformer, at these filament sizes, because the heat could not be removed quickly enough if the superconductor was driven into the normally conducting state.

In a superconductor with a critical current density of 10^6 A/cm^2, filament size would have to approach 1 micron at liquid neon temperature (27K) and 0.1 micron at liquid nitrogen temperature (77K) before efficiency improvements could be realized. At ten times this current density (10^7 A/cm^2), the filament size could be increased by a factor of ten for the same efficiency improvement. Hence, it is possible that neon cooled transformers would precede nitrogen cooled transformers in development because of the difficulty in obtaining this filament size and also maintaining the necessary decoupling between the filaments in the matrix.

High T_c superconducting transformers may have the additional advantage of acting like fault current limiters, hence improving power system stability. This capability reduces the difficulty of mechanical design and may make such transformers more reliable than conventional transformers. However, power system stability for every type of fault may not be improved and further design studies are necessary.

Current Limiters (Utility Systems)

Fault current limiters were pioneered by the International Research and Development Company Ltd., (IRD), UK in the late 1970's as a concept for utilizing variable inductors with superconducting windings to limit transient surges on transmission grids and a 5 MVA test unit was constructed. The concept has to compete with technologies already in place and well proven, but the units offered simplicity and lowered economics as an attraction with the perceived disadvantage of low temperature helium refrigeration. Conseqently, the concept has not, as yet, found favor.

Recent developments

Long lengths of ultra-fine multifilamentary composite conductors with diameters as low as 0.08mm containing over fifty thousand 0.15 micrometer, niobium titanium filaments are now being routinely manufactured. The application of such conductors to 50/60 Hz equipment has the potential of revolutionizing the technology because of the low AC loss. Measurements in Brookhaven National Laboratory indicate that magnetization is still significant, but that these materials are an improvement over earlier multifilamentary types. Thus the inter-filamentary decoupling is not complete and there is room for further improvement.

More recently, various components have been designed and tested by Alsthom Atlantique using these new conductors. These include a three phase stator winding, an 80 kVA power transformer and a superconducting electric valve. In all cases, promising results were reported. Work is continuing on the development of a fully superconducting AC machine with both armature and field windings wound with superconducting wires and without electromagnetic shields. Theoretically, this concept offers many advantages for classical cryoalternators.

The tests of the single phase power transformer have demonstrated that considerable weight reduction is possible and that for power values above about 1 MVA, the efficiency of such a machine is better than one with conventional windings. The tests also demonstrated that the current in fault condition is strongly limited by the high value of the conductor matrix resistivity.

A final conclusion is that more complex machines are feasible, with resultant savings in efficiency, cost and safety. Such a machine would include an alternator, regulator and transformer in one unit for transferring mechanical to electrical power. Thus the design of electrical machines must be reconsidered from the beginning, taking into account all aspects of system design, including the cryogenics.

MAGNETOHYDRODYNAMIC POWER GENERATION (MHD)

MHD R&D has been conducted in several countries for many years. These include the USA, USSR, UK, Japan, the Federal Republic of Germany, Hungary, Italy, the Netherlands and Rumania. However, at the present time, apart from the USSR, the programs have either been severely curtailed or abandoned. Funding continues at a low level in the USA, but the use of superconducting magnets in the facilities has been suspended; at least for the present, in civil programs. There are competing technologies for MHD and this may account for the curtailment of the US program.

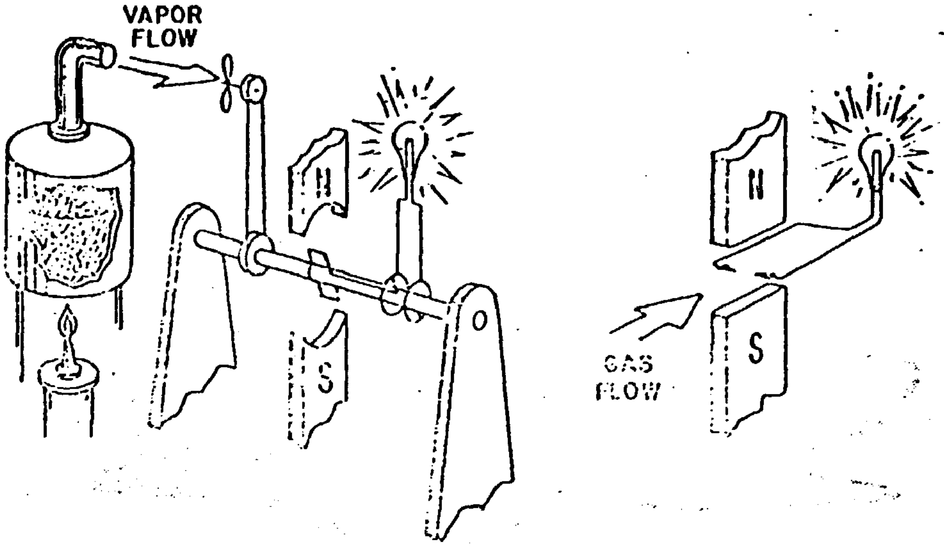

STEAM TURBO-GENERATOR MHD GENERATOR

Figure 20: Principle of MHD Power Generation

In an MHD system, an electrically conducting fluid is forced at high velocity through a duct in which a dipole magnetic field is applied: this results in the generation of an electrical potential mutually perpendicular to the direction of the field and the fluid flow. The effluent gas stream can then be vented to atmosphere as might be the case in some military applications, or it can be used as input to a conventional thermal power station. An essential part of the MHD system is the magnet, which should be superconducting if the output is to be more than that needed for the magnet.

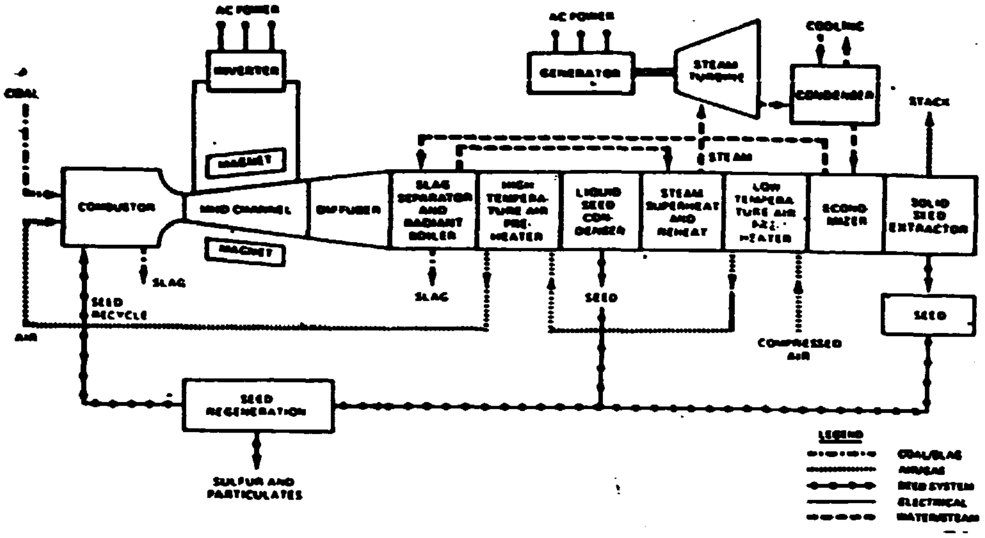

Figure 21: Simplified Schematic of a Coal Fired MHD/Steam plant with Directly Fired Air Pre-heater.

The major components of an MHD system are shown in figure 21. The combustor utilizes the fuel to heat the gas to temperatures of approximately 3000 K thus forming a plasma. In order to achieve these temperatures, the incoming air is preheated to temperatures of around 2000 K. The alkali metal seed is added to the plasma in the combustor to increase the electrical conductivity. If the coal is as a fuel, some slag may be removed from the combustor. The conducting plasma is driven through the dipole magnetic field at very high velocity, thus developing an electrical potential at right angles to the direction of flow and of the magnetic field. Many types of MHD system are feasible, both open ended and closed cycle, and many types of working fluid may be used, including even sea water as in the case of proposed ship drives.

The feasibility of MHD power generation was first recognized by Michael Faraday in 1831 and the principle first appeared in the patent literature in the early 1890's. The first recorded attempt to develop an MHD generator was in the early 1940's. During the last forty years or so, significant steps have been taken on the road to commercial MHD power, but its adoption seems to be many years away. An open cycle MHD generator (Mark V) was operated at the Avco Everett Research Laboratory in 1963 at a peak output power of 30 MW. The first model power plant complex, the UO 2 facility at the High Temperature Institute in Moscow was built in 1964 and was used to gain information for the design of the larger U-25 facility, a 20MW pilot plant with interconnections to the Moscow, USSR power system. The U-25 attained its design output in 1975, by which time it had logged more than 4000 hours of operation, including 200 hours on the Moscow grid, to which it supplied energy.

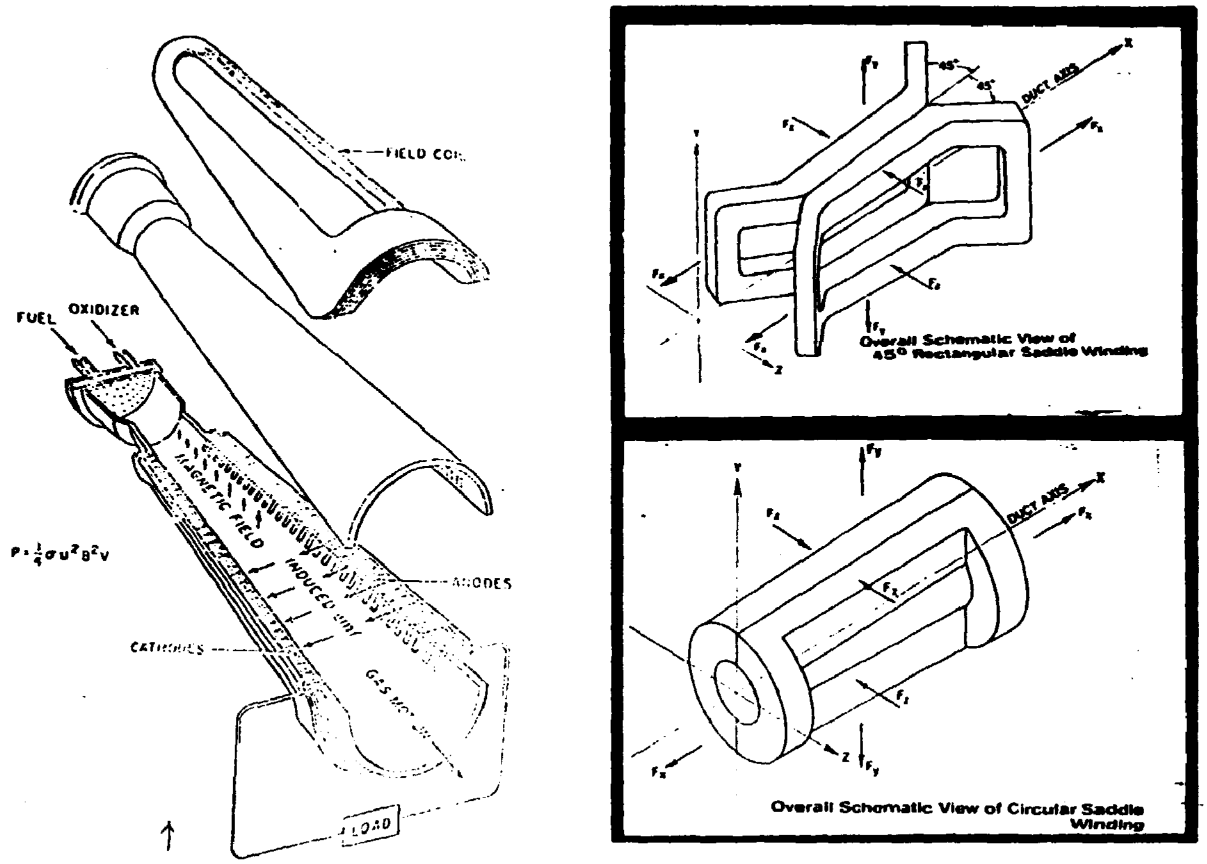

a) MHD DUCT OPERATION b) COMMON WINDING LAYOUTS

Figure 22. Schematics showing a) duct arrangement and b) directions of forces for circular and rectangular MHD saddle windings.

Engineering feasibility of a coal burning MHD facility was established in the US in 1966; the same year in which Avco operated the first demonstration model superconducting MHD type dipole saddle magnet. Operated in the cryogenically stable mode to 3.7T and stored energy of 3.9MJ, it was the largest magnet of its time, but it was not designed for horizontal operation and could not be adapted to an MHD channel. The first MHD generator tests were carried out in the Electrotechnical Laboratory Mark V facility in Japan in 1972. Meanwhile in the US, a generator at the University of Tennessee Space Institute (UTSI) demonstrated that coal could be used as a fuel in an MHD plant in 1973.

Table 6: Recent U.S. Experimental MHD Magnet Designs

	CDIF	CFFF
Inlet Bore(m)	0.85x1.05	0.8 diameter
Outlet Bore(m)	1.05x1.05	1.0 diameter
Active Length(m)	3	3
Peak Field Tesla (on axis)	6	6
Stored Energy (MJ)	240	216
Contractor	General Electric	Argonne Natl. Lab.

CDIF - Component Design and Integration Facility, Montana; Magnet neither completed nor tested.

CFFF - Coal Fired Flow Facility (UTSI)
University of Tennessee Space Institute

Typical successful magnets are those which were developed in Argonne National Laboratory for operation in the U-25 facility, experimental by-pass channel in 1977 as part of a US-USSR collaboration and the circular saddle UTSI magnet which was successfully tested in Argonne At this time, the US MHD development funding was cut and therefore the magnet was not delivered and was never used in the Tennessee facility. The windings and structural components for a superconducting rectangular saddle magnet to be tested in the US Component and Integration Test Facility (CDIF) in Montana were fabricated but the magnet was never completed and tested due to lack of funds to correct construction faults during the same funding cut.

Construction of a large superconducting magnet for the U-500 facility, a 250MW MHD and 250MW thermal plant is under way in the USSR. Design of a 1000MW space based MHD system with a 6T magnet is under consideration in the US for use as a 1MA, 100 second duration fast response power supply.

These successful demonstration magnets, combined with that gained in other large scale applications of superconducting magnets during the past decade have clearly established both the technology and its credibility. The design problems and the techniques to solve them are well understood. The design and construction of a large superconducting magnet does however represent a formidable engineering challenge and because of the very large cost, the number of years needed for design and construction, and the devastating time and cost for repair in the event of failure, these projects must be undertaken with extreme care, caution and a recognition of the need for competent and, most significantly experienced management. The total cost of an

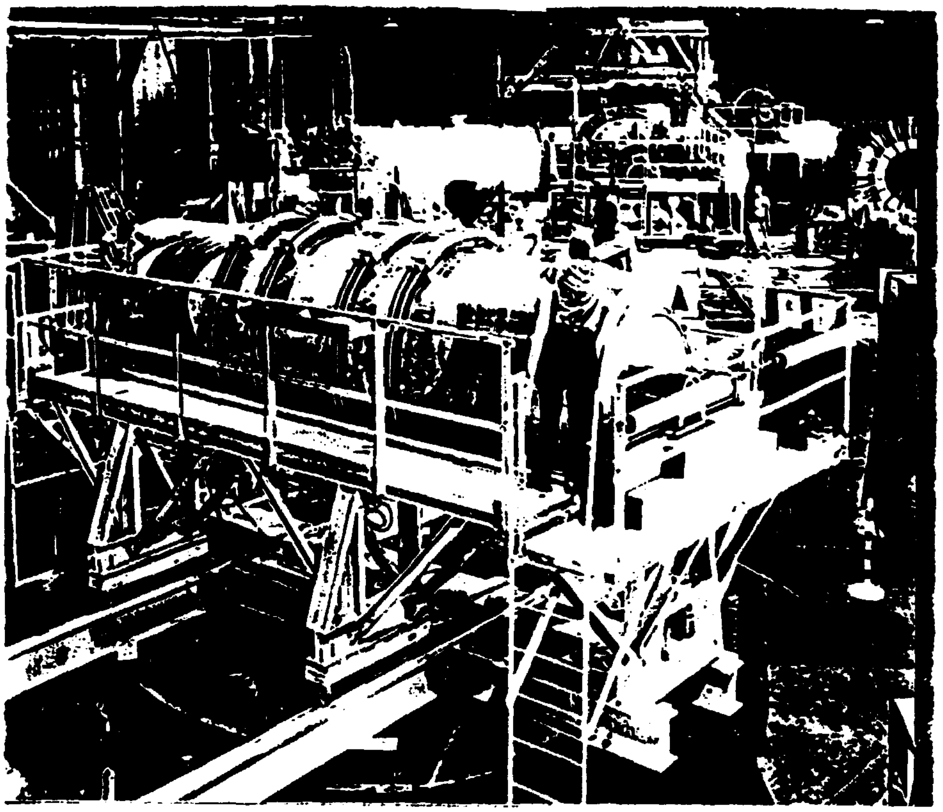

Figure 23. A view of the ANL winding facility used in the construction of the CFFF coil. In this view, a layer of the coil is being wound.

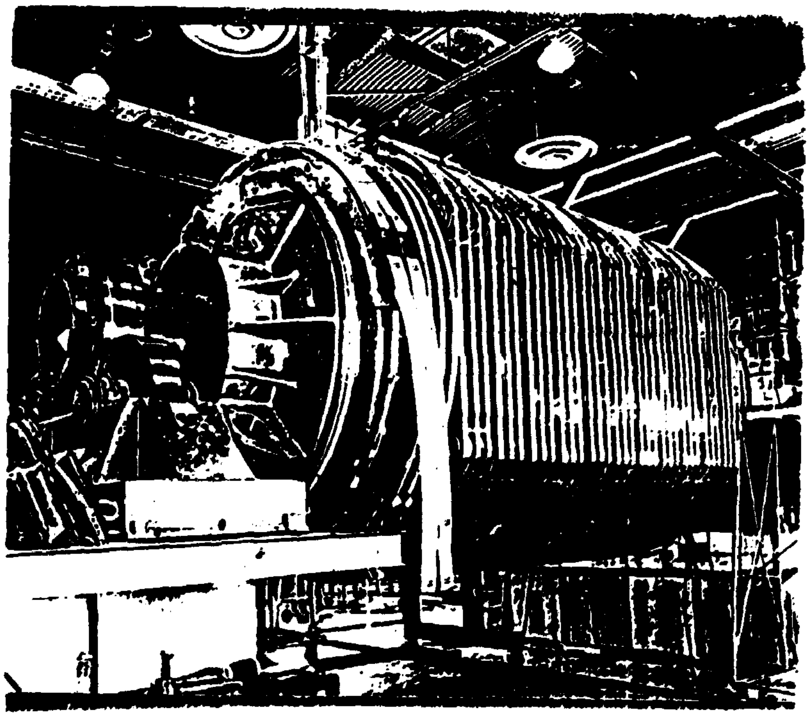

Figure 24. Force containment structure in place on the CFFF/MHD coil. The structure has then to be enclosed in its cryostat for low temperature operation.

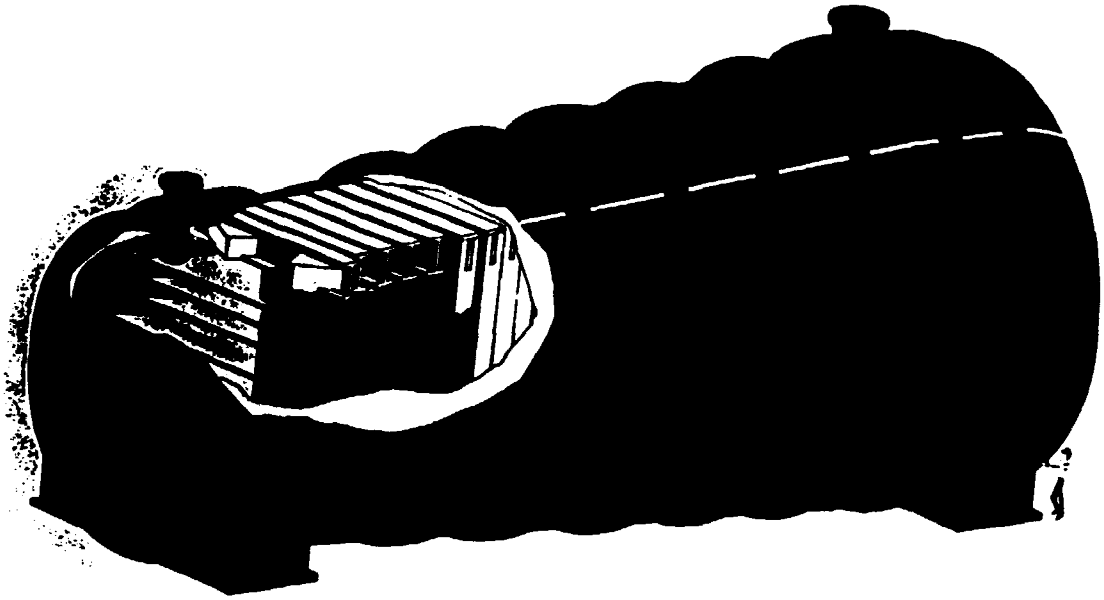

Figure 25. Artists concept of an MHD magnet for a Central Electricity Power Station (note the standard 6 ft. man in the lower right). A commercial scale generator would be between 15-25m long and a few meters in diameter with a field intensity of 6T.

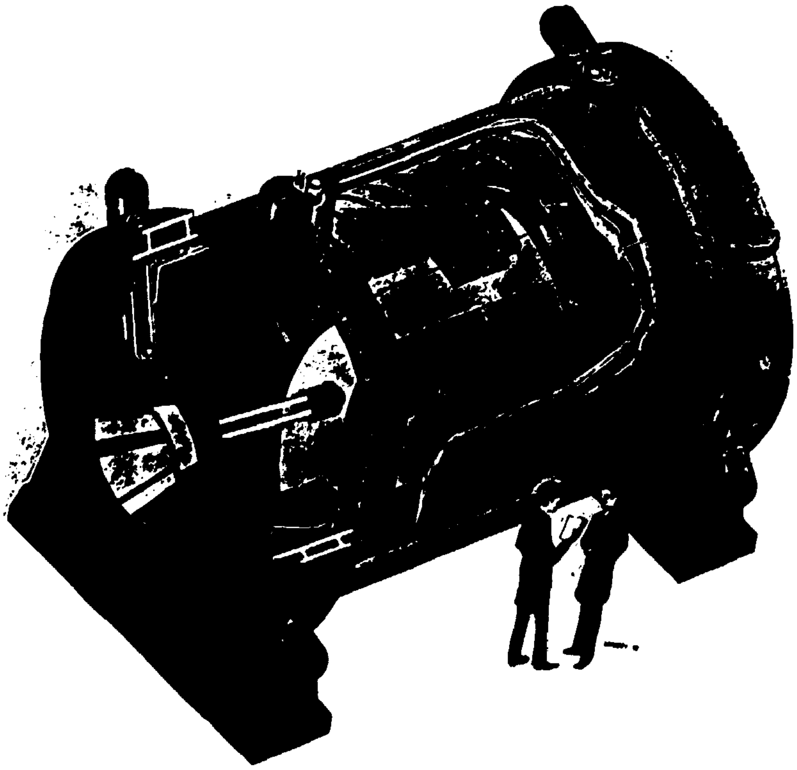

Figure 26. The ANL/CFFF MHD magnet (Artist's rendition). The system was successfully built and tested and was the largest to date

early commercial scale superconducting MHD magnet will be in the range of $50-100M. Pre-production costs are about 25% of production costs. They involve design and integration with the MHD system, magnet system design, verification and simulated service testing, manufacturing engineering and technology development.

Table 7: MHD MAGNET PRODUCTION COSTS. [1]
(Estimated $50-100 Million)

	Percentage
Pre-Production: Design, Testing, Engineering and Manufacturing development	25
Copper stabilized 6-7T, NbTi conductor	11
Cryostat ------------------------------------	15
Refrigeration --------------------------------	2.5
Vacuum System --------------------------------	1.5
Support structure ----------------------------	19
Manufacturing, Installation, Test ------------	23
Power supply, Instrumentation, Control --------	3

Magnet system costs include cryostat and associated helium refrigeration, the heavily stabilized conductor operating at a peak field of around 6-7 T, and items of manufacturing, installation and test. Of these items, 11% represents conductor cost and 19% is support structure. Helium refrigeration represents only 2.5%, with a further 1.5% for the thermally insulating vacuum system.

The magnet system cost is probably around 10% to 20% of MHD system installation cost, and 5% or less of total combined MHD and thermal plant cost. Thus helium system related costs are around 2% of total initial MHD system cost and less than 1% of total plant cost. This is the differential saving attainable with room temperature superconductors of equal cost and performance: the saving at 77K would be less (see Table 7).

---

[1] Table 7 and many of the figures in this section were provided by my friend Peter G. Marston of the MIT Plasma Physics Division, Massachussets Institute of Technology.

CONTROLLED THERMONUCLEAR FUSION RESEARCH (CTR)

CTR development programs were initiated in the developed countries 1951. Eight gallons of water contain about one gram of deuterium, with a cost of extraction of less than one dollar and an energy content equivalent to 2500 gallons of gasoline. This is the attraction of CTR. It offers the dream of unlimited energy from the oceans, at low cost, for the use of mankind.

The controlled fusion reaction is not self sustaining and is therefore inherently safe. Fusion plants could conceivably be placed in cities and urban population centers because of this safety feature and the fact that they would produce much less radioactive contamination than fission reactors. However, parts of the plant would become radioactive because of the production of the neutrons which heat the energy absorbing blanket: this, in turn heats the primary water circuit which transfers heat to the steam plant.

Two principal avenues of investigation are Inertial Fusion and Magnetic Fusion: the latter needs superconducting magnets if it is to generate net power. Most experimental magnetic fusion systems are very large and to date, have used conventional, water cooled, copper conductors in their magnet systems. Both toroidal and magnetic mirror systems are under development. The front runner is the toroidal configuration known as the Tokamak(from the Russian words - Tok a magnet Kamera - meaning current and magnet chamber); an invention of the late Professor Lev Artsimovich, Kurchatov Institute, Moscow, USSR. Tokamak experiments incorporating superconducting magnets are in operation in the USSR, Japan, and France.

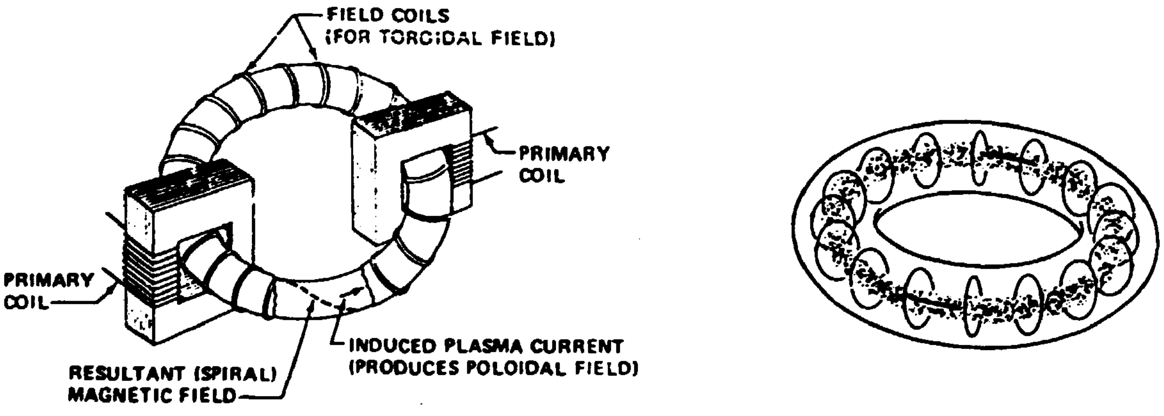

Figure 27. The Tokamak Principle. A pulsed current in the transformer primary induces a current in the plasma contained in the torus which in turn gives rise to a poloidal field around the plasma. This field combines with the toroidal field produced by the field coils to produce a spiral field which stabilizes the plasma.

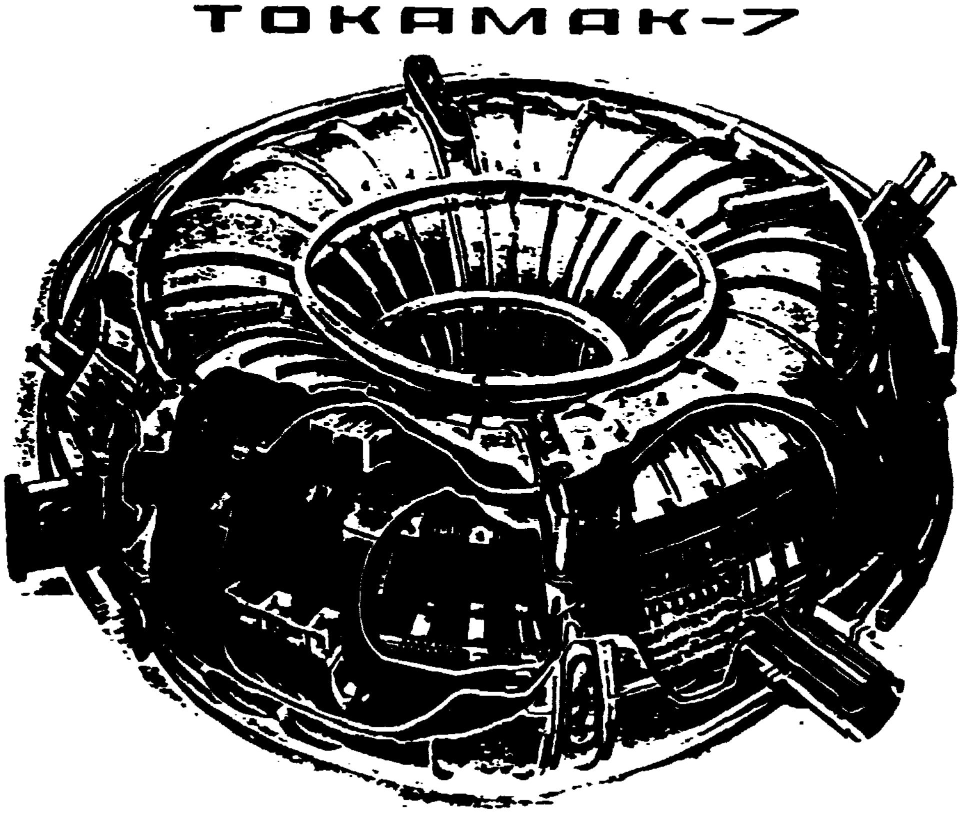

Figure 28: Tokamak T-7: The first superconducting tokamak - 1968

A low field Tokamak system at the Kurchatov Institute has been in operation since 1978. Using niobium titanium conductors in the field windings, the system has proved the convenience and cost saving advantages of superconducting systems, because the toroidal field magnets can be operated continuously rather than as pulsed systems, as is necessary with coils wound from water cooled copper. A larger, higher field, Tokamak system, T-15 is being constructed with toroidal field windings, using the technically superior but brittle niobium tin, and is expected to begin operation in 1989.

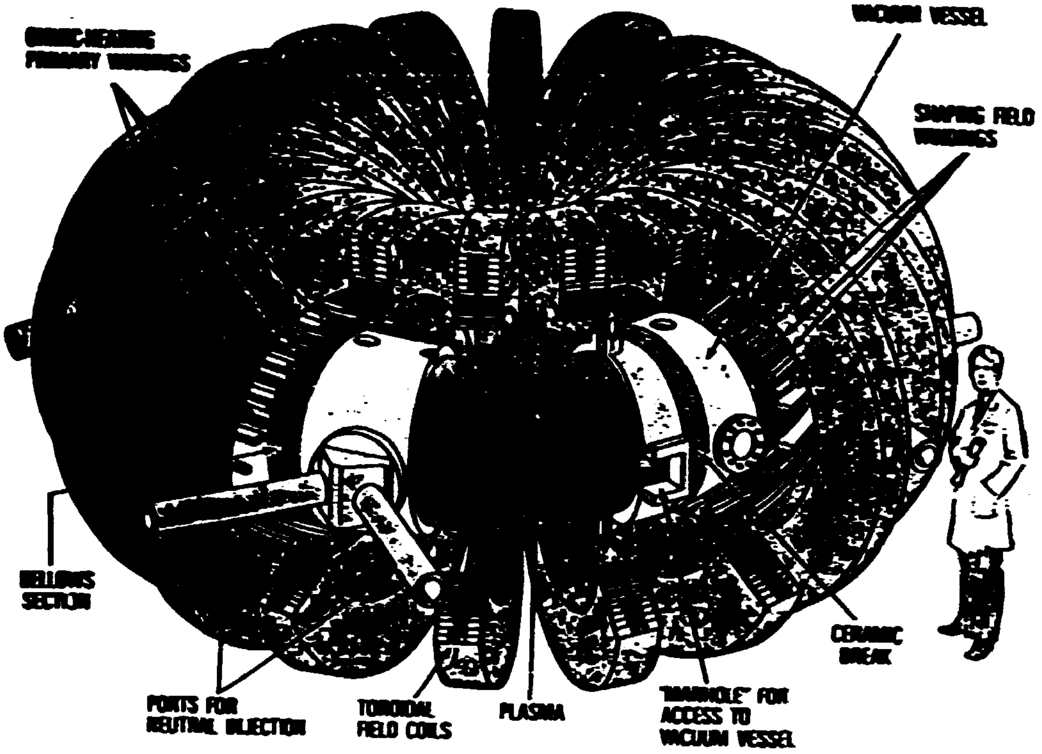

Figure 29. Important Tokamak Components

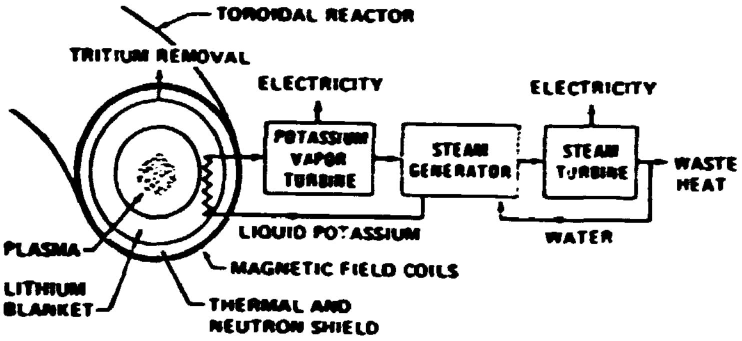

Figure 30. Toroidal Fusion Power Station Concept

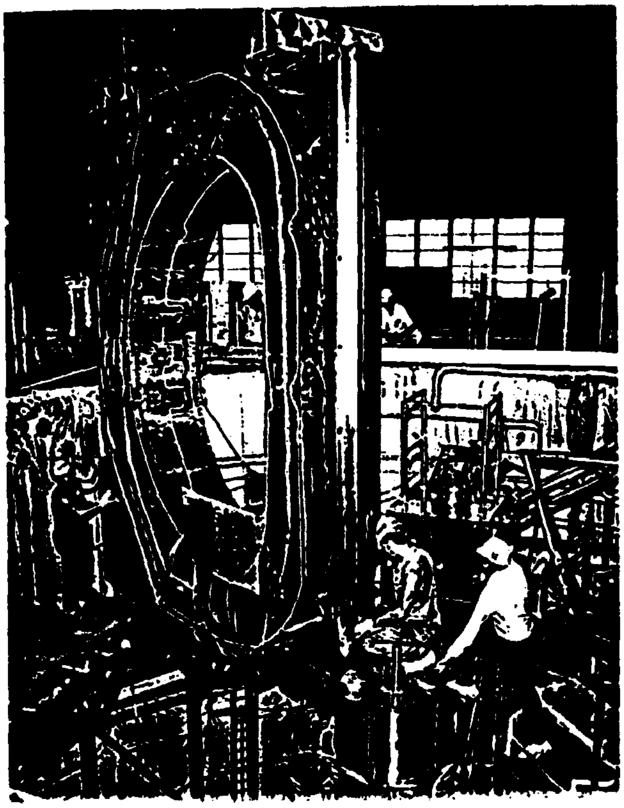

Figure 31. The International Large Coil Test: The General Dynamics coil being installed in the vacuum tank

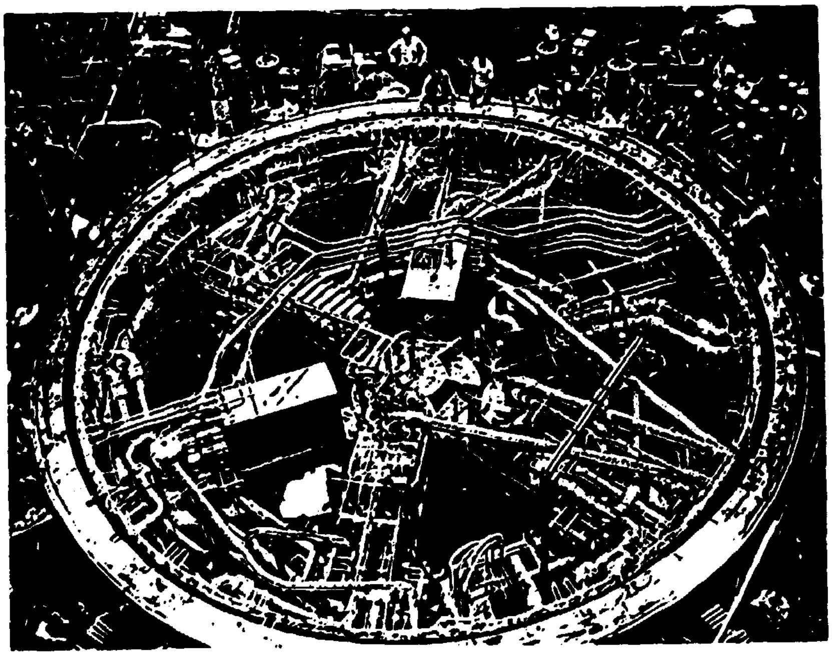

Figure 32. International Large Coil Task: View of the vacuum tank with all six coils installed (Oct. 1985) prior to cool down which began on January 13, 1986.

In 1978 the Large Coil Task agreement was signed between Euratom, Japan, Switzerland and the United States to construct and test six D-shaped coils in Oak Ridge National Laboratory to a design field of 8T and half toroidal reactor scale in order to gain information useful in the design of commercial toroidal reactors. The coils were constructed using different conductor designs and cooling systems, but common mechanical configurations so that they could all be interconnected and tested either separately or together in the test tank.

Industrial experience in large superconductor coil design and construction was gained by having the coils manufactured in industry. The individual coils were built by six different manufacturers: Siemens, Brown Boveri, Hitachi, General Dynamics, Westinghouse and General Electric/ORNL. Five of the coils used composite conductors containing niobium titanium. Westinghouse was chosen to design and construct a niobium tin coil since the superior characteristic of niobium tin beyond 10 T are more suited to the requirements of the fusion community which has consistently expressed a need for magnets of the highest field possible - hopefully 20T or beyond!

All coils performed to design specification and beyond. These coils are the largest ever built to operate at 8T and beyond, weighing 45 tonnes each and with 100 MJ of stored energy at 8T. The Swiss and Euratom coils are the largest adiabatically stablized coils ever built and operated to such fields. In total, the system stored energy when the symmetric torus was energized to design field was 860 MJ (approx 220 kWhr).

The international large coil task has demonstrated the following that D-Shaped Tokamak Coils of size 2.5 x 3m can be successfully operated to approximately 10 kA and 8T. All these coils could be ramped up to full field in about 40 minutes.

The peak fields and currents were as follows:

	Current (kAmp)	Field (Tesla)
a). Coils cooled by pool boiling		
General Dynamics (GD) -	10,	9
Japan (JA) -	10.9	9.1
General Electric/Oak Ridge (GE/ORNL)	11.4	9.2
b). Coils cooled by forced flow systems.		
The Euratom coil (EU) -	13	9.1
The Swiss coil (CH) -	14.3	9
The Westinghouse coil (WH) -	19.8	8.9

It can be seen from these results that a wide range of techniques can be used to make prototype, half reactor scale coils. While fusion systems may not be needed before 2030, proposals for the next step in large, engineered, fusion coils have been made in several countries. However, there is no agreement as yet on a common design or an international project.

The international fusion committee has suggested that the next generation device should be designed to operate at 14T. As a consequence, some work is in hand to develop large magnet systems to operate at these field levels. The US has a 14T coil development project at Livermore for the proposed TIBER Tokamak. (Dr. J.R. Miller).

In JAPAN a 16T development plan is under way at JAERI. The coil will have a 1m inner winding i.d. and an Al stabilized, stainless steel reinforced Nb_3Sn conductor has been developed for this project. The coil conductor will be mounted in a CuNi conduit and wound in grooves in a high strength stainless steel disk structure.

Since Tokamaks work on the transformer principle, a pulsed poloidal field is necessary. Field changes of 10T/sec for several seconds are needed and slower changes of around 1T/sec for times of the order of minuts. The Japanese are also building a Demonstration Poloidal Field Coil (DPC) test facility to facilitate development of poloidal field coils. A 10T, 1m bore 10T/sec coil is expected to be ready for test in this facility in 1989.

The US is hoping to have a similar coil ready for test at the same time in the JAERI facility using a rope-in-pipe conductor based on that developed for the Westinghouse LCT coil. Dr. Hoenig of the Francis Bitter National Magnet Laboratory, MIT, USA, who instigated the rope-in-pipe idea used for the Westinghouse Nb_3Sn coil is overseeing the project.

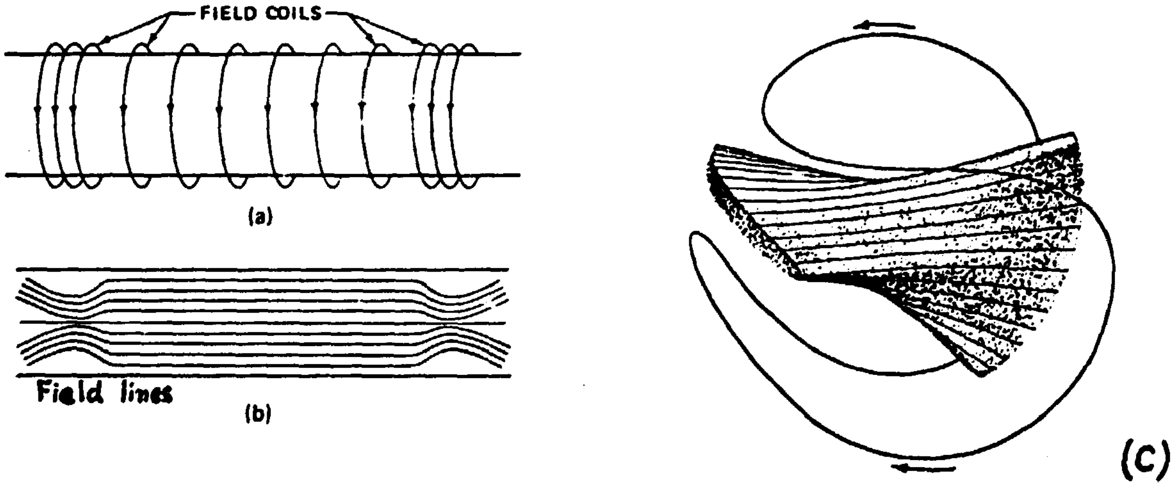

Figure 33. Mirror Concept: a) & b) Solenoid; c) Minimum B or Baseball

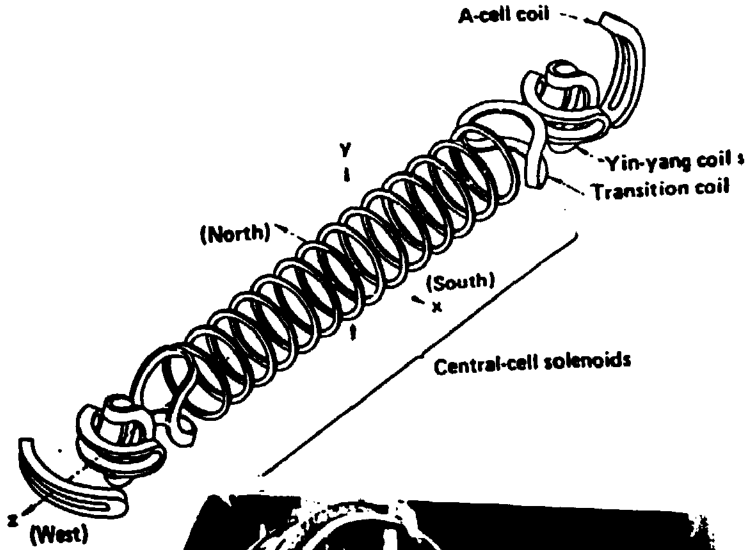

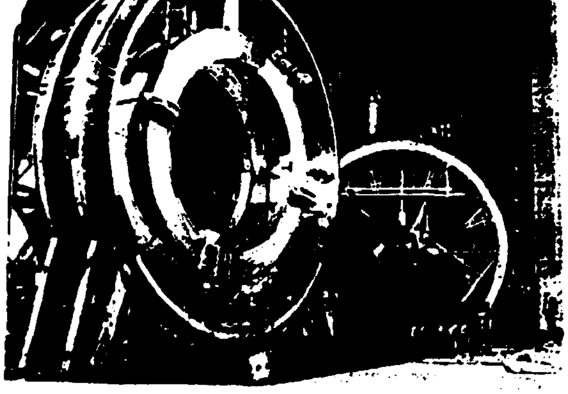

Figure 34. MFTF-B TANDEM MIRROR CONCEPT: A Yin-Yang coil and one central solenoid pair is pictured and an early coil arrangement is shown. In the final design, the A-cell coils were replaced by 12 T multifilamentary Nb$_3$Sn axicell coils as end plugs, four transition magnets replaced the two larger ones shown, two solenoids were removed and the remaining 12 were moved closer together to produce a 1.6 T central field.

The mirror fusion test facility (MFTF-B) in the Lawrence Livermore Laboratory, USA was completed and tested successfully to design field in 1986 and is the largest superconducting magnet facility of its kind. Unfortunately, the facility was shut down before it could be used for experiments.

MFTF-B is a 53m long system containing 42 superconducting magnets weighing over 1200 tonnes in total, with a stored energy of 1200 MJ (approx 330 kWhr) at full field. The concept had its beginning in 1965 in Livermore Laboratory. In 1965 a small model was wound and tested in Argonne Laboratory in a collaboration between C. Laverick and C.E. Taylor of Livermore using cable Laverick developed for the outer sections of the helium bubble chamber magnet. It was then taken to Livermore where it was later rewound and became known as Baseball 1 because the windings followed the contour of the seam of a baseball around a spherical winding form. Two such windings rotated 90 degrees with respect to each other became known as Yin-Yang coils. Design of the large system began in 1974 and testing began in 1986. Containing 2 sets of Yin-Yang coil pairs at each end of the system, separated by six pairs of 3.5 T, 5m bore solenoids and a 12.5T plug coil behind each Yin-Yang to reverse the leakage plasma from the Yin-Yangs, as well as several other coils, this was the largest superconducting system ever built and tested.

HIGH SPEED GROUND TRANSPORTATION

FIGURE 35: SIEMENS- ERLANGEN, TEST CARRIER: OPERATION 1976-1979

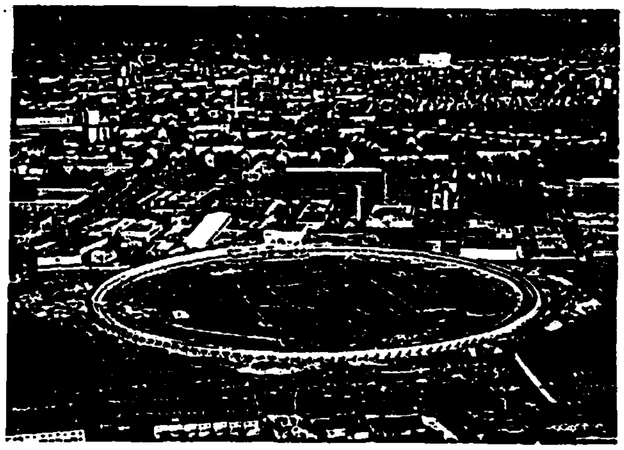

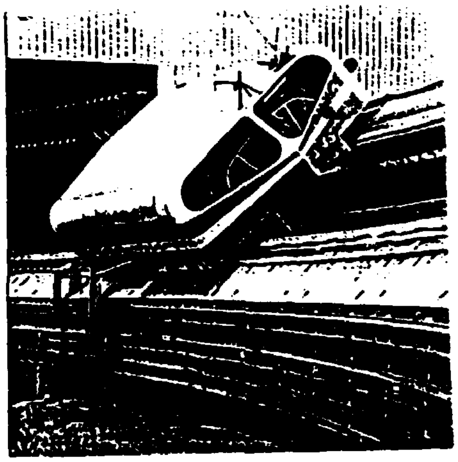

LSM Prototype Magnet: Requirements, Design

TASK	Magnet for Experimental Proof of the Linear Synchronous Motor Scheme with the EET in Rolling Mode
REQUIREMENTS	
thrust	• ± 20 kN (1.43m pole pitch)
operation	• banking 0... 45°; normal/ lateral acceleration $20/\pm 6 m/s^2$ • dynamics: see EET lift magnets
Cooling	• *LHe bath, GHe shield* • reservoir good for >3 hours
DESIGN	
conductor	• Cu: NbTi = 5 • *1000 A rated, 2080 A critical current at 4.2 K; 4.5 T*
winding	• 2 circular pole coils; 1.2 m ϕ • LHe transparent • 2×1.05 MA MMF • $93 A/mm^2$ *overall current density*
circuit	• two coils in series persistent mode • mechanical switch
energy	• 2×1.1 MWs stored
LHe	• 220 l total inventory, 90 l reservoir
mass	• 3380 kg total • 1400 kg cold

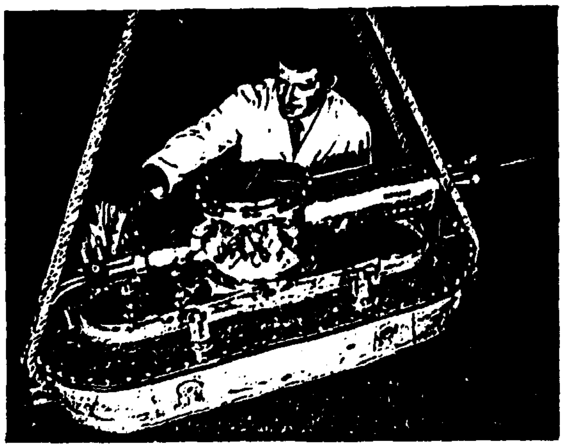

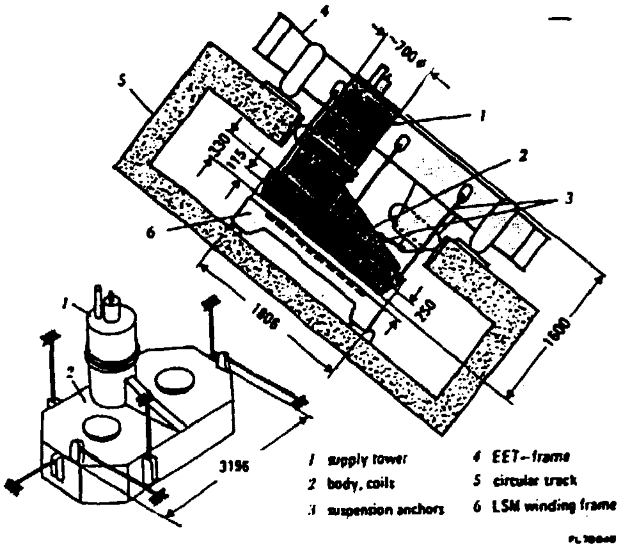

MELOT: Shape, dimensions, suspension und position in the EET

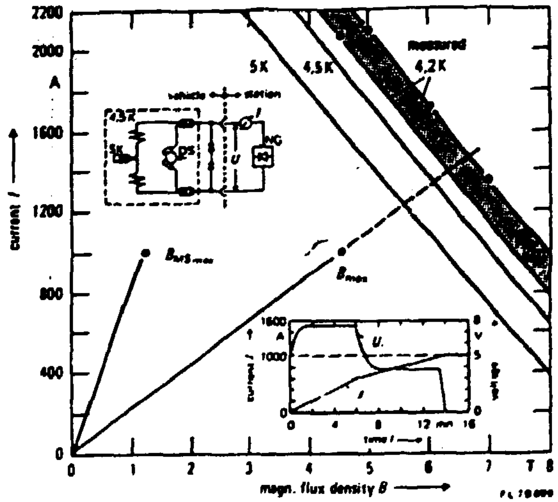

Energizing of MELOT; circuit, rise time, short sample characteristic of s.c., load line (B_{max} within MELOT winding; $B_{MS_{max}}$ at track surface, share of MELOT)

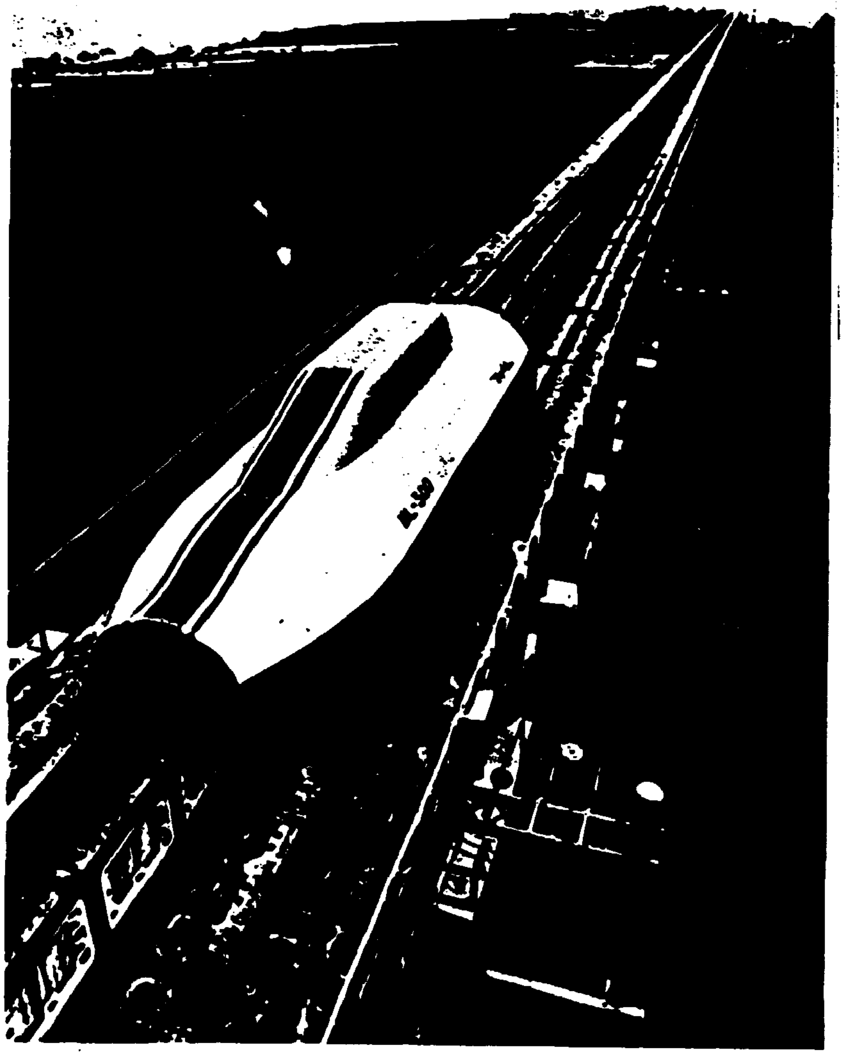

Figure 36 Japanese National Railways Test Vehicle ML-500: 1979

In 1979, both the Japanese test vehicle above and the Siemens vehicle on the previous page operated successfully at high speed after some years of operation at lower speed with earlier models. The ML-500 above ran at over 500 km/hr on the test track. The 7 km long test track was modified to allow thrust to be developed at each side of the carriage instead of in the center as with the ML 500 and a new 44 seat train was first tested in March 1987 to over 400 km/hr at which speed it had to be slowed down because of the short length of track.

The German vehicle developed a thrust of 20 kN up to 120 km/hr. Operating characteristics and magnet sizes are given in the preceding page (Courtesy of Carl Albrecht, Siemens Erlangen Research Center). These parameters are typical of such devices. Following these successful demonstrations, the Siemens work was stopped in favor of a competing scheme using conventional coils and attractive rather than repulsive levitation. This latter work has reached a successful conclusion and a demonstration train has operated.

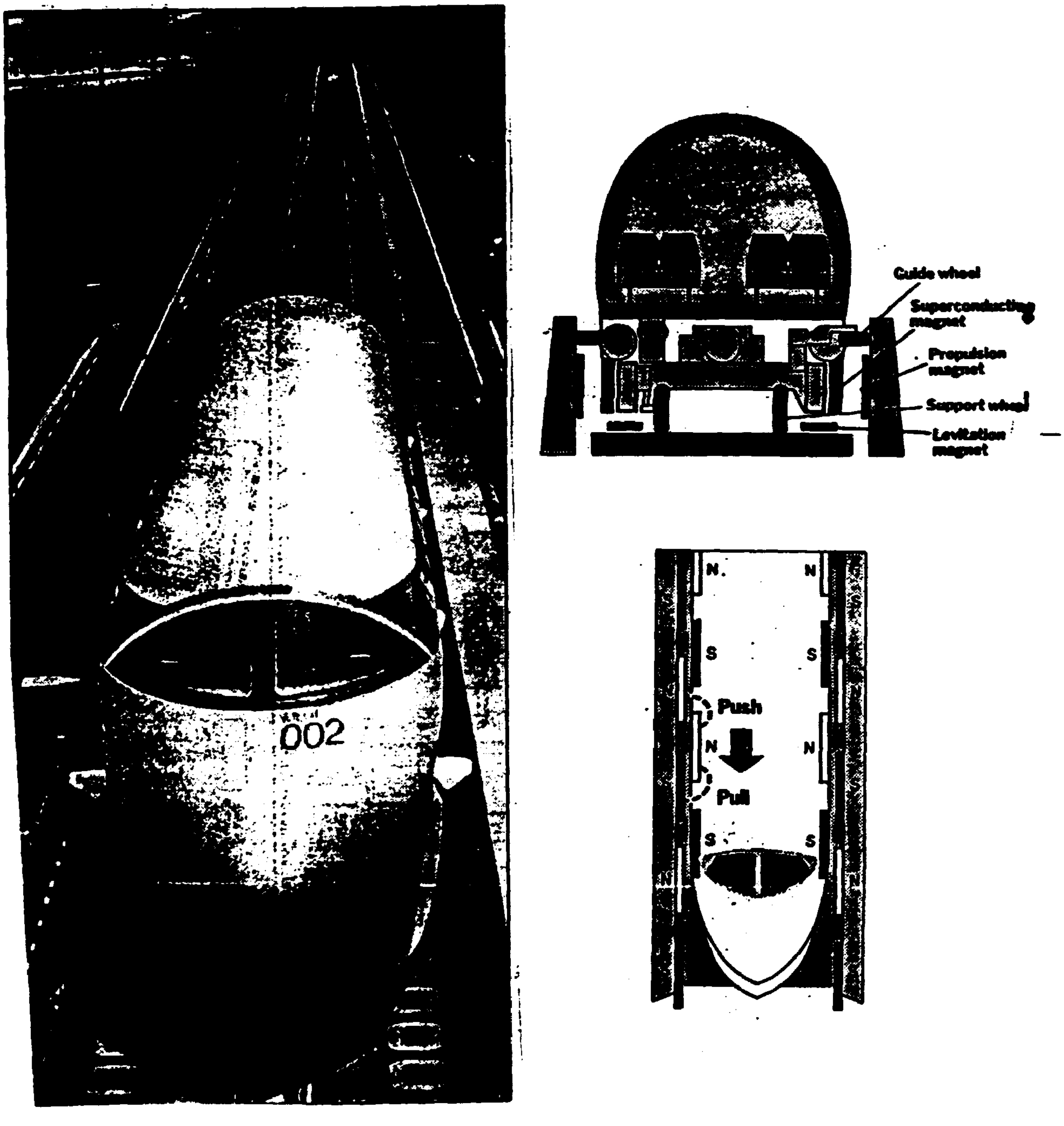

Figure 37. The 22m long, 34 kgm, 44 seat Demonstration Carriage of Japanese National Railways. Its first test run was in March 1987. It has been run at over 400 km/hr on the 7 km long track, but could attain higher speeds on a longer track. The levitation and propulsion coils are shown in the cross-sectional view. The principle of the linear synchronous propulsion system is shown at lower right.

The development of both superconducting repulsive and conventional magnetic systems in Germany and Japan resulted in full scale, successful demonstrations which both countries are continuing. The repulsive systems are intended for very high speed inter-city transport and the attractive systems for lower speed inter-urban or city to airport application. Most recently, several other possibilities have been mentioned, such as utilizing some form of Maglev for increasing the take off speed and reducing runway length for commercial aircraft and for using maglev runways for space vehicle launch. The inter-city systems, if built, would reduce airport crowding and air saturation by commuter planes on short haul routes but the concept faces competition from the established air transport system.

Maglev possibilities were also studied in other countries, such as the USA, Britain, France and the USSR but not reduced to practice. In the U.S. a laboratory scale model, 'the Magneplane' was demonstrated by H. Kolm of MIT's National Magnet Laboratory as part of a consortium involving Raytheon and United Engineers and Constructors Inc. supported by the NSF-RANN (Research Applied to National Needs) program. Studies were carried out by Ford and the Stanford Research Institute. Originally, the U.S., France and Britain placed emphasis on TACV (Tracked Air Cushion Vehicles). The U.S. studies, funded at nominal levels by the Department of Transportation (about $78 million between 1966-1973 on TACV) were eventually discontinued; Britain and France opted for high speed trains on wheels on the grounds that their speeds were adequate for their relatively short inter-city runs.

Sea borne systems are based on the concept of electric drives to ease problems in ship design; the Normandie was such a ship, or on the application of MHD, using sea water as the driving fluid and the ship's hull as the MHD duct. In the former case, the drive motors would use superconducting windings. First investigated by IRD (International Research and Development Company) in England, the work was abandoned, when Government funding was withdrawn In the U.S., studies continued and a small, US Navy experimental ship has undergone successful trials for some years.

Thus superconducting applications to transportation have received attention over the years but, in spite of demonstrated success for both land and sea technologies, they have not been adopted by society. The replacement of the low temperature superconductor by the ceramic conductors, if and when feasible, will have little impact on whether or not such systems are adopted on a societal scale. However, the excitement caused by the advent of the new superconductors and the attention they have received from those responsible for funding military and space programs may help to accelerate demonstration and adoption at some time in the future.

NIOBIUM AND HELIUM NEEDS FOR THE NEXT DECADE

NIOBIUM DEMAND TO 1998

In spite of all the efforts, achievements and publicity over the years, the world superconductor industry is very small and likely to remain so to the turn of the century. Until the advent of MRI in 1982 the activity was supported mainly by long term R&D in Government laboratories. The first need was in high energy physics and successes here led to use in fusion and MHD development programs. The current and projected distribution of effort can be understood by considering the need for niobium in superconductor application over the next few years.

Apart from the proposed SSC, even large superconductor projects need relatively small amounts of niobium and hence, superconductor. Thus, the proposed demonstration energy storage project for Wisconsin now under study would have a stored energy of 100 to 200 times the stored energy of MFTF-B, the largest system so far built (exclusive of the 2,000 magnet Tevatron system), but would need only about 10 tonnes of niobium. This quantity can be considered to be covered in the uncertainty of the scenarios presented here. Developments in high temperature superconductivity are not likely to have sigificant impact on this demand in the next few years.

The probable weight of niobium contained in alloys used for superconducting applications over the next ten years is likely to be around 500 to 1100 tonnes. The lower demand total assumes that around 150 tonnes each will be needed for diagnostic imaging and rf cavities, about 100 tonnes for physics machines and devices, and the remainder for all other applications. The higher total demand assumes that the proposed colliders will be approved and need about an additional 500 - 600 tonnes.

The weights of niobium given here, are for niobium contained in the alloys actually installed in equipment. No attempt was made to extrapolate demand for high purity niobium sheet in rf cavities beyond five or six years. No allowance is made here for wastage at various stages of production, either of the pure niobium, the alloy or final sheet or conductor. Amounts needed for electronics are comparatively small(grams/device): if the new high temperature superconductors replaced the low temperature material in all projected electronic applications foreseen today, the impact on niobium demand would be negligible.

The world-wide superconducting industry seems insignificant compare with steel or even niobium. Niobium consumption in the steel industry, where it is used in small percentages as an additive, is around 15 to 17 thousand tonnes/yr world wide as opposed to the averages of 50-110 t/yr of our scenarios for superconducting applications.

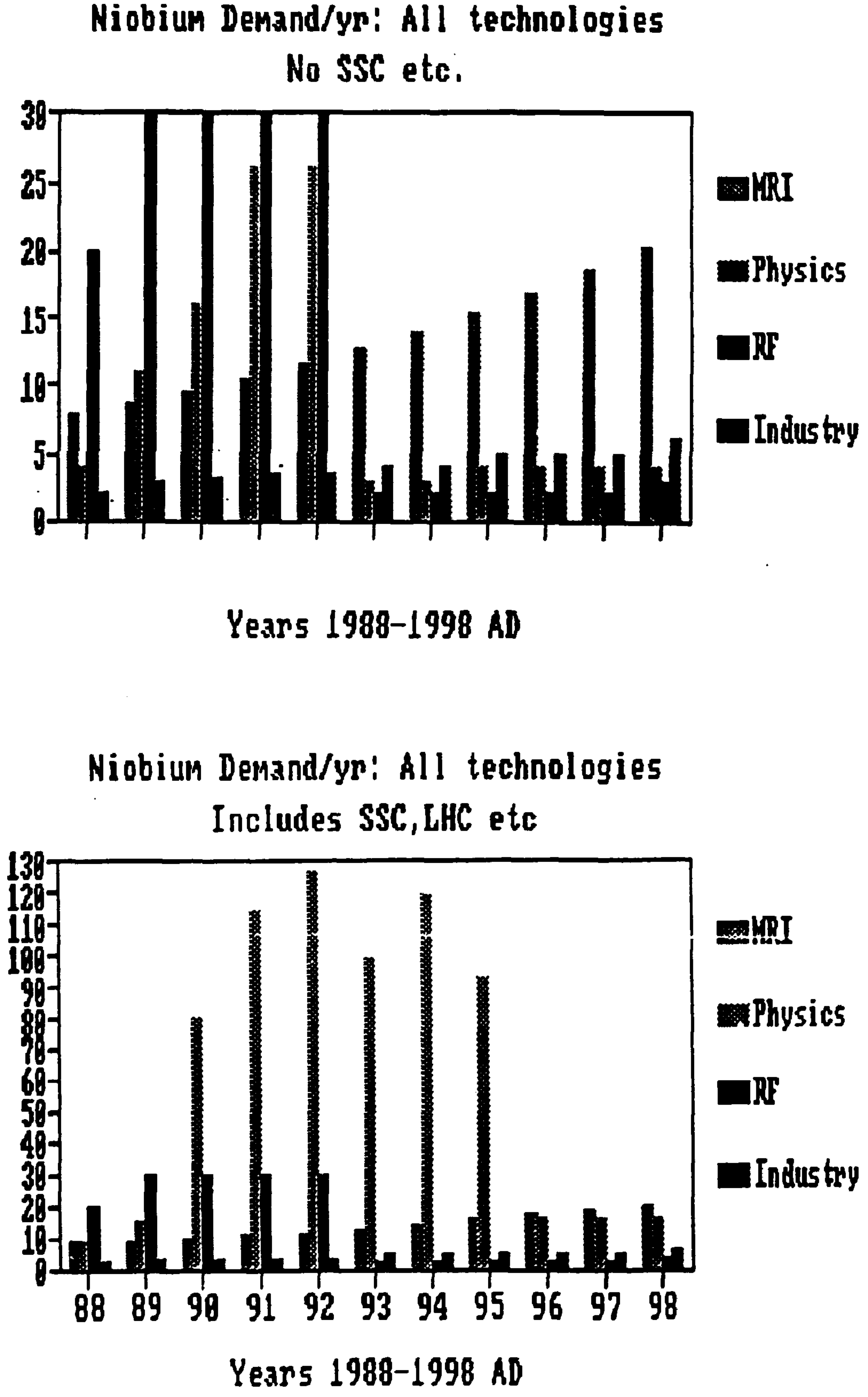

Figure 38 Annual Niobium Demand for Superconductor Application: with and without the proposed Physics Colliders.

HISTORY OF THE U.S. HELIUM CONSERVATION PROGRAM

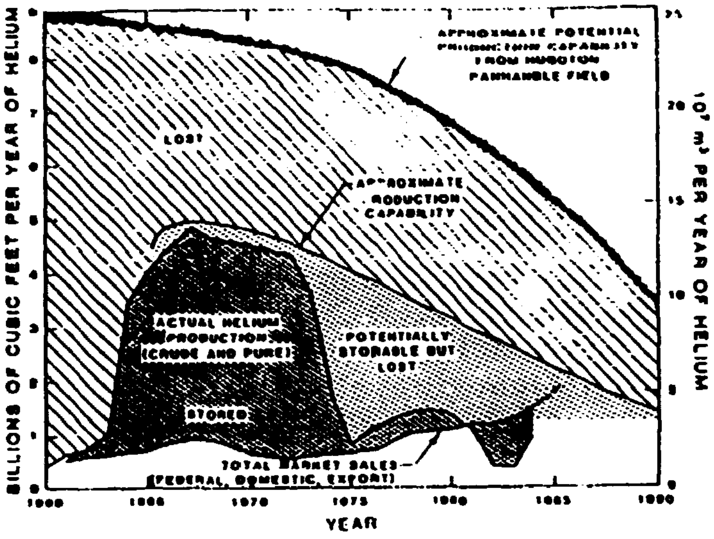

U.S. Helium Supply-Demand Balance

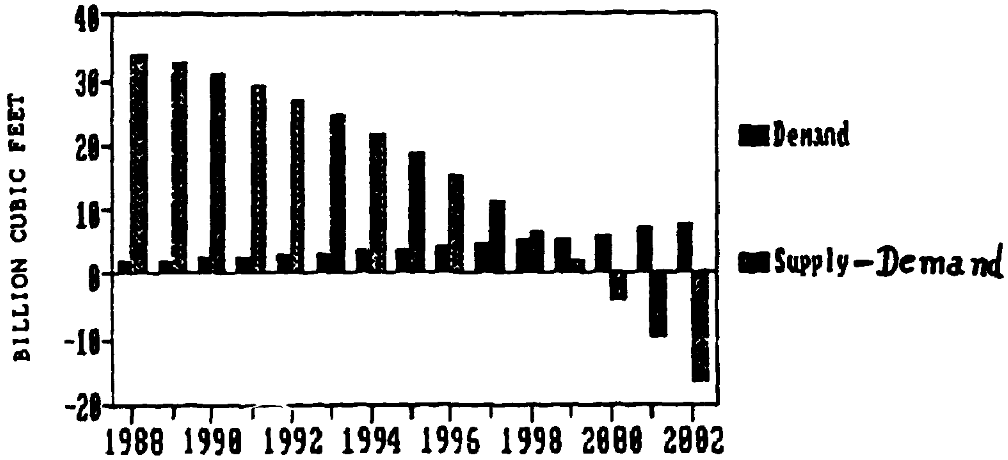

Figure 39 a) History of the U.S. HELIUM CONSERVATION PROGRAM
b) Projected U.S. Helium Supply - Demand Balance to 2002 AD without Policy Changes

HELIUM DEMAND

Over the last few years, helium demand has escalated at 10%/yr, and supply to meet this demand has been possible only because of withdrawals from the helium storage reservoirs of the US helium conservation program. By the turn of the century, demand will exceed supply unless an enlightened management approach is taken to this problem. Availability of helium is no problem, but the richest sources (from natural gas with a helium content of 0.3% or more) are almost completely used. Helium extraction from less rich sources will be increasingly expensive. This could be one incentive to develop and apply the new superconducting materials.

CONDUCTOR NEEDS: SUPERCONDUCTOR APPLICATIONS

The question of conductor availability and fabrication arises in connection with the quest to reduce the new superconducting high temperature materials to practicality. One question is, what can be learned from the low temperature superconductor experience? Niobium titanium, the present workhorse of the industry is a ductile metal, easily bonded to copper or aluminum to provide shunt current protection if the superconductor is driven into the normal state. It can be coextruded with copper, assembled into billets containing thousands of fine niobium rods, drawn into long lengths to produce uniform filaments in diameter ranges from less than one micron to any diameter above that and twisted to reduce coupling between the filaments..

The very finest filaments are needed for ac applications where the ac losses must be kept to the lowest possible value. In physics colliders, filament diameters of around 5 microns are desirable to reduce magnetization at low injection fields which produces slight, but unacceptable field errors in the small bore magnet which guide and focus the particles in their orbits. Because of the high fields which are needed (6.6T in the SSC and possibly as high as 10T in the proposed CERN-LHC), very high current densities are essential to reach such high fields in small bores and intense stresses are induced in the conductor at these field intensities. In the larger, smaller field(0.5-2T), whole body MRI coils, the need is for very long lengths of conductor with precise control of wire diameter to obtain very high field uniformity over relatively large volumes in the magnet bore: the individual multifilaments can be larger and very much smaller in number.

In the large MHD and fusion coils, the need is for conductors of high strength, cryogenic stability, and current carrying capacities in the range of 10,000 to 20,000 A or more at peak fields around 7 T for MHD and 10 to 20 T in fusion. In these large coils, and in the very highest field small coils, the windings may be stress limited rather than field or current limited.

At present, Nb_3Sn and V_3Ga are being explored as candidates for the highest field coils. Vanadium gallium has been used in only very small quantities above 16 T in small bore coils. These materials resemble the new ceramics in being brittle. However the starting materials are metals: thus fabrication processes common to handling metals can be used before firing to produce the final superconducting wire or tape. This is not the case with the new ceramics. Fabrication techniques for producing practical ceramic superconductors represent a new and different discipline.!

COST CONSIDERATIONS

One of the great incentives for the applying the new superconductors is said to be that of great savings in refrigeration and hence, of cost. Until we have some practical ceramic conductors of acceptable specification and proven performance for a specific application this remains to be seen. Operating cost is only one element of total cost and in large systems, the cost of capital may be one of the greatest factors. In the previous text some comments on cost have been included (eg. Table 7,p 46 gives some estimated MHD Magnet Production Costs).

Even total elimination of the refrigeration, implying room temperature superconductivity, is scarcely a significant factor. However, in most instances, the reason for using superconductors in the first place was the actual significant savings in cost, sometimes translated as making something technically and economically feasible which would have been out of the question if conventional technology were the only possibility. Such was the case with the bubble chambers, the Tevatron, the higher field (>0.3 T) whole body MRI systems and high field laboratory magnets. By comparison, the change to liquid nitrogen refrigeration is marginal.

It is too early to compare raw material or superconductor costs because no practical high field/high current/high temperature superconductors have been fabricated. Niobium prices have remained constant for some years, in terms of Swiss francs. Raw material prices for the new ceramics vary by about two orders of magnitude in this early discovery and production stage.

Table 8 - Proposed SSC COSTS

	$BILLION
TOTAL (LAND DONATED)	5.4
COLLIDER	3
MAIN RING DIPOLES	0.7
DIPOLE + QUADRUPOLE CONDUCTOR	0.3
ie. 10% collider & 6% total cost	
CRYOGENICS (2% total cost)	0.12

Contingency costs

TECHNICAL COMPONENTS	0.3
COLLIDER RING	0.25
MAGNETS	0.2

THUS cryogenics and magnets are less than contingency costs: HTSC's would make little difference to cost.

Table 9 - Magnetic Resonance Imaging:
Cost and Demand Scenario; 1988-1998

Year	88	89	90	91	92	93	94	95	96	97	98
Magnetic Resonance											
MR Systems10%/yr	275	302	333	366	403	443	487	536	589	648	713
MR Sys Cumulative	1275	1577	1910	2276	2679	3122	3609	4145	4734	5383	6096
Nb/yr(tonnes)	8	9	9	10	11	13	14	15	17	18	20
Total Nb (t)	8	17	26	36	48	60	74	90	106	125	145
Nb/yr,$Million	1	1	1	1	1	1	1	2	2	2	2
Coil sales/yr $M	57	62	69	75	83	91	100	110	121	134	147
Magnets/yr	95	104	114	126	139	152	168	184	203	223	245
System sales/yr,$M	212	233	257	282	310	341	376	413	454	500	550
End user market	605	665	732	805	886	974	1072	1179	1297	1427	1569
RF cavities(Hi-purity sheet)											
Nb wt t/yr	20	30	30	30	30	2	2	2	2	2	3
Cumulative rf nb	20	50	80	110	140	142	144	146	148	150	153
Industry/R&D Nb/yr	2	3	3	3	4	4	4	5	5	5	6
Cumulative	2	5	8	12	15	19	23	28	33	38	44

10%/yr growth rate & 28.4kgm Nb/average MRI unit assumed.

Makers costs: Nb - $128/kilo; 2T coil - $206K; Magnet - $344K,
System - $771K; End user system cost - $2.2M

This tabulation (to the nearest whole number & averaging niobium weight for a wide range of magnet system) assumes only 2T magnets. Since many systems use 0.5T at present, the table is optimistic in terms of niobium weights and expenditures. However, 2T and even higher systems may come into use if MRS is widely adopted. The table explains some of the myths of estimates for superconductor application totaling $Billions. Examing 1998 we see that Nb sales could be $2 million for 147 system sales, with an installed market of 6100 systems. The coils sales cost would be $147 million, magnets $245 million, systems $550 million, end user expenditures $1.6 billion.

At 2000 scans/yr/installation 12 million scans/yr would be performed at a cost to patients of $6-12 billion assuming costs/scan to average $500-1000. Hospital and physicians fees at say $300/scan would be in the range of $3 billion.

Thus in estimating the market for superconductor technology it is important to distinguish between the various levels in the supply chain. $2 million for the niobium contrasts markedly with a societal cost of up to $12 billion.

POWER TRANSMISSION

In their papers on power transmission, E. Forsyth and R. Thomas have made the following observations.

Lord Kelvin was the first to point out that the choice of conductor size for a transmission system is determined by the minimum annual operating cost obtained by summing the annual cost of losses in the conductor and the annual cost of capital. This is never the condition of minimum energy loss!

The sources of loss in AC superconducting power transmission lines are:-

1. Conductor: hysteretic, eddy current, resistive.
2. Insulation: ac dielectric loss
3. Heat leak.

These losses are removed as heat by the refrigerator. In the case of large efficient refrigerators, the amount of electrical energy to remove 1 watt of heat at low temperature is:-

300Watts/watt at 4.2 K; 200W/W @ 7 K & 10W/W @ 77 K.

Note that the Brookhaven Demonstration SC line operated at 7 K.

A serious study of Bulk Power Transmission comparing 16 different technologies was that by the Philadelphia Electric Company in 1977 for the US DOE. This system was required to carry 10,000 MVA over a distance of 66 miles through Pennsylvania to Philadelphia. BNL chose a 3 circuit 230kVA system in which each circuit has a contingency rating of 5,000 MVA to guarantee reliability. This SC system was rated in top three preferred designs. However it was not competitive with overhead lines. The final transmission cost comparisons for transmission losses were:-

230 kV Superconducting - 0.346 cents/kWhr
500 kV HPOPT Cellulose - 0.605 cents/kWhr
500 kV Aerial/Underground - 0.208 cents/kWhr

Superconducting Power Transmission is technically feasible.
Many problems must be overcome before the new ceramics can be considered for this purpose.
The most economic system may not be that with lowest loss.
Superconducting power transmission is not lossless.
The costs of a new demonstration system would be less than those used in these studies because of the experience gained in its development.
Helium cost was about 3% of total system cost for the BNL line
Using cost figures from the previous line, a line with ceramic superconductors of equivalent performance and cost might reduce overall system costs by 23%. Much more information is needed for a true comparison.

CONCLUSIONS

A sophisticated superconducting electrotechnology has been developed over the last 25 years. The high temperature superconductors of today represent an evolution, not a revolution. Room temperature superconductors are 'Pie in the Sky' at present. The technology has not received widespread societal use for reasons that have nothing to do with the need for liquid helium.

The high temperature superconducting materials of today have adequate properties for use in low power, low magnetic field electronic applications: critical temperatures and magnetic fields far surpass anything we have had previously, but the critical currents are orders of magnitude too low for most magnet and power applications so far conceived. Nitrogen cooled operation (ie. around 77 K) offers the prospect of cheaper, simpler and more reliable systems. However, cryopumping is lost at liquid nitrogen temperatures and some systems such as power transmission lines would need some system to provide the needed thermal isolation for low heat leak.

In MRI, low temperature superconductivity extended the possibilities of the new technology: the new materials may simplify refrigeration and reduce cost/scan by about 6%. Machines such as the Supercollider would not have been contemplated without superconductivity; however the low temperature helium provides cryopumping for the high vacuum system: this would be lost with high temperature superconductors. A similar situation exists in magnetic fusion where the cryopumping helium removes the helium ash of the reaction.

The prospects for magnetic fusion or commercial MHD power plants are not dependent upon superconducting electrotechnology and higher temperature operation would have marginal impact on life cycle cost. Similar reasoning applies to bulk electrical power transmission.

Many problem areas in the development and processing of high temperature superconductors need resolution. The search for new materials which extend the high temperature range to room temperature operation should continue. A thorough theoretical and experimental understanding of the new materials is needed. Many processing problems remain to be solved, both for thin films and the bulk conductors needed in magnet and power applications.

Given suitable conductors, possibilities for application should be explored as quickly as possible. Nitrogen is plentiful and cheap, helium will become increasingly expensive by the turn of the century when there will be a need to develop new sources of supply. This is an added incentive to pursue high temperature superconductor application with vigor and determination.

Thus - in summary:-

Superconducting coils permit continuous DC operation at zero energy loss: with superconducting interconnections they operate as permanent magnets. They offer large cheap high intensity fields in large volumes, if needed.

High temperature superconducting materials cost as much as low temperature materials at present; in fact, the spread in price is at least one order of magnitude for the high temperature materials. High temperature conductors do not yet exist and hence no estimate of cost can be made.

MRI:- Room temperature operation would save 12%/scan; all other factors being equal. Liquid nitrogen temperature operation would save an intermediate amount.

RF cavities are a good bet for high temperature superconductor use if the problems can be solved..

MHD & FUSION:- Refrigeration is about 1.8% of system cost. They might never come to be used in Utility systems.

SSC:- Refrigeration is 2% of total cost; less than magnet contingency. It could be the last big collider.

Transmission:- Savings with high temperature superconductors indeterminate at present: needs time and study.

AC uses are promising for the low temperature materials. It is not known what the new high temperature materials have to offer as yet.

FUTURE WORK

CONTINUE LTSC DEVELOPMENT AND APPLICATION

CONTINUE HTSC MATERIALS DEVELOPMENT

CONTINUE THEORETICAL STUDIES OF HTSC

CONTINUE EXPERIMENTAL STUDIES OF HTSC

APPLY PRESENT HTSC's IN ELECTRONICS WHEN POSSIBLE

HTSC RF CAVITY DEVELOPMENT COULD BE PROMISING

FABRICATE HTSC MAGNET CONDUCTORS

GENERAL REFERENCES

The literature on superconductivity is voluminous. Applications are treated extensively in the proceedings of various topical conferences. These include:

1. The Cryogenic Engineering Conference Series published by Plenum Press.

2. The Applied Superconductivity Series: published as IEEE Transactions on Magnetics since the 1974 conference.

3. The Proceedings of the International Conferences on Magnet Technology series. These have been published in various ways depending on the host institution. MT-9 (1985) was published by SIN - The Swiss Institute for Nuclear Research.

4. The Proceedings of the International Cryogenic Engineering Conferences, beginning in 1967, now published by Butterworths.

5. The Proceedings of the Particle Accelerator Conferences. published as IEEE Nuclear and Plasma Sciences volumes.

6. The Proceedings of the Symposia on Engineering Problems of Fusion Research, published by the IEEE.

Note: A complete listing would take a separate volume!

ACKNOWLEDGEMENTS

The information presented in this paper has been derived from a large number of friends over the years. We have also drawn on material provided by members of the Hulm Panel on High Temperature Superconductivity whose report was published by the U.S. Academy of Sciences in September 1987. Staff members of Westinghouse Research, Brookhaven Laboratory, the SSC Central Design Group and associated organizations and many others contributed papers and photographs as needed. We thank them all for their generous help.

CHAPTER 7

SQUID CONCEPTS AND SYSTEMS

John Clarke

Department of Physics, University of California
and
Materials and Chemical Sciences Division, Lawrence Berkeley Laboratory
Berkeley, California 94720

I. INTRODUCTION

Superconducting QUantum Interference Devices (SQUIDs) are the most sensitive detectors of magnetic flux currently available. They are amazingly versatile, being able to measure any physical quantity that can be converted to a flux, for example, magnetic field, magnetic field gradient, current, voltage, displacement, and magnetic susceptibility. As a result, the applications of SQUIDs are wide ranging, from the detection of tiny magnetic fields produced by the human brain and the measurement of fluctuating geomagnetic fields in remote areas to the detection of gravity waves and the observation of spin noise in an ensemble of magnetic nuclei.

SQUIDs combine two physical phenomena, flux quantization, the fact that the flux Φ in a closed superconducting loop is quantized[1] in units of the flux quantum $\Phi_0 \equiv h/2e \cong 2.07 \times 10^{-15}$ Wb, and Josephson tunneling[2]. There are two kinds of SQUIDs. The first[3], the dc SQUID, consists of two Josephson junctions connected in parallel in a superconducting loop, and is so named because it can be operated with a steady current bias. The second[4,5], the rf SQUID, involves a single Josephson junction interrupting the current flow around a superconducting loop, and is operated with a radiofrequency flux bias. In both cases, the output from the SQUID is periodic with period Φ_0 in the magnetic flux applied to the loop. One generally is able to detect an output signal corresponding to a flux change of much less than one flux quantum.

In this chapter I try to give an overview of the current state of the SQUID art. I cannot hope to describe all of the SQUIDs that have been made or, even less, all of the applications in which they have been successfully used. I begin, in Sec. II, with a brief review of the resistively-shunted Josephson junction, with particular emphasis on the effects of noise. Section III contains a description of the dc SQUID: how these devices are made and operated, and the limitations imposed by noise. Section IV contains a similar description of the properties of rf SQUIDs, but because there has been little development of these devices in the 1980's, I shall keep this section relatively brief. In Sec.V, I describe a selection of instruments based on SQUIDs and mention some of their applications. Section VI contains a discussion of the impact of high temperature superconductivity on SQUIDs, and of future prospects in this area, while Sec.VII contains a few concluding remarks.

II. THE RESISTIVELY SHUNTED JUNCTION

A Josephson junction[2] consists of two superconductors separated by a thin insulating barrier. Cooper pairs of electrons (or holes) are able to tunnel through the barrier, maintaining phase coherence in the process. The applied current, I, controls the difference $\delta = \phi_1 - \phi_2$ between the phases of the two superconductors according to the current-phase relation

$$I = I_0 \sin \delta, \tag{2.1}$$

where I_0 is the critical current, that is, the maximum supercurrent the junction can sustain. When the current is increased from zero, initially there is no voltage across the junction, but for $I > I_0$ a voltage V appears, and δ evolves with time according to the voltage frequency relation

$$\dot{\delta} = 2eV/\hbar = 2\pi V/\Phi_0. \tag{2.2}$$

A high quality Josephson tunnel junction has a hysteretic current-voltage (I - V) characteristic. As the current is increased from zero, the voltage switches abruptly to a nonzero value when I exceeds I_0, but returns to zero only when I is reduced to a value much less than I_0. This hysteresis must be eliminated for SQUIDs operated in the conventional manner, and one does so by shunting the junction with an external shunt resistance. The "resistively shunted junction" (RSJ) model [6,7] is shown in Fig.1(a). The junction has a critical current I_0 and is in parallel with its self-capacitance C and with its shunt resistance R, which has a current noise source $I_N(t)$ associated with it. The equation of motion is

$$C\dot{V} + I_0 \sin\delta + V/R = I + I_N(t). \tag{2.3}$$

Neglecting the noise term for the moment and setting $V = \hbar\dot{\delta}/2e$, we obtain

$$\frac{\hbar C}{2e}\ddot{\delta} + \frac{\hbar}{2eR}\dot{\delta} = I - I_0 \sin\delta = -\frac{2e}{\hbar}\frac{\partial U}{\partial \delta}, \tag{2.4}$$

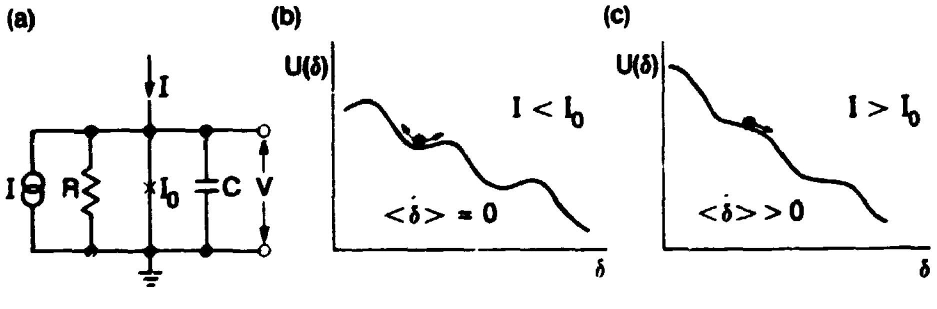

Fig. 1(a) The resistively shunted Josephson junction; (b) and (c) show the tilted washboard model for $I < I_0$ and $I > I_0$.

where

$$U = -\frac{\Phi_0}{2\pi}(I\delta + I_0 \cos\delta). \tag{2.5}$$

One obtains considerable insight into the dynamics of the junction by realizing that Eq. (2.4) also describes the motion of a ball moving on the "tilted washboard" potential U. The term involving C represents the mass of the particle, the 1/R term represents the damping of the motion, and the average "tilt" of the washboard is proportional to -I. For values of $I < I_0$, the particle is confined to one of the potential wells [Fig. 1(b)], where it oscillates back and forth at the plasma frequency[1] $\omega_p = (2\pi I_0/\Phi_0 C)^{1/2}\,[1-(I/I_0)^2]^{1/4}$. In this state $<\dot{\delta}>$ and hence the average voltage across the junction are zero (< > represents a time average). When the current is increased to I_0, the tilt increases, and when I exceeds I_0, the particle rolls down the washboard; in this state $<\dot{\delta}>$ is nonzero, and a voltage appears across the junction [Fig.1(c)]. As the current is increased further, $<\dot{\delta}>$ increases, as does V. For the nonhysteretic case, as soon as I is reduced below I_0 the particle becomes trapped in one of the wells, and V returns to zero. In this, the overdamped case, we require[6,7]

$$\beta_C \equiv (2\pi I_0 R/\Phi_0)RC = \omega_J RC \lesssim 1; \tag{2.6}$$

$\omega_J/2\pi$ is the Josephson frequency corresponding to the voltage $I_0 R$.

We introduce the effects of noise by restoring the noise term to Eq. (2.4) to obtain the Langevin equation

$$\frac{\hbar C}{2e}\ddot{\delta} + \frac{\hbar}{2eR}\dot{\delta} + I_0 \sin\delta = I + I_N(t). \tag{2.7}$$

In the thermal noise limit, the spectral density of $I_N(t)$ is given by the Nyquist formula

$$S_I(f) = 4k_B T/R, \tag{2.8}$$

where f is the frequency. It is evident that $I_N(t)$ causes the tilt in the washboard to fluctuate with time. This fluctuation has two effects on the junction. First, when I is less than I_0, from time to time fluctuations cause the total current $I + I_N(t)$ to exceed I_0, enabling the particle to roll out of one potential minimum into the next. For the underdamped junction, this process produces a series of voltage pulses randomly spaced in time. Thus, the time average of the voltage is nonzero even though $I < I_0$, and the I - V characteristic is "noise-rounded" at low voltages.[8] Because this thermal activation process reduces the observed value of the critical current, there is a minimum value of I_0 for which the two sides of the junction remain coupled together. This condition may be written as

$$I_0\Phi_0/2\pi \gtrsim 5k_BT, \tag{2.9}$$

where $I_0\Phi_0/2\pi$ is the coupling energy of the junction[2] and the factor of 5 is the result of a computer simulation[9]. For $T = 4.2K$, we find $I_0 \gtrsim 0.9\mu A$.

The second consequence of thermal fluctuations is voltage noise. In the limit $\beta_C << 1$ and for $I > I_0$, the spectral density of this noise at a measurement frequency f_m that we assume to be much less than the Josephson frequency f_J is given by[10,11]

$$S_V(f_m) = \left[1+\frac{1}{2}\left(\frac{I_0}{I}\right)^2\right]\frac{4k_BTR_D^2}{R} \cdot \left\{\begin{matrix}\beta_C << 1\\ I > I_0\\ f_m << f_J\end{matrix}\right\} \tag{2.10}$$

The first term on the right-hand side of Eq. (2.10) represents the Nyquist noise current generated at the measurement frequency f_m flowing through the dynamic resistance $R_d \equiv dV/dI$ to produce a voltage noise - see Fig. 2. The

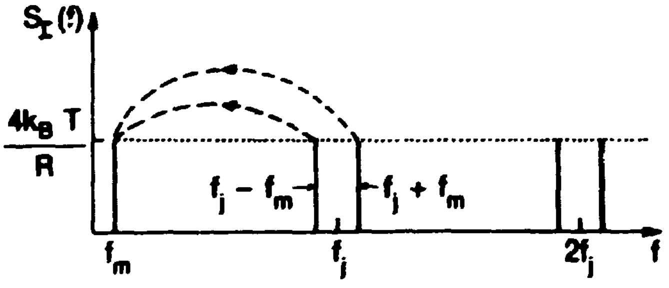

Fig. 2 Schematic representation for the noise terms in Eq.(2.10). The Nyquist noise generated in the resistor at frequency f_m contributes directly at f_m; that generated at $f_J \pm f_m$ is mixed down to f_m.

second term, $(1/2)(I_0/I)^2(4k_BT/R)\,R_d^2$, represents Nyquist noise generated at frequencies $f_J \pm f_m$ mixed down to the measurement frequency by the Josephson oscillations and the inherent nonlinearity of the junction. The factor $(1/2)(I_0/I)^2$ is the mixing coefficient, and it vanishes for sufficiently large bias currents. The mixing coefficients for the Nyquist noise generated near harmonics of the Josephson frequencies, $2f_J, 3f_J$, ---, are negligible in the limit $f_m/f_J \ll 1$.

At sufficiently high bias current, the Josephson frequency f_J exceeds k_BT/h, and quantum corrections[12] to Eq. (2.10) become important, provided the term $(1/2)(I_0/I)^2$ is not too small. The requirement for observing significant quantum corrections is $eI_0R/k_BT \gg 1$. The spectral density of the voltage noise becomes

$$S_V(f_m) = \left[\frac{4k_BT}{R} + \frac{2eV}{R}\left(\frac{I_0}{I}\right)^2 \coth\left(\frac{eV}{k_BT}\right)\right]R_d^2, \quad \left\{\begin{matrix} \beta_C \ll 1 \\ I > I_0 \\ f_m \ll f_J \end{matrix}\right\} \qquad (2.11)$$

where we have assumed that $hf_m/k_BT \ll 1$, so that the first term on the right-hand side of Eq. (2.11) remains in the thermal limit. In the limit $T \to 0$, the second term, $(2eV/R)(I_0/I)^2R_d^2$, represents noise mixed down from zero point fluctuations near the Josephson frequency.

This concludes our review of the RSJ, and we now turn our attention to the dc SQUID.

III. THE DC SQUID

A. A First Look

The essence of the dc SQUID[3] is shown in Fig. 3(a). Two junctions are connected in parallel on a superconducting loop of inductance L. Each junction is resistively shunted to eliminate hysteresis on the I-V characteristics, which are shown in Fig. 3(b) for $\Phi = n\Phi_0$ and $(n + 1/2)\Phi_0$, where Φ is the external flux applied to the loop and n is an integer. If we bias the SQUID with a constant current ($> 2I_0$), the voltage across the SQUID oscillates with period Φ_0 as we steadily increase Φ, as indicated in Fig. 3(c). The SQUID is generally operated on the steep part of the V - Φ curve where the transfer

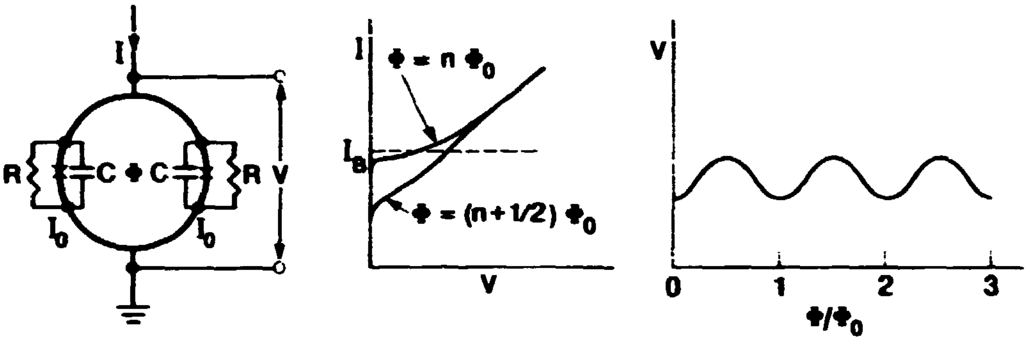

(a) (b) (c)

Fig. 3(a) The dc SQUID; (b) I-V characteristics; (c) V vs. Φ/Φ_0 at constant bias current I_B.

coefficient, $V_\Phi \equiv |(\partial V/\partial \Phi)_I|$, is a maximum. Thus, the SQUID produces an output voltage in response to a small input flux $\delta\Phi$ ($<< \Phi_0$), and is effectively a flux-to-voltage transducer.

Before we give a detailed description of the signal and noise properties of the SQUID, it may be helpful to give a simplified description that, although not rigorous, gives some insight into the operation of the device. We assume the two junctions are identical and arranged symmetrically on the loop. We further assume, for simplicity, that the bias current is swept from zero to a value above the critical current of the two junctions at a frequency much higher than $d\Phi/\Phi_0 dt$. In the absence of any applied flux (or with $\Phi = n\,\Phi_0$), there is no current circulating around the loop and the bias current divides equally between the two junctions. The measured critical current is $2I_0$ (if we ignore noise rounding). If we apply a magnetic flux, Φ, the flux in the loop will be quantized and will generate a current $J = -\Phi / L$, where we have neglected the effects of the two junctions [Figs. 4(a) and (b)]. The circulating current adds to the bias current flowing through junction 1 in Fig. 4(a) and subtracts from that flowing through 2. In this naive picture, the critical current of junction 1 is reached when $I/2 + J = I_0$, at which point the current flowing through junction 2 is $I_0 - 2J$. Thus, the SQUID switches to the voltage state when $I = 2I_0 - 2J$. As Φ is increased to $\Phi_0 / 2$, J increases to $\Phi_0 / 2L$ [Fig. 4(b)], and the critical current falls to $2I_0 - \Phi_0 / L$ [Fig. 4(c)]. As the flux is increased beyond $\Phi_0 / 2$, however, the SQUID makes a transition from the flux state $n = 0$ to $n = 1$, and J changes sign [Fig. 4(b)]. As we increase Φ to Φ_0, J is reduced to zero and the critical current

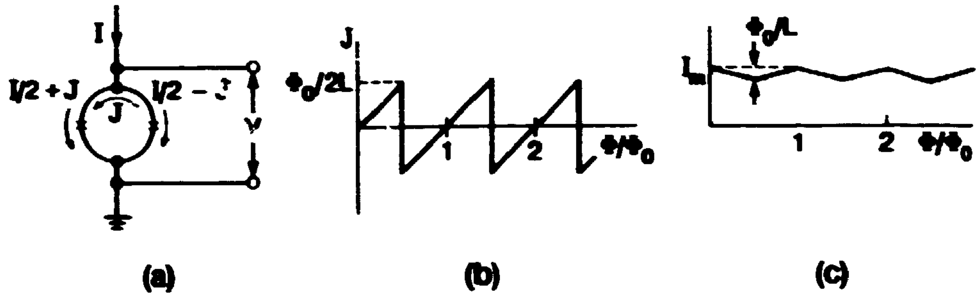

Fig. 4 Simplistic view of the dc SQUID: (a) a magnetic flux Φ generates a circulating current J that is periodic in Φ as shown in (b); as a result (c), the maximum supercurrent I_m is also periodic in Φ.

is restored to its maximum value $I_m = 2I_0$ [Fig. 4(c)]. In this way the critical current oscillates as a function of Φ.

Continuing with our simplified model, we see that the voltage change across the SQUID (at the peak of the current sweep) as we change Φ from 0 to $\Phi_0 / 2$ is $\Delta V = (\Phi_0 / L)R/2$, where R/2 is the parallel resistance of the two shunts. Hence, $V_\Phi = \Delta V / (\Phi_0 / 2) = R / L$.

We also can estimate the equivalent flux noise of the SQUID. If the noise voltage across the SQUID is $V_N(t)$ with a spectral density $S_V(f)$, the corresponding flux noise referred to the SQUID loop is just

$$S_\Phi(f) = S_V(f) / V_\Phi^2. \tag{3.1}$$

A convenient way of characterizing the flux noise is in terms of the noise energy per unit bandwidth,

$$\varepsilon(f) = S_\Phi(f) / 2L. \tag{3.2}$$

If we assume that the noise in the SQUID is just the Nyquist noise in the shunt resistor with spectral density $4k_BT$ (R/2), we find $\varepsilon(f) = k_BTL/R$. Although these results are not quantitatively correct, they do give the correct scaling with the various parameters. For example, we see that to lower $\varepsilon(f)$ we should reduce T and L while using the largest possible value of R subject to the I - V characteristic remaining nonhysteretic.

Exact results for the signal and noise can be obtained only from computer simulation. The results show that the plots of the circulating supercurrent and the critical current vs. Φ become smoothed. Furthermore, the noise voltage is higher than Nyquist noise because of mixed-down noise; unfortunately the magnitude of this noise cannot be obtained analytically.

One final remark is appropriate at this point. To observe quantum interference effects, we require the modulation depth of the critical current, Φ_0 / L, to be much greater than the root mean square noise current in the loop, $<I_N^2>^{1/2} = (k_B T / L)^{1/2}$. This condition can be written $L \lesssim \Phi_0^2 / 5k_B T$, where the factor of 1/5 is the result of a computer analysis[9]. For T = 4.2K, we find L ≲ 15 nH.

B. Thermal Noise in the SQUID : Theory

A model for noise calculations is shown in Fig. 5. This figure shows two independent Nyquist noise currents, $I_{N1}(t)$ and $I_{N2}(t)$, associated with the two shunt resistors. The phase differences across the junctions, $\delta_1(t)$ and $\delta_2(t)$, obey the following equations:[13-15]

$$V = \frac{\hbar}{4e}\left(\dot{\delta}_1 + \dot{\delta}_2\right), \tag{3.3}$$

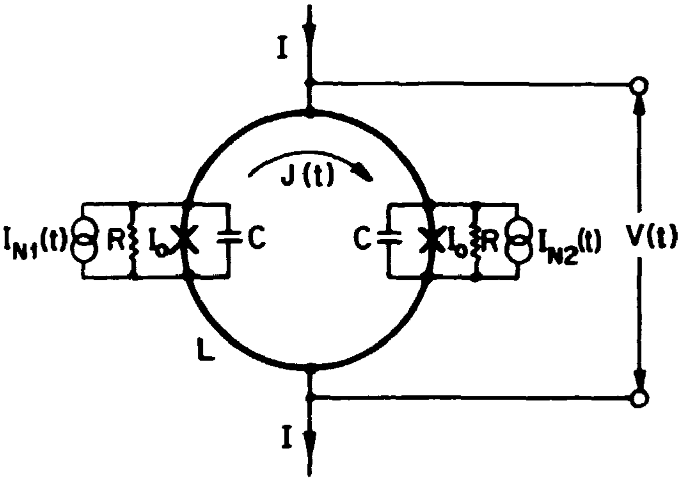

Fig.5 Model of dc SQUID showing noise sources associated with the shunt resistors.

$$J = \frac{\Phi_0}{2\pi L}\left(\delta_1 - \delta_2 - \frac{2\pi\Phi}{\Phi_0}\right) \tag{3.4}$$

$$\frac{\hbar C}{2e}\ddot{\delta}_1 + \frac{\hbar}{2eR}\dot{\delta}_1 = \frac{I}{2} - J - I_0 \sin\delta_1 + I_{N1}, \tag{3.5}$$

and

$$\frac{\hbar C}{2e}\ddot{\delta}_2 + \frac{\hbar}{2eR}\dot{\delta}_2 = \frac{I}{2} + J - I_0 \sin\delta_2 + I_{N2}\,. \tag{3.6}$$

Equation (3.3) relates the voltage to the average rate of change of phase; Eq. (3.4) relates the current in the loop, J, to $\delta_1 - \delta_2$ and to Φ; and Eqs. (3.5) and (3.6) are Langevin equations coupled via J. These equations have been solved numerically for a limited range of values of the noise parameter $\Gamma = 2\pi k_B T / I_0 \Phi_0$, reduced inductance $\beta = 2\,LI_0 / \Phi_0$ and hysteresis parameter β_C. For typical SQUIDs in the ^{4}He temperature range, $\Gamma = 0.05$. One computes the time-averaged voltage V vs. Φ, and hence finds V_Φ, which, for a given value of Φ, peaks smoothly as a function of bias current. The transfer function exhibits a shallow maximum around $(2n + 1)\,\Phi_0 / 4$. One computes the noise voltage for a given value of Φ as a function of I, and finds that the spectral density is white at frequencies much less than the Josephson frequency. For each value of Φ, the noise voltage peaks smoothly at the value of I where V_Φ is a maximum. From these simulations, one finds that the noise energy has a minimum when $\beta \approx 1$. For $\beta = 1$, $\Gamma = 0.05$, $\Phi = (2n + 1)\,\Phi_0 / 4$ and for the value of I at which V_Φ is a maximum, the results can be summarized as follows:

$$V_\Phi \approx R/L, \tag{3.7}$$

$$S_V(f) \approx 16 k_B T R, \tag{3.8}$$

and

$$\varepsilon(f) \approx 9 k_B T L/R. \tag{3.9}$$

We see that our rough estimate of V_Φ in Sec. IIIA was rather accurate, but that the assumption that the noise spectral density was given by the Nyquist result underestimated the computed value by a factor of about 8.

It is often convenient to eliminate R from Eq. (3.9) using the expression $R = (\beta_C \Phi_0 / 2\pi I_0 C)^{1/2}$. We find

$$\varepsilon(f) \approx 16\, k_B T (LC/\beta_C)^{1/2}. \quad (\beta_C \lesssim 1) \tag{3.10}$$

Equation (3.10) gives a clear prescription for improving the resolution: one should reduce T, L and C. A large number of SQUIDs with a wide range of parameters have been tested and found to have white noise energies generally in good agreement with the predicted values. It is common practice to quote the noise energy of SQUIDs in units of $\hbar$ ($\approx 10^{-34}$J sec $= 10^{-34}$JHz^{-1}).

In closing this discussion, we emphasize that although $\varepsilon(f)$ is a useful parameter for characterizing the resolution of SQUIDs with different inductances, it is not a complete specification because it does not account fully for the effects of current noise in the SQUID loop. We defer a discussion of this point to Sec. V.D.

C. Practical dc SQUIDs

Modern dc SQUIDs are invariably made from thin films with the aid of either photolithography or electron beam lithography. A major concern in the design is the need to couple an input coil inductively to the SQUID with rather high efficiency. This problem was elegantly solved by Ketchen and Jaycox,[16,17] who introduced the idea of depositing a spiral input coil on a SQUID in a square washer configuration. The coil is separated from the SQUID with an insulating layer. The version[18] of this design made at UC Berkeley is shown in Fig. 6. These devices are made in batches of 36 on 50mm diameter oxidized silicon wafers in the following way. First, a 30nm thick Au (25 wt % Cu) film is deposited and patterned to form the resistive shunts. Next, we sputter a 100nm thick Nb film and etch it to form the SQUID loop and a strip that eventually contacts the inner end of the spiral coil. The third film is a 200 nm SiO layer with 2 μm diameter windows for the junctions, a larger window to give access to the CuAu shunt, and a window at each end of the Nb strip to provide connections to the spiral coil. The next step is to deposit and lift off the 300 nm thick Nb spiral coil, which has 4, 20 or 50 turns. At this point, we usually dice the wafer into

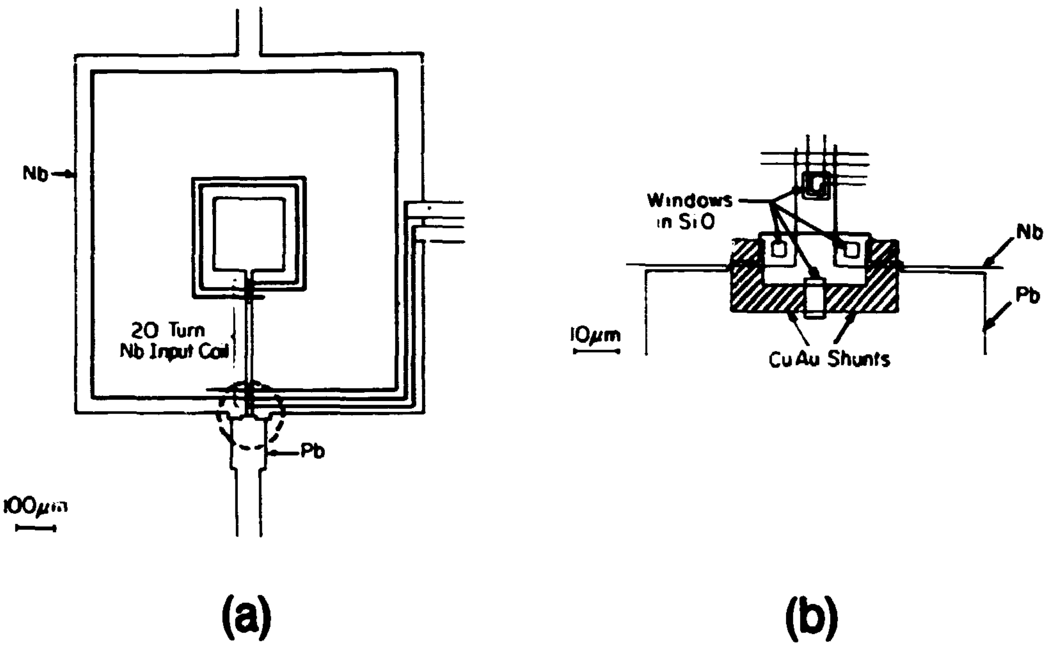

Fig.6 (a) Configuration of planar dc SQUID with overlaid spiral input coil; (b) expanded view of junctions and shunts.

chips, each with a single SQUID which is completed individually. The device is ion milled to clean the exposed areas of Nb and CuAu. We have two procedures for forming the oxide barrier. In one, we oxidize the Nb in a rf discharge in Ar containing 5 vol % O_2, and deposit the 300 nm Pb (5wt % In) counterelectrode which completes the junctions and makes contact with the shunts. In the other process, we deposit approximately 6 nm of Al and form Al_2O_3 by exposing[19] it to O_2. A photograph of the completed SQUID and a scanning electron micrograph of the junctions is shown in Fig. 7. The shunt resistance R is typically 8 Ω, and the estimated capacitance C about 0.5 pF.

Jaycox and Ketchen[17] showed that a square washer (with no slit) with inner and outer edges d and w has an inductance L (loop) = $1.25\mu_0 d$ in the limit w >> d. They gave the following expressions for the inductances of the SQUID, L, and of the spiral coil, L_i, and for the mutual inductance, M_i, and coupling coefficient, α^2, between the spiral coil and the SQUID:

$$L = L\,(\text{loop}) + L_j, \tag{3.11}$$

$$L_i = n^2\,(L-L_j) + L_s, \tag{3.12}$$

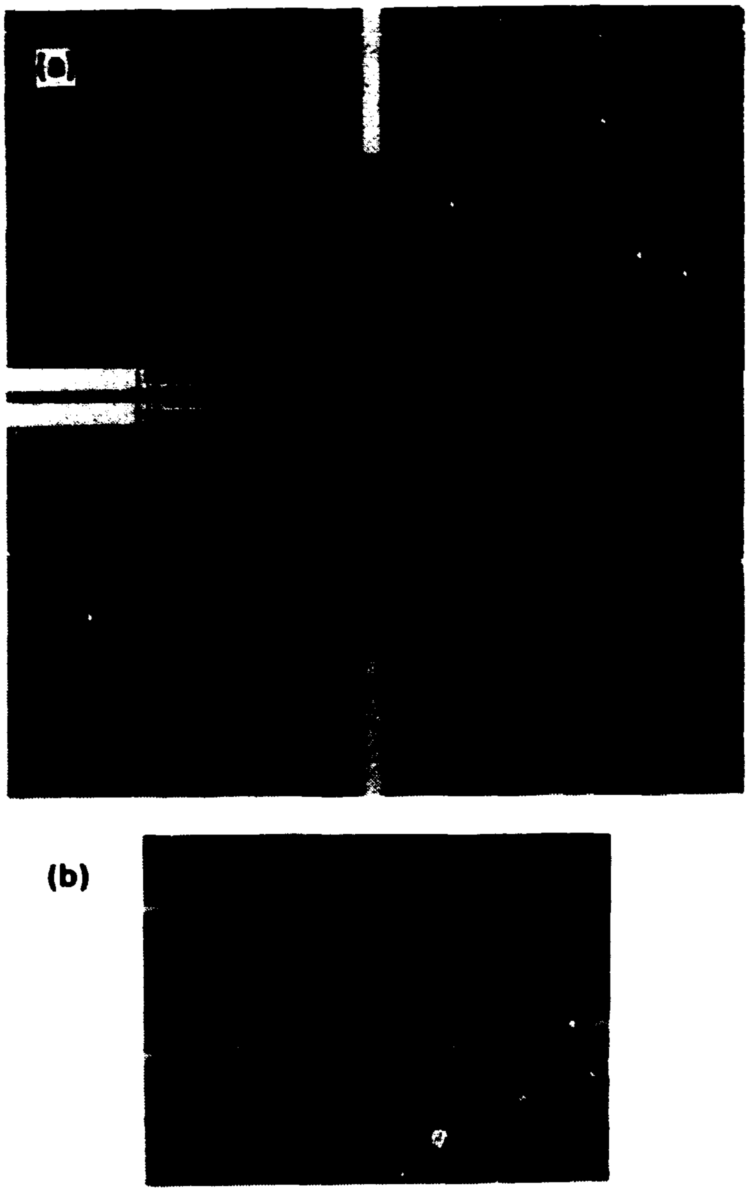

Fig.7(a) Photograph of planar dc SQUID made at UC Berkeley, with 4-turn input coil; the square washer is about 1mm across. (b) Electron micrograph of junctions prior to deposition of counterelectrode; each junction is about 3μm across.

$$M_i = n(L-L_j) \tag{3.13}$$

and

$$\alpha^2 = (1-L_j/L)/\,[1+L_s n^2(L-L_j)]. \tag{3.14}$$

Here, L_j is the parasitic inductance associated with the junctions, n is the number of turns of the input coil and L_s is the stripline inductance of this coil. For the SQUID just described with a 50-turn input coil, one measures $L_i \approx 800$ nH, $M_i \approx 16$ nH and $\alpha^2 \approx 0.75$. These results are in good agreement with the predictions of the above expressions if one takes the predicted value L(loop) ≈ 0.31 nH and assumes $L_j \approx 0.09$ nH to give L ≈ 0.4 nH. The stripline inductance (~10 nH) is insignificant for a 50-turn coil.

References 20-25 are a selection of papers describing SQUIDs fabricated on the basis of the Ketchen-Jaycox design. Some of the devices involve edge junctions in which the counterelectrode is a strip making a tunneling contact to the base electrode only at the edge. This technique enables one to make junctions with a small area and thus a small self-capacitance without resorting to electron-beam lithography. However, stray capacitances are often critically important. As has been emphasized by a number of authors, parasitic capacitance between the square washer and the input coil can produce resonances that, in turn, induce structure on the I-V characteristics and give rise to excess noise. One way to reduce these effects is to lower the shunt resistance in order to increase the damping. A different approach is to couple the SQUID to the signal via an intermediary superconducting transformer[24], so that the number of turns on the SQUID washer and the parasitic capacitance are reduced. Knuutila et al.[25] successfully damped the resonances in the input coil by terminating the stripline with a matched resistor. An alternate coupling scheme has been adopted by Carelli and Foglietti[26], who fabricated thin-film SQUIDs with many loops in parallel. The loops are coupled to a thin-film input coil surrounding them.

D. Flux-locked Loop

In most, although not all, practical applications one uses the SQUID in a feedback circuit as a null detector of magnetic flux[27]. One applies a modulating flux to the SQUID with a peak-to-peak amplitude $\Phi_0/2$ and a frequency f_m usually between 100 and 500 kHz, as indicated in Fig. 8. If the quasistatic flux in the SQUID is exactly $n\Phi_0$ the resulting voltage is a rectified version of the input signal, that is, it contains only the frequency $2f_m$ [Fig. 8(a)]. If this voltage is sent through a lock-in detector referenced to the fundamental frequency f_m, the output will be zero. On the other hand, if the quasistatic flux is $(n + 1/4)\Phi_0$, the voltage across the SQUID is at frequency f_m [Fig. 8(b)], and the output from the lock-in will be a maximum. Thus, as one increases the flux from $n\Phi_0$ to $(n + 1/4)\Phi_0$, the output from the lock-in will increase steadily; if one reduces the flux from $n\Phi_0$ to $(n - 1/4)\Phi_0$, the output will increase in the negative direction [Fig. 8(c)].

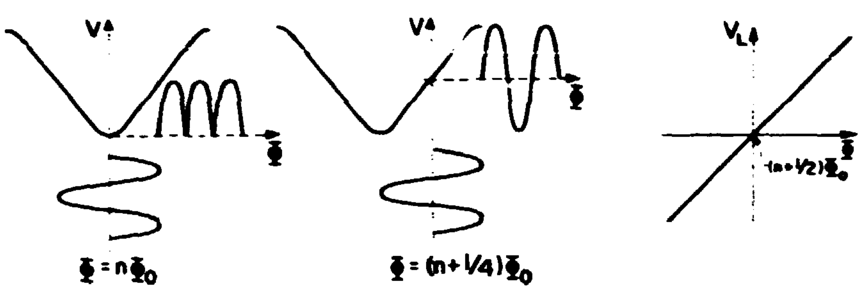

Fig. 8 Flux modulation scheme showing voltage across the SQUID for (a) $\Phi = n\Phi_0$ and (b) $\Phi = (n+1/4)\Phi_0$. The output V_L from the lock-in detector vs. Φ is shown in (c).

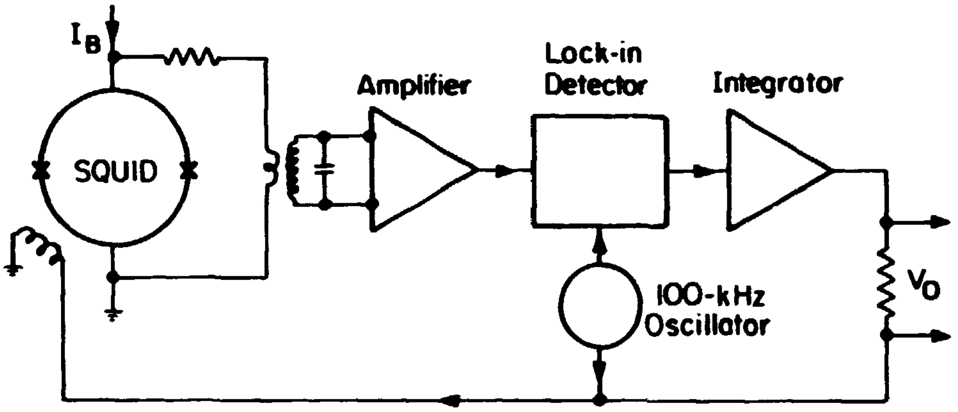

Fig. 9 Modulation and feedback circuit for the dc SQUID.

The alternating voltage across the SQUID is coupled to a low-noise preamplifier, usually at room temperature, via either a cooled transformer[28] or a cooled LC series-resonant circuit[27]. The first presents an impedance N^2R_d to the preamplifier, and the second, an impedance Q^2R_d, where R_d is the dynamic resistance of the SQUID at the bias point, N is the turns ratio of the transformer, and Q is the quality factor of the tank circuit. The value of N or Q is chosen to optimize the noise temperature of the preamplifier; with careful design, the noise from the amplifier can be appreciably less than that from the SQUID at 4.2 K.

Figure 9 shows a typical flux-locked loop in which the SQUID is coupled to the preamplifier via a cooled transformer. An oscillator applies a modulating flux to the SQUID. After amplification, the signal from the SQUID is lock-in detected and sent through an integrating circuit. The smoothed output is connected to the modulation and feedback coil via a large series resistor R_f. Thus, if one applies a flux $\delta\Phi$ to the SQUID, the feedback circuit will generate an opposing flux - $\delta\Phi$, and a voltage proportional to $\delta\Phi$ appears across R_f. This technique enables one to measure changes in flux ranging from much less than a single flux quantum to many flux quanta. The use of a modulating flux eliminates 1/f noise and drift in the bias current and preamplifier. Using ‘ modulation frequency of 500 kHz, a double transformer between the SQUID and the preamplifier, and a two-pole integrator, Wellstood et al.[18] achieved a dynamic range of $\pm 2 \times 10^7$ $Hz^{1/2}$ for signal frequencies up to 6 kHz, a frequency response from 0 to 70 kHz (±3 dB), and a maximum slew rate of $3 \times 10^6 \Phi_0$ sec^{-1}.

E. Thermal Noise in the dc SQUID : Experiment

One determines the spectral density of the equivalent flux noise in the SQUID by connecting a spectrum analyzer to the output of the flux-locked loop. A representative power spectrum[29] is shown in Fig. 10: above a 1/f noise region, the noise is white at frequencies up to the roll-off of the feedback circuit. In this particular example, with L = 200pH and R = 8Ω, the measured flux noise was $S_\Phi^{1/2} = (1.9 \pm 0.1) \times 10^{-6} \Phi_0 Hz^{-1/2}$, in reasonable agreement with the predictions of Eqs. (3.7) and (3.8). The corresponding flux-noise energy was 4×10^{-32} $JHz^{-1} \approx 400\,\hbar$. Many groups have achieved noise energies that are comparable or, with lower values of L or C, somewhat better.

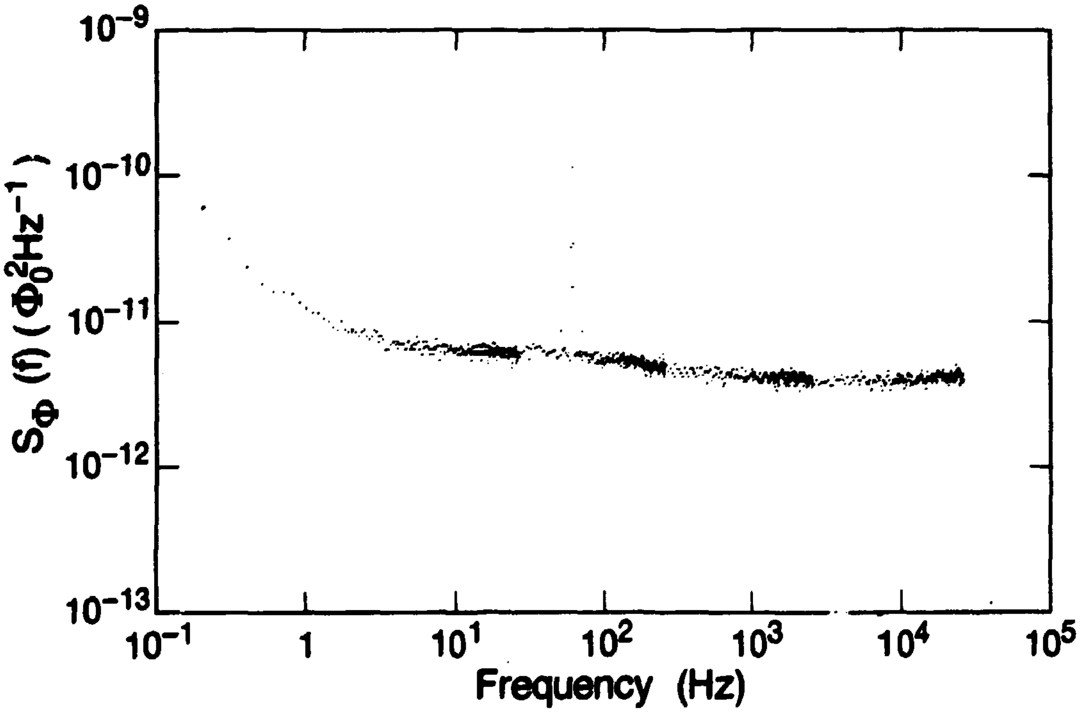

Fig.10 Spectral density of equivalent flux noise for dc SQUID with a Pb body : L = 0.2nH, R = 8Ω, and T = 4.2K (courtesy F.C. Wellstood).

Rather recently, Wellstood et al.[30] have operated SQUIDs in a dilution refrigerator at temperatures T below 1K, using a second dc SQUID as a preamplifier. They found that the noise energy scaled accurately with T at temperatures down to about 150 mK, below which the noise energy became nearly constant. This saturation was traced to heating in the resistive shunts, which prevented them from cooling much below 150mK. This heating is actually a hot-electron effect:[31,32] the bottleneck in the cooling process is the rate at which the electrons can transfer energy to the phonons which, in turn, transfer energy to the substrate. The temperature of the shunts was lowered by connecting each of them to a CuAu "cooling fin" of large volume. The hot electrons diffuse into the fins where they rapidly transfer energy to other electrons. Since the "reaction volume" is now greatly increased, the numbers of electrons and phonons interacting are also increased, and the electron gas is cooled more effectively. In this way, the effective electron temperature was reduced to about 50mK when the SQUID was at a bath temperature of 20mK, with a concomitant reduction in ε to about $5\hbar$. Very recently Ketchen et al.[33] have achieved a noise energy of about $2\hbar$ at 0.3 K in a SQUID with L = 100 pH and C = 0.14 pF.

F. 1/f Noise in dc SQUIDs

The white noise in dc SQUIDs is well understood. However, some applications of SQUIDs, for example neuromagnetism, require good resolution at frequencies down to 0.1 Hz or less, and the level of the 1/f or "flicker" noise becomes very important.

There are at least two separate sources of 1/f noise in the dc SQUID[34]. The first arises from 1/f fluctuations in the critical current of the Josephson junctions, and the mechanism for this process is reasonably well understood[35]. In the process of tunneling through the barrier, an electron becomes trapped on a defect in the barrier and is subsequently released. While the trap is occupied, there is a local change in the height of the tunnel barrier and hence in the critical current density of that region. As a result, the presence of a single trap causes the critical current of the junction to switch randomly back and forth between two values, producing a random telegraph signal. If the mean time between pulses is τ, the spectral density of this process is a Lorentzian,

$$S(f) \propto \frac{\tau}{1+(2\pi f\tau)^2}, \tag{3.15}$$

namely white at low frequencies and falling off as $1/f^2$ at frequencies above $1/2\pi\tau$. In many cases, the trapping process is thermally activated, and τ is of the form

$$\tau = \tau_0 \exp\,(E/k_0T), \tag{3.16}$$

where τ_0 is a constant and E is the barrier height.

In general, there may be several traps in the junction, each with its own characteristic time τ_i. One can superimpose the trapping processes, assuming them to be statistically independent, to obtain a spectral density[36]

$$S(f) \propto \int dE\, D(E)\left[\frac{\tau_0 \exp(E/k_BT)}{1+(2\pi f\tau_0)^2 \exp(2E/k_BT)}\right], \tag{3.17}$$

where D(E) is the distribution of activation energies. The term in square brackets is a strongly peaked function of E, centered at $\tilde{E} \equiv k_BT\ln(1/2\pi f\tau_0)$, with a width ~ k_BT. Thus, at a given temperature, only traps with energies within a range k_BT of $\tilde{E}$ contribute significantly to the noise. If one now assumes D(E) is broad with respect to k_BT, one can take $D(\tilde{E})$ outside the integral, and carry out the integral to obtain

$$S(f,T) \propto \frac{k_BT}{f} D(\tilde{E}). \tag{3.18}$$

In fact, one obtains a 1/f-like spectrum from just a few traps.

The magnitude of the 1/f noise in the critical current depends strongly on the quality of the junction as measured by the current leakage at voltages below $(\Delta_1 + \Delta_2)/e$, where Δ_1 and Δ_2 are the energy gaps of the two superconductors. Traps in the barrier enable electrons to tunnel in this voltage range, a process producing both leakage current and 1/f noise. Thus, for a given technology, junctions with low subgap leakage currents will have low 1/f noise. Figure 11 shows an example of a Nb-Al_2O_3-Nb junction with a single trap[37]. The junction was resistively shunted and voltage biased at typically 1.5 μV; the noise currents were measured with a SQUID. At 4.2 K [Fig.11(a)], the noise is approximately Lorentzian; the switching process producing the noise is shown in the inset. Figure 11(b) shows that at 1.5 K the noise is substantially reduced as the trap freezes out. By measuring the temperature dependence of the random telegraph signal, Savo et al.[37] found that τ obeyed Eq. (3.16) with τ_0 = 10 s and

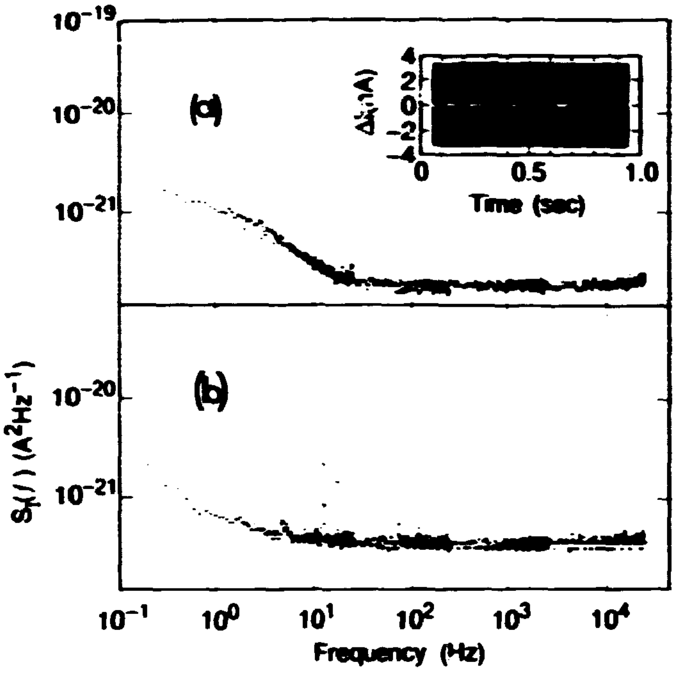

Fig.11 Spectral density of fluctuations in the critical current of a single Nb-Al_2O_3-Nb tunnel junction at (a) 4.2K and (b) 1.5K. Inset in (a) shows fluctuations vs. time (from ref.37).

E = 1.8 meV. Furthermore, τ was exponentially distributed, as expected, with an average value of 107 ms at 4.2 K.

The second source of l/f noise in SQUIDs appears to arise from the motion of flux lines trapped in the body of the SQUID[34], and is less well understood than the critical current noise. This mechanism manifests itself as a flux noise; for all practical purposes the noise source behaves as if an external flux noise were applied to the SQUID. Thus, the spectral density of the l/f flux noise scales as V_Φ^2, and, in particular, vanishes at $\Phi = (n \pm 1/2)\Phi_0$ where $V_\Phi = 0$. By contrast, critical current noise is still present when $V_\Phi = 0$, although its magnitude does depend on the applied flux.

The level of l/f flux noise appears to depend strongly on the microstructure of the thin films. For example, SQUIDs fabricated at Berkeley with Nb loops sputtered under a particular set of conditions show l/f flux noise levels of typically[34] $10^{-10}\ \Phi_0^2\,Hz^{-1}$ at 1 Hz. On the other hand, SQUIDs with Pb loops in exactly the same geometry exhibit a l/f noise level of about $2x10^{-12}\ \Phi_0^2Hz^{-1}$ at 1 Hz, arising from critical current fluctuations. Tesche et al.[38]

reported a l/f noise level in Nb-based SQUIDs of about $3\times10^{-13}\,\Phi_0^2\,\mathrm{Hz}^{-1}$, while Foglietti et al.[39] found a critical current l/f noise corresponding to $2\times10^{-12}\,\Phi_0^2\,\mathrm{Hz}^{-1}$, also in Nb based devices. Thus, we conclude that the quality of the Nb films plays a significant role in the level of l/f flux noise. It is of considerable fundamental and practical interest to understand the mechanism in detail.

There is an important practical difference between the two sources of l/f noise: critical current noise can be reduced by a suitable modulation scheme, whereas flux noise cannot. To understand how to reduce critical current l/f noise, we first note that at constant current bias the spectral density of the l/f voltage noise across the SQUID can be written in the approximate form

$$S_V(f) \approx \frac{1}{2}\left[(\partial V/\partial I_0)^2 + L^2 V_\Phi^2\right] S_{I_0}(f). \tag{3.19}$$

In Eq. (3.19), we have assumed that each junction has the same level of critical current noise, with a spectral density $S_{I_0}(f)$. The first term on the right is the "in-phase mode", in which each of the two junctions produces a fluctuation of the same polarity. This noise is eliminated (ideally) by the conventional flux modulation scheme described in Sec. III D, provided the modulation frequency is much higher than the l/f noise frequency. The second term on the right of Eq. (3.19) is the "out-of phase" mode in which the two fluctuations are of opposite polarity and, roughly speaking, result in a current around the SQUID loop. This term appears, therefore, as a flux noise, vanishing for $V_\Phi = 0$, but is not reduced by the usual flux modulation scheme. Fortunately, there are schemes by which this second term, as well as the first, can be reduced.

One such scheme was described by Koch et al.[34] and is also available on the dc SQUID manufactured by BTi[40]. An alternate scheme, second harmonic detection (SHAD), has recently been developed by Foglietti et al.[39], and we shall briefly describe it. In Fig. 12(a) we see that both I and Φ are switched among the three states A: $(+I, \Phi+\Phi_0/4)$, B: $(0, \Phi+\Phi_0/2)$ and C: $(-I, \Phi+3\Phi_0/4)$. If the static flux is $n\Phi_0$ [dashed curve and pulses in Fig.12(a)], the positive and negative voltage pulses across the SQUID are of equal magnitude, and if one detects this signal at twice the modulation frequency, the output is zero. If we apply an additional flux $\delta\Phi$, however, the V-Φ curve is shifted along the Φ-axis [solid curve and pulses in Fig.12(a)], and the pulse heights become unequal. Lock-in detection at twice the modulation frequency produces an output proportional to $\delta\Phi$. The output from the lock-in detector is integrated and fedback to flux-lock

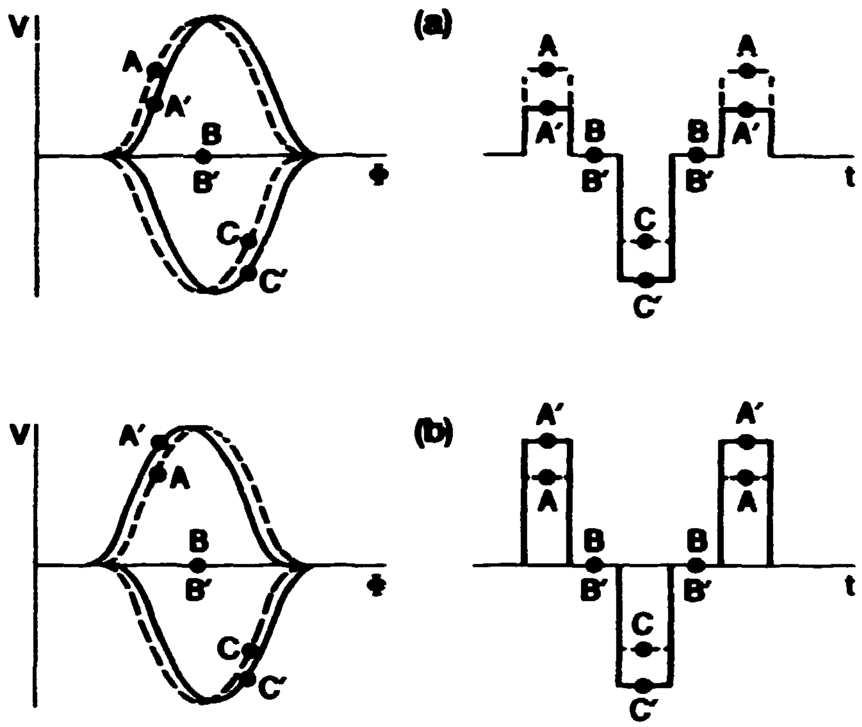

Fig.12 SHAD modulation scheme for a dc SQUID to reduce 1/f noise due to critical current fluctuations: (a) shows the response to an external flux δΦ, and (b) the response to a critical current fluctuation (re-drawn from ref. 39).

the SQUID in the usual way. We note that in-phase fluctuations in critical current increase or decrease the magnitude of the voltage across the SQUID, but do not shift the V-Φ curve along the Φ axis. The magnitudes of the voltage pulses grow or shrink in a symmetric way, and still contain no second harmonic component. Thus, the in-phase fluctuations in critical current produce no response. Similarly, the out-of-phase fluctuations produce no response, as we see in Fig. 12(b). These fluctuations produce an effective flux in the SQUID, with a polarity that depends on the direction of I. Thus, the V-Φ curve shifts to the left for positive bias currents and to the right for negative bias currents. The resulting voltage pulses shrink in a symmetric way, producing no component at the second harmonic of the modulation frequency. Finally, we emphasize that any 1/f flux noise produces an output from the lock-in detector in precisely the same way as the applied flux in Fig. 12(a).

Figure 13 shows an example of the reduction in 1/f noise achieved by Foglietti et al.[34] Figure 13(a) shows the noise as measured with a rf SQUID, and Fig. 13(b), with the conventional flux modulation scheme. The reduction in 1/f noise indicates that in-phase critical current fluctuations have been removed.

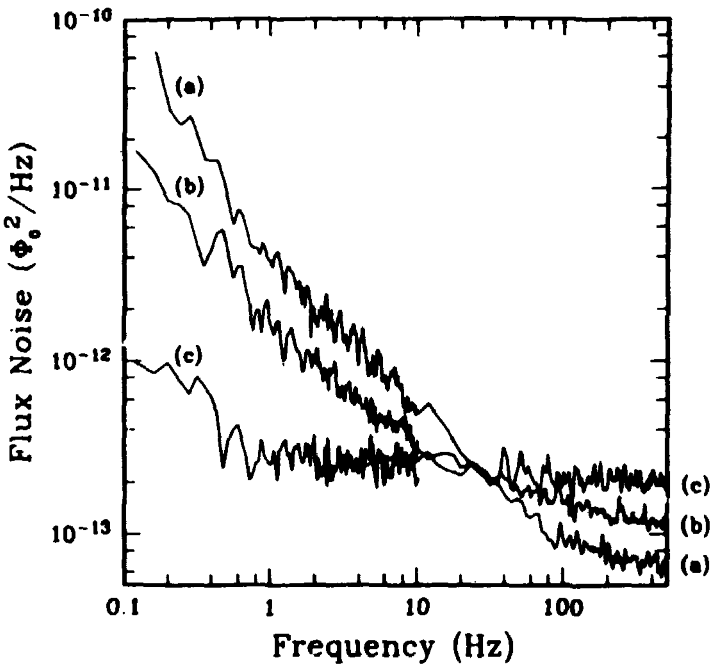

Fig.13 Flux noise spectral density for dc SQUID measured (a) with an rf SQUID small-signal readout scheme, (b) with the flux modulation scheme of Figs.8 and 9 and (c) with SHAD (Fig.12) (re-drawn from ref. 39).

Figure 13(c) shows the considerable reduction in the 1/f noise resulting from SHAD: the measured 1/f noise was $10^{-12}\Phi_0^2\mathrm{Hz}^{-1}$ at 0.1 Hz. We note that SHAD increases the spectral density of the white noise by a factor of 2: V_Φ^2 is reduced by a factor of 4, while the noise is measured only during the 50% of the modulation cycle in which the SQUID is biased.

For measurements at low frequencies, it is clearly advantageous to use a 1/f noise reduction scheme for SQUIDs in which the 1/f noise is dominated by critical current fluctuations. As stressed repeatedly, however, nothing can be done to reduce 1/f flux noise. As we shall see in Sec. VI, 1/f flux noise is a particularly serious problem for high-T_C SQUIDs.

C. Alternate Read-Out Schemes

Although the flux modulation method described in Sec. III.D has been used successfully for many years, alternate schemes recently have been developed. These efforts have been motivated, at least in part, by the need to simplify the electronics required for the multichannel systems used in neuromagnetism - see Sec. V.A. Fujimaki and co-workers[41] and Drung and co-workers[42] have devised schemes in which the output from the SQUID is sensed digitally and fed back as an analog signal to the SQUID to flux-lock the loop. Fujimaki et al.[41] used Josephson digital circuitry to integrate their feedback system on the same chip as the SQUID so that the flux-locked signal was available directly from the cryostat. The system of Drung and co-workers, however, is currently the more sensitive, with a flux resolution of about $10^{-6}\,\Phi_0\mathrm{Hz}^{-1/2}$ in a 50 pH SQUID. These workers also were able to reduce the 1/f noise in the system using a modified version of the modulation scheme of Foglietti et al.[39] Although they need further development, cryogenic digital feedback schemes offer several advantages: they are compact, produce a digitized output for transmission to room temperature, offer wide flux-locked bandwidths, and need not add any noise to the intrinsic noise of the SQUID.

In yet another system, Mück and Heiden[43] have operated a dc SQUID with hysteretic junctions in a relaxation oscillator. The oscillation frequency depends on the flux in the SQUID, reaching a maximum at $(n+1/2)\Phi_0$ and a minimum at $n\Phi_0$. A typical frequency modulation is 100 kHz at an operating frequency of 10 MHz. This technique produces large voltages across the SQUID so that no matching network to the room temperature electronics is required. The room temperature electronics is simple and compact, and the resolution at 4.2 K is about $10^{-5}\Phi_0\mathrm{Hz}^{-1/2}$ with an inductance estimated to be about 80 pH.

IV. THE RF SQUID

A. Principles of Operation

Although the rf SQUID is still the more widely used device because of its long-standing commercial availability, it has seen very little development in recent years. For this reason I will give a rather brief account of its principles and noise limitations, following rather closely descriptions in earlier reviews.[44,45]

The rf SQUID[4,5] shown in Fig.14 consists of a superconducting loop of inductance L interrupted by a single Josephson junction with critical current I_0 and a nonhysteretic current-voltage characteristic. Flux quantization[1] imposes the constraint

$$\delta + 2\pi\Phi_T/\Phi_0 = 2\pi n \qquad (4.1)$$

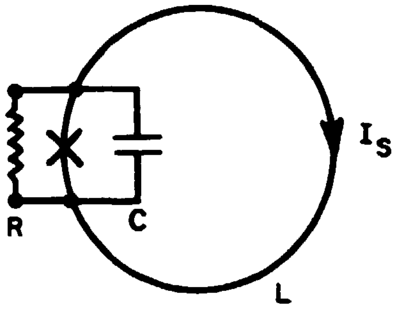

Fig.14 The rf SQUID.

on the total flux Φ_T threading the loop. The phase difference δ across the junction determines the supercurrent

$$I_s = -I_0 \sin(2\pi\Phi_T/\Phi_0) \qquad (4.2)$$

flowing in the ring. A quasistatic external flux Φ thus gives rise to a total flux

$$\Phi_T = \Phi - LI_0 \sin(2\pi\Phi/\Phi_0). \qquad (4.3)$$

The variation of Φ_T with Φ is sketched in Fig.15(a) for the typical value $LI_0 = 1.25\ \Phi_0$. The regions with positive slope are stable, whereas those with negative slope are not. A "linearized" version of Fig.15(a) showing the path traced out by Φ and Φ_T is shown in Fig.15(b). Suppose we slowly increase Φ from zero. The total flux Φ_T increases less rapidly than Φ because the response flux $-LI_S$ opposes Φ. When I_s reaches I_0, at an applied flux Φ_C and a total flux Φ_{TC}, the junction switches momentarily into a nonzero voltage state and the SQUID jumps from the $k = 0$ to the $k = 1$ quantum state. If we subsequently reduce Φ from a value just above Φ_C, the SQUID remains in the $k = 1$ state until $\Phi = \Phi_0 - \Phi_C$, at which point I_s again exceeds the critical current and the SQUID returns to the $k = 0$ state. In the same way, if we lower Φ to below $-\Phi_C$ and then increase it, a second hysteresis loop will be traced. We note that this hysteresis occurs provided $LI_0 > \Phi_0/2\pi$; most practical SQUIDs are operated in this regime. For $LI_0 \approx \Phi_0$, the energy ΔE dissipated when one takes the flux around a single hysteresis loop is its area divided by L:

$$\Delta E \approx I_0\Phi_0. \qquad (4.4)$$

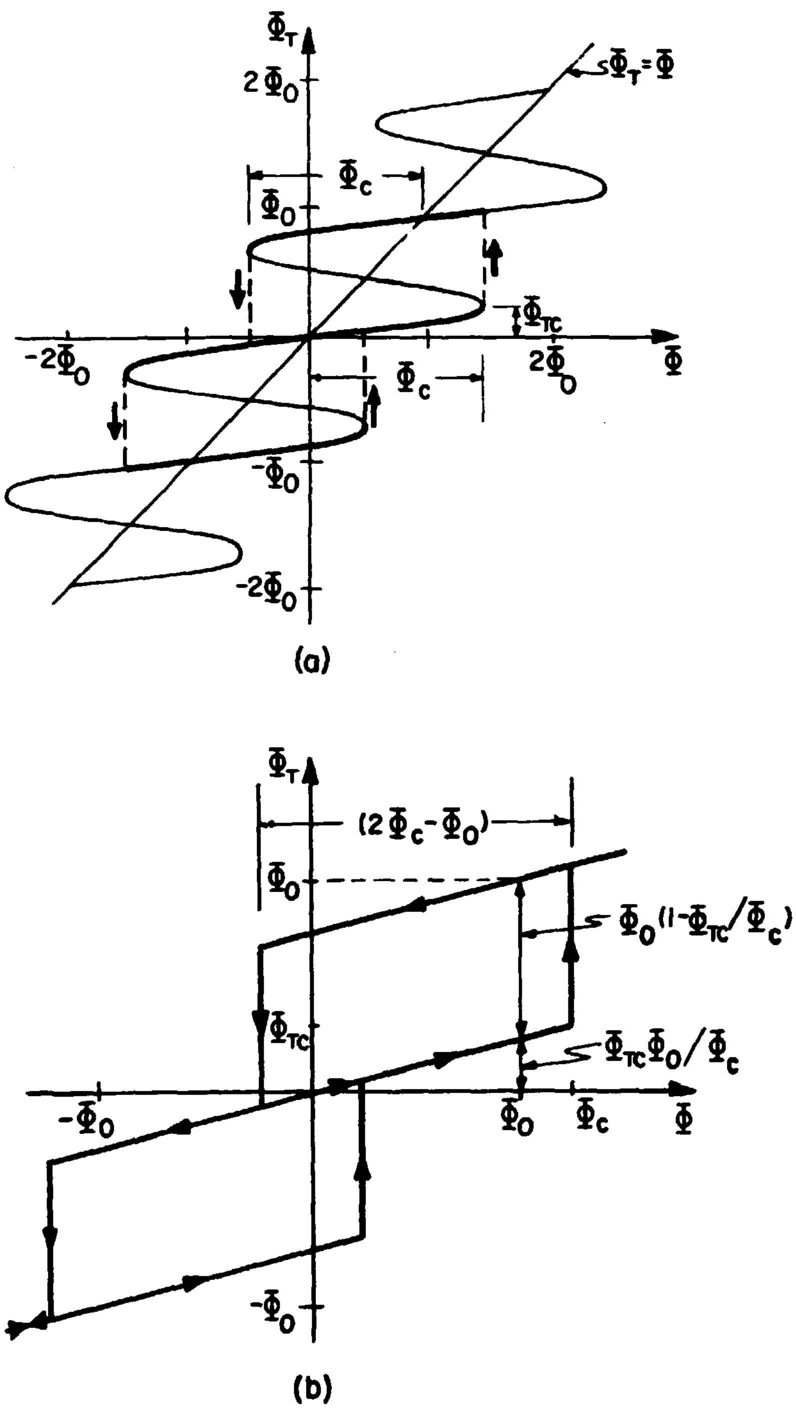

Fig.15 The rf SQUID: (a) total flux Φ_T vs. Φ for $LI_0 = 1.25\,\Phi_0$; (b) values of Φ_T as Φ is quasistatically increased and then decreased.

We now consider the radio frequency (rf) operation of the device. The SQUID is inductively coupled to the coil of an LC-resonant circuit with a quality factor $Q = R_T/\omega_{rf}L_T$ via a mutual inductance $M = K(LL_T)^{1/2}$ - see Fig. 16. Here,

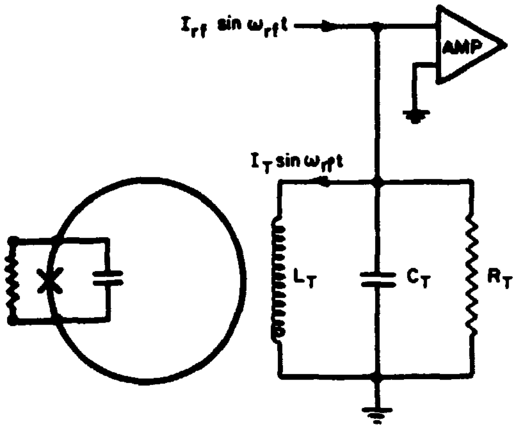

Fig.16 The rf SQUID inductively coupled to a resonant tank circuit.

L_T, C_T, and R_T are the inductance, capacitance and (effective) parallel resistance of the tank circuit, and $\omega_{rf}/2\pi$ is its resonant frequency, typically 20 or 30 MHz. The tank circuit is excited at its resonant frequency by a current $I_{rf} \sin\omega_{rf}t$, which generates a current of amplitude $I_T = QI_{rf}$ in the inductor. The voltage V_T across the tank circuit is amplified with a preamplifier having a high input impedance. First, consider the case $\Phi = 0$. As we increase I_{rf} from zero, the peak rf flux applied to the loop is $MI_T = QMI_{rf}$, and V_T increases linearly with I_{rf}. The peak flux becomes equal to Φ_C when $I_T = \Phi_C/M$ or $I_{rf} = \Phi_C/MQ$, at A in Fig.17. The corresponding peak rf voltage across the tank circuit is

$$V_T^{(n)} = \omega_{rf} L_T \Phi_C/M, \tag{4.5}$$

where the superscript (n) indicates $\Phi = n\Phi_0$, in this case with n=0. At this point the SQUID makes a transition to either the k = +1 state or the k = -1 state. As the SQUID traverses the hysteresis loop, energy ΔE is extracted from the tank circuit. Because of this loss, the peak flux on the next half cycle is less than Φ_C, and no transition occurs. The tank circuit takes many cycles to recover sufficient energy to induce a further transition, which may be into either the k = +1 or -1 states. If we now increase I_{rf}, transitions are induced at the same values of I_T and V_T but, because energy is supplied at a higher rate, the stored energy builds up more rapidly after each energy loss ΔE, and transitions occur more frequently. In the absence of thermal fluctuations (Sec. IV.B), the "step" AB in Fig.17 is at constant voltage. At B, a transition is induced on each positive and negative rf

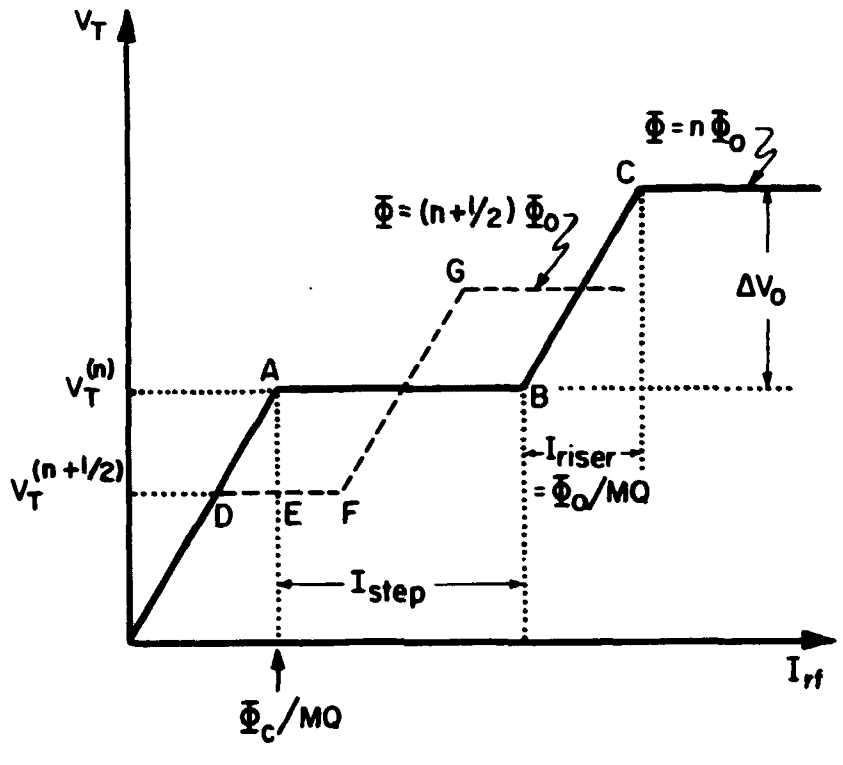

Fig.17 V_T vs. I_{rf} in the absence of thermal noise for $\Phi = n\Phi_0$, $(n+1/2)\Phi_0$.

peak, and a further increase in I_{rf} produces the "riser" BC. At C, transitions from the $k = \pm 1$ to the $k = \pm 2$ states occur, and a second step begins. As we continue to increase I_{rf}, we observe a series of steps and risers.

If we now apply an external flux $\Phi = \Phi_0/2$, the hysteresis loops in Fig.15(b) are shifted by $\Phi_0/2$. Thus, a transition occurs on the positive peak of the rf cycle at a flux $(\Phi_c - \Phi_0/2)$, whereas on the negative peak the required flux is $-(\Phi_c + \Phi_0/2)$. As a result, as we increase I_{rf} from zero, we observe the first step at D in Fig.17 at

$$V_T^{(n+1/2)} = \omega_{rf} L_T(\Phi_C - \Phi_0/2)/M. \tag{4.6}$$

As we increase I_{rf} from D to F, the SQUID traverses only one hysteresis loop, corresponding to the $k = 0$ to $k = +1$ transition at $(\Phi_c - \Phi_0/2)$. A further increase in I_{rf} produces the riser FG, and at G, transitions begin at a peak rf flux $-(\Phi_C + \Phi_0/2)$. In this way, we observe a series of steps and risers for $\Phi = \Phi_0/2$, interlocking those for $\Phi = 0$ (Fig.17). As we increase Φ from zero, the voltage at which the first step appears will drop to a minimum (D) at $\Phi_0/2$ and rise to its maximum value (A) at $\Phi = \Phi_0$. The change in V_T as we increase Φ from 0 to $\Phi_0/2$, found by subtracting Eq. (4.6) from Eq.(4.5), is $\omega_{rf}L_T\Phi_0/2M$. Thus, for a small change in flux near $\Phi = \Phi_0/4$ we find the transfer function

$$V_\Phi = \omega_{rf}L_T/M. \tag{4.7}$$

At first sight, Eq.(4.7) suggests that we can make V_Φ arbitrarily large by reducing K sufficiently. However, we obviously cannot make K so small that the SQUID has no influence on the tank circuit, and we need to establish a lower bound on K. To operate the SQUID, we must be able to choose a value of I_{rf} that intercepts the first step for all values of Φ : this requirement is satisfied if the point F in Fig. 17 lies to the right of E, that is, if DF exceeds DE. We can calculate DF by noting that the power dissipation in the SQUID is zero at D and $\Delta E(\omega_{rf}/2\pi) \approx I_0\Phi_0\omega_{rf}/2\pi$ at F. Thus, $(I_{rf}^{(F)}-I_{rf}^{(D)})V_T^{(n+1/2)}/2 = I_0\Phi_0\omega_{rf}/2\pi$ (I_{rf} and V_T are peak, rather than rms values). Furthermore, we easily can see that $I_{rf}^{(E)} - I_{rf}^{(D)} = \Phi_0/2MQ$. Assuming $LI_0 \approx \Phi_0$ and using Eq.(4.5), we find that the requirement $I_{rf}^{(E)} > I_{rf}^{(D)}$ can be written in the form

$$K^2Q \gtrsim \pi/4. \tag{4.8}$$

If we set $K \approx Q^{-1/2}$, Eq.(4.7) becomes

$$V_\Phi \approx \omega_{rf}(QL_T/L)^{1/2}. \tag{4.9}$$

To operate the SQUID, one adjusts I_{rf} so that the SQUID remains biased on the first step - see Fig.17 - for all values of Φ. The rf voltage across the tank circuit is amplified and demodulated to produce a signal that is periodic in Φ. A modulating flux, typically at 100kHz and with a peak-to-peak amplitude of $\Phi_0/2$, also is applied to the SQUID, just as in the case of the dc SQUID. The voltage produced by this modulation is lock-in detected, integrated, and fed back as a current into the modulation coil to flux-lock the SQUID.

B. Theory of Noise in the rf SQUID

A detailed theory has been developed for noise in the rf SQUID;[46-54] in contrast to the case for the dc SQUID, noise contributions from the tank circuit and preamplifier also are important. We begin by discussing the intrinsic noise

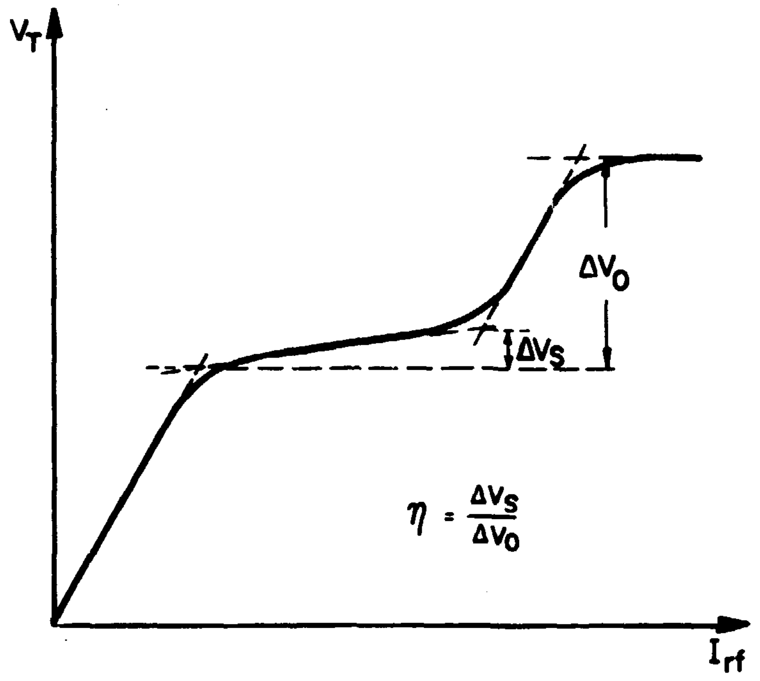

Fig.18 V_T vs. I_{rf} showing the effects of thermal noise.

in the SQUID. In the previous section we assumed that transitions from the $k = 0$ to the $k = 1$ state occurred precisely at $\Phi = \Phi_C$. In fact, thermal activation causes the transition to occur stochastically, at lower values of flux. Kurkijärvi[46] calculated the distribution of values of Φ at which the transitions occur; experimental results[55] are in good agreement with his predictions. When the SQUID is driven with an rf flux, the fluctuations in the value of flux at which transitions occur have two consequences. First, noise is introduced on the peak voltage V_T, giving an equivalent intrinsic flux noise spectral density[47,51]

$$S_\Phi^{(i)} \approx \frac{(LI_0)^2}{\omega_{rf}} \left(\frac{2\pi k_B T}{I_0 \Phi_0} \right)^{4/3} . \tag{4.10}$$

Second, the noise causes the steps to tilt (Fig.18), as we easily can see by considering the case for $\Phi = 0$. In the presence of thermal fluctuations the transition from the $k = 0$ to the $k = 1$ state (for example) has a certain probability of occurring at any given value of the total flux $\Phi + \Phi_{rf}$. Just to the right of A in Fig.17 this transition occurs at the peak of the rf flux once in many rf cycles. Thus, the probability of the transition occurring in any one cycle is small. On the other hand, at B a transition must occur at each positive and negative peak of the rf flux, with unity probability. To increase the transition probability, the peak value of the rf flux and hence V_T must increase as I_{rf} is increased from A to B. Jackel and Buhrman[48], introduced the slope parameter η defined in Fig.18, and showed that it was related to $S_\Phi^{(i)}$ by the relation

$$\eta^2 \approx S_\Phi^{(i)}\omega_{rf}/\pi\Phi_0^2, \tag{4.11}$$

provided η was not too large. This relation is verified experimentally.

The noise temperature T_a of typical rf amplifiers operated at room temperature is substantially higher than that of amplifiers operated at a few hundred kilohertz, and is therefore not negligible for rf SQUIDs operated at liquid ^{4}He temperatures. Furthermore, part of the coaxial line connecting the tank circuit to the preamplifier is at room temperature. Since the capacitances of the line and the amplifier are a substantial fraction of the capacitance of the tank circuit, part of the resistance damping the tank circuit is well above the bath temperature. As a result, there is an additional contribution to the noise which we combine with the preamplifier noise to produce an effective noise temperature T_a^{eff}. The noise energy contributed by these extrinsic sources can be shown to be[48,52] $2\pi\eta k_B T_a^{eff}/\omega_{rf}$. Combining this contribution with the intrinsic noise, one finds

$$\varepsilon \approx \frac{1}{\omega_{rf}}\left(\frac{\pi\eta^2\Phi_0^2}{2L} + 2\pi\eta k_B T_a^{eff}\right). \tag{4.12}$$

Equation (4.12) shows that ε scales as $1/\omega_{rf}$, but one should bear in mind that T_a tends to increase with ω_{rf}. Nonetheless, improvements in performance have been achieved by operating the SQUID at frequencies[56,57] much higher than the usual 20 or 30 MHz. One also can reduce the T_a^{eff} by cooling the preamplifier,[56,58] thereby reducing T_a and reducing the temperature of the tank circuit to that of the bath. However, the best noise energies achieved for the rf SQUID are substantially higher[59] than those routinely obtained with thin-film dc SQUIDs, and for this reason workers requiring the highest possible resolution almost invariably use the latter device.

Fig.19 Cut-away drawing of toroidal SQUID (courtesy BTi, inc.).

C. Practical rf SQUIDs

Although less sensitive than the dc SQUID, the rf SQUID is entirely adequate for a wide range of applications. It is therefore more widely used than the dc SQUID, for the simple reason that reliable, easy-to-operate devices have been commercially available since the early 1970's, notably from BTi (formerly SHE). We therefore shall confine ourselves to a brief description of the device available from this company.

Figure 19 shows a cut-away drawing of the BTi rf SQUID[40], which has a toroidal configuration machined from Nb. One way to understand this geometry is to imagine rotating the SQUID in Fig.14 through 360° about a line running through the junction from top to bottom of the page. This procedure produces a toroidal cavity connected at its center by the junction. If one places a toroidal coil in this cavity, a current in the coil produces a flux that is tightly coupled to the SQUID. In Fig.19, there are actually two such cavities, one containing the tank circuit-modulation-feedback coil and the other the input coil. This separation eliminates cross-talk between the two coils. Leads to the two coils are brought out via screw-terminals. The junction is made from thin films of Nb. This device is self-shielding against external magnetic field fluctuations, and has proven to be reliable and convenient to use. In particular, the Nb input terminals enable one to connect different input circuits in a straightforward way. A typical device has a white noise energy of 5×10^{-29} JHz^{-1}, with a l/f noise energy of perhaps 10^{-28} JHz^{-1} at 0.1 Hz.

V. SQUID-BASED INSTRUMENTS

Both dc and rf SQUIDs are used as sensors in a far-ranging assortment of instruments. I here briefly discuss some of them: my selection is far from exhaustive, but does include the more commonly used instruments.

Each instrument involves a circuit attached to the input coil of the SQUID. We should recognize from the outset that, in general, the presence of the input circuit influences both the signal and noise properties of the SQUID while the SQUID, in turn, reflects a complex impedance into the input. Because the SQUID is a nonlinear device a full description of the interactions is complicated, and we shall not go into the details here. However, one aspect of this interaction, first pointed out by Zimmerman[60], is easy to understand. Suppose we connect a superconducting pick-up loop of inductance L_P to the input coil of inductance L_i to form a magnetometer, as shown in Fig.20(a). It is easy to show that the SQUID inductance L is reduced to the value

$$L' = L[1-\alpha^2 L_i/(L_i+L_P)], \tag{5.1}$$

where α^2 is the coupling coefficient between L and L_i. We have neglected any stray inductance in the leads connecting L_i and L_P, and any stray capacitance. The reduction in L tends to increase the transfer coefficient of both the dc SQUID [Eq.(3.7)] and the rf SQUID [Eq.(4.9)]. In most cases, the reduction of L and the change in the noise properties will be detectable, but they will not have a major effect on the results presented here.

A. Magnetometers and Gradiometers

One of the simplest instruments is the magnetometer [Fig.20(a)]. A pick-up loop is connected across the input coil to make a superconducting flux transformer. The SQUID and input coil are generally enclosed in a superconducting shield. If one applies a magnetic flux, $\delta\Phi^{(p)}$, to the pick-up loop, flux quantization requires that

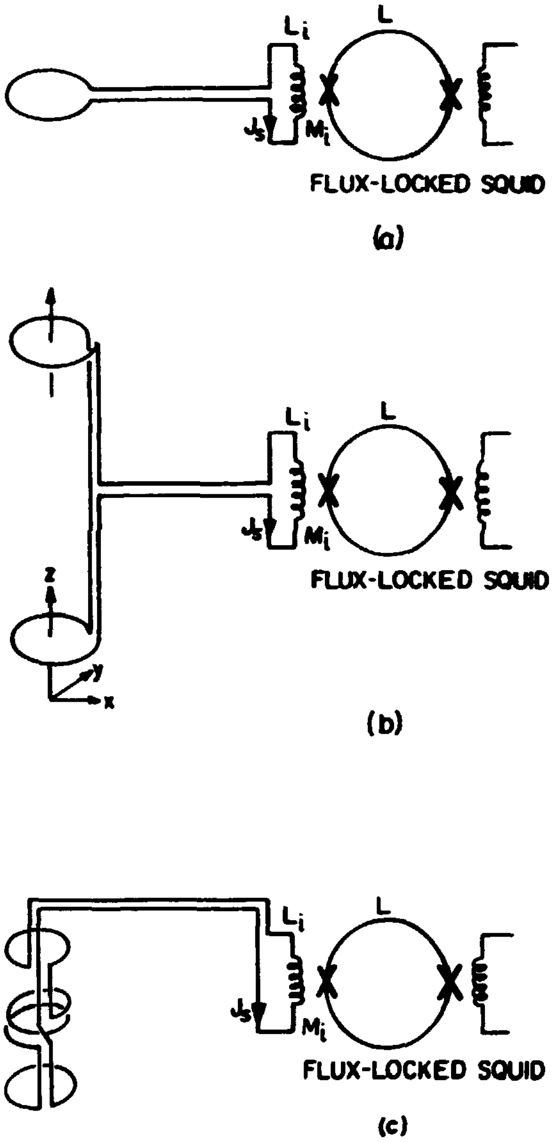

(a)

(b)

(c)

Fig.20 Superconducting flux transformers:(a) magnetometer, (b) first-derivative gradiometer, (c) second-derivative gradiometer.

$$\delta\Phi^{(p)} + (L_i + L_p)J_S = 0, \tag{5.2}$$

where J_S is the supercurrent induced in the transformer. We have neglected the effects of the SQUID on the input circuit. The flux coupled into the SQUID, which we assume to be in a flux-locked loop, is $\delta\Phi = M_i|J_S| = M_i\delta\Phi^{(p)}/(L_i + L_p)$. We find the minimum detectable value of $\delta\Phi^{(p)}$ by equating $\delta\Phi$ with the equivalent flux noise of the SQUID. Defining $S_\Phi^{(p)}$ as the spectral density of the equivalent flux noise referred to the pick-up loop, we find

$$S_\Phi^{(p)} = \frac{(L_p+L_i)^2}{M_i^2} S_\Phi. \tag{5.3}$$

Introducing the equivalent noise energy referred to the pick-up loop, we obtain

$$\frac{S_\Phi^{(p)}}{2L_p} = \frac{(L_p+L_i)^2}{L_i\,L_p}\,\frac{S_\Phi}{2\alpha^2 L}\,. \tag{5.4}$$

We observe that Eq.(5.4) has the minimum value

$$S_\Phi^{(p)}/2L_p = 4\varepsilon(f)/\alpha^2 \tag{5.5}$$

when $L_i = L_p$. Thus, a fraction $\alpha^2/4$ of the energy in the pick-up loop is transferred to the SQUID. In this derivation we have neglected noise currents in the input circuit arising from noise in the SQUID, the fact the the input circuit reduces the SQUID inductance, and any possible coupling between the feedback coil of the SQUID and the input circuit.

Having obtained the flux resolution for $L_i = L_p$, we can immediately write down the corresponding magnetic field resolution $B_N^{(p)} = (S_\Phi^{(p)})^{1/2}/\pi r_p^2$, where r_p is the radius of the pick-up loop:

$$B_N^{(p)} = 2\sqrt{2}L_p^{1/2}\varepsilon^{1/2}/\pi r_p^2\alpha\,. \tag{5.6}$$

For a loop made from wire of radius r_0, one finds[61] $L_p = \mu_0 r_p[\ln(8r_p/r_0) - 2]$, where $\mu_0 = 4\pi \times 10^{-7}$ henries/meter; for a reasonable range of values of r_p/r_0 we can set $L_p \approx 5\mu_0 r_p$. Thus, we obtain $B_N^{(p)} \approx 2(\mu_0\varepsilon)^{1/2}/\alpha r_p^{3/2}$. This indicates that one can, in principle, improve the magnetic field resolution indefinitely by increasing r_p, keeping $L_i = L_p$. Of course, in practice, the size of the cryostat will impose an upper limit on r_p. If we take $\varepsilon = 10^{-28}\,\mathrm{JHz}^{-1}$ (a somewhat conservative value for an rf SQUID), $\alpha = 1$, and $r_p = 25$ mm, we find $B_N^{(p)} \approx 5 \times 10^{-15}$ tesla $\mathrm{Hz}^{-1/2}$ = 5×10^{-11} gauss $\mathrm{Hz}^{-1/2}$. This is a much higher sensitivity than that achieved by any nonsuperconducting magnetometer.

Magnetometers have usually involved flux transformers made of Nb wire. For example, one can make the rf SQUID in Fig.19 into a magnetometer merely by connecting a loop of Nb wire to its input terminals. In the case of the thin-film dc SQUID, one can make an integrated magnetometer by fabricating a Nb loop across the spiral input coil. In this way, Wellstood et al.[18] achieved a magnetic field white noise of 5×10^{-15} tesla $Hz^{-1/2}$ using a pick-up loop with a diameter of a few millimeters.

Magnetometers with typical sensitivities of 0.01 pT $Hz^{-1/2}$ have been used in geophysics in a variety of applications,[42] for example, magnetotellurics, active electromagnetic sounding, piezomagnetism, tectonomagnetism, and the location of hydrofractures. Although SQUID-based magnetometers are substantially more sensitive than any other type, the need to replenish the liquid helium in the field has restricted the extent of their applications. For this reason, the advent of high-temperature superconductors may have considerable impact on this field - see Sec.VI.

An important variation of the flux transformer is the gradiometer. Figure 20(b) shows an axial gradiometer that measures $\partial B_z/\partial z$. The two pick-up loops are wound in opposition and balanced so that a uniform field B_z links zero net flux to the transformer. A gradient $\partial B_z/\partial z$, on the other hand, does induce a net flux and thus generates an output from the flux-locked SQUID. Figure 20(c) shows a second-order gradiometer that measures $\partial^2 B_z/\partial z^2$; Fig.21(a) is a photograph of a practical version.

Thin-film gradiometers based on dc SQUIDs were made as long ago[28] as 1978, and a variety of devices[25,63-67] have been reported since then. To my knowledge, all of the thin film gradiometers made to date have been planar, and therefore measure an off-diagonal gradient, for example, $\partial B_z/\partial x$ or $\partial^2 B_z/\partial x \partial y$. A representative device is shown in Fig.21(b)-(d).

The most important application of the gradiometer thus far is in neuromagnetism[68], notably to detect weak magnetic signals emanating from the human brain. The gradiometer discriminates strongly against distant noise sources, which have a small gradient, in favor of locally generated signals. One can thus use a second-order gradiometer in an unshielded environment, although the present trend is toward using first-order gradiometers in a shielded room of aluminum and mu-metal that greatly attenuates the ambient magnetic noise. In this application, axial gradiometers of the type shown in Fig.20(a) actually sense magnetic field, rather than the gradient, because the distance from the signal source to the pick-up loop is less than the baseline of the gradiometer. The magnetic field sensitivity referred to one pick-up loop is typically 10 fT $Hz^{-1/2}$. Although great progress in this field has been made in recent years, it is generally

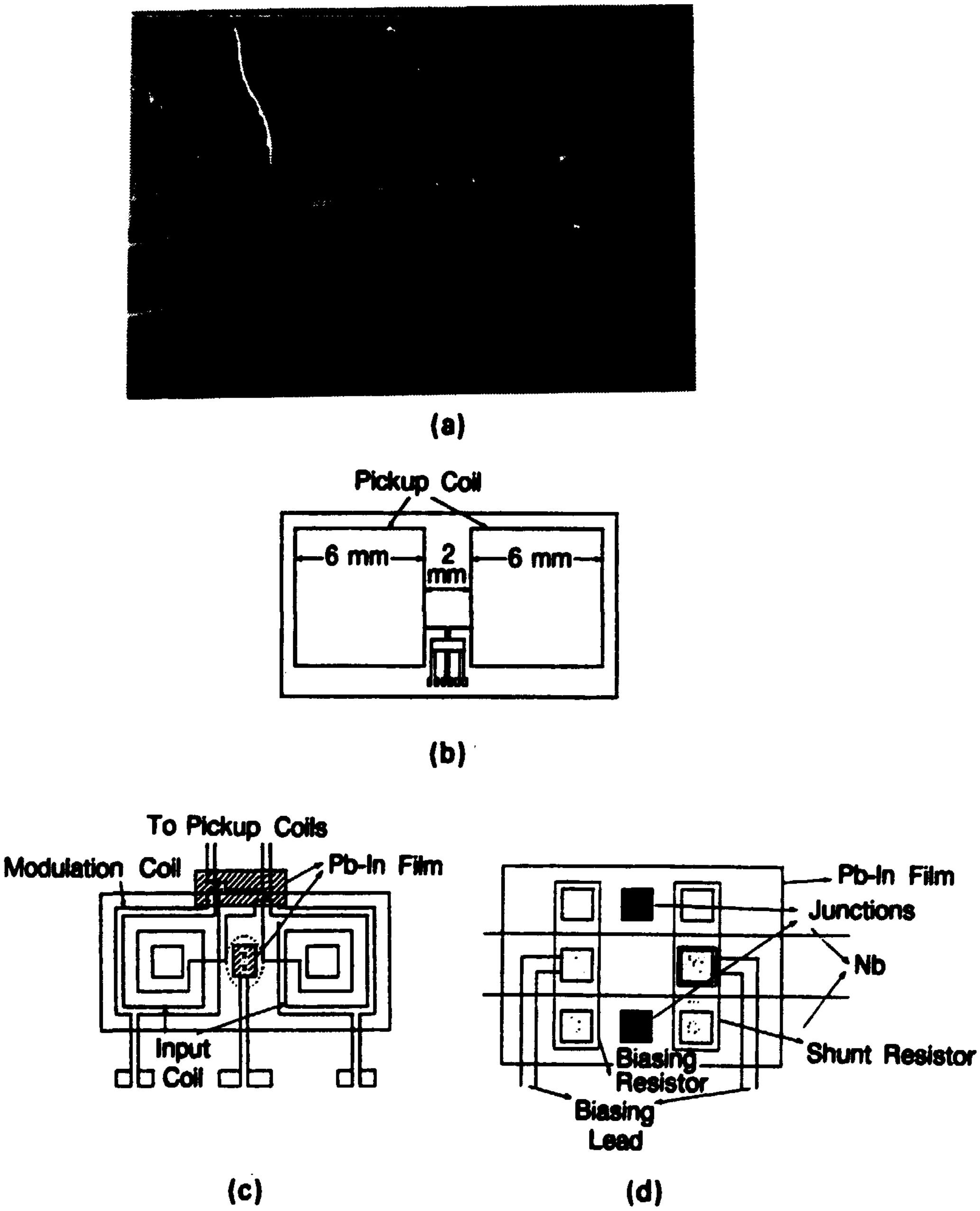

Fig.21 (a) Photograph of wire-wound second-derivative gradiometer for biomedical applications (courtesy BTi, inc.); thin-film first-derivative gradiometer: (b) pick-up loops, (c) two-hole SQUID with spiral input coils, and (d) expanded view of the dotted circle in (c) showing junctions and resistive shunts (from ref. 66).

agreed that one needs an array of 50 to 100 gradiometers to make a clinically viable system. This requirement has greatly spurred the development of integrated, thin-film devices. For example, Knuutila[69] has reported that a 24-channel first-derivative array is under construction.

There are two basic kinds of measurements made on the human brain. In the first, one detects spontaneous activity: a classic example is the generation of magnetic pulses by subjects suffering from focal epilepsy[70]. The second kind involves evoked response: for example, Romani et al.[71] detected the magnetic signal from the auditory cortex generated by tones of different frequencies. Romani has given a extensive review of this work elsewhere in these proceedings.

There are several other applications of gradiometers. One kind of magnetic monopole detector[72] consists of a gradiometer: the passage of a monopole would link a flux h/e in the pick-up loop and produce a step-function response from the SQUID. Gradiometers have recently been of interest in studies of corrosion and in the location of fractures in pipelines and other structures.

B. Susceptometers

In principle, one easily can use the first-derivative gradiometer of Fig.20(b) to measure magnetic susceptibility χ. One establishes a static field along the z-axis and lowers the sample into one of the pick-up loops. Provided χ is nonzero, the sample introduces an additional flux into the pick-up loop and generates an output from the flux-locked SQUID. A very sophisticated susceptometer is available commercially[73]. Room temperature access enables one to cycle samples rapidly, and one can measure χ as a function of temperature between 1.8 K and 400 K in fields up to 5.5 tesla. The system is capable of resolving a change in magnetic moment as small as 10^{-8} emu.

Novel miniature susceptometers have been developed by Ketchen and co-workers[33,74,75]. One version is shown schematically in Fig.22. The SQUID loop incorporates two pick-up loops wound in the opposite sense and connected in series. The two square pick-up loops, 17.5 μm on a side and with an inductance of about 30 pH, are deposited over a hole in the ground plane that minimizes the inductance of the rest of the device. The SQUID is flux biased at the maximum of V_Φ by means of a control current I_C in one of the pick-up loops. One can apply a magnetic field to the two loops by means of the current I_F; by passing a fraction of this current into the center tap I_C, one can achieve a high degree of electronic balance between the two loops. The sample to be studied is placed over one of the loops, and the output from the SQUID when the field is applied is directly proportional to the magnetization. At 4.2 K, the susceptometer is capable of detecting the magnetization due to as few as 3000 electron spins.

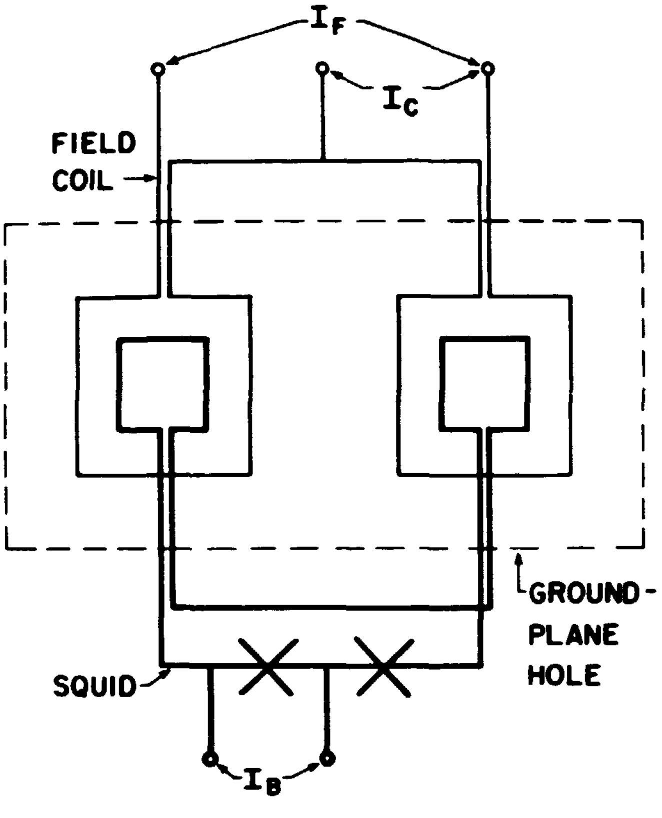

Fig.22 Thin-film miniature susceptometer (from ref. 74).

Awschalom and co-workers[33,75], have used a miniature susceptometer to perform magnetic spectroscopy of semiconductors with picosecond time-resolution. Linearly polarized pulses 4 ps in length are generated with a dye laser and split into a pump train and a weaker probe train. The time delay between the two trains can be varied, and each train is converted to circular polarization by a quarter-wave plate. The beams are chopped at 197 Hz and passed down an optical fiber to the sample in the cryostat. The pump pulses induce a magneto-optical susceptibility χ_{op} which is subsequently measured by means of the much weaker probe pulses of intensity δI that induce a magnetization $\chi_{op}\delta I$. The magnetization is detected by the SQUID at the chopping frequency, and its output is lock-in detected. By varying the time delay between the pump and probe pulses, one can investigate the dynamics of the induced magnetization. One also can vary the dye laser frequency through the red region of the visible spectrum to study the energy dependence of the magnetization. This technique recently has been extended to temperatures down to 0.3K[75].

C. Voltmeters

Probably the first practical application of a SQUID was to measure tiny, quasistatic voltages.[76] One simply connects the signal source -- for example a low resistance through which a current can be passed -- in series with a known resistance and the input coil of the SQUID. The output from the flux-locked loop is connected across the known resistance to obtain a null-balancing measurement of the voltage. The resolution is generally limited by Nyquist noise in the input circuit, which at 4.2 K varies from about 10^{-15} V $\text{Hz}^{-1/2}$ for a resistance of $10^{-8}\,\Omega$ to about 10^{-10} V $\text{Hz}^{-1/2}$ for a resistance of 100 Ω.

Applications of these voltmeters range from the measurement of thermoelectric voltages and of quasiparticle charge imbalance in nonequilibrium superconductors to noise thermometry and the high precision comparison of the Josephson voltage-frequency relation in different superconductors.

D. The dc SQUID as a Radiofrequency Amplifier

Over recent years, the dc SQUID has been developed as a low noise amplifier for frequencies up to 100 MHz or more[77]. To understand the theory for the performance of this amplifier, we need to extend the theory of Sec.III by taking into account the noise associated with the current J(t) in the SQUID loop. For a bare SQUID with $\beta = 1$, $\Gamma = 0.05$ and $\Phi = (2n+1)\Phi_0/4$, one finds the spectral density of the current to be[78]

$$S_J(f) \approx 11\, k_B T/R. \tag{5.7}$$

Furthermore, the current noise is partially correlated with the voltage noise across the SQUID, the cross-spectral density being[78]

$$S_{VJ}(f) \approx 12\, k_B T. \tag{5.8}$$

The correlation arises, roughly speaking, because the current noise generates a flux noise which, in turn, contributes to the total voltage noise across the junction, provided $V_\Phi \neq 0$.

If one imagines coupling a coil to the SQUID, the coil will "see" an impedance Z in the SQUID loop that can be written in the form[79]

$$\frac{1}{Z} = \frac{1}{j\omega L} + \frac{1}{R}\,. \tag{5.9}$$

The dynamic inductance *L* and dynamic resistance *R* are not simply related to L and R, but vary with bias current and flux; for example, 1/*L* is zero for certain values of Φ.

One can make a tuned amplifier, for example, by connecting an input circuit to the SQUID, as shown in Fig.23. In general, the presence of this circuit modifies all of the SQUID parameters and the magnitude of the noise spectral densities.[80] Furthermore, the SQUID reflects an impedance $\omega^2 M_i^2/Z$ into the input circuit. Fortunately, however, one can neglect the mutual influence of the SQUID and input circuit, provided the coupling coefficient α^2 is sufficiently small, as it is under certain circumstances. For the purpose of illustration, we shall derive the noise temperature of the amplifier in Fig.23.

In the weak coupling limit, the noise current $J_N(t)$ induces a voltage $-M_i\dot{J}_N$ into the input circuit, and hence a current $-M_i\dot{J}_N/Z_i$, where

$$Z_i \approx R_i + j\omega L_i + 1/j\omega C_i\ . \qquad (5.10)$$

Here, Z_i is the impedance of the input circuit and L_i and C_i are the series inductance and capacitance. The noise current in the input circuit, in turn, induces a flux $-M_i^2\dot{J}_N/Z_i$ in the SQUID loop and finally a voltage $-M_i^2\dot{J}_N V_\Phi/Z_i$ across the SQUID. Thus, the noise voltage across the SQUID in the presence of the input circuit is[77]

$$V'_N(t) = V_N(t) - M_i^2\dot{J}_N V_\Phi/Z_i\ , \qquad (5.11)$$

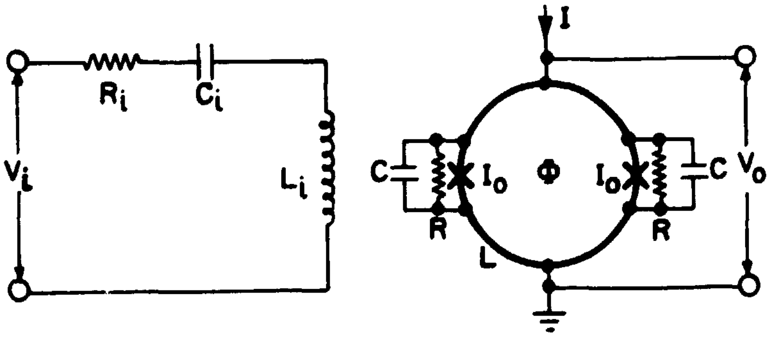

Fig.23 Tuned radiofrequency amplifier based on dc SQUID (from ref.77).

where $V_N(t)$ is the noise voltage of the bare SQUID, which we assume to be unchanged by the input circuit in the limit $\alpha^2 \rightarrow 0$. The spectral density of $V_N'(t)$ is easily found to be

$$S_V'(f) = S_V(f) + \frac{\omega^2 M_i^4 V_\Phi^2 S_J(f)}{|Z_i|^2} - \frac{2\omega M_i^2 V_\Phi(\omega L_i - 1/\omega C_i) S_{VJ}(f)}{|Z_i|^2} \cdot \quad (5.12)$$

We now suppose that we apply a sinusoidal input signal at frequency $\omega/2\pi$, with a mean-square amplitude $<V_i^2>$. The mean-square signal at the output of the SQUID is

$$<V_0^2> = M_i^2 V_\Phi^2 <V_i^2>/|Z_i|^2. \quad (5.13)$$

The signal-to-noise ratio is

$$S/N = <V_0^2>/S_V'(f)B \quad (5.14)$$

in a bandwidth B. It is convenient to introduce a noise temperature T_N for the amplifier by setting $S/N = 1$ with $<V_i^2> = 4k_B T_N R_i B$. This procedure implies that the output noise power generated by the SQUID is equal to the output noise power generated by the resistor R_i when it is at a temperature T_N. We then can optimize T_N with respect to R_i and C_i for a given value of L_i, and find

$$R_i^{(opt)} = \frac{\alpha^2 \omega L_i L V_\Phi}{S_V} (S_V S_J - S_{VJ}^2)^{1/2}, \quad (5.15)$$

$$\frac{1}{\omega C_i^{(opt)}} = \omega L_i \left(1 + \frac{\alpha^2 S_{VJ} L V_\Phi}{S_V}\right). \quad (5.16)$$

and

$$T_N^{(opt)} = \frac{\pi f}{k_B V_\Phi} (S_V S_J - S_{VJ}^2)^{1/2}. \quad (5.17)$$

We note from Eq.(5.16) that the optimum noise temperature occurs off-resonance. It often is more convenient in practice to use the amplifier at the resonant frequency of the tank circuit, given by $\omega^2 L_i C_i = 1$ (neglecting reflected components from the SQUID). In that case, one finds optimum values[77]

$$R_i^{(res)} = \alpha^2 \omega L_i L V_\Phi (S_J/S_V)^{1/2} \tag{5.18}$$

and

$$T_N^{(res)} = \frac{\pi f}{k_B V_\Phi} (S_V S_J)^{1/2}. \tag{5.19}$$

Using the results of Eqs.(3.7), (3.8), (5.7) and (5.8), we can write Eq.(5.18) in the form

$$\alpha^2 \omega L_i / R_i^{(res)} = \alpha^2 Q \approx 1. \tag{5.20}$$

This result shows that high-Q input circuits imply that α^2 is small, thereby justifying the assumption made at the beginning of this section. One also finds

$$T_N(f) \approx 18 f T / V_\Phi \approx 2 f \varepsilon(f) / k_B. \tag{5.21}$$

Thus, although $\varepsilon(f)$ does not fully characterize an amplifier, as noted earlier, within the framework of the model, it does enable one to predict T_N.

One can easily calculate the gain on resonance. For $\alpha^2 << 1$, an input signal V_i produces an output voltage $V_0 \approx (V_i/R_i^{(res)}) M_i V_\Phi$. The power gain is thus $G = (V_0^2/R_D)/(V_i^2/R_i)$, where R_d is the dynamic output resistance $(\partial V/\partial I)_\Phi$ of the SQUID. If we take $R_d \approx R$, we find

$$G \approx V_\Phi/\omega. \tag{5.22}$$

Hilbert and Clarke[77] made several radiofrequency amplifiers with both tuned and untuned inputs, flux biasing the SQUID near $\Phi = (2n + 1)\Phi_0/4$. There was no flux-locked loop. The measured parameters were in good agreement with predictions. For example, for an amplifier with $R \approx 8\ \Omega$, $L \approx 0.4$ nH, $L_i \approx 5.6$

nH, $M_i \approx 1$ nH and $V_\Phi \approx 3 \times 10^{10}$ sec^{-1} at 4.2 K, they found $G = 18.6 \pm 0.5$ dB and $T_N = 1.7 \pm 0.5$ K at 93 MHz. The predicted values were 17 dB and 1.1 K, respectively.

We emphasize that in this theory and these measurements one is concerned only with the noise temperature of the amplifier itself. Nyquist noise from the resistor adds a contribution which, in the example just given, exceeds the amplifier noise. Thus, the optimization procedure just outlined does not necessarily give the lowest system noise, and one would use a different procedure when the value of T_N in Eq.(5.17) or Eq.(5.19) is well below T.

In concluding this section, we comment briefly on the quantum limit for the dc SQUID amplifier. At $T = 0$, Nyquist noise in the shunt resistors should be replaced with zero point fluctuations [Eq.(2.11]. Koch et al.[81] performed a simulation in this limit and concluded that, within the limits of error, the noise temperature of a tuned amplifier in the quantum limit should be given by

$$T_N \approx hf/k_B \ln 2. \tag{5.23}$$

This is the result for any quantum-limited amplifier. The corresponding value for ε was approximately $\hbar$, but it should be emphasized that quantum mechanics does not impose any precise lower limit on ε.[82] A number of SQUIDs have obtained noise energies of $3\hbar$ or less, but there is no evidence as yet that a SQUID has attained quantum-limited performance as an amplifier.

E. Magnetic Resonance

SQUIDs have been used for two decades to detect magnetic resonance.[83] Most of the experiments involved the detection of magnetic resonance at low frequencies or the change in the static susceptibility of a sample induced by a resonance at high frequency. However, the development of the radiofrequency amplifier described in the previous section enables one to detect pulsed magnetic resonance directly at frequencies up to ~300 MHz.

Clarke, Hahn and co-workers have used the radiofrequency amplifier to perform nuclear quadrupole resonance[83] (NQR) and nuclear magnetic resonance[84] (NMR) experiments. They observed NQR in ^{35}Cl, which, in zero magnetic field, has two doubly-degenerate nuclear levels with a splitting of 30.6856 MHz. The experimental configuration is shown in Fig.24. The sample is placed in a superconducting pick-up coil, in series with which is an identical, counterwound coil. These coils are in series with an adjustable tuning capacitor

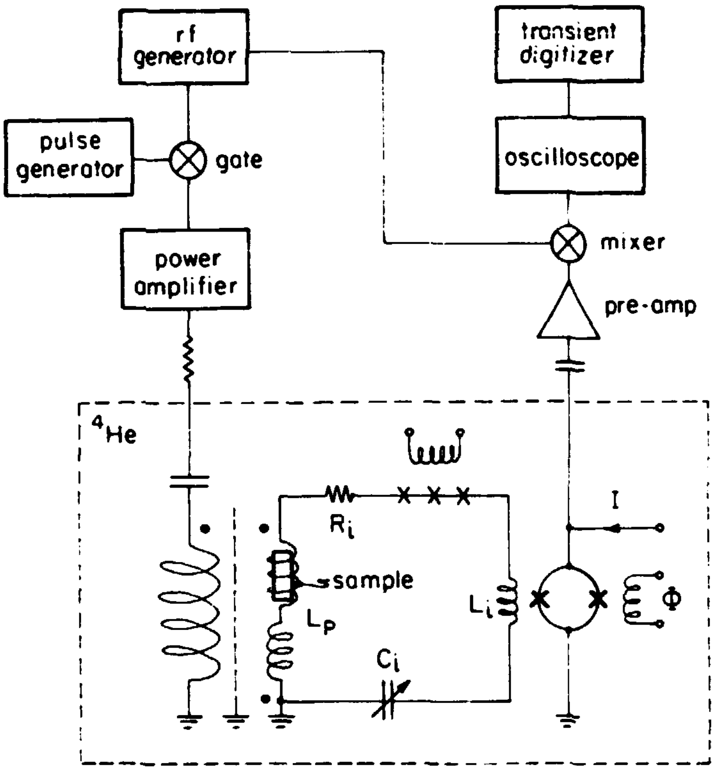

Fig.24 Circuit for NQR with dc SQUID amplifier (from ref. 83).

C_i, the 4-turn input coil of a planar dc SQUID and 20 unshunted Josephson junctions. The resistor R_i represents contact resistance and losses in the capacitor. Radiofrequency pulses applied to the transmitter coil cause the nuclear spins to precess; after each pulse is turned off, the amplifier detects the precessing magnetization. The amplified signal is mixed down with a reference provided by the rf generator, and the mixed-down signal is passed through a low-pass filter, observed on an oscilloscope, and recorded digitally for further analysis.

The major difficulty with this technique, and indeed with other pulsed methods, is the saturation of the amplifier by the very large rf pulse. In the present experiments, the effects of this pulse are reduced in two ways. First, the gradiometer-like configuration gives a common-mode rejection that can be as high as 3×10^4. Second, the series of junctions in the input circuit acts as a Q-spoiler[83]. As the current begins to build in the tuned circuit, the junctions switch to the resistive state with a total resistance of about 1 kΩ, thereby reducing the Q to ~ 1. When the pulse is turned off, the transients die out very quickly and the junctions revert to their zero voltage state, rapidly restoring Q to its full value, usually several thousand. In this way, one can combine the benefits of a high-Q tuned circuit and a sensitive amplifier while retaining a relatively short dead-time after each pulse. In their initial experiments, Hilbert et al.[83] achieved a resolution for a single pulse of ~2 x 10^{16} spins (~2 x 10^{16} nuclear Bohr magnetons) in a bandwidth of 10 kHz.

Subsequently, the Q-spoiler and SQUID amplifier were used to detect atomic polarization induced by precessing nuclear electric quadrupoles.[85] In this experiment, the $NaClO_3$ sample was placed in a capacitor that formed part of the tuned input circuit, and NQR induced in the usual way by radiofrequency pulses. The precessing electric quadruple moments induce a net electric dipole moment in the neighboring atoms, provided the crystal is non-centrosymmetric. These dipole moments, in turn, produce an oscillating electric polarization in the crystal and hence a voltage on the capacitor that is amplified in the usual way. This technique yields information on the location and polarization of atoms near nuclear quadruple moments.

The Q-spoiler and amplifier also have been used to detect nuclear magnetic resonance[84]. In these experiments one applies a magnetic field with an amplitude of several tesla to the crystal, and places the superconducting circuitry some distance away in a relatively low field. In yet another experiment, Sleator et al.[86] observed "spin noise" in ^{35}Cl. An rf signal at the NQR frequency equalized the populations of the two nuclear spin levels, and then was turned off to leave a zero-spin state. A SQUID amplifier (without a Q-spoiler) was able to detect the photons emitted spontaneously as the upper state decayed, even though the lifetime per nucleus for this process was ~ 10^6 centuries. The detected power was about 5 x 10^{-21}W in a bandwidth of about 1.3 kHz.

F. Gravity Wave Antennas

A quite different application of SQUIDs is the detection of minute displacements, such as those of the bar in a gravity wave antenna.[87,88] About a dozen groups worldwide are using these antennas to search for the pulse of gravitational radiation that is expected to be emitted when a star collapses. The radiation induces longitudinal oscillations in the large, freely suspended bar, but because the amplitude is very tiny, one requires the sensitivity of a dc SQUID to detect it. As an example, we briefly describe the antenna at Stanford University, which consists of an aluminum bar 3 meters long (and weighing 4800 kg) suspended in a vacuum chamber at 4.2 K. The fundamental longitudinal mode is at $\omega_a/2\pi \approx 842$ Hz, and the Q is 5 x 10^6. The transducer is shown schematically in

Fig.25. A circular niobium diaphragm is clamped at its perimeter to one end of the bar, with a flat spiral coil made of niobium wire mounted on each side. The two coils are connected in parallel with each other and with the input coil of a SQUID; this entire circuit is superconducting. A persistent supercurrent circulates in the closed loop formed by the two spiral coils. The associated magnetic fields exert a restoring force on the diaphragm so that by adjusting the current, one can set the resonant frequency of the diaphragm equal to that of the bar. A longitudinal oscillation of the bar induces an oscillation in the position of the diaphragm relative to the two coils, thereby modulating their inductances. As a result of flux quantization, a fraction of the stored supercurrent is diverted into the input coil of the SQUID, which detects it in the usual way.

The present Stanford antenna has a root-mean-square strain sensitivity $\langle(\delta\ell)^2\rangle^{1/2}/\ell$ of 10^{-18}, where ℓ is the length of the bar, and $\delta\ell$ is its longitudinal displacement. This very impressive sensitivity, which is limited by thermal noise in the bar, is nonetheless adequate to detect events only in our own galaxy. Because such events are rare, there is very strong motivation to make major improvements in the sensitivity.

If the bar could be cooled sufficiently, the strain resolution would be limited only by the bar's zero-point motion and would have a value of about 3×10^{-21}. At first sight one might expect that the bar would have to be cooled to

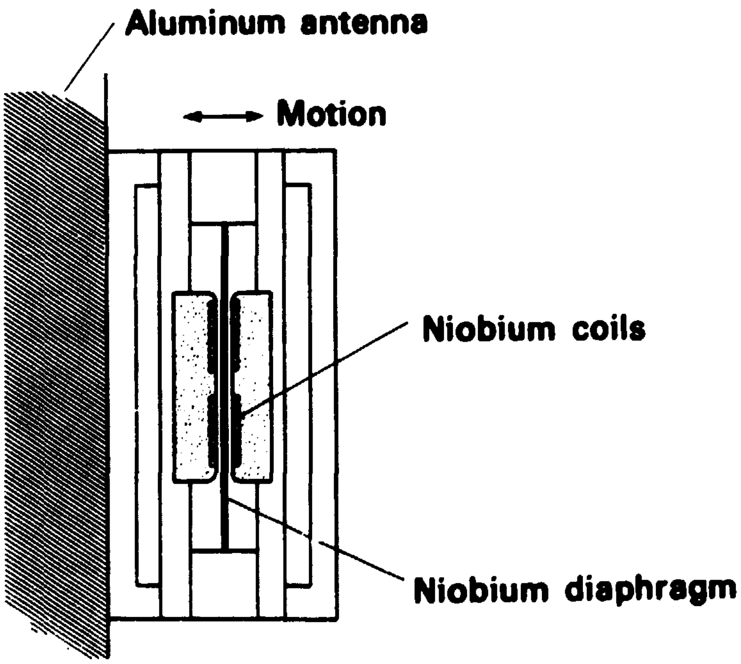

Fig.25 Transducer for gravity wave antenna (courtesy P.F. Michelson).

an absurdly low temperature to achieve this quantum limit, because a frequency of 842 Hz corresponds to a temperature $\hbar\omega_a/k_B$ of about 40 nK. However, it turns out that one can make the effective noise temperature T_{eff} of the antenna much lower than the temperature T of the bar. If a gravitational signal in the form of a pulse of length τ_S interacts with an antenna that has a decay time Q/ω_a, then the effective noise temperature is given approximately by the product of the bar temperature and the pulse length divided by the decay time: $T_{eff} \approx \tau_S\omega_a T/Q$. Thus, one can make the effective noise temperature much less than the temperature of the bar by increasing the bar's resonant quality factor sufficiently. To achieve the quantum limit, in which the bar energy $\hbar\omega_a$ is greater than the effective thermal energy k_BT_{eff}, one would have to lower the temperature T below $Q\hbar/k_B\tau_S$, which is about 40 mK for a quality factor Q of 5×10^6 and a pulse length τ_S of 1 msec. One can cool the antenna to this temperature with the aid of a large dilution refrigerator.

Needless to say, to detect the motion of a quantum-limited antenna, one needs a quantum-limited transducer, a requirement that has been the major driving force in the development of ultra-low-noise dc SQUIDs. As we have seen, however, existing dc SQUIDs at low temperatures are now within striking distance of the quantum limit, and there is every reason to believe that one will be able to operate an antenna quite close to the quantum limit within a few years.

G. Gravity Gradiometers

The gravity gradiometer, which also makes use of a transducer to detect minute displacements, has been pioneered by Paik[89] and Mapoles[90]. The gradiometer consists of two niobium proof masses, each constrained by springs to move along a common axis (Fig.26). A single-layer spiral coil of niobium wire is attached to the surface of one of the masses so that the surface of the wire is very close to the opposing surface of the other mass. Thus, the inductance of the coil depends on the separation of the two proof masses, which, in turn, depends on the gravity gradient. The coil is connected to a second superconducting coil which is coupled to a SQUID via a superconducting transformer. A persistent supercurrent, I, maintains a constant flux in the detector circuit. Thus, a change in the inductance of the pick-up coil produces a change in I, and hence, a flux in the SQUID that is related to the gravity gradient. More sophisticated versions of this design enable one to balance the restoring forces of the two springs electronically,[90] thereby eliminating the response to an

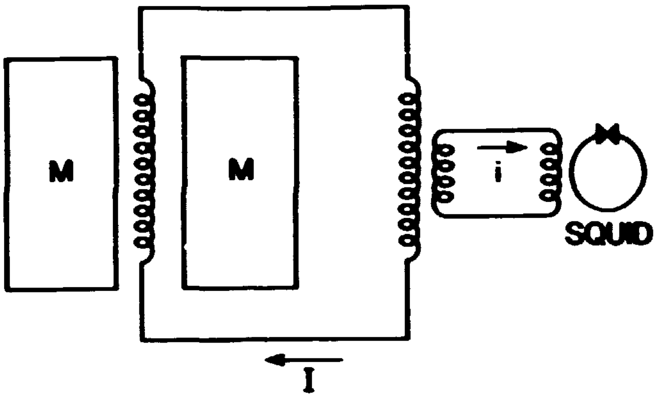

Fig.26 Gravity gradiometer showing two proof masses (M) on either side of a planar spiral coil (from ref. 90).

acceleration (as opposed to an acceleration gradient). Sensitivities of a few Eötvös $Hz^{-1/2}$ have been achieved at frequencies above 2 Hz.

Instruments of this kind could be used to map the earth's gravity gradient, and may be used to test the inverse gravitational square law and in inertial navigation.

VI. THE IMPACT OF HIGH TEMPERATURE SUPERCONDUCTIVITY

The advent of the high-transition-temperature (T_C) superconductors[91] has stimulated great interest in the prospects for superconducting devices operating at liquid (LN) temperature (77 K). Indeed, a number of groups have already successfully operated such SQUIDs. In this section I shall give a brief overview of this work.

A. Predictions for White Noise

In designing a SQUID for operation at LN temperature, one must bear in mind the constraints imposed by thermal noise on the critical current and inductance, $I_0 \gtrsim 10\pi k_B T/\Phi_0$ and $L \lesssim \Phi_0^2/5k_B T$. For T =77 K, we find $I_0 \gtrsim 16\ \mu A$ and $L \lesssim 0.8$ nH. If we take as arbitrary but reasonable values, L = 0.2 nH and $I_0 = 20\ \mu A$, we obtain $2LI_0/\Phi_0 = 4$ for the dc SQUID and $LI_0/\Phi_0 = 2$ for the rf SQUID. These values are not too far removed from optimum, and to a first approximation, we can use the equations for the noise energy given in Secs. III and IV.

For the case of the dc SQUID, the noise energy is predicted by either Eq.(3.9) or Eq.(3.10). However, since nobody has yet made a Josephson tunnel junction with high-T_C materials, it is somewhat unrealistic to use Eq.(3.10), which involves the junction capacitance, and instead we use Eq.(3.9). The value of R is an open question, and we rather arbitrarily adopt 5 Ω, which is not too different from values achieved experimentally for high-T_C grain boundary junctions.[92] With $L = 0.2$ nH, $T = 77$ K and $R = 5\ \Omega$, Eq.(3.9) predicts $\varepsilon = 4 \times 10^{-31}$ J Hz^{-1}. This value is only about one order of magnitude higher that that found at 4.2 K for typical Nb-based, thin-film dc SQUIDs, and is somewhat better than that found in commercially available toroidal SQUIDs. These various values are summarized in Fig.27. If one could actually achieve the predicted resolution in a SQUID at 77 K at frequencies down to 1 Hz or less, it would be adequate for most of the applications discussed in Sec. V.

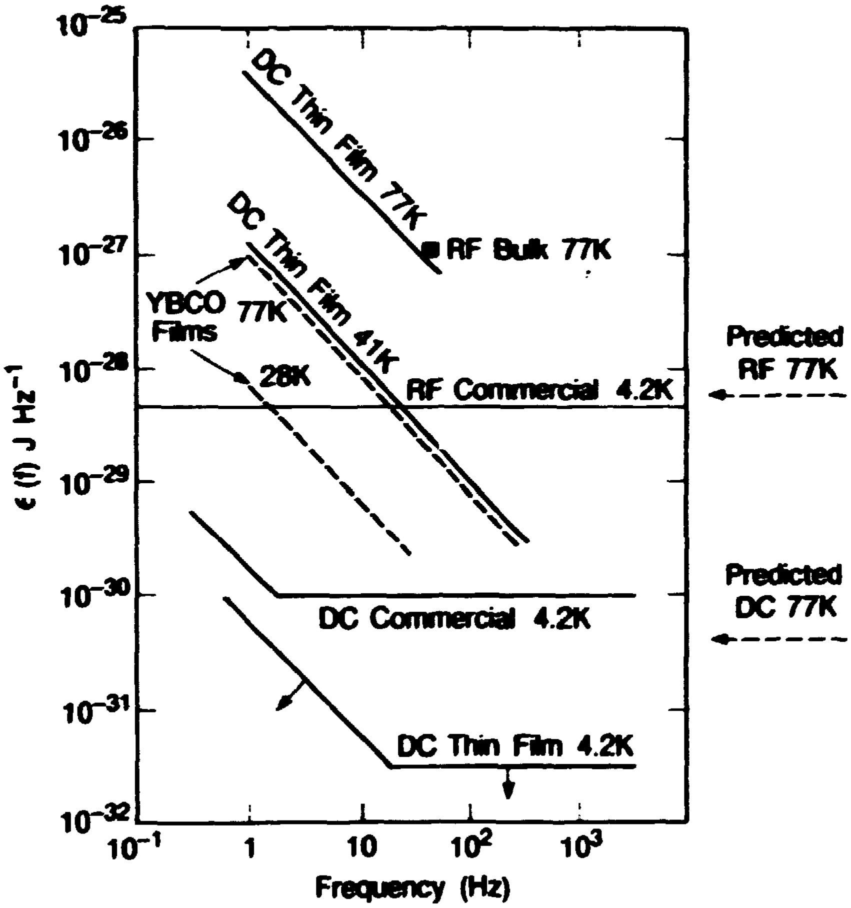

Fig.27 Noise energy ε(f) vs. frequency for several SQUIDs and for a YBCO film.

For the rf SQUID, Eq.(4.10) predicts an intrinsic noise energy of about 6 x 10^{-29} J Hz^{-1} for $I_0 = 20\ \mu A$, $LI_0 = 2\Phi_0$, $\omega_{rf}/2\pi = 20$ MHz and T = 77 K. This value is comparable with the overall value obtained experimentally with 4.2 K devices where the effective noise temperature T_a^{eff} of the preamplifier and tank circuit is much higher than the bath temperature for the case in which the preamplifier is at room temperature - see Sec.IV. B. However, when one operates a SQUID at 77 K, there is no reason for T_a^{eff} to increase and the system noise energy should be comparable with that at 4.2K.

With regard to l/f noise, in general, one might expect both critical current noise and flux noise to contribute. However, it seems impractical to make any a priori predictions of the magnitude of these contributions.

B. Practical Devices

Although a number of dc and rf SQUIDs have been made from YBCO, I shall describe just one of each type. It appears that the first dc SQUID was made by Koch et al.[92] In their devices, they patterned the films by covering the regions of YBCO destined to remain superconducting with a gold film, and ion implanted the unprotected regions so that they became insulators at low temperatures. The configuration is shown in Fig.28. The estimated inductance is 80 pH. The two microbridges exhibited Josephson-like behavior, which actually arose from junctions formed by grain boundaries between randomly oriented grains of YBCO. As the quality of the films has improved, conventional patterning techniques such as lift off and ion etching have become possible. The I-V characteristics of these devices are modulated by an applied flux, although the

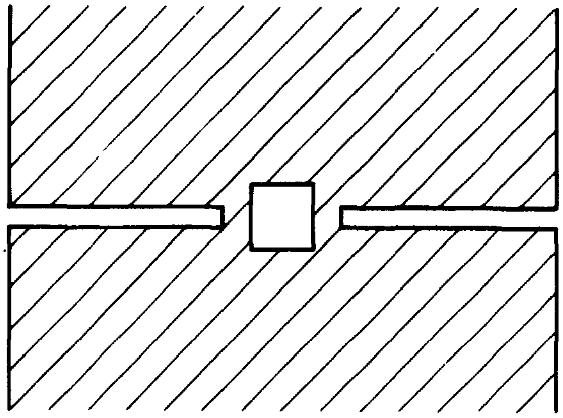

Fig.28 Planar thin-film dc SQUID fabricated from YBCO (re-drawn from ref. 92).

V-Φ curves are often hysteretic and nonperiodic, probably because of flux trapped in the YBCO films. The noise energy scaled approximately as l/f over the frequency range investigated, usually 1 to 10^3 Hz. The lowest noise energies achieved to date at 1 Hz are 4 x 10^{-27} J Hz^{-1} at 41 K and, in a different device, 2 x 10^{-26}J/Hz at 77 K. These values are plotted in Fig.27.

The best characterized rf SQUID reported so far is that of Zimmerman et al.[93] They drilled a hole along the axis of a cylindrical pellet of YBCO, and cut a slot part way along a radius (Fig.29). The pellet was glued into an aluminum holder, also with a slot, and the assembly was immersed in LN. A taper pin forced into the slot in the mount caused the YBCO to break in the region of the cut; when the pin was withdrawn slightly, the YBCO surfaces on the two sides of the crack were brought together, forming a "break junction". The rf SQUID so formed was coupled to a resonant circuit and operated in the usual way. The best flux resolution was 4.5 x $10^{-4}\,\Phi_0\,\text{Hz}^{-1/2}$ at 50 Hz, corresponding to a noise energy of 1.6 x 10^{-27} J Hz^{-1} for L = 0.25 nH - see Fig.27.

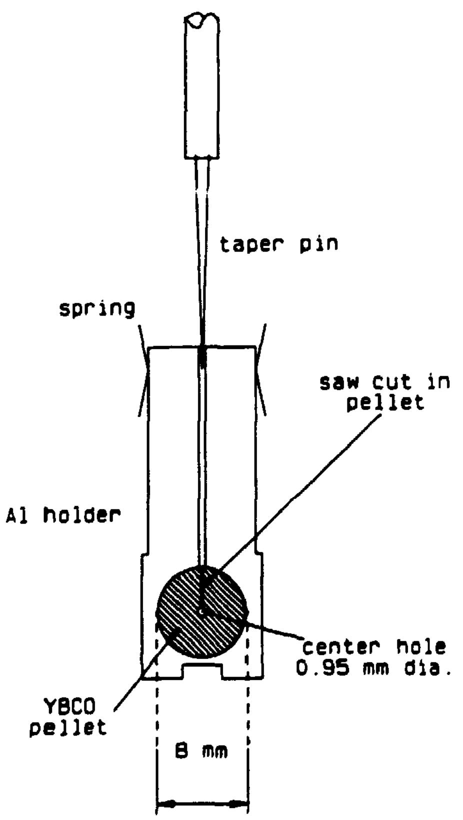

Fig. 29 Break-junction rf SQUID (from ref. 93).

C. Flux Noise in YBCO Films

It is evident that the 1/f noise level in YBCO SQUIDs is very high compared with that in Nb or Pb devices at 4.2K. Ferrari et al.[94] have investigated the source of this noise by measuring the flux noise in YBCO films. Each film, deposited on a $SrTiO_3$ chip, was patterned into a loop and mounted parallel and very close to a Nb-based SQUID (with no input coil) so that any flux noise in the YBCO loop could be detected by the SQUID. The assembly was enclosed in a vacuum can immersed in liquid helium. The SQUID was maintained at 4.2 K, while the temperature of the YBCO film could be increased by means of a resistive heater. Below T_C, the spectral density of the flux noise scaled as 1/f over the frequency range 1 to 10^3 Hz, and increased markedly with temperature. Three films were studied, with microstructure improving progressively with respect to the fraction of grains oriented with the c-axis perpendicular to the substrate. The critical current density correspondingly increased, to a value of 2×10^6 Acm^{-2} at 4.2 K in the best film. The spectral density of the noise measured at 1Hz is shown vs. temperature in Fig.30. We see that in each case the noise increases rapidly as the temperature approaches T_C, and that, at a given

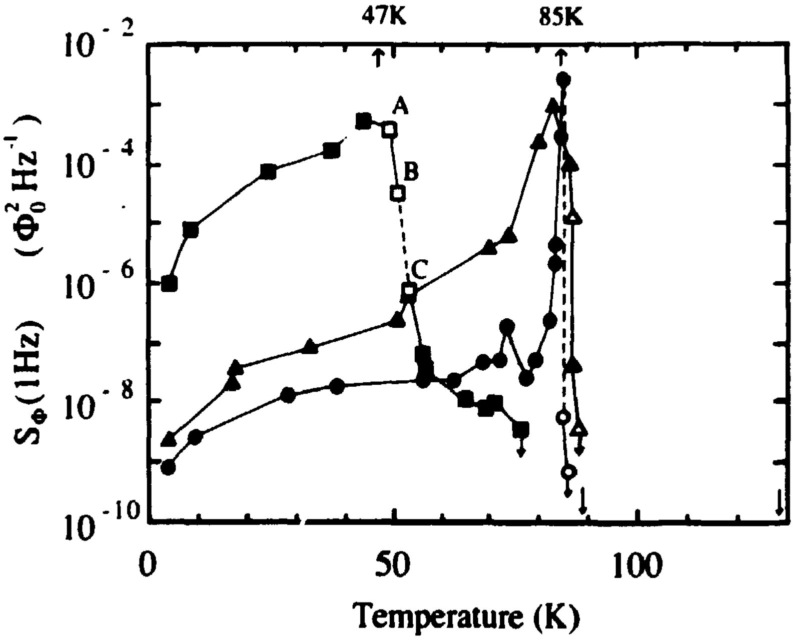

Fig.30 Spectral density of flux noise at 1Hz vs. temperature for three YBCO films: polycrystalline (squares), mixed a- and c-axis (triangles) and >90% c-axis (circles). Solid symbols indicate the noise is 1/f at 1Hz, open that it is white or nearly white (from ref. 94).

temperature, the noise decreases dramatically as the quality of the films is improved. The noise energy estimated at 28 K and 77 K with an assumed inductance of 400 pH is shown in Fig.27.

These results demonstrate that YBCO films are intrinsically noisy. The noise presumably arises from the motion of flux quanta trapped in the films, possibly at grain boundaries. This mechanism is almost certainly the origin of the l/f noise observed in YBCO SQUIDs, and, in general terms, is similar to the origin of l/f flux noise in Nb SQUIDs. It is encouraging that the noise is reduced as the microstructure of the films is improved, and it should be emphasized that there is no reason to believe the lowest noise measured so far represents a lower bound. The implications are that SQUIDs and flux transformers coupled to them should be made of very high quality films.

D. Future Prospects for High-T_c SQUIDs

One rather obvious application of a high-T_C SQUID is as a geophysical magnetometer - see Sec.V.A. At the moment, however, it is not entirely straightforward to predict the performance, since the devices are still evolving, and it is evident from the noise measurements on YBCO films that thin-film flux transformers may introduce considerable levels of low frequency noise. To make an estimate, we assume that we can optimally couple the 77 K dc SQUID with the noise energy shown in Fig.27 to a <u>noiseless</u> flux transformer with a thin-film pick-up loop with a diameter of 50 mm. The estimated loop inductance is about 150 nH. Using Eq.(5.6), we find a magnetic field resolution of roughly 0.1 pT $Hz^{-1/2}$ at 1 Hz, improving to 0.01 pT $Hz^{-1/2}$ at 100 Hz. Although this performance is quite good, one should realize that commercially available coils operated at room temperature offer a resolution of about 0.03 pT $Hz^{-1/2}$ over this frequency range. Furthermore, our assumption of a noise-free flux transformer is rather optimistic. Nonetheless, given the short time over which the high-T_C materials have been available, one should be rather encouraged: a relatively modest reduction in the l/f noise that might be gained from improving the quality of YBCO films or even from using alternate materials might yield a useful geophysical device.

One might note here that the real advantage in using liquid nitrogen as opposed to liquid helium for field applications, is not really the reduction in cost, a savings which is negligible compared with the cost of mounting a field operation, but rather is the very much slower boil-off rate of liquid nitrogen. The latent heat of vaporization of liquid N_2 is about 60 times that of liquid ^4He, so that one should be able to design cryostats of modest size with hold-times of up to a year. It also is noteworthy that liquid Ne, which boils at 27 K, has a latent heat roughly 40 times that of liquid He, and its use also would greatly extend the running time over that of liquid He, for roughly the same cost per day. We see from Fig.30 that the l/f noise in YBCO films can be considerably lower at 27 K than at 77 K, so that the lower temperature operation could be a considerable advantage.

The likely impact of high-T_C SQUIDs on the more demanding neuromagnetic applications is much smaller, at least for the near future. Here, one needs very high sensitivity at frequencies down to 0.1 Hz or less, but is not particularly concerned with the cost of liquid ^4He or the need to replenish it every day or two. Furthermore, low-noise, closed-cycle refrigerators are just becoming available that obviate the need to supply liquid cryogens in environments where electrical power is readily available. Thus, it is difficult to imagine that high-T_C SQUIDs will have a significant impact in this area unless there is a major reduction in the l/f noise.

In concluding this section, we note that two key problems must be solved before high-T_C SQUIDs are likely to become technologically important. The first is the development of a reproducible and reliable Josephson junction. Although great progress has been made with grain boundary junctions, it is not clear that one can base a technology on this technique. Shiota et al.[95] have reported YBCO-insulator-YBCO junctions formed by fluorination of the base electrode, but the I-V characteristics revealed that one of the surfaces was normal. It is hoped that it will be possible to produce all-YBCO junctions exhibiting Josephson tunneling in the near future. An alternative might be a superconductor-normal metal-superconductor junction.[96] The second problem is concerned with the reduction of hysteresis and noise in thin films of high-T_C material. The motion of magnetic flux in the films is responsible for both effects, and one has to learn to produce films with lower densities of flux lines or higher pinning energies. Given the world-wide effort on the new superconductors, there is every reason to be optimistic about the long-term future of SQUIDs based on these materials.

VII. CONCLUDING REMARKS

In this chapter I have tried to give an overview of the current status of dc and rf SQUIDs. I make no pretence that this account is comprehensive. There are many SQUID designs and applications that I have not mentioned, but I hope that I have given some flavor of the amazing versatility of these devices. I find it remarkable that SQUIDs are the basis of both the most sensitive magnetometer available at 10^{-4} Hz and the lowest noise radio frequency amplifier at 10^{8} Hz.

It is somewhat ironic that the best developed devices, thin-film dc SQUIDs, are still not commercially available. This seemingly lamentable state of affairs simply reflects supply and demand. If thin-film SQUIDs were cheaper, people would buy them, and if people would buy them thin-film SQUIDs would be cheaper. The basic problem is that the demand for these devices has not yet been sufficient to convince a company to produce them on a large enough scale to bring the price down to an affordable level. However, some 14 years after low noise dc SQUIDs were first demonstrated, I believe that the situation is finally about to change. After all, one needs only a single major application to make reasonably-priced SQUIDs available for any number of applications, and there now seem to be two such major applications on the horizon. The first is in neuromagnetism: if this application is to become a clinical reality, one will need systems with as many as 100 channels, and the need for 100 channels will inevitably lead to the production of thin-film SQUIDs on a large scale. The second is the advent of high-T_C thin-film SQUIDs. If these devices attain sufficient sensitivity and reliability for geophysical applications, not to mention laboratory-based applications such as voltmeters, they will be in sufficient demand to justify production on a commercial basis.

Either way, I think the next few years are going to be particularly interesting.

ACKNOWLEDGMENTS

I am indebted to D. Crum for supplying Fig. 21(a), P.F. Michelson Fig. 25, D. Paulsen Fig. 19, F. C. Wellstood Fig. 10, and J. E. Zimmerman Fig. 29. For that part of the work carried out at Berkeley, I wish to thank the following for their hard work and dedication: Gordon Donaldson, Wolf Goubau, Mike Heaney, Claude Hilbert, Cristof Heiden, Mark Ketchen, Roger Koch, John Martinis, Bonaventura Savo, Claudia Tesche, Cristian Urbina, Dale Van Harlingen and Fred Wellstood. I thank in particular Roger Koch and Fred Wellstood for helpful conversations during the preparation of this manuscript. I am also grateful to Marty Nisenoff and Harold Weinstock for their careful editing. This work was supported by the Director, Office of Energy Research, Office of Basic Energy Sciences, Materials Sciences Division of the U.S. Department of Energy under contract number W-7405-ENG-48.

REFERENCES

1. London. F.: Superfluids. Wiley, New York 1950
2. Josephson. B.D.: Possible new effects in superconductive tunneling. Phys. Lett. 1. 251-253 (1962); Supercurrents through barriers. Adv. Phys. 14. 419-451 (1965)
3. Jaklevic. R.C., Lambe. J., Silver. A.H., and Mercereau. J.E.: Quantum interference effects in Josephson tunneling. Phys. Rev Lett. 12. 159-160 (1964)
4. Zimmerman. J.E., Thiene. P., Harding. J.T.: Design and operation of stable rf-biased superconducting point-contact quantum devices, and a note on the properties of perfectly clean metal contacts. J. Appl. Phys. 41. 1572-1580 (1970)
5. Mercereau, J.E.: Superconducting magnetometers. Rev. Phys. Appl. 5. 13-20 (1970); Nisenoff. M.: Superconducting magnetometers with sensitivities approaching 10^{-10} gauss. Rev. Phys. Appl. 5. 21-24 (1970)
6. Stewart. W.C.: Current-voltage characteristics of Josephson junctions. Appl. Phys. Lett. 12. 277-280 (1968)
7. McCumber. D.E.: Effect of ac impedance on dc voltage-current characteristics of Josephson junctions. J. Appl. Phys. 39. 3113-3118 (1968).
8. Ambegaokar. V. and Halperin. B. I.: Voltage due to thermal noise in the dc Josephson effect. Phys. Rev. Lett. 22. 1364-1366 (1969)
9. Clarke. J. and Koch. R. H.: The impact of high-temperature superconductivity on SQUIDs. Science 242. 217-223 (1988)
10. Likharev. K. K. and Semenov. V. K.: Fluctuation spectrum in superconducting point junctions. Pis'ma Zh. Eksp. Teor. Fiz. 15. 625-629 (1972). [JETP Lett. 15. 442-445 (1972)]
11. Vystavkin. A. N., Gubankov. V.N., Kuzmin. L.S., Likharev. K.K., Migulin. V.V. and Semenov. V.K.: S-c-s junctions as nonlinear elements of microwave receiving devices. Phys. Rev. Appl. 9. 79-109 (1974)
12. Koch. R.H., Van Harlingen. D.J. and Clarke. J.: Quantum noise theory for the resistively shunted Josephson junction. Phys. Rev Lett. 45. 2132-2135 (1980)
13. Tesche. C.D. and Clarke. J.: dc SQUID: Noise and Optimization. J. Low. Temp. Phys. 27. 301-331 (1977)

14. Bruines. J.J.P., de Waal. V.J. and Mooij. J.E.: Comment on "dc SQUID noise and optimization" by Tesche and Clarke. J. Low. Temp. Phys. **46**. 383-386 (1982)
15. De Waal. V.J., Schrijner. P. and Llurba. R. Simulation and optimization of a dc SQUID with finite capacitance. J. Low. Temp. Phys. **54**. 215-232 (1984)
16. Ketchen. M.B. and Jaycox. J.M.: Ultra-low noise tunnel junction dc SQUID with a tightly coupled planar input coil. Appl. Phys. Lett. **40**. 736-738 (1982)
17. Jaycox J.M. and Ketchen M.B.: Planar coupling scheme for ultra low noise dc SQUIDs. IEEE Trans. Magn., MAG- **17**. 400-403 (1981)
18. Wellstood. F.C., Heiden. C. and Clarke. J.: Integrated dc SQUID magnetometer with high slew rate. Rev. Sci. Inst. **55**. 952-957 (1984)
19. Gurvitch. M., Washington. M.A. and Huggins. H.A.: High quality refactory Josephson tunnel junction utilizing thin aluminum layers. Appl. Phys. Lett. **42**. 472-474 (1983)
20. De Waal. V.J., Klapwijk. T.M. and Van den Hamer. P.: High performance dc SQUIDs with submicrometer niobium Josephson junctions. J. Low. Temp. Phys. **53**. 287-312 (1983)
21. Tesche. C.D., Brown. K.H., Callegari. A.C., Chen. M.M., Greiner. J.H., Jones. H.C., Ketchen. M.B., Kim. K.K., Kleinsasser. A.W., Notarys. H.A., Proto. G., Wang. R.H. and Yogi. T.: Practical dc SQUIDs with extremely low 1/f noise. IEEE Trans. Magn. **MAG-21**. 1032-1035 (1985)
22. Pegrum. C.M., Hutson. D., Donaldson. G.B. and Tugwell. A.: DC SQUIDs with planar input coils. ibid. 1036-1039 (1985)
23. Noguchi. T., Ohkawa. N. and Hamanaka. K.: Tunnel junction dc SQUID with a planar input coil. SQUID 85 Superconducting Quantum Interference Devices and their Applications. Ed. Hahlbohm. H. D. and Lubbig. H. (Walter de Gruyter, Berlin, 1985) 761-766
24. Muhlfelder. B., Beall. J.A., Cromar. M.W. and Ono. R.H.: Very low noise tightly coupled dc SQUID amplifiers. Appl. Phys. Lett. **49**. 1118-1120 (1986)
25. Knuutila. J., Kajola. N., Seppä. H., Mutikainen. R. and Salmi. J.: Design, optimization and construction of a dc SQUID with complete flux transformer circuits. J. Low. Temp. Phys. **71**. 369-392 (1988)
26. Carelli. P. and Foglietti. V.: Behavior of a multiloop dc superconducting quantum interference device. J. Appl. Phys. **53**. 7592-7598 (1982)
27. Clarke. J., Goubau. W.M. and Ketchen. M.B.: J. Low. Temp. Phys. **25**. 99-144 (1976)
28. Ketchen. M.B., Goubau. W.M., Clarke. J. and Donaldson. G.B.: Superconducting thin-film gradiometer. J. Appl. Phys. **44**. 4111-4116 (1978)
29. Wellstood. F.C., and Clarke. J.: unpublished.

30. Wellstood. F.C., Urbina. C. and Clarke. J.: Low-frequency noise in dc superconducting quantum interference devices below 1K. Appl. Phys. Lett. **50**. 772-774 (1987)
31. Roukes. M. L., Freeman. M. R., Germain. R. S., Richardson. R. C. and Ketchen. M. B.: Hot electrons and energy transport in metals at millikelvin temperatures. Phys. Rev. Lett. **55**. 422-425 (1985)
32. Wellstood. F.C., Urbina. C. and Clarke. J.: Hot electron effect in the dc SQUID. Proceedings of the Applied Superconductivity Conference August 21-25 1988 (to be published).
33. Ketchen. M.B., Awschalom. D.D., Gallagher. W.J., Kleinsasser. A.W., Sandstrom. R.L., Rozen. J.R. and Bumble. B.: Design, fabrication and performance of integrated miniature SQUID susceptometers. Proceedings of the Superconductivity Conference August 21-25 1988 (to be published).
34. Koch. R.H., Clarke. J., Goubau. W.M., Martinis. J.M., Pegrum. C.M. and Van Harlingen. D.J.: Flicker (l/f) noise in tunnel junction dc SQUIDs. J. Low. Temp. Phys. **51**. 207-224 (1983)
35. Rogers. C.T. and Buhrman. R.A.: Composition of l/f noise in metal-insulator-metal tunnel junctions. Phys. Rev. Lett. **53**. 1272-1275 (1984)
36. Dutta. P. and Horn. P.M.: Low-frequency fluctuations in solids: l/f noise. Rev. Mod. Phys. **53**. 497-516 (1981)
37. Savo. B., Wellstood. F.C. and Clarke. J.: Low-frequency excess noise in Nb-Al$_2$O$_3$-Nb Josephson tunnel junction. Appl. Phys. Lett. **50**. 1757-1759 (1987)
38. Tesche. C.D., Brown. R. H., Callegari. A. C., Chen. M. M., Greiner. J. H., Jones. H. C., Ketchen. M. B., Kim. K. K., Kleinsasser. A. W., Notarys. H. A., Proto. G., Wang. R. H. and Yogi. T.: Well-coupled dc SQUID with extremely low l/f noise. Proc. 17th International Conference on low temperature physics LT-17. (North Holland, Amsterdam 1984) 263-264
39. Foglietti. V, Gallagher. W. J., Ketchen. M. B., Kleinsasser. A. W., Koch. R. H., Raider. S. I. and Sandstrom. R. L.: Low-frequency noise in low l/f noise dc SQUIDs. Appl. Phys. Lett. **49**. 1393-1395 (1986).
40. Biomagnetic Technologies Inc. 4174 Sorrento Valley Blvd., San Diego, CA 92121.
41. Fujimaki. N., Tamura. H., Imamura. T. and Hasuo. S.: A single-chip SQUID magnetometer. Digest of Tech. papers of 1988 International Solid-state conference. (ISSCC) San Francisco. pp. 40-41. A longer version with the same title is to be published.
42. Drung. D.: Digital Feedback loops for dc SQUIDs. Cryogenics **26**. 623-627 (1986). Drung. D., Crocoll. E., Herwig. R., Neuhaus. M. and Jutzi. W.: Measured performance parameters of gradiometers with digital output. Proceedings of the Applied Superconductivity Conference, August 21-25 1988 (to be published).

43. Mück. M. and Heiden. C.: Simple dc SQUID system based on a frequency modulated relaxation oscillator. Proceedings of the Applied Superconductivity Conference, August 21-25 1988 (to be published).

44. Clarke. J.: Superconducting QUantum Interference Devices for Low Frequency Measurements. Superconductor Applications : SQUIDs and Machines, Ed. Schwartz. B. B.and Foner. S. (Plenum New York 1977). pp 67-124.

45. Giffard. R. P., Webb. R.A. and Wheatley. J.C.: Principles and methods of low-frequency electric and magnetic measurements using rf-biased point-contact superconducting device. J. Low. Temp. Phys. 6. 533-610 (1972)

46. Kurkijärvi. J.: Intrinsic fluctuations in a superconducting ring closed with a Josephson junction. Phys. Rev. B 6. 832-835 (1972)

47. Kurkijärvi. J. and Webb. W.W.: Thermal noise in a superconducting flux detector. Proc. Applied Superconductivity Conf. (Annapolis, MD.) 581-587 (1972)

48. Jackel. L.D. and Buhrman. R.A.: Noise in the rf SQUID. J. Low. Temp. Phys. 19. 201-246 (1975)

49. Ehnholm. G.J.: Complete linear equivalent circuit for the SQUID. SQUID Superconducting Quantum Interference Devices and their Applications. Ed. Hahlbohm. H.D. and Lubbig. H. (Walter de Gruyter, Berlin, 1977) 485-499; Theory of the signal transfer and noise properties of the rf SQUID. J. Low. Temp. Phys. 29. 1-27(1977)

50. Hollenhorst. H.N. and Giffard. R.P.: Input noise in the hysteretic rf SQUID: theory and experiment. J. Appl. Phys. 51. 1719-1725 (1980)

51. Kurkijärvi. J.: Noise in the superconducting flux detector. J. Appl. Phys. 44. 3729-3733 (1973)

52. Giffard. R.P., Gallop. J.C. and Petley. B.N.: Applications of the Josephson effects. Prog. Quant. Electron 4. 301-402 (1976)

53. Ehnholm. G.J., Islander. S.T., Ostman. P. and Rantala. B.: Measurements of SQUID equivalent circuit parameters. J. de Physique 39. colloque C6. 1206-1207 (1978)

54. Giffard. R.P. and Hollenhorst. J.N.: Measurement of forward and reverse signal transfer coefficients for an rf-biased SQUID. Appl. Phys. Lett. 32. 767-769 (1978)

55. Jackel. L. D., Webb. W. W., Lukens. J. E. and Pei. S. S.: Measurement of the probability distribution of thermally excited fluxoid quantum transitions in a superconducting ring closed by a Josephson junction. Phys. Rev. B9. 115-118 (1974)

56. Long. A., Clark. T. D., Prance. R. J. and Richards. M. G.: High performance UHF SQUID magnetometer. Rev. Sci. Instrum. 50. 1376-1381 (1979)

57. Hollenhorst. J. N. and Giffard. R. P.: High sensitivity microwave SQUID. IEEE Trans. Magn. MAG-15. 474-477 (1979)

58. Ahola. H., Ehnholm. G. H., Rantala. B. and Ostman. P.: Cryogenic GaAs-FET amplifiers for SQUIDs. J. de Physique **39**. colloque C6. 1184-1185 (1978); J. Low Temp. Phys. **35**. 313–328 (1979)
59. For a review, see Clarke. J.: Advances in SQUID Magnetometers. IEEE Trans. Election Devices. **ED-27**.1896-1908 (1980)
60. Zimmerman. J. E.: Sensitivity enhancement of Superconducting Quantum Interference Devices through the use of fractional-turn loops. J. Appl. Phys. **42**. 4483-4487 (1971)
61. Shoenberg. D.: Superconductivity (Cambridge University Press 1962) 30.
62. For a review, see Clarke. J.: Geophysical Applications of SQUIDs. IEEE Trans. Magn. **MAG-19**. 288-294 (1983)
63. De Waal. V. J. and Klapwijk. T. M.: Compact Integrated dc SQUID gradiometer. Appl. Phys. Lett. **41**. 669-671 (1982)
64. Van Nieuwenhuyzen G. J. and de Waal. V. J.: Second order gradiometer and dc SQUID integrated on a planar substrate. Appl. Phy. Lett. **46**. 439-441 (1985)
65. Carelli. P. and Foglietti. V.: A second derivative gradiometer integrated with a dc superconducting interferometer. J. Appl. Phys. **54**. 6065-6067 (1983)
66. Koyangi. M., Kasai. N., Chinore. K., Nakanishi. M. and Kosaka. S.: An integrated dc SQUID gradiometer for biomagnetic application. Proceedings of the Applied Superconductivity Conference August 21-25, 1988 (to be published)
67. Knuutila. J., Kajola. M., Mutikainen. R., Salmi. J.: Integrated planar dc SQUID magnetometers for multichannel neuromagnetic measurements. Proc. ISEC '87 p. 261
68. For reviews, see Romani. G. L., Williamson. S. J. and Kaufman. L.: Biomagnetic instrumentation. Rev. Sci. Instrum. **53**. 1815-1845 (1982); Buchanan. D. S., Paulson. D. and Williamson. S. J.: Instrumentation for clinical applications of neuromagnetism. Adv. Cryo. Eng. (to be published)
69. Knuutila. J.: European Physical Society Workshop "SQUID: State of Art, Perspectives and Applications". Rome, Italy June 22-24, 1988 (unpublished)
70. Barth. D. S., Sutherling. W., Engel. J. Jr. and Beatty J.: Neuromagnetic evidence of spatially distributed sources underlying epileptiform spikes in the human brain. Science **223**. 293-296 (1984)
71. Romani. G. L., Williamson. S. J. and Kaufman. L.: Tonotopic organization of the human auditory cortex. Science **216**. 1339-1340 (1982)
72. Cabrera. B.: First results from a superconductive detector for moving magnetic monopoles. Phys. Rev. Lett. **48**. 1378-1381 (1982)
73. Quantum Design, 11568 Sorrento Valley Road, San Diego, CA 92121.

74. Ketchen. M. B., Kopley. T. and Ling. H.: Minature SQUID susceptometer. Appl Phys. Lett. 44. 1008-1010 (1984)
75. Awschalom. D. D. and Warnock. J.: Picosecond magnetic spectroscopy with integrated dc SQUIDs. Proceedings of the Applied Superconductivity Conference August 21-25, 1988 (to be published)
76. Clarke. J.: A superconducting galvanometer employing Josephson tunneling. Phil. Mag. 13. 115-127 (1966)
77. Hilbert. C. and Clarke. J.: DC SQUIDs as radiofrequency amplifiers. J. Low Temp. Phys. 61. 263-280 (1985)
78. Tesche. C. D. and Clarke. J.: DC SQUID: current noise. J. Low Temp. Phys. 37. 397-403 (1979)
79. Hilbert. C. and Clarke. J.: Measurements of the dynamic input impedance of a dc SQUID. J. Low Temp. Phys. 61. 237-262 (1985)
80. Martinis. J. M. and Clarke. J.: Signal and noise theory for the dc SQUID. J. Low Temp. Phys. 61. 227-236 (1985), and references therein.
81. Koch. R.H., Van Harlingen. D. J. and Clarke. J.: Quantum noise theory for the dc SQUID. Appl. Phys. Lett. 38. 380-382 (1981)
82. Danilov. V. V., Likharev. K. K. and Zorin. A. B.: Quantum noise in SQUIDs. IEEE Trans. Magn. MAG-19. 572-575 (1983)
83. Hilbert. C., Clarke. J., Sleator. T. and Hahn. E. L.: Nuclear quadruple resonance detected at 30MHz with a dc superconducting quantum interference device. Appl. Phys. Lett. 47. 637-639 (1985). (See references therein for earlier work on NMR with SQUIDS).
84. Fan. N. Q., Heaney. M.B., Clarke. J., Newitt. D., Wald. L. L., Hahn. E. L., Bielecke. A. and Pines. A.: Nuclear magnetic resonance with dc SQUID preamplifiers. Proceedings of the Applied Superconductivity Conference August 21–25 (1988)
85. Sleator. T., Hahn. E. L., Heaney, M.B., Hilbert. C. and Clarke. J.: Nuclear electric quadrupole induction of atomic polarization. Phys. Rev. Lett. 57. 2756-2759 (1986)
86. Sleator. T., Hahn. E. L., Hilbert, C. and Clarke. J.: Nuclear-spin noise and spontaneous emission. Phys. Rev. B. 36. 1969-1980 (1987)
87. For an elementary review on gravity waves, see Shapiro. S. L., Stark. R.F. and Teukolsky. S. J.: The search for gravitational waves. Am. Sci. 73. 248-257 (1985)
88. For a review on gravity-wave antennae, see Michelson. P. F., Price. J. C. and Taber. R. C.: Resonant-mass detectors of gravitational radiation. Science 237.150-157 (1987)
89. Paik. H. J.: Superconducting tensor gravity gradiometer with SQUID readout. SQUID Applications to Geophysics. Ed. Weinstock H. and Overton. W. C., Jr. (Soc. of Exploration Geophysicists, Tulsa, Oklahoma, 1981) 3-12
90. Mapoles. E.: A superconducting gravity gradiometer. ibid. 153-157
91. Bednorz. J. G. and Muller. K. A.: Possible high T_c superconductivity in the Ba-La-Cu-O system. Z. Phys. B64. 189-193 (1986)

92. Koch. R. H., Umbach. C. P., Clark. G. J., Chaudhari. P. and Laibowitz. R. B.: Quantum interference devices made from superconducting oxide thin films. Appl. Phys. Lett. 51. 200-202 (1987)

93. Zimmerman. J. E., Beall. J. A., Cromar. M. W. and Ono. R. H.: Operation of a Y-Ba-Cu-O rf SQUID at 81K. Appl. Phys. Lett. 51. 617-618 (1987)

94. Ferrari. M. J., Johnson. M., Wellstood. F. C., Clarke. J., Rosenthal. P. A., Hammond. R. H. and Beasley. M. R.: Magnetic flux noise in thin film rings of $YBa_2Cu_3O_{7-\delta}$. Appl. Phys. Lett. 53. 695-697 (1988)

95. Shiota. T., Takechi. K., Takai. Y and Hayakawa. H.: An observation of quasiparticle tunneling characteristics in all Y-Ba-Cu-0 thin film tunnel junctions (unpublished)

96. Mankiewich. P. M., Schwartz. D. B., Howard. R. E., Jackel. L. D., Straughn. B. L., Burkhardt. E. G. and Dayem. A. H.: Fabrication and characterization of an $YBa_2Cu_3O_7$/Au/$YBa_2Cu_3O_7$ S-N-S microbridge. Fifth International Workshop on Future Electron Devices - High Temperature Superconducting Devices. June 2-4, 1988, Miyaki-Zao, Japan. 157-160

Risø National Laboratory **Risø - M - 2756**

Title and author(s)

SUPERCONDUCTIVITY

Lecture notes of basic courses presented at
1st Topsøe Summer School on Superconductivity

Editors: N.H. Andersen and K. Mortensen

Date December 1988

Department or group
Physics

Groups own registration number(s)

Project/contract no.

Pages 241 **Tables** 10 **Illustrations** 128 **References** 219

ISBN 87-550-1477-1

Abstract (Max. 2000 char.)

This report contains lecture notes of the basic lectures presented at the 1st Topsøe Summer School on Superconductivity held at Risø National Laboratory, June 20-24, 1988. The following lecture notes are included: L.M. Falicov: "Superconductivity: Phenomenology", A. Bohr and O. Ulfbeck: "Quantal structure of superconductivity. Gauge angle", G. Aeppli: "Muons, neutrons and superconductivity", N.F. Pedersen: "The Josephson junction", C. Michel: "Physicochemistry of high-T_c superconductors", C. Laverick and J.K. Hulm: "Manufacturing and application of superconducting wires", J. Clarke: "SQUID concepts and systems".

Descriptors

Available on request from Risø Library, Risø National Laboratory, (Risø Bibliotek, Forskningscenter Risø),
P.O. Box 49, DK-4000 Roskilde, Denmark.
Telephone 02 37 12 12, ext. 2262. Telex: 43116, Telefax: 02 36 06 09

Available on exchange from:
Risø Library,
Risø National Laboratory,
P.O. Box 49, DK-4000 Roskilde, Denmark
Phone (02) 37 12 12 ext. 2262

ISBN 87-550-1477-1
ISSN 0418-6435